Baryons, branes, and (striped) black holes

Applications of the gauge / gravity duality to quantum chromodynamics and condensed matter physics

by

Jared Brendan Stang

B.Sc. (Honours), The University of Toronto, 2009

A THESIS SUBMITTED IN PARTIAL FULFILLMENT OF
THE REQUIREMENTS FOR THE DEGREE OF

DOCTOR OF PHILOSOPHY

in

The Faculty of Graduate and Postdoctoral Studies

(Physics)

THE UNIVERSITY OF BRITISH COLUMBIA

(Vancouver)

August 2014

Abstract

The gauge / gravity duality, or holographic correspondence, is a theoretical tool that allows the description of strongly coupled field theory through a dual classical gravity theory. In this thesis, we advance the use of numerical methods in applications of the holographic correspondence to the study of strongly coupled field theories in three situations.

Firstly, we study the relationship between chemical potential and charge density across myriad examples of Lorentz invariant $3+1$ dimensional holographic field theories with the minimal structure of a conserved charge. Solving for the classical gravitational configurations dual to the field theories and extracting the charge density and chemical potential, we enumerate the relationships that can exist in a wide range of holographic theories.

Secondly, we study the spontaneous formation of inhomogeneous (striped) order, a phenomenon that has been observed in the cuprates, in a $2+1$ dimensional strongly coupled field theory. By numerically solving the equations of motion using finite difference techniques, we construct the full nonlinear striped black brane solutions that provide the gravity dual to this field theory. We evaluate the thermodynamics and show that the system undergoes a second order phase transition to the striped phase as the temperature is lowered.

Finally, we apply the holographic correspondence to study particular aspects of quantum chromodynamics (QCD). First, we develop a phenomenological holographic model to describe the colour superconductivity phase of QCD, which is believed to exist at large quark density. We construct the phase diagram for our model, which includes confined, deconfined, and superconducting phases. In a separate project, we revisit the construction of the baryon in the Sakai-Sugimoto model of holographic QCD. In this model, gauge field configurations on the probe D8 flavour branes with non-trivial topological charge (instantons) correspond to baryons in the dual field theory. In order to extend previous studies, we relax an assumption of spherical symmetry and, utilizing pseudospectral methods, numerically construct the deformed instanton in the bulk. Compared to previous studies, we find significantly more realistic values for the mass and size of the baryon.

Preface

A version of chapter 2 has been published: Fernando Nogueira and Jared B. Stang, *Density versus chemical potential in holographic field theories*, Physical Review **D86**, 026001 (2012) [1]. This work was an equal collaboration between the thesis author and a colleague. The thesis author performed and checked all analytical and numerical calculations and produced all figures for the manuscript. Writing and editing the work was a collaborative effort.

Versions of chapters 3 and 4, based on the same project, have been published: *i.* Moshe Rozali, Darren Smyth, Evgeny Sorkin, and Jared B. Stang, *Holographic Stripes*, Physical Review Letters **110**, 201603 (2013) [2], and; *ii.* Moshe Rozali, Darren Smyth, Evgeny Sorkin, and Jared B. Stang, *Striped Order in AdS/CFT correspondence*, Physical Review **D87**, 126007 (2013) [3]. The thesis author was primarily responsible for numerical calculations and provided the majority of the results used in the manuscripts. For manuscript *i*, the thesis author was responsible for editing and presentation, and contributed figures 3.3 through 3.5. For manuscript *ii*, the thesis author was primarily responsible for the writing of the paper, with the exception of section 4.3, which was first drafted by Evgeny Sorkin.

A version of chapter 5 has been published: Pallab Basu, Fernando Nogueira, Moshe Rozali, Jared B. Stang, and Mark Van Raamsdonk, *Towards A Holographic Model of Color Superconductivity*, New Journal of Physics **13**, 055001 (2011) [4]. In addition to performing analytical and numerical computations throughout the project and editing the manuscript, the thesis author contributed results that appeared in section 5.5, including figures 5.9 through 5.12.

A version of chapter 6 has been published: Moshe Rozali, Jared B. Stang, and Mark Van Raamsdonk, *Holographic baryons from oblate instantons*, Journal of High Energy Physics, **1402**, 044 (2014) [5]. The thesis author acted as principal investigator, being responsible for all analytical and numerical computations and for writing the majority of the manuscript. The exceptions were sections 6.1 and 6.5, for which the thesis author's drafts were significantly modified by Mark Van Raamsdonk.

Table of Contents

Appendices

List of Tables

List of Figures

Acknowledgements

There are many people to thank for their contributions to my personal and professional development over the years of my graduate studies.

Firstly, for significant contributions to my development as a researcher and a physicist, guidance in navigating both the subject of string theory and the process of completing a doctoral dissertation, and support to pursue my interests both in my physics research and elsewhere, I thank my supervisor, Mark Van Raamsdonk.

In terms of my professional activities, I also extend my gratitude to: Moshe Rozali, for many hours of discussion and mentorship, even though he had no formal obligation to do so; my supervisory committee (Joanna Karczmarek, Mark Halpern, and Jörg Rottler), for providing useful feedback and benchmarks for me as I progressed through the stages of my degree; my collaborators (Pallab Basu, Fernando Nogueira, Darren Smyth, and Evgeny Sorkin), for shared discoveries and frustrations; Ido Roll, for taking me on to pursue an interesting side project; members of PHASER-G (especially Georg Rieger and Joss Ives), for providing productive distractions from my physics research; the Natural Science and Engineering Research Council of Canada and the Killam Trusts, for financial support; Matt Choptuik, for enabling my access to computational resources; and my fellow graduate students, for providing a stimulating and enjoyable environment throughout my studies.

In terms of my personal life, I thank my brothers (Dustin and Conner Stang) for their camaraderie. I thank Brenda Shkuratoff dearly for her continual love, support, and friendship. Finally, and most importantly, I thank my parents (Bernadine and Bruce Stang) for making it all possible: although I walked through the doors, you held them open for me.

To my parents.

Chapter 1

Introduction

1.1 Motivation

Quantum field theory is one of the most ubiquitous and useful theoretical frameworks ever developed. It provides the backbone underlying two of the largest and most prominent areas of modern physics: particle physics and condensed matter physics. Within these contexts, the framework has been extremely successful as a theoretical description of experimentally observed phenomena. In particular, quantum electrodynamics (quantum field theory applied to the theory of photons and electrons) has provided the most precise match between theory and experiment ever.[1]

A key feature of quantum electrodynamics, which allows such precise calculations and which is shared by many of the situations successfully described by quantum field theory, is that the theory is *weakly coupled*. Physically, this means that if the system is perturbed slightly (say we grab and shake an electron), the configuration will not change very much (other electrons will only be slightly bothered). Mathematically, weakly coupled theories admit a perturbative description, in which the effect of interactions can be computed by expanding around the simpler non-interacting system, resulting in a series expression for the result. Depending on the precision needed for a calculation, this series may be truncated at some point and higher order interactions may be neglected.

However successful the perturbative approach is, it is fundamentally limited to the description of weakly coupled theories. There are many systems in nature which are properly described as *strongly coupled* quantum field theories. A prime example of this is quantum chromodynamics (QCD, quantum field theory for quarks and gluons) at low energies. For these theories, if the system is perturbed slightly (if we grab and shake a quark), the entire configuration may change significantly. From a calculational perspective, the perturbative approach is no longer applicable, as the first few terms in the

[1] This is for the magnetic moment of the electron, the most recent measurement of which was reported in [6].

series will not be a good approximation of the exact result, and we need different methods with which to study the theory.

One possible route to study strongly coupled field theory is through lattice techniques. Schematically, one Euclideanizes the theory before discretizing spacetime by putting it on a lattice. The problem of solving the theory becomes the problem of minimizing the (Euclidean) action on this lattice. Established techniques, such as the Monte Carlo method, can then be applied to find the minimized action. Lattice techniques, however, have several shortcomings. Firstly, the computational power needed to study these theories becomes very large very quickly as one tries to increase the accuracy of calculations. Secondly, and perhaps more importantly, these techniques are limited to field theory at zero charge density. Finite density systems are interesting in a variety of situations, including, for example, neutron stars and superconductors. Upon analytically continuing the action, a chemical potential term will become imaginary, resulting in highly oscillatory behaviour in the path integral, which is not amenable to study with Monte Carlo techniques. Thus, lattice techniques are limited in their ease of implementation and applicability.

A more contemporary and flexible approach to the study of strongly coupled field theory, the application of which is the topic of this thesis, is the gauge / gravity duality.[2] First proposed in 1997 [7–9], this remarkable correspondence states that a strongly coupled field theory describes identical physics as a classical theory of gravity (in one higher dimension). Under the duality, the problem of calculating observables in the field theory is mapped to the relatively simpler problem of solving classical equations of motion. The correspondence provides calculational access to many novel regimes of strongly coupled field theory, including field theory at finite density.

In the years since the discovery of the holographic correspondence, it has been applied to the study of strongly coupled field theories in many interesting ways. One example and success story is a study of viscosity in strongly coupled field theories [10], which provides some theoretical explanation for the small viscosities of the quark-gluon plasma seen at the Relativistic Heavy Ion Collider. Further examples of applications of the correspondence include

[2]The *holographic correspondence* is a general term to describe the correspondence between a gravitational theory in $d+1$ dimensions and a theory without gravity in d dimensions. Specifying to the *gauge / gravity duality* identifies the d-dimensional theory as a gauge field theory. Finally, the *AdS/CFT correspondence* (anti-de Sitter / conformal field theory) refers to a specific class of theories that exhibit this relationship, in which a gravity theory with anti-de Sitter asymptotics is dual to a conformal field theory. In this thesis, as is common, we use these three labels synonymously.

models of superconductors [11], superfluids [12], and QCD (for example, [13]). While exact holographic descriptions of QCD or high-T_c superconductivity, as seen in experiments, are not yet possible, models that elucidate universal features of similar classes of systems are available for study. In this way, the correspondence currently offers tremendous potential for general results from which qualitative and (in some cases) quantitative lessons may be drawn.

In this thesis, the gauge / gravity duality is applied to the study of various strongly coupled field theoretic phenomena, with the goal of contributing to and advancing the literature on holographic techniques and results. To this end, we describe projects focused in three domains: general holographic field theories, applications to condensed matter systems, and applications to QCD. To facilitate these studies, we make extensive use of numerical techniques, from the application of standard 'blackbox' solvers for ordinary differential equations to the use of finite difference and pseudospectral methods for the partial differential classical field equations that arise in inhomogeneous situations. The studies applying the latter techniques contribute to the forefront of the emerging research direction combining numerical techniques and holographic methods.

A brief outline of this introductory chapter is as follows. In section 1.2, we provide a more detailed background for the gauge / gravity duality, including a more precise statement of the correspondence, a sketch of the original 'derivation', and examples of the explicit mapping between field theory and gravitational observables. In section 1.3, we provide a summary of each of the four projects that comprise the content of this thesis.

1.2 Introduction to the gauge / gravity duality

Here we provide a brief review of certain salient features of the gauge / gravity duality, the main theoretical tool used in this thesis.[3] In section 1.2.1, we describe the gauge / gravity duality in generality, defining it more precisely than above and providing a conceptual argument as to why it may be true. In section 1.2.2, we review the specific construction that motivated the original statement of the conjecture. This is the duality between strongly coupled $\mathcal{N} = 4$ $SU(N)$ super-Yang-Mills theory on $3+1$ dimensional Minkowski space and type IIB string theory on $AdS_5 \times S^5$. This subsection contains technical details which depend on some prior knowledge

[3]There are many existing reviews of the holographic correspondence, including [14–17]. Reports the thesis author found particularly useful are [18–21].

of string theory. In section 1.2.3, we provide some of the standard entries in the holographic 'dictionary', which relates observables and constructions on either side of the correspondence. Finally, section 1.2.4 briefly motivates the use of and need for numerical techniques in the study of strongly coupled field theory using the holographic correspondence.

1.2.1 The gauge / gravity duality

In this section, we discuss the gauge / gravity duality in generality, limiting ourselves to features that are present across examples, and providing an argument as to why such a correspondence may exist. For a particular construction manifesting the correspondence, see section 1.2.2.

The gauge / gravity duality, in general, is the conjectured equivalence between a quantum field theory in d spacetime dimensions and a theory of quantum gravity in $d+1$ spacetime dimensions.[4] This equivalence is a complete equivalence of the physical spectra at any value of the parameters in the theory, "including operator observables, states, correlation functions and full dynamics" [16]. There is an established dictionary (see section 1.2.3) that describes the precise mapping between objects in the field theory and objects on the quantum gravity side. If computational tools were available for both theories in every region of parameter space, one could in principle precisely match up every result in each theory: every physical question and corresponding result in one theory has a dual version in the theory on the other side of the correspondence. Put very shortly, the two theories describe the same physics.

How could such a correspondence exist? At first blush, it sounds absurd to claim that a quantum field theory and a theory of quantum gravity could be alternate descriptions of the same physics. On one side of the duality is a standard field theory on a fixed spacetime background, which in particular cannot contain a massless spin-2 (graviton) field [22]. On the other side is a theory of quantum gravity,[5] which necessarily contains a spin-2 field, in one higher dimension. Further, the descriptions of these theories are manifestly different. In particular, quantum gravity must admit phenomena and characteristics that do not seem to have any obvious description in a

[4] Although the focus of this thesis is on strongly coupled quantum field theory, we begin by discussing the holographic correspondence as applied to a general field theory, before specializing to the limit of strong coupling (and the corresponding region of validity for classical gravity) below.

[5] In the earliest examples of the duality the theory of quantum gravity was a string theory.

field theory, including black holes, wormholes, and diffeomorphism invariance. Thus, we have two theories with two very different descriptions that purportedly describe the same physics.

A key realization lies in the fact that quantum gravity is holographic in that the number of degrees of freedom in a region is proportional to the surface area surrounding the region, and not the volume as is the case for a local quantum field theory.[6] To see why this must be the case, consider for a moment the following gedanken experiment in a theory of gravity. Assume you have some volume V of space (bounded by the area A) which contains more information, or entropy, than a corresponding black hole of the same size: $S > S_{BH}$. For a sufficiently large volume, general relativity will provide a good description irrespective of the underlying theory, so that the entropy of the black hole will be given by the Bekenstein-Hawking formula $S_{BH} = A/4G_N$. Since our configuration is not a black hole, its mass is less than the critical mass for the volume V. Now, add matter to the region V such that its mass exceeds the critical mass; the configuration will gravitationally collapse, forming a black hole. Before adding the matter, the total entropy of the system was $S_{\text{before}} = S + S_{\text{out}}$, where S_{out} is the entropy of the matter that we threw into the region. After the region collapses, the total entropy of the system is described by the Bekenstein-Hawking formula: $S_{\text{after}} = S_{BH}$. By our initial assumption, we have $S_{\text{before}} > S_{\text{after}}$, showing that this process violates the second law of thermodynamics. Therefore, the assumption that we could have a region with larger entropy than a black hole of the same size must be false. We arrive at the conclusion that, in a theory of quantum gravity, the information in the region V is bounded by $S_{BH} = A/4G_N$.

Given the above discussion, we see that the number of degrees of freedom in a theory of quantum gravity in $d+1$ dimensions scales as a volume in d dimensions. This is the same behaviour one expects from a d dimensional quantum field theory.[7] Thus, it becomes at least plausible that the holographic correspondence could connect two such theories.

A particular salient feature of the duality is the relationship between the parameters on either side of the correspondence. The dimensionless coupling λ of the field theory is directly related to the typical length scale of the curvature in the quantum gravity theory: at large coupling λ the geometry of

[6] See [23, 24] for discussions of the holographic principle. The entropy bound described here is called the Bekenstein bound [25]. See, for example, [21] for a version of the argument given here.

[7] In section 1.2.2, we will match the number of degrees of freedom more precisely in a particular example of the duality.

the dual theory is weakly curved and classical gravity is a good approximation, while for small λ the curvature of the gravity side is large in units of the string length and the full quantum gravity theory is needed. Thus, for large λ, the gravity side is accessible with current tools for classical general relativity, while for small λ, the field theory side is accessible via perturbative quantum field theory. This mutual exclusivity of reliable calculational domains makes the holographic correspondence difficult to prove, as explicit matching of the sides is only possible in certain symmetrical situations. However, it makes it extremely useful as a tool for the study of strongly coupled field theories. In order to describe the physics of the strongly coupled quantum field theory, one simply has to find classical saddle-point of the gravity action. In cases with gravitational backreaction, this reduces to solving the Einstein equations of general relativity. While this may be technically difficult, established techniques exist for this integration, in contrast to the dual problem of studying a strongly coupled quantum theory.

In this way, using the holographic correspondence, many questions about strongly coupled quantum field theories may be phrased in the context of a classical gravity theory. By considering different theories on the gravitational side (for example, different geometries or different matter content), one may study a variety of strongly coupled field theories which display a rich array of behaviours. Relatively straightforward classical gravity computations thus provide access to certain previously intractable field theory calculations. This thesis utilizes the gauge / gravity duality in this way to study strongly coupled field theory in various contexts.

It is useful to have a mental image of the correspondence. Let us specialize to large λ and consider the particular example of the classical global anti-de Sitter (AdS) space in $2+1$ dimensions (AdS_3, a solution to Einstein gravity with a negative cosmological constant), dual to strongly coupled conformal field theory on $S^1 \times \mathbf{R}$. In Figure 1.1, we provide a visualization of the geometries involved in this correspondence. The gravity side, AdS_3, is conformal to the bulk of a cylinder. On the field theory side, at the right of the figure, we have $S^1 \times \mathbf{R}$, which maps out the boundary of a cylinder, and which is conformal to the boundary of AdS_3. Then, the degrees of freedom of the field theory live on a space which can be conformally mapped to the boundary of the gravity side; this motivates the label of the holographic correspondence. The extra direction on the gravity side in this case is parametrized by the radial coordinate from the axis of the cylinder. Often, these two images are amalgamated into one, with the field theory considered to be defined on the boundary of the bulk spacetime.

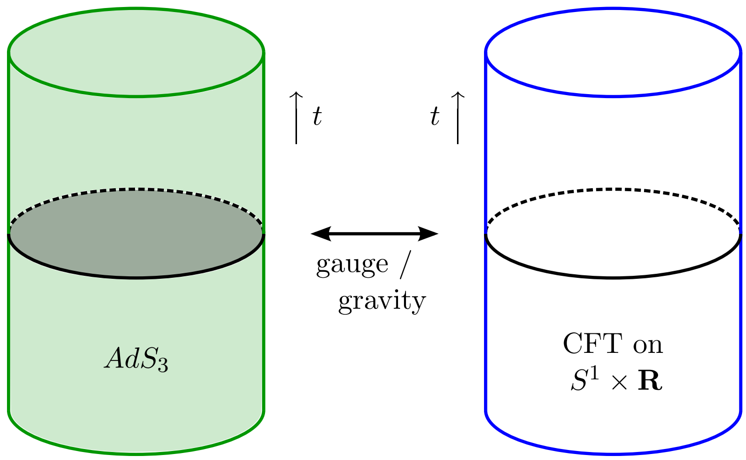

Figure 1.1: A visualization of the geometries involved in the holographic correspondence for the example of classical global anti-de Sitter space in 2+1 dimensions (AdS_3, pictured at left, is conformal to a solid cylinder) dual to strongly coupled conformal field theory on $S^1 \times \mathbf{R}$ (right, on the boundary of a cylinder). The physics of the gravity theory in the solid cylinder is completely encoded in the field theory on the cylindrical surface, and vice versa. In these images, the time direction is vertical; the shaded disc on AdS_3 at left represents a spatial slice of the gravity theory, at constant time, while the drawn-in ring on $S^1 \times \mathbf{R}$ at right is the corresponding spatial slice in the field theory. The geometry of the field theory, $S^1 \times \mathbf{R}$, is conformally equivalent to the boundary of the gravity spacetime. Due to this, these pictures are often amalgamated into one image, with the field theory mapped onto the boundary of the bulk spacetime. (In Figure 1.4 and beyond we adopt this representation.)

1.2.2 More justification for the correspondence

The original and perhaps most concrete example of the gauge / gravity duality is the equivalence of type IIB string theory on $AdS_5 \times S^5$ and strongly coupled $\mathcal{N} = 4$ $SU(N)$ super-Yang-Mills theory on 3+1 dimensional Minkowski space.[8] It was through this example that this remarkable correspondence was first proposed by Maldacena [7].[9] In this technical section, using results

[8] $\mathcal{N} = 4$ $SU(N)$ super-Yang-Mills theory is a supersymmetric field theory with gauge fields, fermions, and scalars connected by the $\mathcal{N} = 4$ supersymmetry generators. The gauge fields in this theory transform in the adjoint of $SU(N)$ and are described by the Yang-Mills Lagrangian.

[9] See also [8, 9] for important early developments.

from string theory, we will briefly review the argument for the equivalence of these theories, focussing on the limit in which the gravity side becomes weakly curved and classical gravity is a good approximation. Given this specific example, we go on to make explicit the relationship between parameters on either side of the duality and more precisely compare the numbers of degrees of freedom on either side of the correspondence. The content in this section is intended to provide a more detailed motivation for the correspondence.

The basic argument for the correspondence, in this case, relies on the commutativity of certain limits or scalings. We will begin with a well-defined string theory construction before taking two limits: the large coupling λ limit[10] and the low-energy limit. If we perform these operations in different orders, we arrive at the disparate theories. Assuming that the limits commute then gives the correspondence. The string theory construction we consider is a stack of N coincident D3 branes (in type IIB string theory), where $N \gg 1$. The parameters in the string theory will be the number of branes N and the string coupling g, which controls the strength of string interactions. Recall that D-branes are surfaces on which strings can end and are dynamical objects themselves in string theory. Two aspects of D-branes that will be important here are that the string endpoints generate a field theory on the world-volume of the branes (whose massless states include gauge fields described by a Yang-Mills theory) and that the branes carry energy, which causes gravitational effects around the branes. First, we will take the low-energy limit before going to strong coupling, giving the field theory part of the correspondence, before performing the operations in the reverse order to arrive at the gravity side.

To find the field theory part of the correspondence, consider the physics on the world-volume of the branes. The string endpoints give a field theory on the branes, the effective coupling ($g_{\rm YM}$) of which is related to the string coupling as $g_{\rm YM}^2 = g$. However, for a large number N of coincident branes, the gauge group of the field theory has large rank (is a 'large-N' theory), so that the relevant coupling is the 't Hooft coupling $\lambda = g_{\rm YM}^2 N = gN$ [26]. If we consider these branes at small coupling λ, the physics can be described perturbatively using field theory techniques on the branes. If we now take the low-energy limit, the massive open string states decouple, leaving massless open string states on the branes, which, in this case, gives precisely the $\mathcal{N} = 4$ $SU(N)$ super-Yang-Mills theory, with coupling λ, on

[10] λ refers to coupling on the field theory side. Below, we describe the interpretation of λ in terms of parameters on the gravity side.

$3+1$ dimensional Minkowski space (on the world-volume of the branes).[11] Taking the coupling λ large, we get the super-Yang-Mills theory at strong coupling.

Now, by taking the limits in the opposite order, we may find the gravity side of our correspondence. We begin again at our stack of N D3 branes, where $N \gg 1$. We would like to replace this configuration by a classical supergravity geometry, which will provide a good description of the system when the typical curvatures in the geometry are small. Given that D-branes carry energy (and charge), we solve the classical supergravity equations to find the spacetime that describes the brane configuration. The resulting spacetime is the p-brane supergravity solution, which is somewhat similar to a standard black hole solution (but with different geometry and in a different number of dimensions). The characteristic length of curvature in this spacetime is proportional to λ; if we take λ large, the branes source a spacetime with small curvature, and we can effectively replace the stack of D3 branes with this supergravity geometry. Then, after taking the large λ limit, we are left with type IIB string theory on this supergravity background. At this point, we now take the low-energy limit. From the point of view of an observer infinitely far from the branes, all string states sufficiently close to the horizon of the branes have vanishing energy. Therefore, the low-energy limit is synonymous with the 'near-horizon' limit, where we focus in on the geometry very close to the branes and keep all the string states. This near-horizon geometry is $AdS_5 \times S^5$, which may be written as

$$ds^2 = \frac{r^2}{L^2}\left(\eta_{\mu\nu}dx^\mu dx^\nu\right) + \frac{L^2}{r^2}dr^2 + L^2 d\Omega^2_{S^5}, \tag{1.1}$$

where L is the characteristic length scale of the geometry and $\eta_{\mu\nu}$ is the $3+1$ dimensional Minkowski metric. The field theory directions, or those parallel to the D3 branes, are described by the $\eta_{\mu\nu}dx^\mu dx^\nu$ part of the metric, while r labels the radial distance from the branes (the horizon being at $r=0$). The result of taking the limits in this way is that we are left with type IIB string theory on the near-horizon geometry (1.1).[12]

[11] In addition to the theory on the branes, the physical degrees of freedom in this situation include closed strings away from the branes. In the low-energy limit, massive closed string states decouple, leaving massless closed string states (supergravity) in the bulk, and interactions between the closed strings in the bulk and the open strings on the brane are suppressed. Thus, we have also bulk free supergravity in the space away from the branes, which is decoupled from the field theory on the branes. Below, we will see that we have an identical decoupled supergravity sector in additional to the gravity side of the correspondence, so that this sector does not play a role in the duality.

[12] In the low-energy limit, we also keep massless string states away from the near-horizon

In summary, taking the low-energy and strong coupling λ limits in different orders (and with $N \gg 1$), we have arrived at either strongly coupled $\mathcal{N} = 4$ $SU(N)$ super-Yang-Mills theory on $3+1$ dimensional Minkowski space or type IIB string theory on $AdS_5 \times S^5$. Assuming that the limits commute gives us the conjectured equivalence of these two theories. This discussion is summarized in Figure 1.2.

Given this explicit construction, we can identify relationships between the parameters of the string theory (or gravity side) and the field theory (or gauge theory side). The parameters of the gravity side can be taken to be the AdS radius L/l_s (in units of the string length l_s) and the string coupling g. On the field theory side, we have the rank of the gauge group N and the 't Hooft coupling λ. In the duality described here, the relations between these are given by

$$\lambda = gN, \quad L^4 = 4\pi\alpha'^2 gN, \tag{1.2}$$

where $\alpha' = l_s^2$. We see here the precise dependence of the characteristic size L on the coupling $\lambda = gN$.

For classical supergravity to be a good approximation on the gravity side, the characteristic length scale L of the curvature must be large so that the space is weakly curved. The relevant length scales for stringy and quantum effects are the string length l_s and the Planck length l_P; L must be large compared to these for the classical supergravity description. Using $G_N = l_P^8 = g^2 l_s^8$ for this ten dimensional space, we have

$$\frac{L}{l_P} \sim N^{1/4} \gg 1 \tag{1.3}$$

as the condition which suppresses quantum effects. Using the string length, we find that

$$\frac{L}{l_s} \sim \lambda^{1/4} \gg 1 \tag{1.4}$$

will control corrections from the tower of massive string states.[13]

Now, using the specific duality developed above, we can again compare the degrees of freedom in each theory, as in section 1.2.1. This time, given more information about the theories involved and the relations (1.2) we will

region, which gives us free supergravity away from the branes and which decouples from the brane physics. This is precisely the same as the supergravity sector we arrived at away from the branes in the alternative ordering above, so that these sectors can be trivially identified.

[13] Schematically, the states of the string have masses $m^2 \sim n/\alpha'$, where n is the level of excitation. For large λ, these masses become large and the massive string states are not accessible.

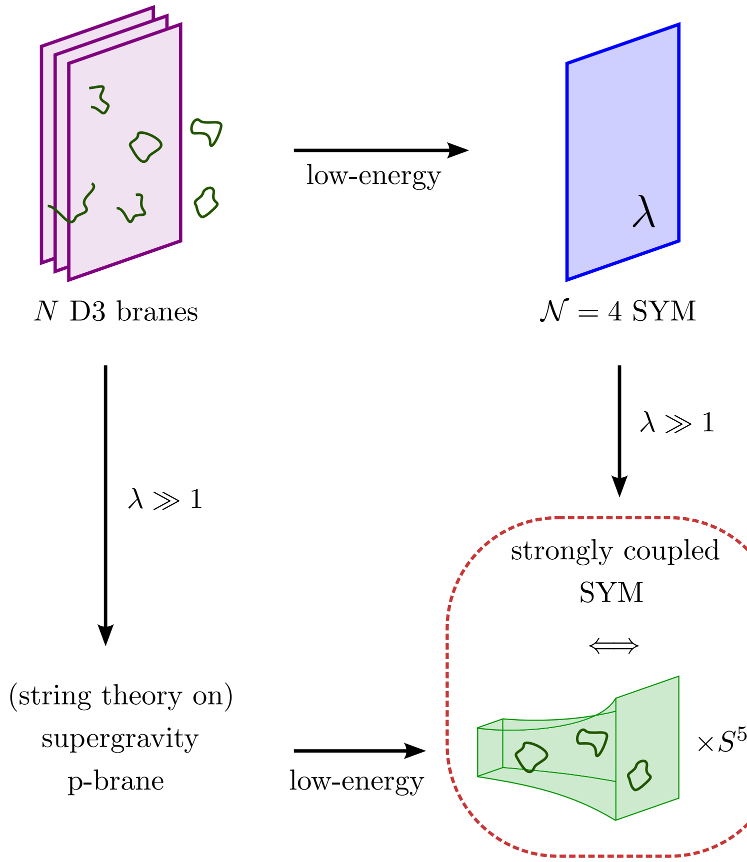

Figure 1.2: Motivating the AdS/CFT correspondence via string theory. Beginning with a stack of N D3 branes (top left, shown with strings) and taking the large coupling $\lambda = gN$ and low-energy limits in different ways, one arrives at the correspondence. Taking the low-energy limit of the D3 brane system gives the $\mathcal{N} = 4$ super-Yang-Mills (SYM) theory on $3+1$ dimensional Minkowski space with coupling λ (top right). Then, we may take the coupling λ large to get the strongly coupled theory. Starting again with the stack of branes, and taking λ to be large first, one can replace the branes with a corresponding classical supergravity p-brane geometry (bottom left). Taking the low-energy limit in this geometry leaves type IIB string theory in the near-horizon region, $AdS_5 \times S^5$. (See Figure 1.3 for a description of AdS space, depicted here in green.) Finally, we identify the two theories in the bottom right corner to arrive at the correspondence.

be able to observe the dependence on more parameters of the theories (in addition to seeing the scaling with the field theory volume).

We begin with the field theory side, which we will consider generically as an $SU(N)$ field theory with matter content in the adjoint representation. We will consider the theory in a finite volume V_3, to regulate infrared divergences, and introduce a short-distance cutoff δ, to control ultraviolet divergences. The number of cells in the volume will then be V_3/δ^3. For this type of field theory, the field degrees of freedom in each cell will be $N \times N$ matrices, with N^2 degrees of freedom each. Therefore, the total number of degrees of freedom will be given by

$$d.o.f._{\text{field theory}} \sim \frac{N^2 V_3}{\delta^3}. \tag{1.5}$$

Now, consider the gravity side. As discussed above, the information in gravity is holographic, so that the degrees of freedom of the system should be proportional to the area surrounding the system. In the metric (1.1), the boundary which surrounds the system is at $r = \infty$; it is the area of this boundary which we wish to compute. Before we calculate this area, however, we should also consider that we must regulate the gravity side in the same way as we did our field theory. To impose an infrared regulator, we will simply consider a finite volume V_3 of the directions parallel to the original D3 branes (this is the $\eta_{\mu\nu}dx^\mu dx^\nu$ term of the metric). To impose an ultraviolet cutoff in the gravity theory is not so straight-forward. It turns out (as discussed further below, section 1.2.3) that the near-boundary region of the spacetime corresponds to the ultraviolet of the field theory. Thus, to impose a similar cutoff, we should compute the area of the surface just inside the boundary.

For convenience in this calculation, we will change coordinates in (1.1) as $r = L^2/z$, to get the metric

$$ds^2 = \frac{L^2}{z^2}\left(\eta_{\mu\nu}dx^\mu dx^\nu + dz^2\right) + L^2 d\Omega^2_{S^5}. \tag{1.6}$$

The boundary, previously at $r = \infty$, is now at $z = 0$. By computing the area of the surface near the boundary, at $z = \delta$, we will be imposing an ultraviolet cutoff as desired. In the background described by equation (1.6), the area of the surface at constant $z = \delta$, constant time, and with volume V_3 in the field theory directions is given by

$$A = V_3 \cdot \sqrt{\frac{L^6}{\delta^6}} \cdot L^5, \tag{1.7}$$

where the factor L^5 gives the volume of the S^5 part of the geometry. The number of degrees of freedom, or information, is given by the Bekenstein formula $S = A/4G_N$. Using also equation (1.2) and the string theory result that $G_N \sim g^2 l_s^8 = g^2 \alpha'^4$, we find the information of the gravity theory to be

$$d.o.f._{\text{gravity theory}} = \frac{A}{4G_N} \sim \frac{V_3 L^8}{\delta^3 g^2 \alpha'^4} \sim \frac{N^2 V_3}{\delta^3}, \tag{1.8}$$

in agreement with the field theory result (1.5).

In addition to finding the expected scaling with the field theory volume V_3, we have added the information of how the two theories behave with respect to an ultraviolet cutoff δ and how the information scales with the rank N of the field theory gauge group. We find that the results on both sides of the correspondence match up as needed.

1.2.3 The holographic dictionary

Above, in section 1.2.2, we motivated the equivalence of strongly coupled $\mathcal{N} = 4$ $SU(N)$ super-Yang-Mills theory on $3+1$ dimensional Minkowski space and type IIB string theory on $AdS_5 \times S^5$. The construction discussed there represents a precise example of the more general class of holographic relationships known as the AdS/CFT correspondence.[14] In this section, we zoom out from this specific situation and examine the holographic duality with the minimal ingredient of asymptotically AdS gravity, which, as we will discuss further below, is the minimal structure for the dual of a conformal field theory. We will build some physical intuition for the correspondence while enumerating some of the standard entries in the holographic dictionary, which relates quantities on both sides of the duality. Through this, we will develop some of the practical computational tools one can use to address questions in holographic field theories.

First, we elaborate on the structure of AdS space and connect the isometries of the spacetime to the symmetries of the field theory. Next, we discuss the direct correspondence between the path integrals on either side of the duality and detail how the classical gravitational action can be used to get information about the field theory partition function. Finally, from a phenomenological perspective, we discuss how one may add structure to the dual field theory by including different matter fields in the gravity action.

[14] $\mathcal{N} = 4$ $SU(N)$ super-Yang-Mills theory is a conformally invariant field theory.

Symmetries of AdS space and the UV/IR relation

In this subsection, we discuss AdS space in more detail, connecting the symmetries of this spacetime to those in the field theory, and building an intuition about how dynamics at different coordinate positions in the gravity side correspond to dynamics at different energy scales in the field theory.

We will consider AdS_{d+1}, with metric given by

$$ds^2 = \frac{r^2}{L^2}\left(\eta_{\mu\nu}dx^\mu dx^\nu\right) + \frac{L^2}{r^2}dr^2, \tag{1.9}$$

where $\eta_{\mu\nu}$ is the d-dimensional Minkowski metric. We will refer to x^μ as the field theory directions and r as the radial direction. In Figure 1.3, we provide a caricature of this space. r varies from 0 to ∞; $r = 0$ is the Poincaré horizon while $r = \infty$ is the asymptotic boundary of the space. The geometry of the boundary at $r = \infty$ is conformal to d-dimensional Minkowski space, which is the spacetime on which the dual field theory is defined. AdS_{d+1} is a space with constant negative curvature, which implies that radial geodesics diverge as they approach the asymptotic boundary. If we have a box with a certain area in the field theory directions, at a fixed r_1, and we move the box to a larger radial coordinate r_2, the area of the box will increase by a factor r_2^{d-1}/r_1^{d-1}. The typical length scale of this curvature is L; if L is large in units of the Planck length, the space is weakly curved. Finally, we note that AdS_{d+1} is a solution of the Einstein-Hilbert action with cosmological constant:

$$S = \int d^{d+1}x\sqrt{-g}\left(\mathcal{R} + \frac{d(d-1)}{L^2}\right). \tag{1.10}$$

It is this action which will define the partition function for the gravity side.

AdS space is highly symmetric; that it is dual to a conformal field theory (which is also highly symmetric) is no coincidence. The isometries of the AdS space include Poincaré transformations in the field theory directions, dilatations (scalings of the coordinates), and special coordinate transformations. Taken together, the isometry group of AdS_{d+1} is isomorphic to $SO(d,2)$. Now, the conformal group in d spacetime dimensions is precisely $SO(d,2)$ [27]. Thus, there is a direct relationship between isometries of the gravity side and the conformal symmetry of the field theory. The gravity side allows a geometrical realization of the conformal symmetry through isometries of the spacetime.

As an example of this relation, consider in particular scale transformations in the field theory, which, through the duality, are directly 'geometrized' in the extra gravity coordinate. In the field theory, these are

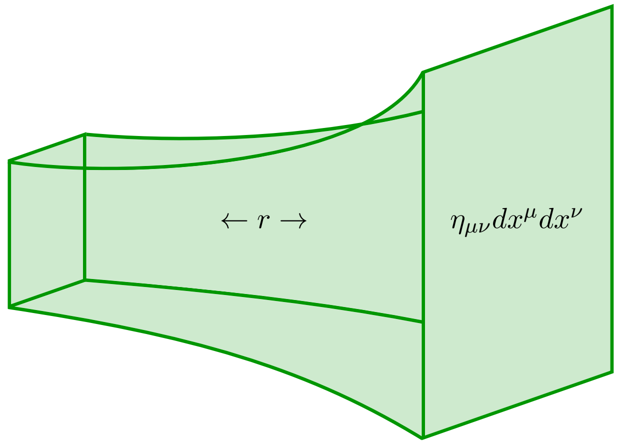

Figure 1.3: A caricature of AdS space, as described by equation (1.9). The radial direction, r, increases from left to right; at fixed r, the metric is proportional to d-dimensional Minkowski space. The space has a horizon at $r = 0$, past the left of the diagram, where the square will pinch off (the factor multiplying $\eta_{\mu\nu} dx^\mu dx^\nu$ in the metric goes to zero). There is an asymptotic boundary as $r \to \infty$, on the right of the diagram. The geometry of the boundary of AdS_{d+1} is conformal to d-dimensional Minkowski space. AdS_{d+1} is a negatively curved space, which implies that radial geodesics diverge as they approach the asymptotic boundary, and which inspires the shape of this schematic.

given by $x^\mu \to a x^\mu$. The energy in the field theory, conjugate to time, scales as $E \to a^{-1} E$. The corresponding symmetry in the AdS space is the dilatation $x^\mu \to a x^\mu$, $r \to a^{-1} r$. Thus, scaling to high-energy processes (or dynamics at small distances) corresponds to moving the bulk process towards the boundary at $r = \infty$. This behaviour is captured in the statement that the radial coordinate on the gravity side behaves like an energy in the field theory. Fields deep in the interior, at small r, represent processes in the infrared of the field theory, while excitations near the boundary at $r = \infty$ correspond to the ultraviolet of the field theory. On the gravity side, an infrared cutoff would correspond to placing a cutoff before the asymptotic boundary, to regulate the long-range excitations. Thus, through the correspondence, the infrared of the gravity side is mapped to the ultraviolet of the field theory, so that this is often called the UV/IR relation. See Figure 1.4 for a schematic image of this relationship.[15]

[15] A particular interesting implication of the UV/IR relation is that a cutoff of the gravity

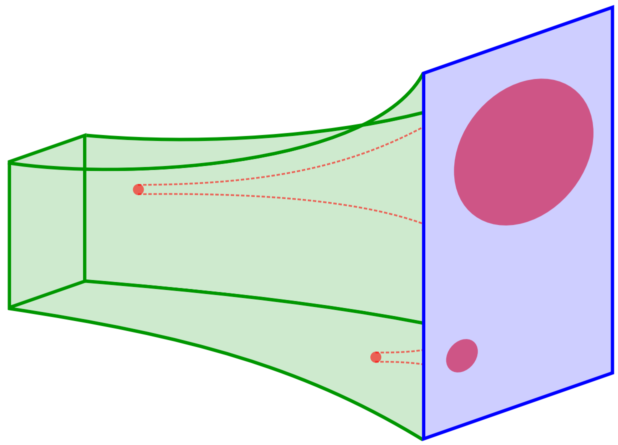

Figure 1.4: The UV/IR relationship between the bulk and boundary. Dynamics at short distances, or high energy scales, in the boundary theory correspond to excitations near the boundary in the gravity theory (excitations at long distances, or in the infrared of the gravity theory). Infrared dynamics, or low-energy excitations of the field theory, correspond to dynamics deep in the gravity bulk. (This image was inspired by a similar figure in [14].)

Equivalence of path integrals and the computation of expectation values

In this subsection, we make explicit the correspondence between the partition functions on either side of the duality and discuss how, in the limit of strong coupling, we may approximate the partition function of the gravity theory by using its classical action.

In order to use the gauge / gravity duality to perform calculations, we need a mathematical relationship between the two theories. The main practical statement of the correspondence is the equivalence of the gravitational partition function with the generating functional of the field theory:

$$\mathcal{Z}_{AdS}[\text{certain b.c.s}] = \mathcal{Z}_{CFT}[J_A] = \left\langle e^{i\int J_A \mathcal{O}_A} \right\rangle . \tag{1.11}$$

J_A are sources with $\mathcal{O}_A$ the corresponding operators in the field theory, where the label A includes all information about the operators, including

side at a minimum radius r_{min} (restricting r to (r_{min}, ∞)) will introduce a minimum energy for excitations, or a mass gap, into the field theory. This understanding gives some intuition about how we might use the correspondence to model theories with an energy gap.

Lorentz indices. As we will detail shortly, the presence of sources for operators in the field theory is dual to the existence of fields in the bulk gravity side. $\mathcal{Z}_{AdS}$ must also be supplemented with particular boundary conditions (at the asymptotic boundary), as indicated in equation (1.11). These boundary conditions typically enforce the value of the source J_A.

In this work, we are interested in using the gravity side to answer questions about the field theory. Through the relation (1.11), knowing the behaviour of the gravity theory allows one to perform computations in the field theory, using the standard expression

$$\langle \mathcal{O}_A \rangle = -i \frac{\delta \mathcal{Z}_{CFT}[J_A]}{\delta J_A}. \tag{1.12}$$

Our main focus is on applying the correspondence to strongly coupled field theories. In this limit, classical gravity is a good description of the bulk and we can approximate the gravity partition function as

$$\mathcal{Z}_{AdS} \approx e^{iS_0}, \tag{1.13}$$

where S_0 is the gravity action evaluated on the classical solution. Combining equations (1.11), (1.12), and (1.13) gives

$$\langle \mathcal{O}_A \rangle = \frac{\delta S_0}{\delta J_A}. \tag{1.14}$$

Thus, to compute field theory expectation values, one may solve the classical equations of motion on the gravity side to find the on-shell action S_0 before using (1.14) to arrive at the field theory result. The holographic correspondence translates the problem of computing correlation functions to finding the classical gravity action.

Mapping (gravity) fields to (field theory) operators

Given the equivalence of the partition functions of the theories on either side of the correspondence, equation (1.11), and the prescription for computing correlation functions, equation (1.14), it is important to describe how we may add structure to the field theory, in the form of sources J_A and operators $\mathcal{O}_A$, through manipulations of the gravity theory (which we have full control over). In this subsection, we precisely state how the content of the two theories connects and present three examples of this mapping. The information reviewed here provides some of the necessary basis for building up holographic field theories in a phenomenological manner.

As touched on briefly above, the content of the field theory is determined by sources for the operators of the theory. Generically, there are many types of operators that could appear in a field theory (for example, with different Lorentz indices). What might be the corresponding content on the gravity side? Components that we can add to the gravity side, which also display a rich array of possibilities, are fields of various types. Included in the statement of the holographic correspondence is that (in the strong coupling limit) classical fields in the gravity bulk are in correspondence with operators of the field theory. As we will see in the examples below, the source and expectation value for the dual operator are encoded in the asymptotic, near-boundary behaviour of the classical field. Three important components of this mapping are:

1. The Lorentz structure of the field in the bulk carries over to the operator in the field theory.
2. The mass of the field on the gravity side is in correspondence with the scaling dimension of the operator in the conformal field theory.
3. Gauge symmetries in the bulk map to global symmetries on the boundary.

These details begin to illuminate how we might use the holographic correspondence to build up conformal field theories with certain operator content.

As a first example of how the duality between fields and operators works in practice, let us consider the simplest case of a massive real scalar field ψ in AdS space. From an effective-theory or naturalness perspective, we will use the action

$$S_\psi = \int d^{d+1}x\sqrt{-g}\left\{\frac{1}{2}(\partial\psi)^2 + \frac{1}{2}m^2\psi^2\right\}, \tag{1.15}$$

where m is the mass of the scalar field. Since ψ is a scalar field, it will be dual to some scalar operator in the field theory, which we will call $\mathcal{O}_\psi$. Including this scalar field on the gravity side corresponds to considering a source $\psi_{(0)}$ for $\mathcal{O}_\psi$, so that we are studying the generating functional

$$\mathcal{Z}_{CFT}[\psi_{(0)}] = \left\langle e^{i\int \psi_{(0)}\mathcal{O}_\psi}\right\rangle. \tag{1.16}$$

In terms of the scalar field in the bulk, it is the value of ψ at the boundary that determines the source $\psi_{(0)}$. By solving the equation of motion following from (1.15) in the AdS background (1.9), for large r, and comparing to the definition for expectation values from partition functions, equation (1.12), we arrive at the expansion

$$\psi = \frac{\psi_{(0)}}{r^{d-\Delta}} + \cdots + \frac{\langle \mathcal{O}_\psi \rangle}{r^\Delta} + \ldots , \tag{1.17}$$

where

$$\Delta = \frac{1}{2}\left(d + \sqrt{d^2 + 4m^2L^2}\right) \tag{1.18}$$

and ... denotes terms higher order in $1/r$ (additional terms may appear at orders lower than the $\langle \mathcal{O}_\psi \rangle$ term, as indicated). As anticipated, the source $\psi_{(0)}$ and expectation value of the operator $\mathcal{O}_\psi$ are encoded in the asymptotics of the scalar field.[16] Δ, which depends on the mass m, is the scaling dimension of the operator in the field theory, meaning that we can write the field theory correlation function of $\mathcal{O}_\psi$ schematically as[17]

$$\langle \mathcal{O}_\psi(x)\mathcal{O}_\psi(y) \rangle \sim \frac{1}{|x-y|^{2\Delta}}. \tag{1.19}$$

In practice, the value of the source $\psi_{(0)}$ is part of the boundary conditions imposed on the gravity theory. Posing the equations of motion for the classical configuration of ψ in the AdS background as subject to the boundary condition $r^\Delta \psi \to \psi_{(0)}$ as $r \to \infty$ gives a well-defined problem, the solution of which allows one to read off the expectation value $\langle \mathcal{O}_\psi \rangle$.

Next, let us consider a $U(1)$ vector field A_μ in the bulk, with Maxwell action

$$S_A = \int d^{d+1}x \sqrt{-g}\, \frac{1}{4} F^2, \tag{1.20}$$

where F is the field strength for the gauge field. The gauge field will couple to an operator with one Lorentz index, which we will call j_μ. The generating functional for the dual field theory will be

$$\mathcal{Z}_{CFT}[A_{(0)\mu}] = \left\langle e^{i \int A_{(0)\mu} j^\mu} \right\rangle , \tag{1.21}$$

where we are reminded that, as above for the scalar field, we must include boundary conditions on the gauge field A_μ in the bulk. Once again we can write the solution for this field near the asymptotic boundary, finding

$$A_\mu = A_{(0)\mu} + \frac{\langle j_\mu \rangle}{r^{d-2}} + \ldots . \tag{1.22}$$

[16] Generically, the source is encoded in the non-normalizable mode of the field while the response is dual to the normalizable portion of the field.

[17] To see this, one may again use the symmetry $x^\mu \to a x^\mu$, $r \to a^{-1} r$. Under this scaling, the scalar field ψ should be invariant. Using equation (1.17), we can then read off how $\mathcal{O}_\psi$ should scale under this transformation.

The allowed set of local $U(1)$ gauge transformations on the gravity side reduce to global $U(1)$ transformations at the boundary $r \to \infty$, implying that the current j_μ is a global $U(1)$ symmetry current. Notice also that the scaling dimension of j_μ is $\Delta_j = d - 1$, which agrees with the scaling dimension of a conserved current in a d-dimensional conformal field theory [27].

In particular, this correspondence provides a straightforward method with which to study a field theory at finite density. One may turn on a chemical potential μ for a global $U(1)$ charge by fixing the boundary condition $A_{(0)t} = \mu$; the corresponding response $j_t = \rho$ will be the conserved charge density. Thus, to study strongly coupled field theory at finite density, one simply has to study the dynamics of an electric field (arising from the gauge potential A_t) in a gravitational background (see Figure 1.5).[18]

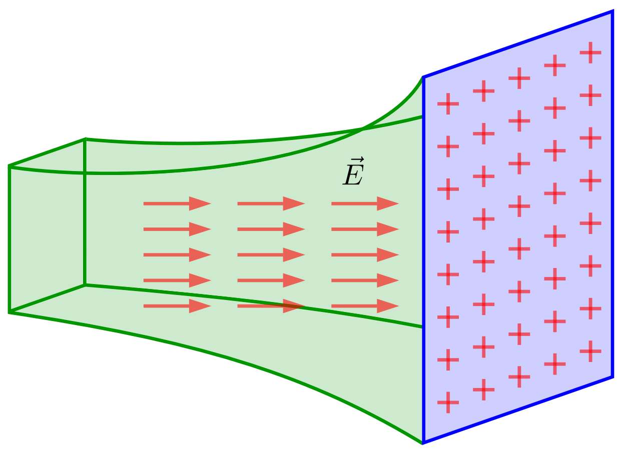

Figure 1.5: Including an electric field in the bulk is dual to a field theory at finite charge density. (This image was inspired by a similar figure in [14].)

Finally, we consider the metric $g_{\mu\nu}$, a tensor field in the bulk. The minimal action for the metric is the Einstien-Hilbert action, given above in equation (1.10). To understand the field theory quantities that are encoded in the metric, recall that, in a field theory, the energy-momentum tensor $T_{\mu\nu}$ arises as the conserved current associated with Lorentz transformations. As for the gauge field above, the local gauge freedom of the metric in the bulk will reduce to a global transformation on the boundary: Diffeomorphism

[18] The situation described here corresponds to studying the field theory in the grand canonical ensemble, in which we fix the chemical potential. By using alternate boundary conditions for the gauge field, we could study the canonical ensemble, in which we fix the charge density.

invariance in the bulk becomes the freedom of global (Lorentz) coordinate transformations in the field theory. Thus, it is natural to identify the (boundary value of the) metric with the source for the energy-momentum tensor $T_{\mu\nu}$. Written in the same manner as the scalar and gauge fields above, the field theory generating functional will be

$$\mathcal{Z}_{CFT}[g_{(0)\mu\nu}] = \left\langle e^{i\int g_{(0)\mu\nu}T^{\mu\nu}} \right\rangle, \tag{1.23}$$

where $g_{(0)\mu\nu}$ refers to the boundary value of the metric $g_{\mu\nu}$. Once again we may solve the equations perturbatively near the boundary, finding the schematic expansion [28]

$$g_{\mu\nu} \sim r^2 g_{(0)\mu\nu} + \cdots + \frac{\langle T_{\mu\nu}\rangle}{r^{d-2}} + \ldots, \tag{1.24}$$

where $\ldots$ denotes terms higher order in $1/r$ (additional terms may appear at orders lower than the $\langle T_{\mu\nu}\rangle$ term, as indicated). In the field theory, $T_{\mu\nu}$ is the symmetry current that results from a change of coordinates. As can be seen in these expressions, the metric of the field theory (the tensor that couples to $T_{\mu\nu}$) is $g_{(0)\mu\nu}$, conformal to the boundary value of the bulk metric $g_{\mu\nu}$. It is this relationship that drives the notion that the field theory 'lives on the boundary' of the gravity bulk. As a final check, notice that the dimension of the $T_{\mu\nu}$ is $\Delta_T = d$, as required by the conformal symmetry in the field theory [27].

1.2.4 Holography and numerics

As discussed above, a typical application of holography to the modelling of some strongly coupled physics involves solving the classical field equations of a gravitating system. In low-dimensionality or in cases with high symmetry, analytic solutions are known. For example, the possible solutions for Einstein gravity (with negative cosmological constant) include AdS space and the Schwarzschild-AdS black hole. However, restricting to analytic solutions greatly restricts the characteristics of the corresponding field theory, and if we wish to model more interesting types of field theories, we quickly arrive at systems for which no closed-form solutions exist. There are two ways we might want to extend the known solutions, which we discuss here: we could include more fields on the gravity side (scalar, gauge, fermion, or tensor fields, for example) or we could examine situations with reduced symmetry. In both cases, we must turn to numerical methods in order to make progress.

As discussed in the previous subsection, the correspondence between bulk fields and field theory operators means that if one wishes to add content to the field theory, then one should consider a gravity side with more fields (the nature of which are determined by the desired operator content). Upon adding fields to the gravity side, one quickly arrives at systems for which analytic solutions are not known.[19] In these cases, numerical techniques become useful tools with which to find solutions. If we maintain symmetry in the field theory directions, the equations of motion reduce to ordinary differential equations, which depend only on the holographic radial coordinate r. For example, in the expression (1.17), this would imply that $\delta\psi$ and $\langle\mathcal{O}_\psi\rangle$ are independent of the field theory directions. In this case, the equations of motion may be solved in a straightforward manner using, for example, standard computer mathematics software. The majority of studies in the literature have focussed in this way on homogeneous field theory.

In order to provide contact with real experimental systems in which the assumption of homogeneity does not apply, one needs to introduce a dependence on the field theory directions (so that $\delta\psi = \delta\psi(x)$ and $\langle\mathcal{O}_\psi\rangle = \langle\mathcal{O}_\psi(x)\rangle$). To use the correspondence to its full capacity, we should also apply it to studying strongly coupled theories in these less symmetric situations. Generically, if we introduce a dependence on the field theory directions, the equations of motion will take the form of coupled partial differential equations, and any hope of an analytic solution is lost. Therefore, numerical methods are necessary to address this entire new sector of problems concerning strongly coupled theories. In particular, for static problems, the equations take the form of well-defined boundary value problems, for which standard numerical techniques exist. Many of these may reasonably be implemented with only modest computational resources; thus, these problems are accessible to many researchers with current technologies and equipment. However, only recently have some research groups began to study field theory in inhomogeneous situations in this way.

A portion of this thesis (the projects described in chapters 3, 4, and 6) is dedicated to applying numerical techniques to certain holographic situations with reduced symmetry. In appendix A, we briefly review the numerical procedures used in these studies.

[19] An exception is the Reissner-Nordström-AdS black hole, which solves the Einstein-Maxwell system (a gauge field in dynamical gravity), and is dual to a field theory at finite density.

1.3 Thesis overview

This thesis consists of four projects covering three distinct domains of applicability. In this section, for each project, we briefly describe the motivation, methods, and main results. First, summarized in section 1.3.1, we study holographic field theories in generality, seeking results for generic finite density theories. Next, we apply holography to the study of phases which spontaneously break translation invariance (section 1.3.2). These have applications in condensed matter physics. Finally, we turn to QCD, and study two separate problems. First, we model the existence of a colour superconductivity phase at high densities (section 1.3.3). Second, we examine the construction of the baryon in a holographic model (section 1.3.4).

1.3.1 Density versus chemical potential in holographic probe theories[20]

One difficult regime of strongly coupled field theory that holography is particularly suited to study is that of finite charge density. Here, lattice techniques fail due to the 'sign problem', whereby at finite chemical potential, the Euclidean action becomes complex, resulting in a highly oscillatory path integral. We can avoid this difficulty by mapping the problem to a gravity dual. As reviewed above, in section 1.2.3, according to the holographic dictionary, in order to have a chemical potential (indicating a global $U(1)$ symmetry) in the field theory, one must simply include a $U(1)$ gauge field in the gravity bulk. Given this simple access to finite density configurations, it is interesting to characterize the types of field theories which have a dual formulation and to extract qualitative (and, ideally, quantitive) results from the gravity approach.

In this work, we study systems with the minimal structure of a conserved charge, finding in particular which relations between charge density (ρ) and chemical potential (μ) are possible in field theories with a gravity dual. We focus on Lorentz invariant $3+1$ dimensional holographic field theories with the goal of offering a survey of results in the context of holography. Comparing and contrasting the results of such a study can provide an understanding of the behaviour of strongly interacting matter that is common across all models and those features that are particular to certain constructions, and may provide qualitative results applicable to QCD and other strongly coupled systems.

[20] This section is a summary of the work presented in chapter 2 and published in [1].

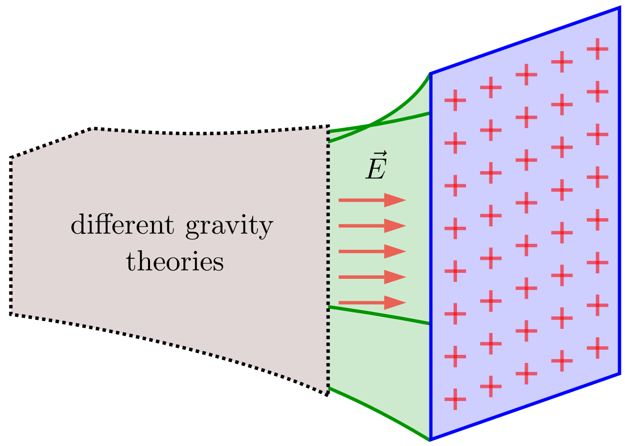

Figure 1.6: In chapter 2, we study holographic field theories with the minimal structure of a conserved charge, which corresponds to having a gravity bulk with an electric field. We enumerate the results for the relationship between chemical potential μ and charge density ρ across a large number of $3+1$ dimensional example field theories. These field theories differ in their dual gravity description which is indicated by the shaded area at the left of the figure. (This image was inspired by a similar figure in [14].)

We find that, at large μ, a large class of theories are well-modelled by a power law relationship of the form

$$\rho = c\mu^{\alpha} + \dots, \tag{1.25}$$

where the dots denote terms subdominant in powers of μ. By studying various general and specific examples of holographic field theories, we may enumerate the possible values of the parameters α and c. The particular situations we examine in this work may be split into general results and specific examples. We summarize the cases we consider:

1. General considerations:

   (a) Using thermodynamic stability and causality as general field theory constraints, we derive the condition $\alpha \geq 1$, restricting the power that can appear in the relationship.

   (b) For a holographic field theory in which the gauge field is governed by the probe Maxwell action (that is, in a fixed gravitational background), we find that, analytically, $\alpha = 1$.

(c) For a holographic field theory using a Born-Infeld gauge field action, we derive $\alpha > 1$.

2. Specific examples:

   (a) We consider Dp-Dq brane systems, given by a single probe Dq brane embedded in the black brane background generated by a stack of N Dp branes, for various (p, q). In these systems, the Born-Infeld action describes the dynamics of the gauge field on the probe brane and determines the possible behaviours (powers α) that may arise. We analytically determine the different possible behaviours.

   (b) Next, we consider bottom-up models,[21] both probe and backreacted, in both black hole and soliton (horizon-less) geometries, and with and without a scalar field. Depending on the example, we use analytical or numerical approaches to solve the equations of motion on the gravity side before using the correspondence to interpret our results in terms of the dual field theory and to evaluate the dependence of α and c on both the model and the parameters within each model.

These results, the main output of our study, are summarized in Table 2.1 (for Dp-Dq systems) and in Table 2.2 (for bottom-up models).

1.3.2 Holographic stripes[22]

High temperature superconductivity is one of the most interesting and technologically relevant problems in condensed matter physics. Experiments have recorded many novel results in materials that exhibit high temperature superconductivity. One of these is the observation of translation-symmetry breaking states, or stripes, which have been observed in the form of charge density waves (see Figure 1.7), in which the charge density varies with position, and spin density waves, in which the spin density varies with position. Striped phases are believed to be due to strong coupling effects and a tractable theoretical model is not yet available. By applying the holographic

[21]'Bottom-up' models are those in which the theory does not arise from an explicit string theory construction. Starting with the action (1.10) would be considered a bottom-up approach, while Dp-Dq brane systems are examples of 'top-down' models.

[22]This section is a summary of the work presented in chapters 3 and 4 and published in [2] and [3]. Chapter 3 presents a concise version of the study while chapter 4 provides full results and the complete details of the analysis.

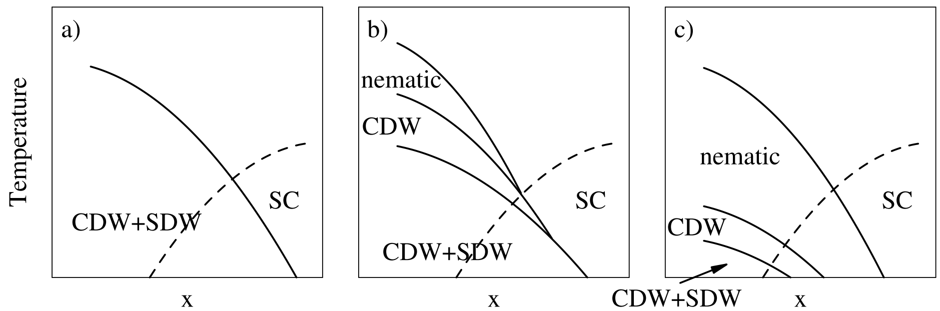

Figure 1.7: A schematic phase diagram for the cuprates. The vertical axis is temperature while the horizontal axis represents doping. Shown are schematic diagrams at: a) weak coupling; b) coupling that varies with x, and; c) strong coupling. Phases of the cuprates include the superconducting phase (SC) and inhomogeneous phases: the nematic phase, the charge density wave (CDW), and the spin density wave (SDW). In chapters 3 and 4, we study a holographic model of a strongly coupled system which exhibits an inhomogeneous phase. (Reprinted with permission from [29], ©2009 Taylor & Francis.)

correspondence, one may study strongly coupled systems that share important features with these experimental materials. In this project, we seek to model the spontaneous transition to a translation-symmetry-breaking phase, in hopes that general lessons may be extracted from the results and applied to the experimental systems. To this end, our goal is to find the gravity dual of a $2+1$ dimensional model system with spontaneous striped order.

To find the gravity dual of a system with stripes, we need a mechanism to break the translational invariance. One mechanism to introduce spatial inhomogeneities is the inclusion of a Chern-Simons-type term in the gravity Lagrangian. The specific model we study, due to Donos and Gauntlett [30], is

$$\mathcal{L} = \frac{1}{2}(\mathcal{R}+12) - \frac{1}{2}\partial^\mu\psi\partial_\mu\psi - \frac{1}{2}m^2\psi^2 - \frac{1}{4}F^{\mu\nu}F_{\mu\nu} - \frac{1}{\sqrt{-g}}\frac{c_1}{16\sqrt{3}}\,\psi\,\epsilon^{\mu\nu\rho\sigma}F_{\mu\nu}F_{\rho\sigma}. \tag{1.26}$$

The Chern-Simons coupling between the scalar field ψ and the gauge field A_μ (the term proportional to c_1) promotes the formation of stripes for large enough chemical potential and for a range of wave-vectors. Through a perturbative analysis, Donos and Gauntlett showed that instabilities of the homogeneous background towards the formation of stripes indeed exist in the above model [30]. These stripes appear in the charge density, current density, and energy-momentum tensor of the dual field theory. In this project, we perform the full analysis of the system, solving for the nonlinear inhomogeneous solutions and characterizing the phase transition between the homogeneous and the striped phases.

The equations governing our gravitational model are the Einstein equations, $G_{\mu\nu} = T_{\mu\nu}$, and the matter field equations. The fields will vary in both the holographic radial direction and the inhomogeneous direction of the field theory, resulting in coupled nonlinear partial differential equations. To solve the equations, we discretize on a rectangular grid before applying a Gauss-Seidel relaxation method on the resulting algebraic equations; see appendix A.2 for more details about the numerical approach in this project.

With the solutions for varying temperature and wave-vectors in hand, we can study the thermodynamics of the homogeneous and inhomogeneous phases in order to determine which phase dominates. For the field theory on a domain of finite size, we make this comparison in each of the microcanonical, canonical, and grand canonical ensembles, confirming that the striped solution dominates (when it exists) in all cases, and finding a second order transition to the inhomogeneous phase as the temperature is lowered. For the experimentally interesting case of the field theory on an infinite domain, we compare the free energy density of the homogeneous solution to that of all stripes available at the given temperature in order to determine the dominant stripe width. We find a second order transition to the striped phase as the temperature is lowered and that, once inside the domain of the striped phase, the width of the dominant stripe increases with decreasing temperature. This main result is shown in Figure 3.5.

1.3.3 Towards a holographic model of colour superconductivity[23]

As discussed above, low energy QCD is the prototypical strongly coupled field theory. Since the domains of applicability of typical field theory approaches (perturbative quantum field theory and lattice simulations) are restricted to limited regions of the phase diagram, the holographic correspondence, which provides access to the thermodynamics of the theory across the parameter space, offers a promising avenue for study. Unfortunately, the precise gravity dual of QCD is not know. However, certain

[23]This section is a summary of the work presented in chapter 5 and published in [4].

features of QCD may be modelled in the holographic approach, offering (at the least) qualitative information about the phase diagram of QCD. One such feature that is particularly amenable to the gravity approach is the existence of a colour superconductivity quark matter phase at high density. (See Figure 1.8.)

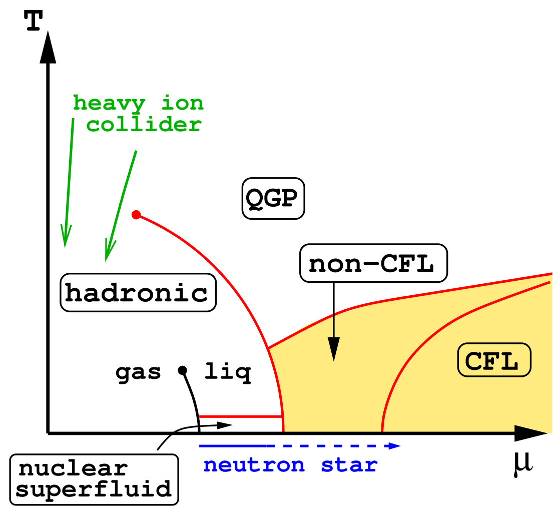

Figure 1.8: A schematic of the conjectured QCD phase diagram. At small densities and temperatures is the hadronic phase while at larger temperatures and densities is the quark-gluon plasma (QGP). At very high densities, we find phases which exhibit colour superconductivity (shaded in yellow), labelled by whether or not they are expected to exhibit the phenomenon of colour-flavour-locking (CFL). In chapter 5, we study a phenomenological holographic model of the colour superconductivity phase. (Reprinted with permission from [31], ©2008 the American Physical Society.)

In this project, we employed a bottom-up, phenomenological approach to model a confining gauge theory on $3+1$ dimensional Minkowski space which displays a colour superconductivity phase at large densities. The key features in our model include a QCD (confinement) scale,[24] a conserved baryon current (dual to a $U(1)$ gauge field A_μ), and an operator to characterize the colour superconductivity phase (dual to a scalar field ψ). The

[24]This is provided by the addition of an extra periodic direction in the geometry. On the gravity side, this allows a phase transition between a geometry with a black hole horizon and one without (a soliton configuration). The soliton geometry cuts off the gravity bulk at a minimum radius, introducing a mass gap in the dual field theory and resulting in a confining phase [32].

phenomenological gravity action describing this minimal set of ingredients is given by

$$S = \int d^6x\sqrt{-g}\left\{\mathcal{R} + \frac{20}{L^2} - \frac{1}{4}F^2 - |\partial_\mu\psi|^2 - m^2|\psi|^2\right\}. \tag{1.27}$$

The standard solution to this model is the charged AdS black hole (with $\psi = 0$), which is dual to the deconfined phase of the field theory. The existence of a confinement scale admits a second, horizon-less gravity solution, which translates to the confined phase of the field theory. Finally, it is known that in this model, for large chemical potential, there is an instability towards a 'hairy' black hole, with non-zero scalar field ψ. In this phase, the operator $\mathcal{O}_\psi$ dual to the scalar field will acquire a non-zero expectation value: $\langle\mathcal{O}_\psi\rangle \neq 0$. Within our model, $\mathcal{O}_\psi$ is interpreted as some quark operator whose expectation value indicates the presence of a (colour) superconducting condensate. Thus, the field theory dual to the system described by the action (1.27) exhibits three distinct phases: a confined phase, a deconfined phase, and a colour superconducting phase.

Solving the system of ordinary differential equations derived from the action and computing the free energy of each phase at various temperatures and chemical potentials allows us to construct the phase diagram given in Figure 5.1, which is the main result of this study. A particular interesting outcome is that our model predicts a very small temperature for the onset of the colour superconducting phase.

1.3.4 Holographic baryons from oblate instantons[25]

In this project, we again seek to apply the holographic correspondence in the study of particular aspects of QCD. This time, we turn our attention to the construction of the baryon in a holographic model of large-N_c two-flavour QCD.

The model we consider is based on the Sakai-Sugimoto model of holographic QCD [13], a top-down string theory construction. The Sakai-Sugimoto construction begins with a stack of N_c D4 branes,[26] compactified on a circle and considered in the low energy limit. On the field theory side, this gives pure massless $SU(N_c)$ Yang-Mills theory, representing the gluonic degrees of freedom of QCD. In order to introduce flavour into the theory, one adds N_f

[25] This section is a summary of the work presented in chapter 6 and published in [5].

[26] The construction of the D4 brane background here closely resembles the D3 brane system used in the original derivation of the correspondence, as reviewed in section 1.2.2 above.

D8 branes to the construction; strings extending from the background D4 branes to the flavour D8 branes give states transforming in the fundamental of $SU(N_c)$, corresponding to the quarks of the theory. The gravity dual of this theory is found by replacing the stack of D4 branes by the metric they source. If the number of D8 branes is small, $N_f \ll N_c$, the effect of the D8 branes on the geometry can be neglected, and we are left with D8 branes embedded in the background sourced by the D4 branes. In this model, baryons arise on the gravity side as configurations of the $U(N_f)$ gauge field on the flavour D8 branes that possess a non-trivial topological charge. See Figure 1.9 for a visualization of this situation.

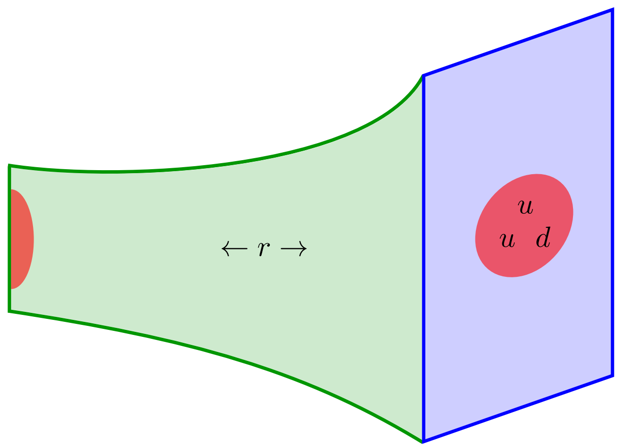

Figure 1.9: A visualization of the duality between the instanton in the bulk (at the left, viewed side-on) and the baryon in the boundary field theory. The instanton, a configuration of the bulk gauge fields with non-trivial topological charge, is oblate: it is squashed in the gravity radial direction r and spherical in the field theory directions. In chapter 6, we numerically solve for the minimal energy instanton configuration in the bulk.

The action describing gauge field configurations on $N_f = 2$ D8 branes is given by

$$\begin{aligned} S \propto \int d^4x dr \, \mathrm{tr} \left[\frac{1}{2} h(r) \mathcal{F}_{\mu\nu}^2 + k(r) \mathcal{F}_{\mu r}^2 \right] \\ + \gamma \int_{M_5} \mathrm{tr} \left(\mathcal{A} \mathcal{F}^2 - \frac{i}{2} \mathcal{A}^3 \mathcal{F} - \frac{1}{10} \mathcal{A}^5 \right), \end{aligned} \tag{1.28}$$

where $\mathcal{A}$ is a $U(2)$ gauge field with field strength $\mathcal{F}$, and $h(r)$ and $k(r)$ are known functions. Then, our task of solving for a baryon in this theory reduces to finding gauge field configurations with a non-zero topological charge described by the action (1.28). The solution to this is an instanton[27] in the three spatial field theory directions and the holographic radial direction r of the bulk.

There are three effects which determine the size and shape of the instanton. Firstly, the coupling γ, the only parameter in the model (1.28), controls the strength of the Coulomb self-repulsion of the instanton. For large γ, the instanton tends to spread out in all directions. Second, the gravitational well of the underlying geometry seeks to keep the instanton at small radial coordinate r. For small γ, the instanton is small and the geometry does not play a large role. However, for large γ, the geometry does become important and the minimum energy configuration is an oblate instanton, squashed in the r-direction and $SO(3)$-symmetric in the field theory directions. Finally, the form of the gauge field action plays a role in restricting the deformation. Since a spherical instanton minimizes the Yang-Mills action, this acts to restrict the squashing of the configuration.

Previous studies have approximated the gravity dual of the baryon as an $SO(4)$-symmetric BPST instanton. However, at non-zero values of the coupling γ, as detailed above, the solution will only possess $SO(3)$ symmetry. It has been shown that the $SO(4)$ approximation to the baryon fails to satisfy certain model-independent form-factor relations [33]. In this project, we seek to find the precise, $SO(3)$-symmetric solution to the field equations, in order to improve upon the previous calculations of holographic baryons in this model.

We assume only an $SO(3)$ symmetry and solve the resulting partial differential field equations using pseudospectral differentiation on a Chebyshev grid and a Newton's method for the resulting algebraic equations (see appendix A.3 for a review of these methods). Our approach allows us to compute the properties of the baryon, including the charge profile and mass, at a range of couplings γ. Our main results may be found in Figures 6.4 and 6.7. In particular, we may evaluate our solution at the value of γ that has been found to best fit the mesonic spectrum of QCD, finding significantly more realistic values than previous studies for the mass and size of the baryon. These results are found in equations (6.24) and (6.30).

[27] This is a misnomer, due to the fact that the original studies used the Belavin-Polyakov-Schwarz-Tyupkin (BPST) instanton as the static solution for the four spatial directions; the solution is more precisely described as a soliton in the spatial directions, and static in time.

Chapter 2

Density versus chemical potential in holographic probe theories[1]

2.1 Introduction

The AdS/CFT correspondence [7–9], which conjectures the equivalence of a gravity theory in $d+1$ dimensions and a gauge theory in d dimensions, has become a valuable tool for the study of strongly coupled field theories. Using the correspondence, many questions about quantum field theories may be phrased in the context of a gravity theory; in the limit of strong coupling, certain previously intractable field theory calculations are mapped to relatively simple classical gravity computations.

Holography and finite density

One difficult regime of strongly coupled field theory that gauge / gravity duality is particularly suited to study is that of finite charge density. Here, lattice techniques fail due to the 'sign problem': at finite chemical potential, the Euclidean action becomes complex which results in a highly oscillatory path integral. We can avoid this difficulty by mapping the problem to a gravity dual using the AdS/CFT dictionary. According to the dictionary, in order to have a global $U(1)$ symmetry in the field theory, one needs to include a $U(1)$ gauge field in the gravity bulk. The charge density and chemical potential are encoded in the asymptotic behaviour of the gauge field. At strong coupling in the field theory, the bulk theory is well described by classical gravity, and one may solve the classical equations of motion on the gravity side to study the field theory at finite density.

Given this relatively simple access to finite density configurations, we might hope that some physically realistic strongly interacting systems may

[1] A version of this chapter has been published [1].

be approximately described by a holographic dual. In this case, qualitative features of the holographic theory would carry over to the exact theory. It would be useful to characterize the types of finite density field theories that have a dual formulation and admit this type of study.

In this paper, we seek to answer this question from the perspective of the holographic theory. Specializing to holographic probes, in which fields are considered as small fluctuations on fixed gravitational backgrounds, we study systems with the minimal structure of a conserved charge and find the $\rho-\mu$ relations that are possible in the field theory duals. We attack this problem by first deriving constraints on the relationship based on general grounds before studying several specific examples of holographic field theories.

Summary of results

In our study, we observe that, at large densities, the field theory dual to a substantial class of gravity models can be described by a power law relation of the form[2]

$$\rho = c\mu^{\alpha}. \tag{2.1}$$

Firstly, we look to understand the constraints on the the $\rho - \mu$ relationship from the point of view of the field theory, using local stability and causality. Usually, results here depend on the particular form of the free energy. In all cases with $\rho - \mu$ behaviour (2.1), local thermodynamic stability places the condition $\alpha > 0$ on the exponent. In general, for a theory at low temperature, we may write the particular free energy expansion $f \propto -\mu^{\alpha+1} - a\mu^{\beta}T^{\gamma}$, with $\gamma > 0$ and $a > 0$, with corresponding charge density $\rho \propto (\alpha+1)\mu^{\alpha} + a\beta\mu^{\beta-1}T^{\gamma}$. Combined, local stability and causality demand that $\alpha \geq 1$ and $\gamma > 1$.

Next, we consider Born-Infeld and Maxwell actions for the gauge field in a generic background. Under mild assumptions, in both cases, the power α is constrained. For the Born-Infeld action, the condition

$$\alpha > 1 \qquad \text{(Born-Infeld action)} \tag{2.2}$$

arises,[3] while, for the Maxwell action, the power law coefficient is fixed to

$$\alpha = 1. \qquad \text{(Maxwell action)} \tag{2.3}$$

[2]Here and throughout, α refers to the power in this form of $\rho - \mu$ relationship.

[3]Naively, we could construct systems for which $\alpha \leq 1$, however, in these situations, the contribution of the constant charge density to the total energy diverges, consequently we can not say that there is a power law relation. This divergence signals a breakdown of the probe approximation rendering these systems outside the scope of these notes. Notice that $\alpha > 1$ is consistent with the bound derived from stability and causality.

Interestingly, these conditions are in agreement with those derived from field theory considerations, giving rise to the same range of possible values of α. In summary, all power law relationships consistent with stability and causality can be realized in simple probe gauge field setups by varying the background metric.

To see which values of α arise for backgrounds corresponding to specific models, we explore a variety of $3+1$ Poincaré-invariant holographic field theories dual to Dp-Dq brane systems and 'bottom-up' models with gauge and scalar fields. The former have been used, for example, in studies of holographic systems with fundamental matter [13, 34–37], producing many features of QCD, including confinement,[4] chiral symmetry breaking, and thermal phase transitions [39–42]. Bottom-up, phenomenological models have been studied in various model-building applications including superconductors[5] [11, 18, 44–47] and superfluids [12, 48, 49].

In the Dp-Dq systems, Table 2.1, a variety of powers α in the range $1 < \alpha \leq 3$ are realized, respecting the $\alpha > 1$ constraint. Note that these results only involve the Born-Infeld action and neglect couplings of the brane to other background spacetime fields.

	Probe brane								
	$d=4$						$d=5$		
Background branes	D9	D8	D7	D6	D5	D4	D8	D7	D6
D3	3		3		3				
D4		5/2		2		3/2	3		5/2
D5			2					2	
D6				3/2					

Table 2.1: The power α in the relationship $\rho \propto \mu^{\alpha}$ at large ρ for $3+1$ dimensional field theories dual to the given brane background with the indicated probe brane, with $d-1$ shared spacelike directions. For $d=5$ the theory is considered to have a small periodic spacelike direction while for background Dp branes with $p > 3$, the background is compactified to $3+1$ dimensions.

In the phenomenological probe models, Table 2.2, in all cases except one (the probe gauge field in the black hole background), the dominant power

[4] It was recently pointed out that the usual identification of the black D4 brane as the strong coupling continuation of the deconfined phase in the field theory is not valid [38].

[5] A top-down realization of a gauge / gravity superconductor has been found in [43].

α is determined by conformal invariance, since we consider asymptotically AdS backgrounds.[6] Since μ and T are the only dimensionful parameters, the density must take the form $\rho = \mu^{d-1}h(T/\mu)$, where the underlying space has d spacetime dimensions. At large μ and fixed T, we can expand h to see that μ^{d-1} dominates the $\rho - \mu$ relationship. In systems with one small periodic spacelike direction, the dominant power α is larger than the corresponding theory without a periodic direction since, at large densities, on the scale of the distance between charges, the theory is effectively higher dimensional.[7] Our study of bottom-up models also includes an analysis of the gravity models in the full backreacted regime. As seen in Table 2.2, the power law α in these cases is also determined by the same conformal invariance argument.

In these bottom-up models we are more interested in the detailed behaviour at intermediate values of μ. It is found that, in general, when the scalar field condenses in the bulk, the corresponding field theory is in a denser state than that without the scalar field. As well, the field theory dual to the gauge field and scalar field in the soliton background is in a denser state than that dual to the same fields in the black hole background. In the systems with a scalar field, at large μ, the $\rho - \mu$ relationship is well fit by the form $\rho = c(q, m^2)\mu^\alpha$,[8] where q and m^2 are the charge and mass-squared of the scalar field. While the power α is fixed by the conformal invariance, we find that the scaling coefficient $c(q, m^2)$ increases with increasing q or decreasing m^2.

[6] Different power laws can arise for holographic theories on different backgrounds, such as Lifshitz spacetimes. However, these will not be considered here.

[7] The phase transition that holographic theories with a periodic direction undergo as the density increases was studied in [50].

[8] In the probe cases we can scale q to 1, leaving $c = c(m^2)$.

Regime	Background	Fields	$d=4$	$d=5$
probe	black hole	ϕ	1	1
		ϕ,ψ	3	4
	soliton	ϕ,ψ		4
backreacted	black hole	ϕ	3	4
		ϕ,ψ	3	4
	soliton	ϕ,ψ		4

Table 2.2: The power α in the relationship $\rho \propto \mu^{\alpha}$ at large ρ for $3+1$ dimensional field theories dual to the given gravitational background with the stated fields considered in either the probe or backreacted limits. ϕ is the time component of the gauge field, ψ is a charged scalar field, and d is the number of spacetime dimensions. For $d=5$ the theory is considered to have a small periodic spacelike direction.

Organization

In section 2.2, we discuss some possible general examples of finite density field theories and attempt to establish bounds on the $\rho-\mu$ relationship by imposing thermodynamical constraints on these systems. In section 2.3 we briefly introduce holographic chemical potential and find, for Maxwell and Born-Infeld types of action, under mild assumptions, to what extent they reproduce the relationship found in section 2.2. In section 2.4 we investigate the probe limit of both top-down and bottom-up theories; first we study Dp-Dq systems, then we move to gauge and scalar fields in both black hole and soliton (with one extra periodic dimension) backgrounds. Section 2.5 extends the analysis of the bottom-up models to include the backreaction of the fields on the metric.

Relation to previous work

Some of the results presented in these notes have appeared previously in the literature. Finite density studies for probe brane systems have appeared for the Sakai-Sugimoto model [42, 51–53], the D3-D7 system [35, 36, 54–56], and the D4-D6 system [57]. The bottom-up models we consider are naturally studied at finite chemical potential (see, for example, [18] for the black hole case and [58] for the soliton dual to a $2+1$ dimensional field theory) due to the presence of the gauge field.

Our work focusses on the $\rho-\mu$ relation at large chemical potential over a broad class of theories that are dual to 3+1 dimensional field theories. We find, on very general grounds, constraints on the $\rho-\mu$ relation in holographic models constructed from Maxwell and Born-Infeld actions. Additionally, we use thermodynamical considerations to constrain the $\rho-\mu$ relation from the field theory point of view and find that these constraints are in agreement with those derived holographically. Further, we extend the analysis in the above references to the large density regime and include additional examples, collecting the results of a large range of models.

2.2 CFT thermodynamics

In this section, by appealing to local thermodynamic stability and causality in the field theory, we attempt to establish generic constraints satisfied by the coefficient α from a purely field theory stand point. The results found here will lay ground for our intuition when approaching this problem from the holographic side.

Generic system at large chemical potential

In order to study the density and chemical potential from the field theory perspective, we begin with a general ansatz for the free energy of a hypothetical system. In the large density limit, we expect that the chemical potential will dominate the expression, so we may write[9]

$$f \propto -\mu^{\alpha+1} - a\mu^{\beta}T^{\gamma} + \dots, \tag{2.4}$$

where the dots denote corrections higher order in T/μ. For a positive, imposing a positive entropy density $s = -(\partial f/\partial T)|_{\mu} > 0$ implies $\gamma > 0$, consistent with the second term being subleading in the low temperature expansion.

Considering the field theory as a thermodynamical system and imposing local stability demands that [59][10]

$$\chi = \left(\frac{\partial \rho}{\partial \mu}\right)_T > 0, \tag{2.5}$$

and

$$C_\rho = T\left(\frac{\partial s}{\partial T}\right)_\rho = -T\left[\frac{\partial^2 f}{\partial T^2} - \left(\frac{\partial^2 f}{\partial T \partial \mu}\right)^2 \frac{1}{\frac{\partial^2 f}{\partial \mu^2}}\right] > 0. \tag{2.6}$$

[9]Recall $\rho = -(\partial f/\partial \mu)_T$ so that, again, $\rho \propto \mu^{\alpha}$.

[10]χ is the charge susceptibility and C_ρ is the specific heat at constant volume.

Applying these to (2.4) in the $T/\mu \to 0$ limit gives the constraints $\alpha > 0$ and $\gamma > 1$.

Examining the speed of sound v_s of our system also allows us to establish a constraint. To ensure causality, we impose

$$0 \leq v_s \leq 1, \tag{2.7}$$

with the speed of sound given by [12]

$$v_s^2 = -\frac{\left[\left(\frac{\partial^2 f}{\partial T^2}\right)\rho^2 + \left(\frac{\partial^2 f}{\partial \mu^2}\right)s^2 - 2\left(\frac{\partial^2 f}{\partial T \partial \mu}\right)\rho s\right]}{(sT + \rho\mu)\left[\left(\frac{\partial^2 f}{\partial T^2}\right)\left(\frac{\partial^2 f}{\partial \mu^2}\right) - \left(\frac{\partial^2 f}{\partial T \partial \mu}\right)^2\right]}, \tag{2.8}$$

where ρ and s are the charge and entropy densities. For $\gamma > 1$, this implies the stronger bound of $\alpha \geq 1$. This is the same bound as derived in section 2.3 from consideration of the bulk dual of field theories. It is interesting that it arises from very general circumstances in both cases.

Zero temperature

In the zero temperature limit of ansatz (2.4) only the first term survives, so that $f \propto -\mu^{\alpha+1}$. In this case, the only condition for local stability is given by equation (2.5), which trivially leads to $\rho \propto \mu^\alpha$ with $\alpha > 0$. Computing the speed of sound and enforcing causality leads again to $\alpha \geq 1$.

General conformal theory

For a conformal field theory in d spacetime dimensions, the most general free energy density is

$$f = -\mu^d g\left(\frac{T}{\mu}\right), \tag{2.9}$$

where $g(x)$ is an arbitrary dimensionless function. Local stability depends on the details of the function g, and a general statement is not possible at this point. To ensure causality, we compute equation (2.8), finding the speed of propagation to be

$$v_s^2 = \frac{1}{d-1}, \tag{2.10}$$

from which it follows directly that a conformal theory obeys requirement (2.7) only in dimension $d \geq 2$. This result is trivial, as sound waves are not possible if there are no spacelike dimensions to propagate in.

Free fermions

As an example, we will compute the $\rho - \mu$ relationship for a system of free fermions. In the grand canonical ensemble, the partition function for spin 1/2 particles of charge q in a 3 dimensional box and subjected to a large chemical potential is

$$\mathcal{Z}(\mu, T) = \prod_{\vec{n}} (1 + e^{-\beta(E_{\vec{n}} - \mu q)}), \tag{2.11}$$

where the product is over available momentum levels. The partition function for antiparticles follows with the replacement $q \to -q$ so we include antiparticles by considering the total partition function $\tilde{\mathcal{Z}}(\mu, T) = \mathcal{Z}(\mu, T)\mathcal{Z}(-\mu, T)$. Passing to the continuum limit, approximating the fermions as massless, and setting $q = 1$, the resultant charge density is

$$\rho = \frac{\mu^3}{3\pi^2} + \frac{\mu T^2}{3}. \tag{2.12}$$

The dominant power in this case is the same as is expected in a generic conformal field theory.

2.3 General holographic field theories at finite density

It was shown in the previous section how local stability and causality lead to $\alpha \geq 1$. In this section, under mild assumptions, we investigate the Born-Infeld and Maxwell actions in the large μ regime and observe to what extent they fall under the general results from section 2.2.

2.3.1 Finite density

To find constraints on the $\rho - \mu$ relation in holographic field theories, we begin by studying very general systems with the minimal structure of a conserved charge. The holographic dictionary gives that a conserved charge in the field theory is dual to a massless $U(1)$ gauge field A in the bulk [60]. If the gauge field is a function only of the radial coordinate r, the chemical potential and the charge density are encoded in the behaviour of A as

$$\mu = A_t(\infty) \tag{2.13}$$

and

$$\rho = -\frac{\partial S_E}{\partial A_t(\infty)}, \tag{2.14}$$

where S_E is the Euclidean action evaluated on the saddle-point and the derivative is taken holding other sources fixed. As discussed in [36], an equivalent expression for the charge density is[11]

$$\rho = \left(\frac{1}{d-2}\right)\frac{\partial \mathcal{L}}{\partial(\partial_r A_t)}, \tag{2.15}$$

where the normalization of ρ has been chosen for later convenience. After writing down the gravitational Lagrangian, our prescription for computing the charge density at a given chemical potential is to solve the equations of motion with a fixed boundary condition for the gauge field, equation (2.13), before reading off the density using equation (2.15).

2.3.2 Gauge field actions

To include a gauge field in our AdS/CFT construction, we simply include it in the bulk action. Two gauge field Lagrangians that have appeared in holographic studies are the Maxwell and the Born-Infeld Lagrangians. Typically, the Maxwell action is used in bottom-up holographic models while the Born-Infeld action appears in the study of brane dynamics. Below, in section 2.4 we will consider holographic models using both types of Lagrangians. However, much insight can be gained by investigating these actions under generic conditions. Therefore, in this section, we study general versions of these two Lagrangians, at fixed temperature and large chemical potential, in the probe approximation.[12] Interpreting our results using (2.13) and (2.15), we will develop some constraints for the $\rho - \mu$ relationship in holographic theories described by these actions.

The Maxwell action

Consider a gauge field described by the Maxwell action $\int \sqrt{-g}F^2$ in a general background of the form

$$ds^2 = g^{FT}_{\mu\nu}(r)dx^\mu dx^\nu + g_{rr}(r)dr^2. \tag{2.16}$$

If we assume homogeneity in the field theory directions and consider a purely electrical gauge field (keeping only its time-component), the Lagrangian is

[11] Generically, A_t is a cyclic variable, so that the conjugate momentum is conserved, and we may evaluate this expression at any r.

[12] In the probe approximation, we assume there is no backreaction on the gravity metric. This is enforced in this case by studying the gauge field Lagrangian on a fixed background geometry.

simply

$$\mathcal{L} = g(r)\,(\partial_r A_t)^2\,, \tag{2.17}$$

for some function $g(r)$. From this we find

$$\rho = \left(\frac{2}{d-2}\right) g(r)\partial_r A_t. \tag{2.18}$$

In the systems considered below, the spacetime either has a horizon or smoothly cuts off at some radius $r_{\rm min}$. The value of the gauge field at this point is a boundary condition for the problem. Below, $A_t(r_{\rm min})$ is either zero or a constant, neither of which affect the $\rho - \mu$ behaviour; we take $A_t(r_{\rm min}) = 0$ here. Integrating (2.18), we find

$$\mu = \rho\left(\frac{d-2}{2}\right)\int_{r_{\rm min}}^{\infty}\frac{dr}{g(r)}. \tag{2.19}$$

Provided the integral is finite, we have

$$\rho \propto \mu. \tag{2.20}$$

Thus, for any holographic field theory with the gauge field described only by the Maxwell Lagrangian in a fixed metric we have $\alpha = 1$.

The Born-Infeld action

The Born-Infeld action is the non-linear generalization of Maxwell electrodynamics and is the appropriate language in which to describe the dynamics of gauge fields living on branes. Assuming homogeneity in the field theory directions, so that the gauge potential varies only with the radial direction, these systems are governed by an action of the generic form[13]

$$\mathcal{L} = \sqrt{g(r) - h(r)(\partial_r A_t)^2}, \tag{2.21}$$

where again, we take A_t to be the only non-zero part of the gauge field. The charge density is given by the constant of motion

$$\rho = \left(\frac{1}{d-2}\right)\frac{h(r)\partial_r A_t(r)}{\sqrt{g(r) - h(r)(\partial_r A_t)^2}}. \tag{2.22}$$

[13] $g(r)$ and $h(r)$ are arbitrary functions; $g(r)$ is not related to the previous discussion.

Here, we assume that the gauge field is sourced by a charged black hole horizon at r_+.[14] Euclidean regularity of the potential A_t fixes its value at the horizon as $A_t(r_+) = 0$ [36]. Then, we can integrate to find

$$\mu = \int_{r_+}^{\infty} dr \sqrt{\frac{g(r)}{h(r)}} \frac{(d-2)\rho}{\sqrt{h(r) + (d-2)^2\rho^2}}. \tag{2.23}$$

To extract the large ρ behaviour, we split the integral at $\Lambda \gg 1$. For $\rho \gg \Lambda$, the integral from r_+ to Λ approaches a constant, while the functions in the integral from Λ to ∞ can be approximated by their large r forms, which will be denoted with a ∞ subscript. The expression for the chemical potential now becomes

$$\mu \approx \int_{r_+}^{\Lambda} dr \sqrt{\frac{g(r)}{h(r)}} + \int_{\Lambda}^{\infty} dr \sqrt{\frac{g_\infty(r)}{h_\infty(r)}} \frac{(d-2)\rho}{\sqrt{h_\infty(r) + (d-2)^2\rho^2}}. \tag{2.24}$$

The ρ dependence of μ comes from the second term. If $g_\infty(r)/h_\infty(r) \approx r^{2m}$ and $h_\infty(r) \approx r^n$, by putting $x = r/\rho^{2/n}$ we find that

$$\mu \sim \rho^{(2+2m)/n} \int_{\frac{r_+}{\rho^{2/n}}}^{\infty} dx \frac{x^m}{\sqrt{x^n + 1}}. \tag{2.25}$$

The convergence of the integral here requires that $n/(2+2m) > 1$, resulting in the relationship

$$\rho \propto \mu^\alpha \quad \text{with} \quad \alpha > 1, \tag{2.26}$$

where the power α depends on the specific bulk geometry.

2.4 Holographic probes

With the general constraints of the previous sections in hand, we move on to study particular holographic field theories in the probe approximation, to see which specific values of α are realized. Here, we study two common probe configurations that have arisen in previous holographic studies. These are extensions of the actions considered in section 2.3. First, we examine probe branes in the black brane background using the Born-Infeld action.

[14] To have a non-trivial field configuration, a source for the gauge field in the bulk is required. In the low temperature, horizon-free versions of these models, this source is given by lower dimensional branes wrapped in directions transverse to the probe branes [61].

Then, we move on to the phenomenological perspective, in which we write down an effective gravity action without appealing to the higher dimensional string theory. In this approximation, using the Maxwell action, we look at the gauge field in both the planar Schwarzschild black hole and soliton backgrounds, with and without a coupling to a scalar field.

In both cases, in the systems we consider, the only sources in the field theory are the temperature T and chemical potential μ. Below, we fix T and work at large μ (such that $\mu/T \gg 1$). In this regime, we look for a relationship $\rho \propto \mu^\alpha + \dots$, where the dots denote terms higher order in T/μ.

2.4.1 Probe branes and the Born-Infeld action

In the systems we will consider here, the background consists of N_c D-branes; in the large N_c limit, these branes are replaced with a classical gravity metric. In this regime, fundamental matter is added by placing N_f probe branes in the geometry [62].

The brane action

Assuming that the background spacetime metric $G_{\mu\nu}$ is given, the action governing the dynamics of a single Dq probe brane is the Born-Infeld action

$$S \propto \int d^{q+1}\sigma e^{-\phi}\sqrt{-\det(g_{ab} + 2\pi\alpha' F_{ab})}. \tag{2.27}$$

Here, latin indices refer to brane coordinates and greek indices denote spacetime coordinates, while $X^\mu(\sigma^a)$ describes the brane embedding. g_{ab} is the induced metric on the probe brane given by $g_{ab} = \partial_a X^\mu \partial_b X^\nu G_{\mu\nu}$, F_{ab} is the field strength for the $U(1)$ gauge field on the brane, and ϕ is the dilaton field. Following the previous discussion, the only component of the gauge field we choose to turn on is A_t, additionally, we assume it depends only on the radial coordinate r, $A_t = A_t(r)$. Considering that the probe brane is extended in the r direction and the spacetime metric is diagonal, the Lagrangian simplifies to

$$\mathcal{L} \propto e^{-\phi}\sqrt{-\det(g_{ab})\left(1 + \frac{(\partial_r A_t)^2}{g_{tt}g_{rr}}\right)}, \tag{2.28}$$

where we rescaled A_t to absorb the $2\pi\alpha'$ term. In the notation of equation (2.21), we can write

$$g(r) = -\det(g_{ab})e^{-2\phi}, \tag{2.29}$$

$$h(r) = \frac{\det(g_{ab})e^{-2\phi}}{g_{tt}g_{rr}}. \tag{2.30}$$

The background

For N_c Dp branes, at large N_c, the high temperature background is the black Dp brane metric, given by[15]

$$ds^2 = H^{-1/2}(-f dt^2 + d\vec{x}_p^2) + H^{1/2}\left(\frac{dr^2}{f} + r^2 d\Omega_{8-p}^2\right), \tag{2.31}$$

with

$$H(r) = \left(\frac{L}{r}\right)^{7-p}, \quad f(r) = 1 - \left(\frac{r_+}{r}\right)^{7-p}, \quad e^{\phi} = g_s H^{(3-p)/4}. \tag{2.32}$$

L is the characteristic length of the space, while g_s is the string coupling. This metric has a horizon at $r = r_+$.

Our probe Dq brane is fixed to share $d-1$ spacelike directions with the Dp branes. If $p > d-1$, the fundamental matter propagates on a d dimensional defect and we may consider the extra $p-(d-1)$ directions along the background brane to be compactified, giving an effective d dimensional gauge theory at low energies. Alternatively, we can build a $d-1$ dimensional gauge theory by compactifying one or more of the directions shared by the probe and background branes. Below, we will study field theories that are effectively $3+1$ dimensional using both methods.

We stipulate that the Dq probe brane wraps an S^n inside the S^{8-p} and extends along the radial direction r. These quantities are related by $q = d + n$. The induced metric on the Dq brane is

$$ds^2 = H^{-1/2}(-f dt^2 + d\vec{x}_{d-1}^2) + \left(\eta(r) + \frac{H^{1/2}}{f}\right) dr^2 + H^{1/2} r^2 d\Omega_n^2, \tag{2.33}$$

where

$$\eta(r) = \partial_r X^\mu \partial_r X^\nu G_{\mu\nu} - G_{rr}. \tag{2.34}$$

[15] More details on this solution can be found in [34].

Calculating equations (2.29) and (2.30) gives[16]

$$g(r) = r^{2n} f H^{\frac{1}{2}(p+n-d-3)} \left(\eta(r) + \frac{H^{1/2}}{f} \right), \tag{2.35}$$

$$h(r) = r^{2n} H^{\frac{1}{2}(p+n-d-2)}, \tag{2.36}$$

from which (2.23) gives the chemical potential

$$\mu = \int_{r_+}^{\infty} dr \frac{(d-2)\rho}{\sqrt{r^{2n}\left(\frac{L}{r}\right)^{\left(\frac{7-p}{2}\right)(p+n-d-2)} + (d-2)^2\rho^2}} \sqrt{\frac{f\eta(r)}{H^{1/2}} + 1}. \tag{2.37}$$

Now, $\eta(r)$ will be some combination of $(\partial_r \chi_i)^2$, where the χ_i denote the directions of transverse brane fluctuations. By writing down the equations of motion we can observe that $\partial_r \chi_i = 0$ is a solution, in which case the probe brane goes straight into the black hole along the radial direction r. This describes the high temperature, deconfined regime; we set $\eta(r) = 0$ in the following.

For large ρ we find

$$\rho \propto \mu^{\frac{1}{4}[(p-7)(p-d-2)+(p-3)(q-d)]}, \tag{2.38}$$

so that for the probe brane systems,

$$\alpha = \frac{1}{4}[(p-7)(p-d-2) + (p-3)(q-d)]. \tag{2.39}$$

As above, α is constrained as $\alpha > 1$ for convergence of the integral. If $\alpha \leq 1$, the contribution of the constant charge density to the total energy diverges, signalling a breakdown of the probe approximation. At this point, we can use equations (2.38) and (2.39) to investigate what type of $\rho - \mu$ behaviours can arise from Dp-Dq brane constructions.

Example: the Sakai-Sugimoto model

The well-known Sakai-Sugimoto model [13] consists of N_f probe D8-$\overline{\text{D8}}$ branes in a background of N_c D4 branes compactified on a circle. We have $p = 4$, $q = 8$, and $d = 4$. Putting these numbers into (2.38) yields

$$\rho \propto \mu^{5/2}, \tag{2.40}$$

consistent with previous results [42, 53].

[16] We leave the constant factors of g_s from e^{ϕ} out of the Lagrangian, as our goal here is just the power law dependence.

$\rho - \mu$ in $3+1$ dimensional probe brane theories

Equation (2.39) determines the dominant power law behaviour in all Dp-Dq configurations relevant to $3+1$ dimensional field theory. As discussed above, we can set the number of shared probe and background directions to be $d-1=3$ or put $d-1=4$ and demand one of the the spacelike shared directions to be periodic; see Table 2.1 for the results. The power $\alpha = 3$ is an upper bound for the $3+1$ dimensional probe brane gauge theories we have considered.

Our calculation above involves only the Born-Infeld action for the probe brane and in particular neglects any possible Chern-Simons terms that appear due to the coupling between the brane and a spacetime tensor field. The Chern-Simons term is important in the D4-D4 system, for example [37].

2.4.2 Bottom-up models and the Einstein-Maxwell action

We now turn our attention to bottom-up AdS/CFT models in the probe regime. To construct a phenomenological gauge / gravity model, we begin with a theory of gravity with a cosmological constant, such that the geometry is asymptotically AdS. To study the relationship between charge density and chemical potential in the dual field theory, we demand that there must be a gauge field in the bulk. At this point, our model has the ingredients for us to compute our desired result. But, one may ask what type of extensions are possible. Motivated by superconductivity and superfluidity studies, we will consider also a charged scalar field in our gravity theory. Adding a scalar field alters the dynamics of the system, notably resulting in different phases [63, 64]. When the scalar field takes on a non-zero expectation value, this breaks the $U(1)$ gauge symmetry in the bulk and corresponds to the presence of a $U(1)$ condensate in the boundary theory.

The particular model we study is the Einstein-Maxwell system with a charged scalar field:

$$S = \int d^{d+1}x\sqrt{-g}\left\{\mathcal{R} + \frac{d(d-1)}{L^2} - \frac{1}{4}F^{\mu\nu}F_{\mu\nu} - |\partial_\mu\psi - iqA_\mu\psi|^2 - V(|\psi|)\right\}. \tag{2.41}$$

Different dual field theories may be obtained by considering this action in different regimes and with different parameters. Below, we make the following ansatz for the gauge and scalar fields:

$$A = \phi(r)dt, \quad \psi = \psi(r). \tag{2.42}$$

The r component of Maxwell's equations will give that the phase of the complex field ψ is constant, so without loss of generality we take ψ real. For the remainder of the study, we choose units such that $L = 1$ and consider the potential $V(\psi) = m^2\psi^2$.

The probe limit

To get the probe approximation for the system described by (2.41), we rescale $\psi \to \psi/q$ and $A \to A/q$ before taking $q \to \infty$ while keeping the product $q\mu$ fixed (to maintain the same $A - \psi$ coupling). The gauge and scalar fields decouple from the Einstein equations and we study the fields in a fixed gravitational background.

The background is governed by the action

$$S = \int d^{d+1}x\sqrt{-g}\,\{\mathcal{R} + d(d-1)\}\,. \tag{2.43}$$

One solution here is the planar Schwarzschild-AdS black hole, given by

$$ds^2_{bh} = (-f_{bh}(r)dt^2 + r^2 dx_i dx^i) + \frac{dr^2}{f_{bh}(r)}, \tag{2.44}$$

with

$$f_{bh}(r) = r^2\left(1 - \frac{r_+^d}{r^d}\right), \tag{2.45}$$

where r_+ is the black hole horizon. Below, we consider two systems in the Schwarzschild-AdS background: the probe gauge field, and the probe gauge and scalar fields.

Computing μ and ρ

If the kinetic term for the gauge theory on the gravity side is the Maxwell Lagrangian,

$$\mathcal{L} = \frac{1}{4}\sqrt{-g}F_{\mu\nu}F^{\mu\nu}, \tag{2.46}$$

then for an asymptotically AdS space the field equation for the time component of the gauge field is

$$\phi'' + \frac{d-1}{r}\phi' + \cdots = 0, \tag{2.47}$$

where $'$ denotes an r derivative and $\ldots$ denotes terms that have higher powers of $1/r$. The solution is

$$\phi(r) = \phi_1 + \frac{\phi_2}{r^{d-2}} + \ldots . \tag{2.48}$$

Recalling that $\phi(\infty) = \mu$ determines that $\phi_1 = \mu$, while we can plug (2.48) into (2.46) and compute, using (2.15), that $\phi_2 = \rho$. We have that

$$\phi(r) = \mu - \frac{\rho}{r^{d-2}} + \ldots , \tag{2.49}$$

so that in practice, below, we just have to read off the coefficients of the leading and next to leading power of $1/r$ to find the chemical potential and the charge density.

The scalar field

Solving the scalar field equation at large r in an asymptotically AdS space results in the behaviour

$$\psi = \frac{\psi_1}{r^{\lambda_-}} + \frac{\psi_2}{r^{\lambda_+}} + \ldots , \tag{2.50}$$

where

$$\lambda_\pm = \frac{1}{2}\left\{d \pm \sqrt{d^2 + 4m^2}\right\}. \tag{2.51}$$

For m^2 near the Breitenlohner-Freedman (BF) bound [65, 66], in the range $-(d-1)^2/4 \geq m^2 \geq -d^2/4$, the choice of either $\psi_1 = 0$ or $\psi_2 = 0$ results in a normalizable solution [63]. For $m^2 > -(d-1)^2/4$, ψ_1 is a non-normalizable mode and ψ_2 is a normalizable mode. For the cases with the scalar field, we define our field theory by taking $\psi_1 = 0$, so that we never introduce a source for the operator dual to the scalar field.

The probe gauge field

Here, we study the probe gauge field, without the scalar field, in the Schwarzschild-AdS background (2.44). The equation of motion for ϕ is

$$\phi'' + \frac{d-1}{r}\phi' = 0. \tag{2.52}$$

Regularity at the horizon demands that $\phi(r_+) = 0$ and the AdS/CFT dictionary gives $\phi(\infty) = \mu$, leading to

$$\phi(r) = \mu\left(1 - \frac{r_+^{d-2}}{r^{d-2}}\right). \tag{2.53}$$

Then, applying (2.49), we have

$$\rho = \mu r_+^{d-2}. \tag{2.54}$$

The horizon r_+ depends only on the temperature, $T = r_+ d/4\pi$,[17] so this is a linear relationship between ρ and μ, in accordance with (2.20).

Adding a scalar field

We now turn on the scalar field in (2.41), and consider the dynamics in the Schwarzschild-AdS background (2.44).

The field equations become

$$\psi'' + \left(\frac{f'_{bh}}{f_{bh}} + \frac{d-1}{r}\right)\psi' + \left(\frac{q^2\phi^2}{f_{bh}^2} - \frac{m^2}{f_{bh}}\right)\psi = 0, \tag{2.55}$$

$$\phi'' + \frac{d-1}{r}\phi' - \frac{2q^2\psi^2}{f_{bh}}\phi = 0. \tag{2.56}$$

At this point, we can scale q to 1 by scaling ϕ and ψ, and so m is the only parameter here.

The coupling allows the gauge field to act as a negative mass for the scalar field. At small chemical potentials, $\psi = 0$ is the solution. As we increase μ, the effect of the gauge field on the scalar field becomes large enough such that the effective mass of the scalar field drops below the BF bound of the near horizon limit of the geometry, so that a non-zero profile for ψ is possible, and we have a phase transition to the field theory state with broken $U(1)$ symmetry. A smaller (more negative) squared mass results in a smaller critical chemical potential, at which the scalar field turns on.

Using a simple shooting method, for $d = 4$ we numerically solve equations (2.55, 2.56) and arrive at the relationship

$$\rho = c_{bh}^p(m^2)\mu^3, \tag{2.57}$$

where $c_{bh}^p(m^2)$ is a scaling constant that depends on the mass of the scalar field. The coupling to the scalar field has resulted in the larger power ($\alpha = 3$) in the scaling of ρ. A smaller squared mass corresponds to a larger value of c_{bh}^p and, for a given chemical potential, is dual to field theory with a higher charge density. In Figure 2.1, we can see the existence of a denser state when the scalar field turns on as well as the relative relation between the mass of the scalar field and the charge density in the field theory.

[17] For a Euclidean metric $ds^2 = \alpha(r)d\tau^2 + \frac{dr^2}{\beta(r)}$ with periodic $\tau = it$ coordinate and $\alpha(r_+) = \beta(r_+) = 0$, regularity at the horizon demands that the temperature (the inverse period of τ) be given by $T = \sqrt{\alpha'(r_+)\beta'(r_+)}/4\pi$.

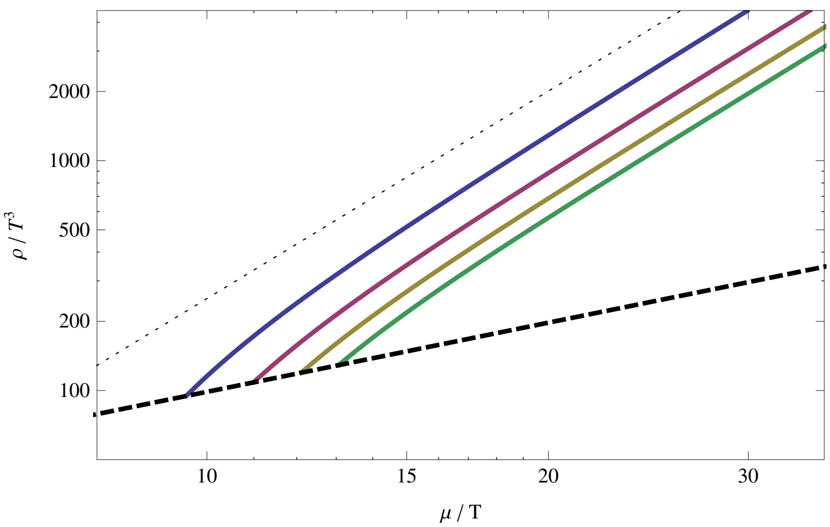

Figure 2.1: Charge density versus chemical potential for the probe gauge and scalar fields in the $d = 4$ black hole background, on a log-log scale. The thick dashed line is for the system with no scalar field for which, analytically, $\rho \propto \mu$. At a critical chemical potential, depending on the mass of the scalar field, configurations with non-zero scalar field become available. The thin dotted line is a model power law $\rho \propto \mu^3$, as described in equation (2.57). From left to right, the thick solid lines are for scalar field masses $m^2 = -15/4$, $-14/4$, $-13/4$, and -3. A more negative scalar field mass results in a denser field theory state at a given chemical potential.

The soliton probe

Motivated by recent work [4, 58, 67], we now add more structure to the bulk theory in the form of an extra periodic dimension. To model a $3+1$ dimensional field theory, we set $d = 5$ and stipulate that this includes one periodic spacelike coordinate w of length $2\pi R$. At energies much less than the scale set by this length, $E \ll 1/R$, the dual field theory will be effectively 3+1 dimensional. The extra dimension sets another scale for the field theory and enables a richer phase structure in the system.[18]

With the extra periodic direction, there is another solution to the back-

[18] The phase diagram including both black hole and soliton solutions, was studied in [58] for a $2+1$ dimensional field theory in the context of holographic superconductors and in [4] for a $3+1$ dimensional field theory in the context of holographic QCD and colour superconductivity.

ground described by (2.43). This is the AdS-soliton, given as the double-analytic continuation of the Schwarzschild-AdS solution (2.44):

$$ds^2_{sol} = (r^2 dx_\mu dx^\mu + f_{sol}(r)dw^2) + \frac{dr^2}{f_{sol}(r)}, \tag{2.58}$$

with

$$f_{sol} = r^2\left(1 - \frac{r_0^5}{r^5}\right). \tag{2.59}$$

Here, r_0 is the location of the tip of the soliton. For regularity, it is fixed by the length of the w dimension as

$$r_0 = \frac{2}{5R}. \tag{2.60}$$

By computing the free energy of the systems, it can be shown that the soliton background dominates over the black hole background for small enough temperatures and chemical potentials. As the temperature or chemical potential is increased, there is a first order phase transition to the black hole, which is the holographic version of a confinement / deconfinement transition.

For zero scalar field, the soliton can be considered at any temperature and chemical potential; the period of the Euclidean time direction defines the temperature while $\phi = \mu =$ constant is a solution to the field equations. In this case, $\rho = 0$ and we do not have an interesting $\rho - \mu$ relation. Considering a non-zero scalar field provides a source for the gauge field and allows non-trivial configurations.

In the soliton background (2.58), the equations of motion are

$$\psi'' + \left(\frac{f'_{sol}}{f_{sol}} + \frac{4}{r}\right)\psi' + \left(\frac{q^2\phi^2}{r^2 f_{sol}} - \frac{m^2}{f_{sol}}\right)\psi = 0, \tag{2.61}$$

$$\phi'' + \left(\frac{f'_{sol}}{f_{sol}} + \frac{2}{r}\right)\phi' - \frac{2q^2\psi^2}{f_{sol}}\phi = 0. \tag{2.62}$$

As in the black hole case, at this point we can set $q = 1$ by scaling the fields.

After numerically integrating, we have

$$\rho = c^p_{sol}(m^2)\mu^4. \tag{2.63}$$

Compared to the black hole case, above, we find a larger power of μ. At large densities, the average distance between charges becomes small compared to the size R of the periodic direction. In this limit, the system becomes effectively higher dimensional and so we would expect a larger power α in the $\rho - \mu$ relationship. The numerics were consistent with this result.

As can be seen in Figure 2.2, a more negative mass squared results in a smaller critical chemical potential and a denser field theory state at a given chemical potential. This is as expected by comparing the structure of the equations to those in the black hole case. Further, at a given chemical potential, the soliton solution corresponds to a denser field theory state than the black hole solution with the same scalar field mass.

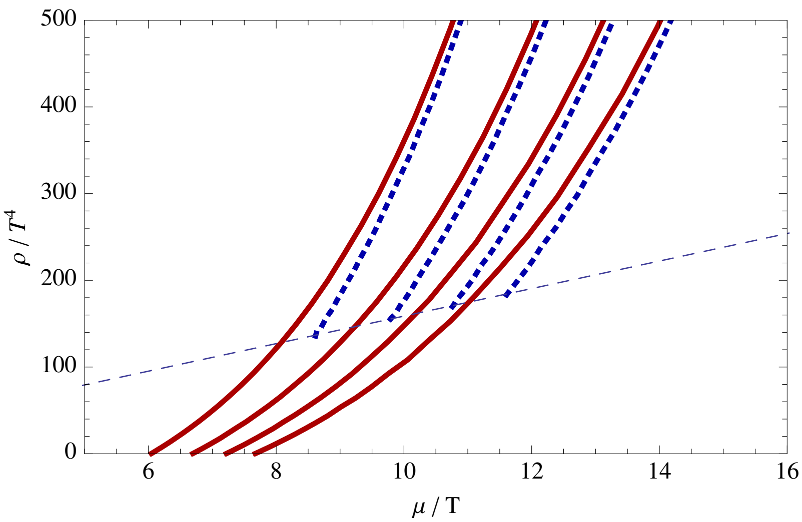

Figure 2.2: Charge density versus chemical potential for the probe gauge and scalar fields in the soliton background and the $d = 5$ black hole background. The thin dashed line is the probe gauge field in the black hole background for which, analytically, $\rho \propto \mu$. The thick solid lines are the soliton results (from left to right, the squared mass of the scalar field is $-22/4$, -5, $-18/4$, and -4) while the thick dashed lines are the black hole results (again, from left to right, $m^2 = -22/4$, -5, $-18/4$, and -4). Each of the thick lines approaches the power law $\rho \propto \mu^4$, equation (2.63). At a given chemical potential, the soliton background gives a field theory in a denser state.

2.5 $\rho - \mu$ in backreacted systems

Despite our analysis in section 2.4 relying on the probe approximation, it is interesting to ask how much of a difference allowing for backreaction on the bottom-up models could make to the $\rho - \mu$ relation and the bounds found previously. Henceforth we generalize the bottom-up model introduced in section 2.4.2 and allow for the backreaction of the gauge and scalar field on the metric. Recall that the action is

$$S = \int d^{d+1}x\sqrt{-g}\left\{\mathcal{R} + d(d-1) - \frac{1}{4}F^{\mu\nu}F_{\mu\nu} - |\partial_\mu\psi - iqA_\mu\psi|^2 - m^2\psi^2\right\}. \tag{2.64}$$

We start by studying the well-known Reissner-Nordstrom-AdS (RN-AdS) solution to the Einstein equation, in which $\psi = 0$. Later, we allow the scalar field to acquire a non-zero profile and investigate its consequences on the $\rho - \mu$ profile. We finish with the investigation of the backreacted version of the solitonic solution.

2.5.1 Charged black holes

The backreacted solution with no scalar field is the planar RN-AdS black hole, given by

$$ds^2 = (-f_{\mathrm{RN}}(r)dt^2 + r^2 dx_i dx^i) + \frac{dr^2}{f_{\mathrm{RN}}(r)}, \tag{2.65}$$

with[19]

$$f_{\mathrm{RN}}(r) = r^2\left(1 - \left(1 + \frac{(d-2)\mu^2}{2(d-1)r_+^2}\right)\frac{r_+^d}{r^d} + \frac{(d-2)\mu^2}{2(d-1)}\frac{r_+^{2(d-2)}}{r^{2(d-1)}}\right). \tag{2.66}$$

The gauge potential is

$$\phi(r) = \mu\left(1 - \frac{r_+^{d-2}}{r^{d-2}}\right), \tag{2.67}$$

so that, using (2.49), we have $\rho = \mu r_+^{d-2}$. Here, the horizon r_+ can be expressed as a function of the temperature and chemical potential through the Hawking temperature

$$T = \frac{1}{4\pi}\left(dr_+ - \frac{(d-2)^2\mu^2}{2(d-1)r_+}\right). \tag{2.68}$$

[19]We parametrize this solution in terms of the location of the horizon r_+ and the asymptotic value of the gauge field (the chemical potential μ) instead of the usual choices of the charge and mass of the black hole.

Eliminating r_+ in favour of ρ and μ in (2.68), we may solve for ρ to find

$$\rho = \left(\frac{(d-2)^2}{2d(d-1)}\right)^{\frac{d-2}{2}} \mu^{d-1} \left[\left(\frac{2(d-1)}{d}\right)^{\frac{1}{2}} \frac{2\pi T}{(d-2)\mu} + \sqrt{1 + \frac{8\pi^2(d-1)T^2}{d(d-2)^2\mu^2}}\right]^{d-2}. \tag{2.69}$$

Notice that the dominant power in the $\rho-\mu$ relationship is μ^{d-1}, as expected in a d dimensional conformal field theory. For $d = 4$, the particular large μ expansion is

$$\rho = \frac{1}{6}\mu^3 + \frac{\pi}{\sqrt{6}}\mu^2 T + \frac{1}{2}\pi^2\mu T^2 + \frac{1}{4}\sqrt{\frac{3}{2}}\pi^3 T^3 + \dots. \tag{2.70}$$

2.5.2 Hairy black holes

If we turn on the scalar field, an analytic solution to the equations of motion is no longer possible and we turn to numerical calculation. We take as our metric ansatz

$$ds^2 = -g(r)e^{-\chi(r)}dt^2 + \frac{dr^2}{g(r)} + r^2(dx_i dx^i), \tag{2.71}$$

where $g(r)$ will be fixed to have a zero at r_+, giving a horizon. We arrive at the following equations of motion:

$$\psi'' + \left(\frac{g'}{g} - \frac{\chi'}{2} + \frac{d-1}{r}\right)\psi' + \frac{1}{g}\left(\frac{q^2\phi^2 e^{\chi}}{g} - m^2\right)\psi = 0, \tag{2.72}$$

$$\phi'' + \left(\frac{\chi'}{2} + \frac{d-1}{r}\right)\phi' - \frac{2q^2\psi^2}{g}\phi = 0, \tag{2.73}$$

$$\chi' + \frac{2r\psi'^2}{d-1} + \frac{2rq^2\phi^2\psi^2 e^{\chi}}{(d-1)g^2} = 0, \tag{2.74}$$

$$g' + \left(\frac{d-2}{r} - \frac{\chi'}{2}\right)g + \frac{re^{\chi}\phi'^2}{2(d-1)} + \frac{rm^2\psi^2}{d-1} - dr = 0. \tag{2.75}$$

The first two equations can be derived via the Euler-Lagrange equations for ϕ and ψ, while the final two equations are the tt and rr components of Einstein's equation.

In this system, as in the probe case, section 2.4.2, at small chemical potentials the scalar field is identically zero. As we increase the chemical potential above a critical value, the system undergoes a second order phase transition to a state with non-zero scalar field. When the scalar field condenses, the corresponding field theory is in a denser state at the same chemical potential than for the system without scalar field.

We solve the equations numerically for $d = 4$, to yield the result, in the phase with the scalar field,

$$\rho = c_{bh}(q, m^2)\mu^3. \tag{2.76}$$

As we increase the charge or decrease the mass squared of the scalar field, the critical chemical potential, at which the scalar condenses, decreases, while the scaling coefficient c_{bh} increases. The scaling coefficient $c_{bh}(q, m^2)$ is, in all cases we checked, larger than the coefficient of the μ^3 term in the AdS-Reissner-Nordstrom black hole, equation (2.70), indicating that the density scales faster with the chemical potential when the scalar field is present.

When we include metric backreaction for the black hole, the dominant power in the $\rho - \mu$ relationship is greater than the probe case when there is no scalar field and is the same as the probe case when there is a scalar field, indicating that, at least for the systems considered, the bounds found for the $\rho - \mu$ behaviour apply to the backreacted cases as well.

2.5.3 Backreacted soliton

Motivated by the form of the soliton background (2.58) we choose the metric ansatz

$$ds^2 = \frac{dr^2}{r^2 B(r)} + r^2 \left(e^{A(r)} B(r) dw^2 - e^{C(r)} dt^2 + dx_i dx^i\right), \tag{2.77}$$

where we constrain $B(r_0) = 0$ so that the tip of the soliton is at r_0. The field and Einstein equations give

$$\psi'' + \left(\frac{6}{r} + \frac{A'}{2} + \frac{B'}{B} + \frac{C'}{2}\right)\psi' + \frac{1}{r^2 B}\left(\frac{e^{-C}(q\phi)^2}{r^2} - m^2\right)\psi = 0, \tag{2.78}$$

$$\phi'' + \left(\frac{4}{r} + \frac{A'}{2} + \frac{B'}{B} - \frac{C'}{2}\right)\phi' - \frac{2\psi^2 q^2 \phi}{r^2 B} = 0, \tag{2.79}$$

$$\begin{aligned} B'\left(\frac{4}{r} - \frac{C'}{2}\right) + B\left(\psi'^2 - \frac{1}{2}A'C' + \frac{e^{-C}\phi'^2}{2r^2} + \frac{20}{r^2}\right) + \\ + \frac{1}{r^2}\left(\frac{e^{-C}(q\phi)^2\psi^2}{r^2} + m^2\psi^2 - 20\right) = 0, \end{aligned} \tag{2.80}$$

$$C'' + \frac{1}{2}C'^2 + \left(\frac{6}{r} + \frac{A'}{2} + \frac{B'}{B}\right)C' - \left(\phi'^2 + \frac{2(q\phi)^2\psi^2}{r^2B}\right)\frac{e^{-C}}{r^2} = 0, \quad (2.81)$$

$$A' = \frac{2r^2C'' + r^2C'^2 + 4rC' + 4r^2\psi'^2 - 2e^{-C}\phi'^2}{r(8 + rC')}. \quad (2.82)$$

We solve equations (2.78-2.81) numerically with asymptotically AdS boundary conditions before integrating (2.82) to find A.[20] The results are consistent with a $\rho - \mu$ relationship of the form

$$\rho = c_{sol}(q, m^2)\mu^4. \quad (2.83)$$

As in the probe case, the effective higher dimension of the space dictates the power in the relationship. The dependence of $c_{sol}(q, m^2)$ on q and m^2 is as in the backreacted black hole case, section 2.5.2. Like the black hole with scalar field, the backreacted soliton with scalar field gives the same dominant power α as the corresponding probe case.

2.6 Discussion

In these notes we studied the $\rho - \mu$ relation for a variety of holographic field theories, and set conditions for physically consistent relationships based on local stability and causality. We observed that all of the examples considered are well modelled by a power law $\rho = c\mu^\alpha$ in the large μ regime and that none of them fail to satisfy any of the general constraints established in sections 2.2 and 2.3. Except for the case of a probe gauge field in the Schwarzschild-AdS black hole background, the power α in all the bottom-up models obeyed the generic dimensional argument discussed in the introduction, as can be seen in Table 2.2. This resulted in a larger power for the models with an extra periodic dimension. The brane constructions, Table 2.1, displayed a larger variety of power laws, with the range $1 < \alpha \leq 3$, where α depended on the particular dimensions of the probe and background branes.

The study of bottom-up models led to the conclusion that, in general, the presence of a non-zero profile for the scalar field in the bulk induces a larger charge density on the boundary. In most cases, this change was realized as an increase of the scaling coefficient c while the power law was

[20] More details on the numerical process can be found in [4].

kept unaltered. The only exception was the probe Einstein-Maxwell case, section 2.4.2. Here, in the absence of a scalar field, the probe Maxwell field enjoys its standard linear equations of motion, and naturally we find a linear $\rho-\mu$ relationship. With a non-zero scalar field, the power law becomes $\rho \propto \mu^{d-1}$, as expected for the underlying CFT. In systems with an extra periodic direction, the numerical results displayed in Figure 2.2 support the conclusion that at a given (large enough) chemical potential, the solitonic phase is denser than the corresponding black hole phase.

Despite our attempt to survey a large variety of holographic models, we do not claim to have presented a complete report and we do not discard the possibility of finding different $\rho - \mu$ relations in other types of bottom-up and top-down models. For example, one generalization would be to include $N_f > 1$ flavour branes in the Dp-Dq systems; this has been shown to change the power α in the relation [53]. It would be interesting to extend this study to other classes of systems and to see how the results compare to those given here.

Chapter 3

Holographic stripes[1]

3.1 Introduction and summary

The gauge / gravity duality describes phenomena in strongly coupled field theories via their relation to classical or semi-classical gravitational systems. From the perspective of the boundary quantum field theory, this relation can be used to construct and study models for ill-understood phenomena which arise in such strongly coupled systems. On the other hand, the relation to local quantum field theory helps motivate and interpret new results in classical and quantum gravity. In this chapter we apply holography to study the spontaneous breaking of translation invariance and the formation of striped order.

Stripes are known to form in a variety of strongly coupled systems, from large N QCD [68, 69] to systems of strongly correlated electrons (for a review see [29]). The formation of stripes and the associated reduced dimensionality are speculated to be related to the mechanism of superconductivity in the cuprates [70]. It is therefore useful to study striped phases in the holographic context.

Besides its interest in the boundary theory, this study has an intrinsic interest in the bulk gravitational context.[2] We describe striking bulk and boundary properties of our bulk solutions, including frame dragging effects, the magnetic field, the curvature and the geometry. Some of the features can be understood as the emergence of a near horizon region which acts as a bulk topological insulator. The magnetoelectric effect is then responsible for the patterns we observe for the bulk magnetic field and vorticity.

Our study is facilitated by a numerical solution of the set of coupled nonlinear Einstein and matter equations in the bulk, which exhibit a nor-

[1] A version of this chapter has been published [2]. This chapter presents a concise version of the study of holographic stripes while chapter 4 provides full results and the complete details of the analysis.

[2] Our model describes a black hole whose instability to the formation of inhomogeneous structures resembles the black string instability [71] which is known to be of the second order for high enough dimensions [72].

malizable inhomogeneous mode. Previous studies of inhomogeneous solutions in asymptotically AdS spacetimes concentrated on non-normalizable modes [73] (i.e. *explicit* rather than spontaneous breaking of translation invariance) or the study of co-homogeneity one solutions [74–77], where one of the translational Killing vectors is replaced by a helical Killing vector. More recently, such spontaneous breaking was exhibited in a probe model, which was shown to have a magnetic field induced lattice ground state [78]. In contrast to the above, our solutions are co-homogeneity two, they backreact on the geometry, and exhibit *spontaneous* breaking of translation invariance below a critical temperature.

These features are analyzed as a function of temperature. In particular, we find that the horizon of the black hole develops a 'neck' and a 'bulge' in the transverse direction which shrink with temperature, such that the ratio of their sizes contracts as fast as $\sim T^{\sigma}$, with an order $\sigma \sim 0.1$ exponent. Simultaneously, the proper length of the horizon in the transverse direction grows at a rate $\sim 1/T^{0.1}$. However, the curvature remains finite, and its maximal value, occurring at the bulge, tends to a constant in the limit $T \to 0$.

The bulk black hole solutions give rise to the holographic stripes on the boundary, characterized by non vanishing momentum and electric current and modulations in charge and mass density. Starting small near T_c, the amplitudes of the modulations grow steadily at lower temperatures, approaching finite values at $T \to 0$.

Finally, we study the thermodynamics of the system by constructing phase diagrams in various ensembles. For small values of the axion coupling, where the thermodynamic potentials in both phases are nearly degenerate, our numerical method is not accurate enough to sharply distinguish between weak first order and second order transitions. However, for sufficiently large values of the axion coupling we discover a clear second order phase transition in the canonical (fixed charge), the grand canonical (fixed chemical potential) and the micro-canonical ensembles. We describe both the finite system (of fixed length) and the infinite system, where we find that the dominant stripe width changes as function of temperature.

3.2 The holographic setup

The Lagrangian describing our coupled system is [30]

$$\begin{aligned}
\mathcal{L} &= \frac{1}{2}\mathcal{R} - \frac{1}{2}\partial^\mu\psi\partial_\mu\psi - \frac{1}{4}F^{\mu\nu}F_{\mu\nu} - V(\psi) - \mathcal{L}_{int}, \\
V(\psi) &= -6 + \frac{1}{2}m^2\psi^2, \\
\mathcal{L}_{int} &= \frac{1}{\sqrt{-g}}\frac{c_1}{16\sqrt{3}}\,\psi\,\epsilon^{\mu\nu\rho\sigma}F_{\mu\nu}F_{\rho\sigma},
\end{aligned} \tag{3.1}$$

where $\mathcal{R}$ is the Ricci scalar, $F_{\mu\nu}$ is the Faraday tensor, $\mathcal{L}_{int}$ describes the axion coupling and g is the determinant of the metric. We use units in which the AdS radius $l^2 = 1/2$, Newton's constant $8\pi G_N = 1$, and $c = \hbar = 1$, and choose $m^2 = -4$ and several values of c_1.

Perturbative instabilities towards the formation of charge and current density waves were identified in [30] for a range of wave numbers and temperatures.[3] We note the appearance of *axion electrodynamics* in the bulk theory. It is curious that here, as in several examples of inhomogeneous instabilities (see also [80]), the topology of the bulk fields seems to play an important role, though the analysis performed to discover the instability is local in nature.[4]

In this chapter we investigate the end-point of the instability. Part of the boundary data is the spatial periodicity, and we focus mostly on the wave number with the largest critical temperature T_c [30]. This state is a co-homogeneity two solution, thus we construct the family of stationary solutions that emerge from the critical point, assuming all the fields to be functions of the radial coordinate r and one spatial coordinate x.

Our ansatz includes the scalar field $\psi(r,x)$, the gauge field components $A_t(r,x)$ and $A_y(r,x)$ and the metric

$$\begin{aligned}
ds^2 &= -2r^2 f(r)e^{2A(r,x)}dt^2 + 2r^2e^{2C(r,x)}(dy - W(r,x)dt)^2 \\
&\quad + e^{2B(r,x)}\left(\frac{dr^2}{2r^2f(r)} + 2r^2dx^2\right),
\end{aligned} \tag{3.2}$$

where for the sake of convenience we included in the definition of the metric functions the factor $f(r)$ characterizing the metric of the AdS Reissner-

[3] An interesting application of the instability in this model has appeared very recently [79].

[4] It is not generic, however, that the topology of the bulk fields is essential for inhomogeneous instabilities. See [81] for an example system whose bulk does not involve an axion.

Nordström (RN for short) solution, with horizon at $r = r_0$:

$$f(r) = 1 - \left(1 + \frac{\mu^2}{4r_0^2}\right)\left(\frac{r_0}{r}\right)^3 + \frac{\mu^2}{4r_0^2}\left(\frac{r_0}{r}\right)^4 .$$

The inhomogeneous solutions reduce to the RN solution above the critical temperature.

The conformal in r, x plane ansatz (3.2) is convenient in constructing co-homogeneity two solutions. With this ansatz, the Einstein and matter equations reduce to seven coupled elliptic equations and two constraint equations. Moreover, the constraint system can be solved elegantly using its similarity to a Cauchy-Riemann problem [82].

The boundary conditions we impose correspond to regularity conditions at the horizon and asymptotically AdS conditions at the conformal boundary. With these boundary conditions, the set of solutions we find depend on three parameters: the temperature T, the chemical potential μ and the periodicity in the x direction L. Using the conformal symmetry inherent in asymptotically AdS spaces, the moduli space of solution depends only on the two dimensionless combinations of these parameters. To focus on the dominant critical mode that becomes unstable at the largest temperature T_c we choose $L = 2\pi/k_c$.

On the spatial boundaries it is useful to impose 'staggered' periodicity conditions. Using two reflection symmetries which are preserved by the form of the unstable perturbation, one can reduce the numerical domain to a quarter period and impose[5] $\partial_x\psi(x=0) = 0$, $\psi(x = L/4) = 0$, $h(x = 0) = 0$, $\partial_x h(x = L/4) = 0$ and $\partial_x g(x = 0) = 0$, $\partial_x g(x = L/4) = 0$, where h represents the fields A_y and W, and g refers collectively to A, B, C and A_t.

The elliptic equations derived from (3.1) are discretized using finite difference methods and are solved numerically by a straightforward relaxation with the specified boundary conditions. In this method the equations are iterated starting with an initial guess for all fields, until successive changes in the functions drop below the desired tolerance. We verify that the remaining two constraints are satisfied by those solutions. More details of this numerical procedure are given in chapter 4 and appendix A.2.

[5]Our boundary conditions do not exclude the homogeneous solution, but since that solution is unstable we find that in practice our numerical procedure converges to the inhomogeneous solution unless we are very close to the critical point.

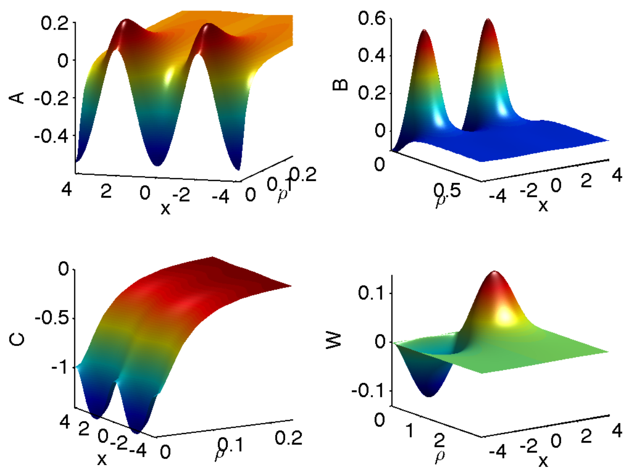

Figure 3.1: Metric functions for $\theta \simeq 0.11$ and $c_1 = 4.5$. Note that the metric functions A, B and C have half the period of W. The variation is maximal near the horizon, located at $\rho = 0$, and it decays as the conformal boundary is approached, when $\rho \to \infty$. The matter fields (not shown) behave in a qualitatively similar manner.

3.3 The solutions

A convenient way to parametrize our inhomogeneous solutions is by the dimensionless temperature $\theta = T/T_c$, relative to the critical temperature T_c. Our method allows us to find solutions in the range $0.003 \lesssim \theta \lesssim 0.9$ for $c_1 = 4.5$ and the range $0.00016 \lesssim \theta \lesssim 0.96$ for $c_1 = 8$, for fixed μ.

Bulk Geometry. For subcritical temperatures, as we descend into the inhomogeneous regime, the metric and the matter fields start developing increasing variation in x. Figure 3.1 displays the metric functions for $\theta \simeq 0.11$, over a full period in the x direction, in the case $c_1 = 4.5$. The matter fields have qualitatively similar behaviour. The variation of all fields is maximal near the horizon of the black hole at $\rho \equiv \sqrt{r^2 - r_0^2} = 0$, and it gradually decreases toward the conformal boundary, $\rho \to \infty$.

Many of the special features of the solutions we find are related to the presence of axion electrodynamics, the effective description of the electromagnetic response of a topological insulator, in the gravity action. In the broken phase we have an axion gradient in the near horizon geometry, which therefore realizes a topological insulator interface.[6] The presence and the pattern of a near horizon magnetic field, summarized in the field A_y, can be related to the *magnetoelectric* effect in such interfaces.

In curved space the magnetic field is accompanied by *vorticity*, which is manifested by the function W. This causes frame dragging effects in the y direction. Test particles will be pushed along y with speeds $W(r, x)$, in particular the direction of the flow reverses every half the period along x. The drag vanishes at the horizon and at the location of the nodes of W where $x = Ln/2$, for integer n (see Figure 3.1). In general, the dragging effect remains bounded, the vector ∂_t is everywhere timelike, and no ergoregion forms.

The Ricci scalar of the RN solution is $\mathcal{R}_{RN} = -24$, constant in r and independent of the parameters of the black hole. This is no longer true for the inhomogeneous phases, where the Ricci scalar becomes position dependent. The right panel of Figure 3.2 illustrates the spatial variation of the Ricci scalar, relative to the $\mathcal{R}_{RN}$ for $\theta \simeq 0.003$. The plot corresponds to $c_1 = 4.5$, however we observe qualitatively similar results for other values of the coupling.

The maximal curvature is always along the horizon at $x = n\,L/2$ for integer n. It grows when the temperature decreases and approaches the finite value of $\mathcal{R} \simeq -94$ in the small temperature limit.

The left panel in Figure 3.2 shows the variation of transverse extent of the horizon in the y direction, $r_y(x) \equiv \sqrt{2}\,r_0 \exp[C(r_0, x)]$, along x for $\theta \simeq 0.003$. Typically there is a 'bulge' occurring at $x = n\,L/2$ and a 'neck' at $x = (2\,n+1)\,L/4$, for integer n. Note that Ricci scalar curvature is maximal at the bulge and not at the neck as would happen, for instance, in the spherically symmetric black string case. The size of both the neck and the bulge monotonically decrease with temperature, however, the neck is shrinking faster. We find that the ratio scales as a power law $r_y^{\text{neck}}/r_y^{\text{bulge}} \sim \theta^\sigma$ near the lower end of the range of θ's that we investigated. The exponent σ depends on the coupling, ranging from about 0.5 for $c_1 = 4.5$ to approximately 0.1 for $c_1 = 8$.

Another aspect of the geometry is the proper size of the stripe in the x direction at fixed r, $l_x(r) \equiv \int_0^L \exp[B(r, x)]\,dx$. The proper length tends to the coordinate length as $1/r^3$ asymptotically as $r \to \infty$, but it exceeds that as the horizon is approached. Namely, the inhomogeneous phase 'pushes space' around it along x, resembling the 'Archimedes effect'. The proper length of

[6] It would be interesting to discuss localized matter excitations on the interface, especially fermions, along the lines of [83].

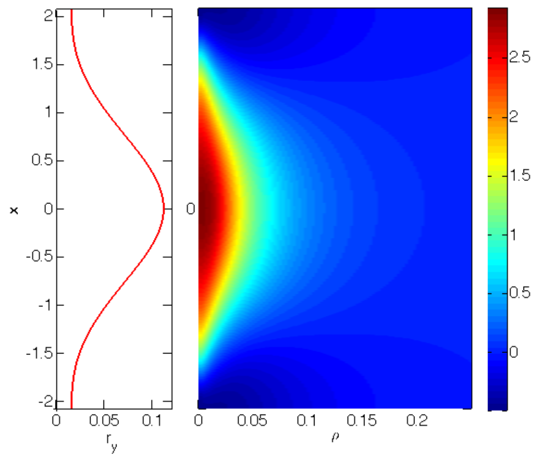

Figure 3.2: Left panel: The variation along x of the size of the horizon in the y direction includes alternating 'necks' and 'bulges'. Right panel: Ricci scalar relative to that of RN black hole, $\mathcal{R}/\mathcal{R}_{RN} - 1$ for $\theta \simeq 0.003$ over half the period. The scalar curvature is maximal along the horizon at the bulge $x = n\,L/2$ for integer n. The axion coupling here is $c_1 = 4.5$ and similar results appear for other c_1's.

the horizon is maximal and it grows as the temperature decreases. We find that at small θ the proper length of the horizon diverges approximately as $\sim \theta^{-0.1}$.

Boundary Observables. Near the conformal boundary the fields decay to their AdS values, and the subleading terms in their variation are used to define the asymptotic charge densities of our solutions. The subleading fall-offs of the metric functions in our ansatz determine the boundary stress-energy tensor, whereas the fall-offs of the gauge field determine the charge and current densities of the boundary theory. Finally, the subleading term of the scalar field near infinity determines the scalar condensate.

For our inhomogeneous solutions we find that all charge and current densities are spatially modulated, except for $\langle T_{xx} \rangle$, which is constant, consistent with the conservation of boundary energy-momentum. We define the total charges of a single stripe by integrating the charge densities over the full period L. These integrated quantities are charge densities per unit length in the translationally invariant direction y.

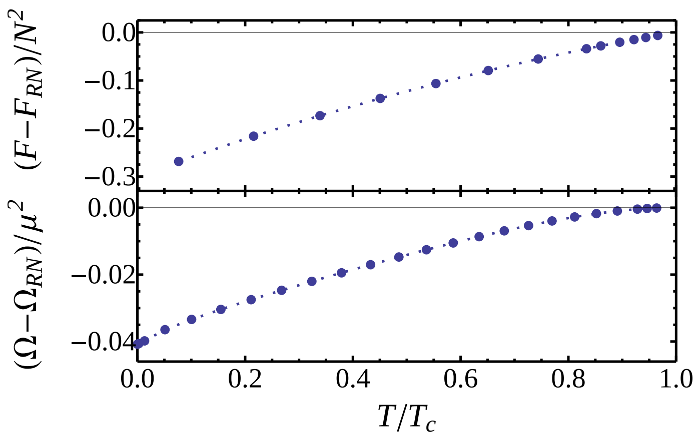

Figure 3.3: Difference in the thermodynamic potentials between the inhomogeneous phase and the RN solution for $c_1 = 8$, plotted against the temperature. In both ensembles there is a second order phase transition, with the inhomogeneous solution dominating below the critical temperature.

3.4 Thermodynamics

We demonstrated that below the critical temperature T_c there exists a new branch of solutions which are spatially inhomogeneous. The question of which solution dominates the thermodynamics depends on the ensemble used. We start our discussion by fixing the boundary periodicity, corresponding to working in a finite system of length L.[7] We discuss the system with infinite length in the inhomogeneous x-direction below.

The canonical ensemble corresponds to fixing the temperature and the total charge. This describes the physical situation in which the system is immersed in a heat bath consisting of uncharged particles. In the upper panel of Figure 3.3 we plot the difference of the normalized total free energy, $F = M - TS$, between the two classical solutions as function of the temperature T, for $c_1 = 8$. In our ensemble the total charge N is fixed, and we use the scaling symmetry of the boundary theory to set $N = 1$, or in other words measure all quantities in terms of N. As a result the free energy is a function of one parameter, the temperature T. The figure displays a second order phase transition, where the inhomogeneous solution dominates

[7]Here, we mostly discuss the case $L = 2\pi/k_c$, where k_c is the wavelength of the dominant instability, that with the highest critical temperature. Results for other values of L appear in chapter 4, and are qualitatively similar.

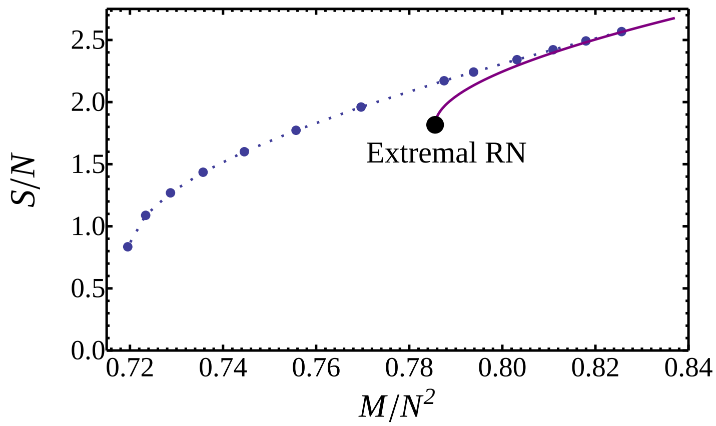

Figure 3.4: The entropy of the inhomogeneous solution for $c_1 = 8$ (points with dotted line) and of the RN solution (solid line). Below the critical temperature, the striped solution has higher entropy than the RN. The RN branch terminates at the extremal RN black hole, while the striped solution persists to smaller energies.

the thermodynamics below the critical temperature T_c, the temperature at which inhomogeneities first develop.

If we fix the chemical potential instead of the charge, we discuss a situation where the system is immersed in a plasma made of charged particles. To study the thermodynamics we use the grand canonical free energy $\Omega = M - TS - \mu N$, displayed in the lower panel of Figure 3.3. In this ensemble it is convenient to measure all quantities in units of the fixed chemical potential μ. Then, again, the free energy is a function of only the temperature T. In the fixed chemical potential ensemble we find a similar second order transition, where the inhomogeneous charge distribution starts dominating the thermodynamics at the temperature where the inhomogeneous instability develops.

The physical situation relevant to the study of the real time dynamics of the instability corresponds to fixing the mass and the charge. This is the microcanonical ensemble, describing an isolated system in which all conserved quantities are fixed. In this ensemble it is convenient to measure all quantities in terms of the (fixed) charge, and the remaining control parameter is then the mass M. We find that in this ensemble as well, the striped solutions dominate the thermodynamics (have higher entropy) for all temperature below the critical temperature T_c, at least when the axion

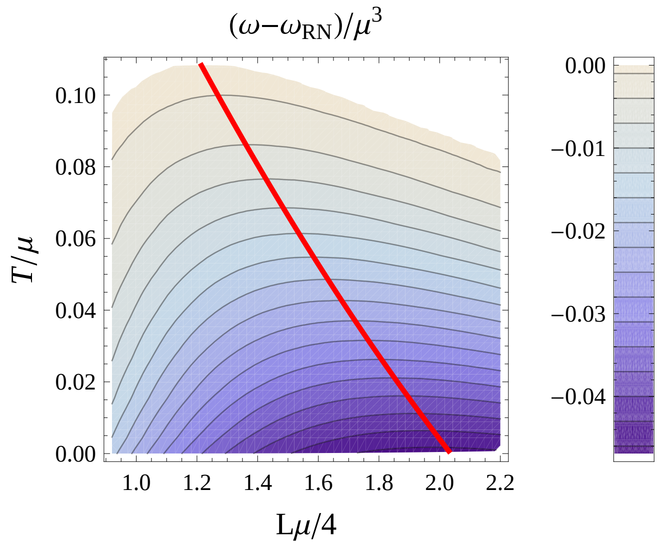

Figure 3.5: A contour plot of the free energy density, relative to the homogenous solution. The red line shows the variation of the dominant stripe width as function of the temperature for $c_1 = 8$.

coupling c_1 is sufficiently large. This is shown in Figure 3.4.

Finally, we can also study the infinite system in the inhomogeneous x-direction, which we choose to look at in the canonical ensemble. In this case we are in a position to compare the free energy *density* of different stripes, of different lengths in the x-direction. This comparison is shown in Figure 3.5, where we see that the qualitative picture is the same as in the finite system – a second order transition with striped solutions dominating at every temperature below the critical temperature. Just below the critical temperature, the dominant stripe is that corresponding to the critical wavelength k_c. However, for lower temperature different stripes will dominate, in fact we see in Figure 3.5 that the dominant stripe width tends to increase with decreasing temperature.

Chapter 4

Striped order in the AdS/CFT correspondence[1]

4.1 Introduction and summary

The gauge / gravity duality is a relationship between a strongly coupled field theory and a gravity system in one higher dimension. This correspondence has been fruitful in studying various field theory phenomena by translating the problem to the gravitational context. In particular, the duality has shone new light on many condensed matter systems - see [18, 21, 84, 85] for reviews.

Early models in this area, such as the holographic superconductor [11], focused on homogeneous phases of field theories. In this case, the fields on the gravity side depend only on the radial coordinate in the bulk and the problem reduces to the solution of ordinary differential equations. However, many interesting phenomena occur in less symmetric situations. Generically, the problem of finding the gravity dual to an inhomogeneous boundary system will necessitate solving relatively more difficult partial differential equations, almost always resulting in the need for numerical methods. While these become technically hard problems, there exist established numerical approaches. Due to the success of the holographic method in studying homogeneous situations, it is worthwhile to push the correspondence to these less symmetric situations in order to describe more general phenomena in this context.

One particular area of condensed matter that appears to be amenable to a holographic description is the appearance of striped phases in certain materials.[2] These phases are characterized by the spontaneous breaking of translational invariance in the system. Examples include charge density waves and spin density waves in strongly correlated electron systems, where

[1] A version of this chapter has been published [3]. A concise presentation of this study is given in chapter 3.

[2] Stripes are also known to form in large-N QCD [68, 69].

either the charge and/or the spin densities become spatially modulated (for a review see [29]). The formation of stripes is conjectured to be related to the mechanism of superconductivity in the cuprates [70]. To approach this striking phenomenon from the holographic perspective, one would look for an asymptotically AdS gravity system which allows a spontaneous transition to a modulated phase.

Recently, several interesting spatially modulated holographic systems have been studied. One way to study stripes on the boundary is to source them by imposing spatial modulation in the non-normalizable modes of some fields, explicitly breaking the translation invariance, as in [73, 86].[3] However, if one wishes to make contact with the context described above, it is important that the inhomogeneity emerges spontaneously rather than be introduced explicitly.

In some cases, the spatially modulated phase has an extra symmetry, allowing the situation to be posed as a co-homogeneity one problem on the gravity side. Examples include systems in which one of the translational Killing vectors is replaced by a helical Killing vector [74–76, 80, 90, 91]. More general inhomogeneous instabilities, in which one of the translation symmetries is fully broken, have been described in phenomenological model [30, 92] and in certain $\#ND = 6$ brane systems [93–95].[4]

In this chapter, we study the full non-linear co-homogeneity two striped solutions to the Einstein-Maxwell-axion model that stem from the normalizable, inhomogeneous modes of the Reissner-Nordström-AdS solution detailed in [30]. In this model, below a critical temperature, stripes spontaneously form in the bulk and on the boundary. We study the properties of the stripes in both the fixed length system, in which the wavenumber is set by the size of the domain and charges are integrated over the stripe, and the infinite system, in which the corresponding thermodynamic densities are studied. For the black hole at fixed length, we examine the behaviour in different thermodynamic ensembles as we vary the temperature and wavenumber.

The study is facilitated by a numerical solution to the set of coupled Einstein and matter equations in the bulk. Inspired by the black string case [82, 98], we fix the metric in the conformal gauge, resulting in a set of field equations and a set of constraint equations. Then, as described in [82], the resulting constraint equations can be solved by imposing particular

[3] In a similar vein, more recently, lattice-deformed black branes have been of interest in studies of conductivity in holographic models [79, 87–89].

[4] Other studies of inhomogeneity in the context of holography include [78, 83, 96, 97].

boundary conditions on the fields.

As well as being of interest from the holographic perspective these numerical solutions are important as they represent new inhomogeneous black hole solutions in AdS. We find strong evidence that the unstable homogeneous branes transition smoothly to the striped state below the critical temperature.[5] As we approach zero temperature the relative inhomogeneity is seen to grow without bound and the black hole horizon tends to pinch off, signalling the formation of a spacetime singularity in this limit.

A subset of our results has already been reported in chapter 3; in this chapter we provide full details. The summary of the results follow:

Boundary field theory

- We calculate the fully back-reacted normalizable inhomogeneous modes.
- The stripes have momentum, electric current and modulations in charge and mass density (see [100] for a recent study of angular momentum generation).
- As a function of temperature, the modulations start small, then grow and saturate as $T \to 0$.
- We study the stripe of fixed length in various ensembles, finding a second order phase transition, for sufficiently large axion coupling, in each of the grand canonical (temperature T, chemical potential μ fixed), canonical (T, charge N fixed) and microcanonical (mass M, N fixed) ensembles. We compute corresponding critical exponents.
- For the infinite length system, there is a second order transition to a striped phase. The width of the dominant stripe grows as the temperature is decreased.
- In the zero temperature limit, within the accuracy of our numerics, the entropy appears to approach a non-zero value.

Bulk geometry

The new inhomogeneous black brane solutions that we find have peculiar features, including

[5] The instability to the formation of the striped black branes resembles the black string instability [71] which is known to be of the second order for high enough dimensions [72, 99].

- The inhomogeneities are localized near the horizon, and die off asymptotically following a power law decay.
- The phenomena of vorticity, frame dragging and the magneto-electric effect similar to one produced by a near horizon topological insulator are observed.
- The inhomogeneous black brane has a neck and a bulge. In the curvature at the horizon, the maximum is at the bulge. In the limit of small temperatures, the neck shrinks to zero size.
- The proper length of the horizon grows when temperature is decreasing, and diverges as $1/T^{0.1}$ in the limit $T \to 0$. The proper length in the stripe direction increases from the boundary to the horizon, which can be thought of as a manifestation of an 'Archimedes effect'.

In section 4.2, we define our model and set up our numerical approach, describing our ansatz, boundary conditions and solving procedure. Then, in section 4.3, we report on interesting geometrical features of the bulk solutions. Section 4.4 studies the solutions at fixed length from the point of view of the boundary theory. There, we make the comparison to the homogeneous solution and find a second order transition, in addition to describing the observables in the theory. In section 4.5, we relax the fixed length condition and find the striped solution that dominates the thermodynamics for the infinite system. Appendix B.1 provides details about computing the observables of the inhomogeneous solutions while appendix B.2 gives more details on the numerics, including checks of the solutions and validations of our numerical method.

Note added: As the manuscript that forms the basis for this chapter was being completed, [101] and [102, 103] appeared, which use a different method and have some overlap with this work.

4.2 Numerical set-up: Einstein-Maxwell-axion model

In [30], perturbative instabilities of the Reissner-Nordström-AdS (RN for short) black brane were found within the Einstein-Maxwell-axion model. In [2] and here, we construct the full non-linear branch of stationary solutions following this zero mode.

4.2.1 The model and ansatz

The Lagrangian describing our coupled system can be written as [30]

$$\mathcal{L} = \frac{1}{2}(\mathcal{R}+12) - \frac{1}{2}\partial^\mu\psi\partial_\mu\psi - \frac{1}{2}m^2\psi^2 - \frac{1}{4}F^{\mu\nu}F_{\mu\nu} - \frac{1}{\sqrt{-g}}\frac{c_1}{16\sqrt{3}}\,\psi\,\epsilon^{\mu\nu\rho\sigma}F_{\mu\nu}F_{\rho\sigma}, \tag{4.1}$$

where $\mathcal{R}$ is the Ricci scalar, $F_{\mu\nu}$ is the Faraday tensor, ψ is a pseudo-scalar field and g is the determinant of the metric. We use units in which the AdS radius $l^2 = 1/2$, Newton's constant $8\pi G_N = 1$ and $c = \hbar = 1$, and choose $m^2 = -4$. The constant c_1 controls the strength of the axion coupling.

For this choice of scalar field mass, instabilities exist for all choices of c_1. For $c_1 = 0$, the instability is towards a black hole with neutral scalar hair. For $c_1 > 0$, inhomogeneous instabilities along one field theory direction exist for a range of wavenumbers k. The critical temperature at which each mode becomes unstable depends on the wavenumber: $T_c(k)$. For a given c_1, there is a maximum critical temperature, above which there are no unstable modes. As one increases c_1, the critical temperature of a given mode k increases, such that for a fixed temperature a larger range of wavenumbers will be unstable. See appendix B.2.1 for more details on the perturbative analysis.

One may consider generalizations of this action, including higher order couplings between the scalar field and the gauge field. In particular, as discussed in [30], generalizing the Maxwell term as $-\frac{\tau(\psi)}{4}F^{\mu\nu}F_{\mu\nu}$, where $\tau(\psi)$ is a function of the scalar field, results in a model that can be uplifted to a $D = 11$ supergravity solution (for particular choices of c_1, m, and the parameters in $\tau(\psi)$). In this study, we wish to study the formation of holographic stripes phenomenologically. The existence of the axion-coupling term ($c_1 \neq 0$) is a sufficient condition for the inhomogeneous solutions and so we set $\tau(\psi) = 1$ here.

We are looking for stationary black hole solutions that can be described by an ansatz of the form

$$\begin{aligned} ds^2 &= -2r^2 f(r)e^{2A(r,x)}dt^2 + 2r^2 e^{2C(r,x)}(dy - W(r,x)dt)^2 \\ &\quad + e^{2B(r,x)}\left(\frac{dr^2}{2r^2 f(r)} + 2r^2 dx^2\right), \end{aligned}$$

$$\psi = \psi(r,x), \quad A = A_t(r,x)dt + A_y(r,x)dy, \tag{4.2}$$

where r is the radial direction in AdS and x is the field theory direction along which inhomogeneities form. We term the scalar field and gauge fields collectively as the matter fields. $f(r)$ is a given function whose zero defines the black brane horizon. We take $f(r)$ to be that of the RN solution,

$$f(r) = 1 - \left(1 + \frac{\mu^2}{4r_0^2}\right)\left(\frac{r_0}{r}\right)^3 + \frac{\mu^2}{4r_0^2}\left(\frac{r_0}{r}\right)^4, \tag{4.3}$$

so that the horizon is located at $r = r_0$. The homogeneous solution is the RN black brane, given by

$$A = B = C = W = \psi = A_y = 0, \quad A_t(r) = \mu(1 - r_0/r), \tag{4.4}$$

where μ is the chemical potential. Above the maximum critical temperature, this is the only solution to the system.

To find the non-linear inhomogeneous solutions, we numerically solve the equations of motion derived from the ansatz (4.2). The Einstein equation results in four second order elliptic equations, formed from combinations of $G^t_t - T^t_t = 0$, $G^t_y - T^t_y = 0$, $G^y_y - T^y_y = 0$, and $G^r_r + G^x_x - (T^r_r + T^x_x) = 0$, and two hyperbolic constraint equations, $G^r_x - T^r_x = 0$ and $G^r_r - G^x_x - (T^r_r - T^x_x) = 0$, for the metric functions. The gauge field equations and scalar field equation give second order elliptic equations for the matter fields. For completeness, the full equations are given in appendix B.2.2. Our strategy will be to solve these seven elliptic equations subject to boundary conditions that ensure that the constraint equations will be satisfied on a solution. Below, we describe the constraint system and our boundary conditions. For more details about the numerical approach, we refer to appendix B.2.

4.2.2 The constraints

The two equations $G^r_x - T^r_x = 0$ and $G^r_r - G^x_x - (T^r_r - T^x_x) = 0$, which we do not explicitly solve, are the constraint equations. Using the Bianchi identities [82], we see that the constraints satisfy

$$\partial_x\left(\sqrt{-g}(G^r_x - T^r_x)\right) + 2r^2\sqrt{f}\partial_r\left(r^2\sqrt{f}\sqrt{-g}(G^r_r - G^x_x - (T^r_r - T^x_x))\right) = 0, \tag{4.5}$$

$$2r^2\sqrt{f}\partial_r\left(\sqrt{-g}(G^r_x - T^r_x)\right) - \partial_x\left(r^2\sqrt{f}\sqrt{-g}(G^r_r - G^x_x - (T^r_r - T^x_x))\right) = 0. \tag{4.6}$$

Defining $\hat{r}$ by $\partial_{\hat{r}} = 2r^2\sqrt{f}\partial_r$ gives Cauchy-Riemann relations

$$\partial_x\left(\sqrt{-g}(G^r_x - T^r_x)\right) + \partial_{\hat{r}}\left(r^2\sqrt{f}\sqrt{-g}(G^r_r - G^x_x - (T^r_r - T^x_x))\right) = 0, \tag{4.7}$$

$$\partial_{\hat{r}}\left(\sqrt{-g}(G^r_x - T^r_x)\right) - \partial_x\left(r^2\sqrt{f}\sqrt{-g}(G^r_r - G^x_x - (T^r_r - T^x_x))\right) = 0, \quad (4.8)$$

showing that the weighted constraints satisfy Laplace equations. Then, satisfying one constraint on the entire boundary and the other at one point on the boundary implies that they will both vanish on the entire domain. In practice we will take either zero data or Neumann boundary conditions at the boundaries in the x-direction. The unique solution to Laplace's equation with zero data on the horizon and the boundary at infinity and these conditions in the x-direction is zero. Therefore, as long as we fulfill one constraint at the horizon and the asymptotic boundary and the other at one point (on the horizon or boundary), the constraints will be satisfied if the elliptic equations are. Our boundary conditions will be such that $\sqrt{-g}(G^r_x - T^r_x) = 0$ at the horizon and conformal infinity and that $r^2\sqrt{f}\sqrt{-g}(G^r_r - G^x_x - (T^r_r - T^x_x)) = 0$ at one point on the horizon.

4.2.3 Boundary conditions

The elliptic equations to be solved are subject to physical boundary conditions. There are four boundaries of our domain (see Figure 4.1): the horizon, the conformal boundary, and the periodic boundaries in the x-direction, which are described next.

Staggered periodicity

To specify the boundary conditions in the x direction we look at the form of the linearized perturbation which becomes unstable (see appendix B.2.1). To leading order in the perturbation parameter λ, they are of the form:

$$\begin{aligned}
\psi(x) &\sim \lambda\cos(kx), \\
A_y(x) &\sim \lambda\sin(kx), \\
g_{ty}(x) &\sim \lambda\sin(kx),
\end{aligned} \quad (4.9)$$

where k is the wavenumber of the unstable mode. To second order in the perturbation parameter, the functions g_{tt}, g_{xx}, g_{yy} and A_t (which we denote collectively as h) are turned on, with the schematic behaviour

$$h(x) \sim \lambda^2(\cos(2kx) + C), \quad (4.10)$$

where C are independent of x.

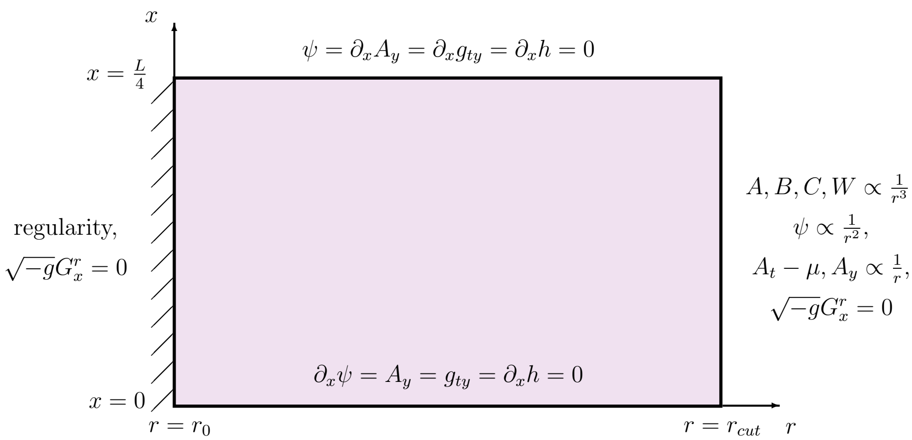

Figure 4.1: A summary of the boundary conditions on our domain. At the horizon, $r = r_0$, we impose regularity conditions. At the conformal boundary, $r \to \infty$, we have fall off conditions on the fields (imposed at large but finite $r = r_{cut}$) such that we do not source the inhomogeneity. In the x-direction, we use symmetries to reduce the domain to a quarter period $L/4$. Then, we impose either periodic or zero conditions on the fields, according to their behaviour under the discrete symmetries discussed in the text. (h collectively denotes the fields $\{g_{tt}, g_{xx}, g_{yy}, A_t\}$.) In addition to these, we explicitly satisfy the constraint equation $\sqrt{-g}G^r_x = 0$ on the horizon and the conformal boundary.

All these functions are periodic with period $L = 2\pi/k$. However, they are not the most general periodic functions with period L. For numerical stability it is worthwhile to specify their properties further and encode those properties in the boundary conditions we impose on the full solution. We concentrate on the behaviour of the perturbation with respect to two independent Z_2 reflection symmetries.

The first Z_2 symmetry is that of $x \to -x$, $y \to -y$, which is a rotation in the x, y plane. This is a symmetry of the action and of the linearized perturbation (keeping in mind that A_y and g_{ty} change sign under reflection of the y coordinate). We conclude therefore that this is a symmetry of the full solution.

Similarly, the Z_2 operation $x \to \frac{L}{2} - x$, $y \to -y$ is a symmetry of the action, which is also a symmetry of the linearized system when accompanied by $\lambda \to -\lambda$. In other words the functions ψ, A_y, g_{ty} are restricted to be odd with respect to this Z_2 operation, while the rest of the functions, which we collectively denoted as h, are even.

The two symmetries defined here restrict the form of the functions that can appear in the perturbative expansions for each of the functions above. For example, it is easy to see that the function $\psi(x)$ gets corrected only in odd powers of λ and the most general form of the harmonic that can appear in the perturbative expansion is $\cos(nkx)$, for n odd. Similar comments apply to the other functions above.

We restrict ourselves to those harmonics which may appear in the full solution. The most efficient way to do so is to work with a quarter of the full period L (reconstructing the full periodic solution using the known behaviour of each function with respect to the two Z_2 operations defined above). The specific properties of each function appearing in our solutions are imposed by demanding the following boundary conditions:

$$\begin{aligned}
\partial_x\psi(x=0) &= 0, \qquad \psi\left(x=\frac{L}{4}\right)=0, \\
A_y(x=0) &= 0, \qquad \partial_x A_y\left(x=\frac{L}{4}\right)=0, \\
g_{ty}(x=0) &= 0, \qquad \partial_x g_{ty}\left(x=\frac{L}{4}\right)=0, \\
\partial_x h(x=0) &= 0, \qquad \partial_x h\left(x=\frac{L}{4}\right)=0.
\end{aligned} \tag{4.11}$$

At the horizon

In our coordinates (4.2) the horizon is at fixed $r=r_0$. For numerical convenience we introduce another radial coordinate $\rho=\sqrt{r^2-r_0^2}$, such that the horizon is at $\rho=0$.[6] Expanding the equations of motion around $\rho=0$ yields a set of Neumann regularity conditions,

$$\partial_\rho A = \partial_\rho C = \partial_\rho W = \partial_\rho \psi = \partial_\rho A_t = \partial_\rho A_y = 0, \tag{4.12}$$

and two conditions in the inhomogeneous direction along the horizon,

$$\partial_x W = \partial_x(A_t + W A_y) = 0. \tag{4.13}$$

Thus, both W and the combination A_t+WA_y are constant along the horizon. The boundary conditions in the x direction (4.11) imply that $W=0$. Then,

[6] In the rest of the paper, we use r and ρ interchangeably as our radial coordinate. We use the coordinate ρ in the numerics.

the second condition together with regularity of the vector field A on the Euclidean section give that $A_t = 0$ on the horizon.

The regularity conditions give eight conditions for the six functions A, C, W, ψ, A_t and A_y. In principle, we would choose any six of these to impose at the horizon. If we find a non-singular solution to the equations, then the other two conditions should also be satisfied. In practice, some of these conditions work better than others for finding the numerical solution. We find that using Neumann conditions for A, C, ψ, and A_y and Dirichlet conditions for W and A_t results in a more stable relaxation.[7]

The conditions for B are determined using the constraint equations. Expanding the weighted constraints at the horizon, we find

$$\begin{aligned} \sqrt{-g}(G^r_x - T^r_x) &\propto \partial_x(A-B) + O(\rho), & (4.14)\\ r^2\sqrt{f}\sqrt{-g}(G^r_r - G^x_x - (T^r_r - T^x_x)) &\propto \partial_\rho B + O(\rho). & (4.15) \end{aligned}$$

The first condition gives constant surface gravity (or temperature) along the horizon. As discussed above, we will impose one constraint at the horizon and the boundary, and the other at one point. In practice, we will satisfy $r^2\sqrt{f}\sqrt{-g}(G^r_r - G^x_x - (T^r_r - T^x_x))$ at $(\rho, x) = (0, 0)$, updating the value of B at this point using the Neumann condition $\partial_\rho B = 0$. This will set the difference $(B-A)|_{(\rho,x)=(0,0)} \equiv d_0$, which we will then use to update B using a Dirichlet condition along the rest of the horizon, satisfying $\sqrt{-g}(G^r_x - T^r_x) = 0$.

At the conformal boundary

In our coordinates, the boundary is at $r = \infty$. Since we are looking for spontaneous breaking of homogeneities, our boundary conditions will be such that the field theory sources are homogeneous. This implies that the non-normalizable modes of the bulk fields are homogeneous. The inhomogeneity of the striped solutions will be imprinted on the normalizable modes of the fields, or the coefficient of the next-to-leading fall-off term in the asymptotic expansions.

The form of our metric ansatz is such that the metric functions A, B, C and W represent the normalizable modes of the metric. Imposing that the geometry is asymptotically AdS with Minkowski space on the boundary implies that these four metric perturbations must vanish as $r \to \infty$. By expanding the equations of motion near the boundary, one can show that A, B, C and W fall off as $1/r^3$. In practice, we place the outer boundary of our domain at large but finite r_{cut} and impose the fall-off conditions there.

[7] Using Neumann conditions at the horizon for W and A_t results in values at the horizon that converge to zero with step-size, consistent with the above analysis.

As in the RN solution, we source the field theory charge density with a homogeneous chemical potential, corresponding to a Dirichlet condition for the gauge field A_t at the boundary. In the inhomogeneous solutions, we expect the spontaneous generation of a modulated field theory current $j_y(x)$, dual to the normalizable mode of A_y. Solving the equations near the boundary with these conditions reveals the expansions $A_t = \mu + O(1/r)$ and $A_y = O(1/r)$, which we impose numerically at r_{cut}.

The scalar field equation of motion gives the asymptotic solution

$$\psi = \frac{\psi^{(1)}}{r^{\lambda_-}} + \frac{\psi^{(2)}}{r^{\lambda_+}} + \dots, \tag{4.16}$$

where

$$\lambda_\pm = \frac{1}{2}\left(3 \pm \sqrt{9 + 4(lm)^2}\right). \tag{4.17}$$

For the range of scalar field masses $-9/2 \leq m^2 \leq -5/2$, both modes are normalizable, and fixing one mode gives a source for the other. In our study we will choose $m^2 = -4$, giving $\lambda_- = 1$, $\lambda_+ = 2$. Since we are looking for spontaneous symmetry breaking, in this case we must choose either $\psi^{(1)} = 0$ or $\psi^{(2)} = 0$. We choose the former, so that ψ falls off as $1/r^2$.

Now, consider the weighted constraint $\sqrt{-g}G^r_x$. As discussed above, in order to solve the constraint system, we require this to disappear at the conformal boundary. Near the boundary, $\sqrt{-g} \propto r^2 + \dots$, so for $\sqrt{-g}G^r_x$ to disappear we must have $G^r_x = O(1/r^3)$. Expanding the equations near the boundary we have

$$G^r_x - T^r_x \propto \frac{3\partial_x A^{(3)}(x) + 2\partial_x B^{(3)}(x) + 3\partial_x C^{(3)}(x)}{r^2} + O\left(\frac{1}{r^3}\right), \tag{4.18}$$

where $X = X^{(3)}(x)/r^3 + \dots$ for $X = \{A, B, C\}$. Therefore, in addition to the boundary conditions mentioned above, for $\sqrt{-g}G^r_x = 0$ to be satisfied at $r = \infty$, it appears that we should have that $3A^{(3)}(x) + 2B^{(3)}(x) + 3C^{(3)}(x) = const$. The means to impose this addition condition comes from the fact that our metric (4.2) has an unfixed residual gauge freedom [104], allowing one to transform to new $\tilde{r} = \tilde{r}(r, x), \tilde{x} = \tilde{x}(r, x)$ coordinates which are harmonic functions of r and x. Performing such a transformation generates an additional function in (4.18), which can then be chosen to ensure that the constraint is satisfied (in appendix B.2 we describe how). This condition implies the conservation of the boundary energy momentum tensor, see appendix B.1.

4.2.4 Parameters and algorithm

The physical data specifying each solution is the chemical potential μ, the temperature T, and the periodicity L.[8] Since the boundary theory is conformal, it will only depend on dimensionless ratios of these parameters. This manifests itself in the following scaling symmetry of the equations:

$$r \to \lambda r, \quad (t,x,y) \to \frac{1}{\lambda}(t,x,y), \quad A_\mu \to \lambda A_\mu. \tag{4.19}$$

We use this to select $\mu = 1$. Then, our results are functions of the dimensionless temperature T/μ and the dimensionless periodicity $L\mu$.

The temperature is controlled by the coordinate location of the horizon. For a given r_0, the temperature of the RN phase is $T_0 = (1/8\pi r_0)(12r_0^2 - 1)$ while the temperature of the inhomogeneous solution is $T = e^{-d_0}T_0$. Recall that $(B - A)|_{r_0} = d_0$ is dynamically generated by satisfying the constraints at the horizon. From our numerical solutions, we find that d_0 monotonically increases as we lower the temperature, so that T_0 gives a reliable parametrization of the physical temperature T. In practice, we generate solutions by choosing values of T_0 below the critical temperature $T_c(k)$.

We solve the equations by finite-difference approximation techniques. We use second order finite-differencing on the equations (B.27) – (B.33) before using a point-wise Gauss-Seidel relaxation method on the resulting algebraic equations.[9] For the results in this paper, for $c_1 = 4.5$, a cutoff of $\rho_{cut} = \{6, 8\}$ was used while for $c_1 = 5.5$ and $c_1 = 8$, for which the modulations were larger, a cutoffs of $\rho_{cut} = 10$ and $\rho_{cut} = 12$ correspondingly were used. Grid spacings used for the finite-difference scheme were in the range $d\rho, dx = 0.04 - 0.005$. Neumann boundary conditions are differenced to second order using one-sided finite-difference stencils in order to update the boundary values at each step. At the asymptotic boundary ρ_{cut} we impose the boundary conditions by second order differencing a differential equation based on the fall-off (for example, $\partial_r A = -3A/r$) to obtain an update rule for the boundary value. As a result we find quadratic convergence as a function of grid-spacing for our method, see appendix B.2.5.

[8] Fixing μ, T and L gives the system in the grand canonical ensemble. Once the phase space has been mapped in one ensemble other ensembles can be considered via appropriate reinterpretation of the numerical data. See section 4.4 for a description of this process.

[9] See appendix A.2 for a description of this procedure.

4.3 The solutions

The system of equations (B.27) – (B.33) is solved subject to the boundary conditions described in the previous sections. The details of our numerical algorithm are found in appendices A.2 and B.2. Here we focus on the properties of the solutions and their geometry.

Unless otherwise specified the following plots were obtained using the axion coupling of $c_1 = 4.5$. In this section, we consider solutions for which the periodicity is determined by the dominant critical wavenumber k_c; for $c_1 = 4.5$, this gives $L\mu/4 \simeq 2.08$, see Table B.1. We found that the geometry and most of the other features are qualitatively similar for the couplings $c_1 = 5.5$ and $c_1 = 8$. A convenient way to parametrize our inhomogeneous solutions is by the dimensionless temperature T/T_c, relative to the critical temperature T_c, below which the translation invariance along x is broken. For $c_1 = 4.5$, our method allows us find solutions in the range $0.003 \lesssim T/T_c \lesssim 0.9$.

4.3.1 Metric and fields

For subcritical temperatures, as we descend into inhomogeneous regime, the metric and the matter fields start developing increasing variation in x. Figure 4.2 displays the metric functions, and Figure 4.3 shows the non vanishing components of the vector potential field and of the scalar field for $T/T_c \simeq 0.11$ over a full period in the x direction. The variation of all fields is maximal near the horizon of the black hole at $\rho = \sqrt{r^2 - r_0^2} = 0$, and it gradually decreases toward the conformal boundary, $\rho \to \infty$.

Many of the special features of the solutions we find may be explained via axion electrodynamics as seen in the effective description of the electromagnetic response of a topological insulator. This effect is mediated by the interaction term in our Lagrangian (4.1). In the broken phase we have an axion gradient in the near horizon geometry, which realizes a topological insulator interface, see Figure 4.3. The characteristic patterning of the near horizon magnetic field, $\mathbf{B} = \nabla \times \mathbf{A}$, shown in Figure 4.4, is reminiscent of the magnetoelectric effect at such interfaces. The magnetic vortices are localized near the black hole horizon and have alternating direction of magnetic field lines.

In curved space the magnetic field is accompanied by vorticity, which is manifested by the function W. This causes frame dragging effects in the y direction. Test particles will be pushed along y with speeds $W(r, x)$, in particular the direction of the flow reverses every half the period along x.

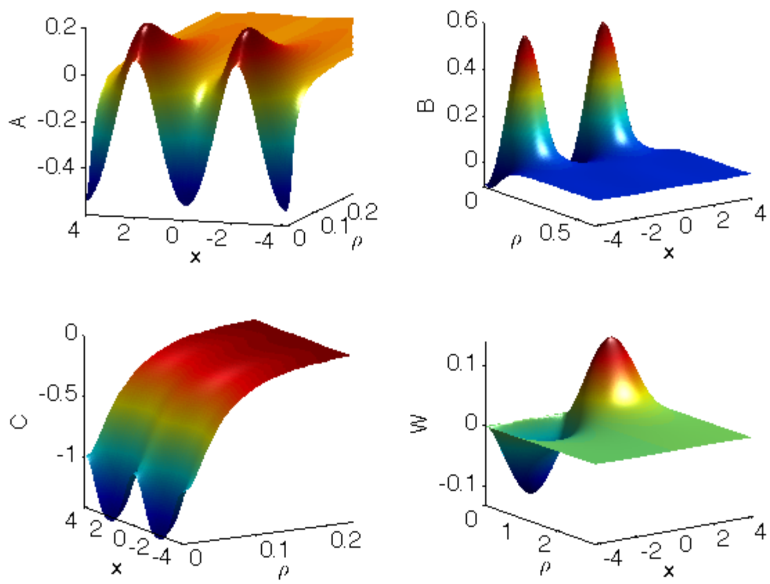

Figure 4.2: Metric functions for $T/T_c \simeq 0.11$. Note the metric functions A, B and C have half the period of W. The variation is maximal near the horizon, located at $\rho = 0$, and it decays as the conformal boundary is approached, when $\rho \to \infty$.

The drag vanishes at the horizon and at the location of the nodes of W where $x = n\,L/2$, for integer n, see Figure 4.2. In general, the dragging effect remains bounded, and no ergoregion forms, where the vector ∂_t becomes spacelike.

4.3.2 The geometry

There are several ways to envisage the geometry of our solutions, we discuss them in turn.

The Ricci scalar of the RN solution is $\mathcal{R}_{RN} = -24$, constant in r and independent of the parameters of the black hole. This is no longer true for the inhomogeneous phases, where the Ricci scalar becomes position dependent. Figure 4.5 illustrates the spatial variation of the Ricci scalar, relative to $\mathcal{R}_{RN}$ for $T/T_c \simeq 0.054$. The maximal curvature is always along the horizon at $x = n\,L/2$ for integer n. It grows when the temperature decreases

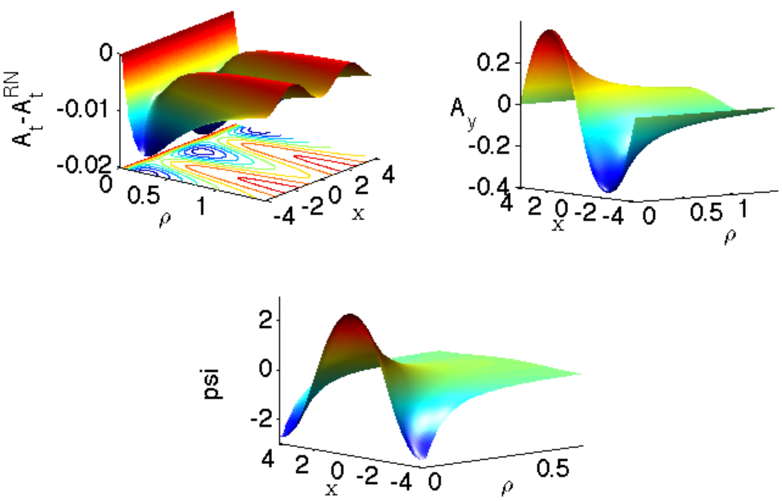

Figure 4.3: A_t relative to the corresponding RN solutions, A_y and ψ for $T/T_c \simeq 0.11$. The period of A_t is twice that of ψ and A_y. The x-dependence dies off gradually as the conformal boundary is approached, at $\rho \to \infty$.

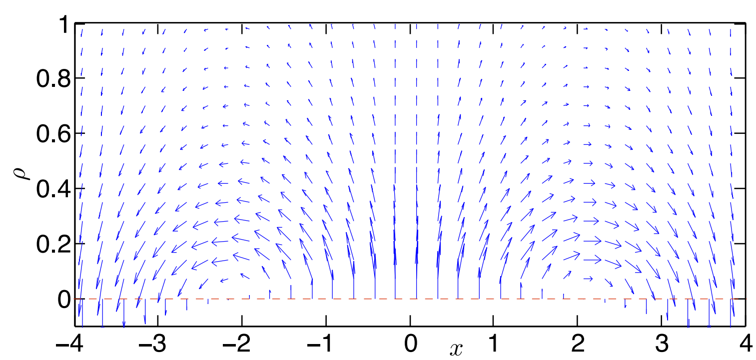

Figure 4.4: Magnetic field lines for solution with $T/T_c \simeq 0.07$. The pattern of vortices of alternating field directions form at the horizon (located at $\rho = 0$).

and approaches the finite value of $\mathcal{R} \simeq -94$ in the small temperature limit.

Embedding in a given background space is a convenient way to illustrate curved geometry. We consider the embedding of 2-dimensional spatial slices

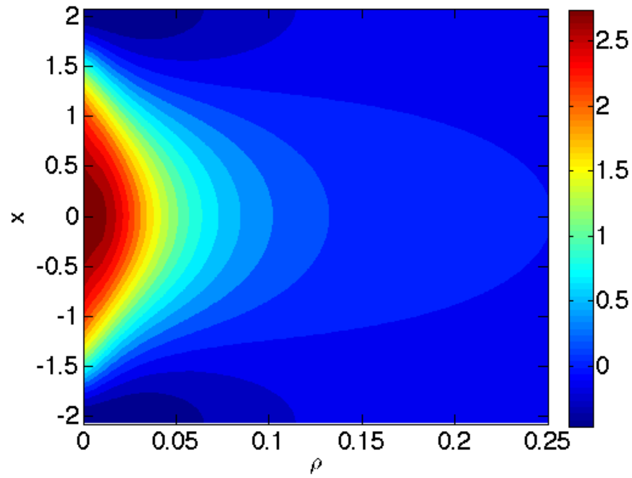

Figure 4.5: Ricci scalar relative to that of RN black hole, $\mathcal{R}/\mathcal{R}_{RN}-1$, $\mathcal{R}_{RN}=-24$, for $T/T_c \simeq 0.054$ over half the period. The scalar curvature is maximal along the horizon at $x = n\,L/2$ for integer n.

of constant x of the full geometry (4.2)

$$ds_2^2 = \frac{e^{2\,B(r,x)}}{2\,r^2\,f(r)}dr^2 + 2\,r^2\,e^{2\,C(r,x)}dy^2 \tag{4.20}$$

as a surface in 3-dimensional AdS space

$$ds_3^2 = 2\,\tilde{r}^2\,dz^2 + \frac{d\tilde{r}^2}{2\,\tilde{r}^2} + 2\,\tilde{r}^2 dy^2. \tag{4.21}$$

We are looking for a hypersurface parametrized by $z = z(\tilde{r})$. Then the metric on such a hypersurface reads

$$ds_2^2 = \left[1 + 2\,\tilde{r}^2\left(\frac{dz}{d\tilde{r}}\right)^2\right]\frac{d\tilde{r}^2}{2\,\tilde{r}^2} + 2\,\tilde{r}^2 dy^2. \tag{4.22}$$

Comparing (4.22) and (4.20) we obtain set of the relations

$$\begin{aligned} \tilde{r} &= r\,e^{C}, \\ \left[\frac{1}{2\,\tilde{r}^2} + 2\,\tilde{r}^2\left(\frac{dz}{d\tilde{r}}\right)^2\right]\left(\frac{d\tilde{r}}{dr}\right)^2 &= \frac{e^{2\,B(r,x)}}{2\,r^2\,f(r)}, \end{aligned} \tag{4.23}$$

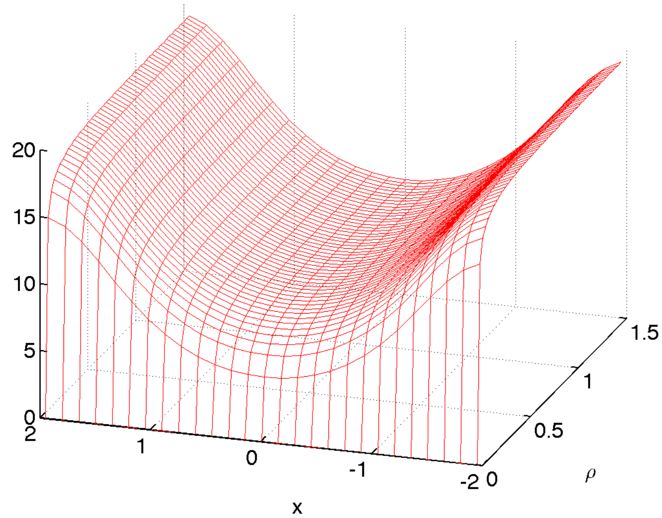

Figure 4.6: The embedding diagram of constant x spatial slices, as a function of x at given y for $T/T_c \simeq 0.035$. The geometry of $\rho = const$ slices is maximally curved at $x = n\,L/2$ for integer n.

resulting in the embedding equation

$$\frac{dz}{dr} = \frac{1}{2\,r^2}\sqrt{f(r)^{-1}\,e^{2\,B(r,x)-2\,C(r,x)} - (1 + r\,\partial_r C(r,x))^2}. \tag{4.24}$$

We integrate this equation for a given x, and in Figure 4.6 show the embedding at constant y. The maximal curvature along $\rho = const$ slices occurs at $x = n\,L/2$ for integer n, which is consistent with Figure 4.5.

The proper length of the stripe along x relative to the background AdS spacetime at given r is

$$l_x(r)/l_x(r=\infty) = \int_0^{L/4} e^B(r,x)\,dx. \tag{4.25}$$

Figure 4.7 shows the dependence of the normalized proper length on the radial distance from the horizon. The proper length tends to the coordinate length as $1/r^3$ asymptotically as $r \to \infty$, but it exceeds that as the horizon is approached. Namely, the inhomogeneous black brane 'pushes space' around it along x, in a manner resembling the 'Archimedes effect'.

The proper length of the horizon in x direction is obtained calculating (4.25) at r_0. Figure 4.8 demonstrates the dependence of this quantity on

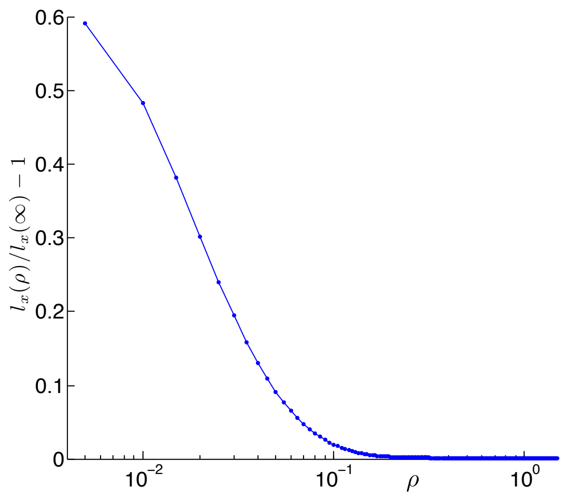

Figure 4.7: Radial dependence of the normalized proper length along x for $T/T_c \simeq 0.054$. While asymptotically the proper length coincides with the coordinate size of the strip, it grows as the horizon is approached. This is a manifestation of the 'Archimedes effect'.

the temperature. For high temperatures the length of the horizon resembles that of the homogeneous RN solution, however, it grows when temperature decreases. We find that at small T/T_c the proper length of the horizon diverges approximately as $(T/T_c)^{-0.1}$.

The transverse extent of the horizon, per unit coordinate length y, is given by

$$r_y(x) = \sqrt{2}\, r_0\, e^{C(r_0,x)}. \tag{4.26}$$

Figure 4.9 shows the variation of $r_y(x)$ along the horizon for $T/T_c \simeq 0.054$. Typically there is a 'bulge' occurring at $x = n\,L/2$ and a 'neck' at $x = (2\,n+1)\,L/4$, for integer n. Comparing this with Figure 4.5 we note that Ricci scalar curvature is maximal at the bulge and not at the neck as would happen, for instance, in the cylindrical geometry in black string case [98]. Figure 4.10 displays the dependence of the sizes of the neck and bulge on T/T_c. Both sizes monotonically decrease with temperature, however the rate at which the neck is shrinking exceeds that of the bulge. This is demonstrated in Figure 4.11. In fact, we find that for $c_1 = 4.5$, $r_y^{neck}/r_y^{bulge} \sim (T/T_c)^{1/2}$ near the lower end of the range of temperatures that we investigated. For other values of the axion coupling the scaling of the ratio is again power-law, with an exponent of the same order of magni-

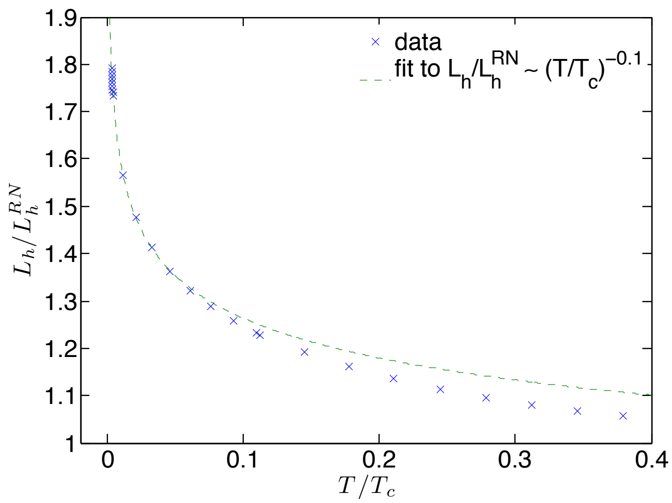

Figure 4.8: Temperature dependence of the proper length of the horizon along the stripe. Starting from as low as L at high temperatures, the proper length grows monotonically and for small T/T_c the growth is well approximated by the power-law dependence $\sim (T/T_c)^{-0.1}$.

tude, e.g. for $c_1 = 8$, the exponent is about 0.12. This signals a pinch-off of the horizon in the limit $T \to 0$.

4.4 Thermodynamics at finite length

In this section we consider the thermodynamics and phase transitions in the system, assuming that the stripe length is kept fixed. For the finite system the length of the interval is part of the specification of the ensemble and is kept fixed. In the next section we discuss the infinite system, for which the stripe width can adjust dynamically.

4.4.1 The first law

We demonstrated that below the critical temperature there exists a new branch of solutions which are spatially inhomogeneous. In the microcanonical ensemble the control variables of the field theory are the entropy S, the charge density N, and the length of the x-direction L, with corresponding conjugate variables temperature T, chemical potential μ, and tension in the

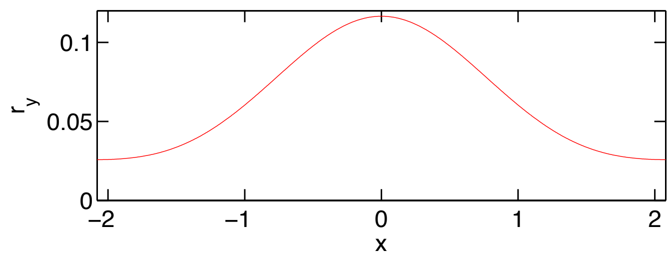

Figure 4.9: The extent of the horizon in the transverse direction, r_y, as a function of x for $T/T_c \simeq 0.054$ in $x \in [-L/2, L/2]$. The characteristic pattern of alternating 'necks' and 'bulges' forms along x.

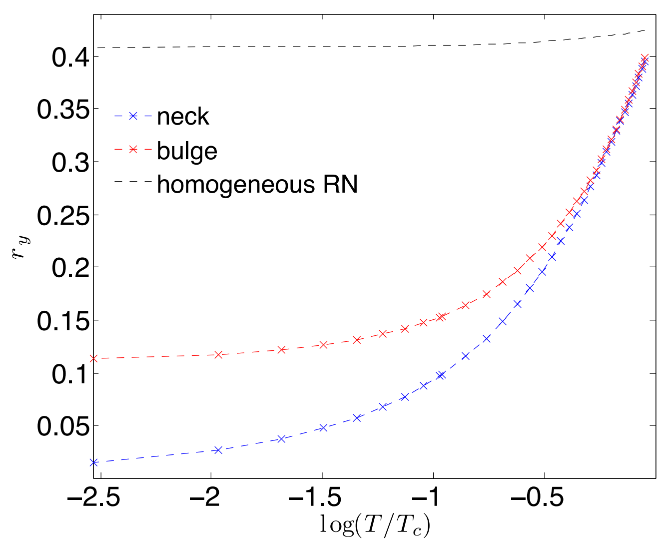

Figure 4.10: The dependence of the size of the neck and the bulge on temperature.

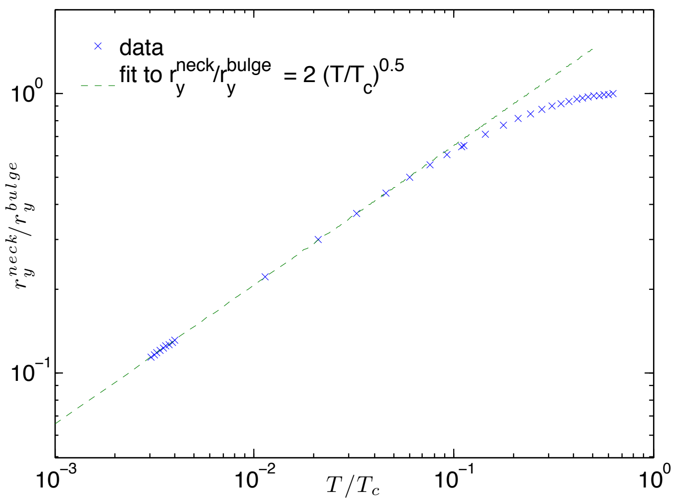

Figure 4.11: The ratio of the transverse extents of the neck and the bulge shrinks as $r_y^{neck}/r_y^{bulge} \sim (T/T_c)^{1/2}$ at small temperatures, indicating a pinch-off of the horizon in the limit $T \to 0$.

x-direction τ_x.[10] The usual first law is augmented by a term corresponding to expansions and contractions in the x-direction and is given by

$$dM = TdS + \mu dN + \tau_x dL. \tag{4.27}$$

where M, S, and N are quantities per unit length in the trivial y direction, but are integrated over the stripe.

Our system has a scaling symmetry given by (4.19). In the field theory, this corresponds to a change of energy scale. Under this transformation, the thermodynamic quantities scale as

$$\begin{gathered} M \to \lambda^2 M, \quad T \to \lambda T, \quad S \to \lambda S, \quad \mu \to \lambda \mu, \\ N \to \lambda N, \qquad \tau_x \to \lambda^3 \tau_x, \qquad L \to \frac{1}{\lambda} L. \end{gathered} \tag{4.28}$$

Using these in (4.27) with $\lambda = 1 + \epsilon$, for ϵ small, yields

$$2M = TS + \mu N - \tau_x L, \tag{4.29}$$

the Smarr's-like expression that our solutions must satisfy and that can be used as a check of our numerics. For all of our solutions, we have verified that this identity is satisfied to one percent.

[10] Explicit expressions for these quantities in terms of our ansatz are given in appendix B.1.

4.4.2 Phase transitions

The question of which solution dominates the thermodynamics depends on the ensemble considered. In the holographic context the choice of thermodynamic ensemble is expressed through the choice of boundary conditions. The corresponding thermodynamic potential is computed as the on-shell bulk action, appropriately renormalized and with boundary terms rendering the variational problem well-defined. We examine each ensemble in turn.

The grand canonical ensemble

In our numerical approach, the natural ensemble to consider is the grand canonical ensemble, fixing the temperature T, the chemical potential μ, and the periodicity of the asymptotic x direction as L. The corresponding thermodynamic potential is the grand free energy density

$$\Omega(T, \mu, L) = M - TS - \mu N. \tag{4.30}$$

Different solutions of the bulk equations with the same values of T, μ, L correspond to different saddle point contributions to the partition function. The solution with smallest grand free energy Ω is the dominant configuration, determining the thermodynamics in the fixed T, μ, L ensemble. In our case we have two solutions for each choice of T, μ, L, one homogeneous and one striped. Exactly how one one saddle point comes to dominate over the other at temperatures below the critical temperature determines the order of the phase transition.

In this ensemble it is convenient to measure all quantities in units of the fixed chemical potential μ. Then, after fixing L from the critical mode appearing at the highest T_c (see Figure B.1 and Table B.1 in appendix B.2.1), we have that Ω/μ^2 is a function only of the dimensionless temperature T/μ. In the fixed chemical potential ensemble for large enough axion coupling we find a second order transition, where the inhomogeneous charge distribution starts dominating the thermodynamics immediately below the temperature at which the inhomogeneous instability develops. Near the critical temperature, the behaviour of the grand free energy difference is consistent with $(\Omega - \Omega_{RN})/\mu^2 \propto (1 - T/T_c)^2$, while the entropy difference goes as $(S - S_{RN})/\mu \propto T/T_c - 1$. This is as expected from a second order transition. As can be seen in Figure 4.12 and Figure 4.13, we find this second order transition for a range of lengths, L, and for a variety of values of the axion coupling c_1. With the current accuracy of our numerical procedure, we find it increasingly difficult to resolve the order of the phase transition

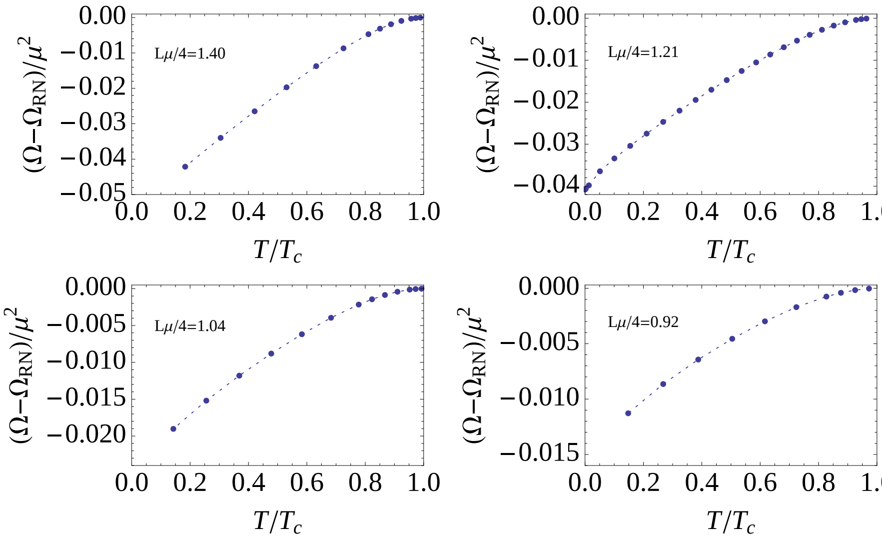

Figure 4.12: The grand free energy relative to the RN solution for several solutions of different fixed lengths at $c_1 = 8$. In all cases shown we observe a second order phase transition. The critical exponents determined near the critical points in each case are consistent with the quadratic behaviour $(\Omega - \Omega_{RN})/\mu^2 \propto (1 - T/T_c)^2$.

for smaller values of c_1. In fact, for $c_1 = 4.5$ the grand free energies of the homogeneous and inhomogeneous phases are nearly degenerate but still allow us to determine the phase transition as second order. It would be interesting to see if the phase transition remains of second order or changes to the first order for smaller values of the axion coupling.

To examine the observables in the striped phase further, we focus on $c_1 = 8$ and the corresponding dominant critical mode, $L\mu/4 \simeq 1.21$, and consider solutions for the temperatures $0.00016 \lesssim T/T_c \lesssim 0.96$. Various quantities are plotted with the corresponding homogeneous results in Figure 4.14. Along this branch of solutions, the mass of the stripes is more than the RN solution and the entropy is always less. We plot the maximum of the boundary current density $\langle j_y \rangle$, momentum density $\langle T_{y0} \rangle$ and pseudo-scalar operator vev $\langle \mathcal{O}_\psi \rangle$. Fitting the data near the critical point to the function $(1 - T/T_c)^\alpha$, we find the approximate critical exponents $\alpha_{j_y} = 0.40$, $\alpha_{T_y 0} = 0.41$ and $\alpha_{\mathcal{O}_\psi} = 0.38$ with relative fitting error of about 10%.

We find evidence that the entropy of the striped black branes does not tend to zero in the small temperature limit, see Figure 4.14. This is further

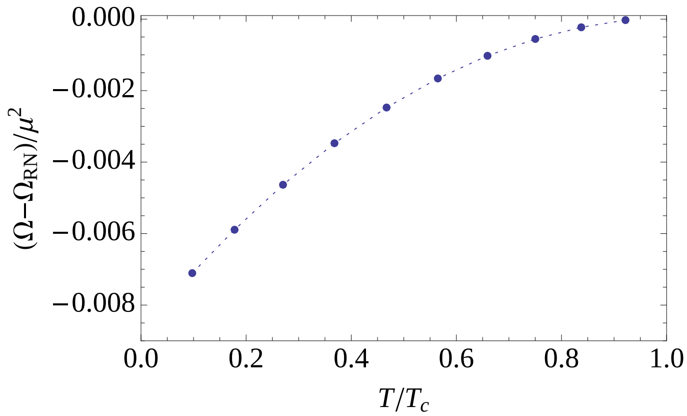

Figure 4.13: The grand free energy relative to the RN solution for $c_1 = 4.5$ and fixed $L\mu/4 = 2.08$. The grand free energies of the homogeneous and inhomogeneous phases are nearly degenerate, such that their maximal fractional difference is about 1%.

supported by the behaviour of the transverse size of the horizon (4.26). Here the bulge seems to contract at a much slower rate than the neck, which evidently shrinks to zero size in the limit $T \to 0$. However, strictly speaking, this conclusion is based on extrapolation of the finite temperature data to $T = 0$. Checking whether the entropy asymptotes to a finite value or goes to zero in this limit, as suggested in [102, 103], will require further investigation with a method of higher numerical accuracy.

The canonical ensemble

To study the system in the canonical ensemble we fix the temperature, total charge and length of the system. This describes the physical situation in which the system is immersed in a heat bath consisting of uncharged particles. The relevant thermodynamic potential in this ensemble is the free energy density

$$F(T, N, L) = M - TS. \tag{4.31}$$

If we measure all quantities in units of the fixed charge N, then, again, the free energy F/N^2 is only a function of the dimensionless temperature T/N.

To solve our system with a fixed charge, we would need to fix the integral in x of the coefficient of the $1/r$ term in the asymptotic expansion of the gauge field A_t. Numerically, it is much easier to fix the chemical potential, as this gives a Dirichlet condition on A_t at the boundary. In the grand

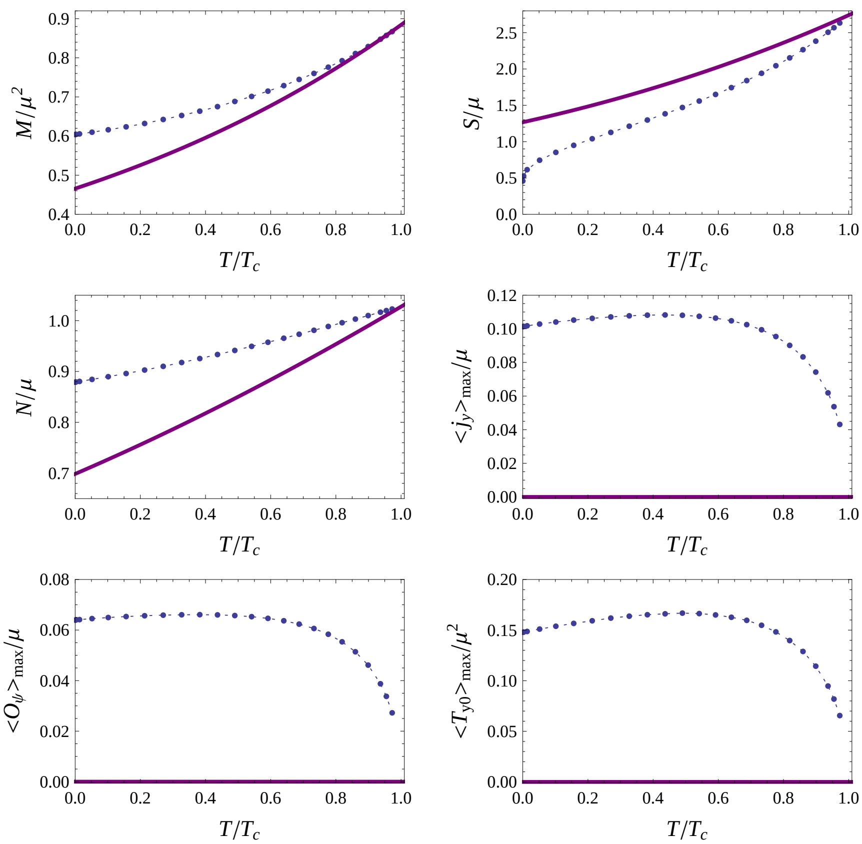

Figure 4.14: The observables in the grand canonical ensemble for $c_1 = 8$ and $L\mu/4 = 1.21$ (points with dotted line) plotted with the corresponding quantities for the RN black hole (solid line). Fitting the data near the critical point to the function $(1 - T/T_c)^\alpha$, we find the approximate critical exponents $\alpha_{j_y} = 0.40$, $\alpha_{T_y 0} = 0.41$ and $\alpha_{\mathcal{O}_\psi} = 0.38$ with relative fitting error of about 10%.

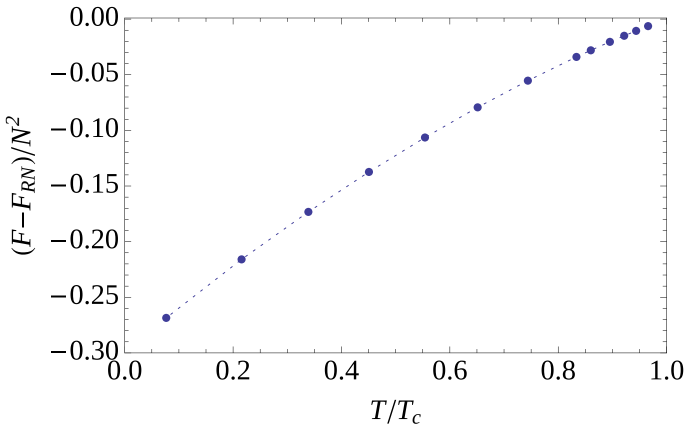

Figure 4.15: The difference in canonical free energy, at $c_1 = 8$ and fixed length $LN/4 = 1.25$, between the striped solution and the RN black hole. The striped solution dominates immediately below the critical temperature, signalling a second order phase transition.

canonical ensemble, we solved for one-parameter families of solutions at fixed $L\mu$, labelled by the dimensionless temperature T/μ. Equivalently, in the $(L\mu, T/\mu)$ plane, we solve along the line of fixed $L\mu$. Translated to the situation in which we measure quantities in terms of the charge density N, these solutions become one-parameter families of solutions with varying LN, or a curve in the $(LN, T/N)$ plane with LN a function of T/N. By varying the length $L\mu$ (or solving with $\mu = 1$ and varying L), we can find a collection of solutions that intersect the desired fixed LN line. By interpolating these solutions and evaluating the interpolants at fixed LN, we can study the stripes in the canonical ensemble.

In this ensemble we find a similar second order transition, in which the inhomogeneous solution dominates the thermodynamics below the critical temperature (Figure 4.15). The scaling of the free energy below the critical temperature is nearly quadratic in $|T - T_c|$, a mean field theory exponent as is common in large N models.

The microcanonical ensemble

The microcanonical ensemble describes an isolated system in which all conserved charges (in this case the mass and the charge) are fixed. This ensemble describes the physical situation relevant to the study of the real time dynamics of an isolated black brane at fixed length. In this case, the state

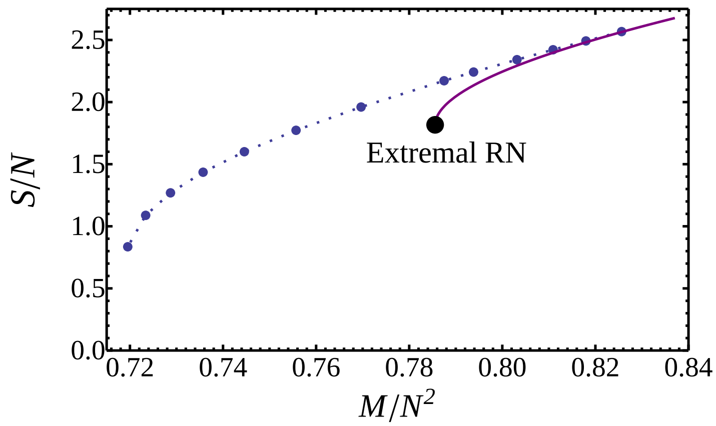

Figure 4.16: The entropy of the inhomogeneous solution for $c_1 = 8$ (points with dotted line) and of the RN solution (solid line). Below the critical temperature, the striped solution has higher entropy than the RN. The RN branch terminates at the extremal RN black hole, while the striped solution persists to smaller energies.

that maximizes entropy is the dominant solution. As shown in Figure 4.16, we find that the entropy of our inhomogeneous solutions is always greater than that of the RN black hole of the same mass. Furthermore, the mass of the inhomogeneous solutions is always smaller than that of the critical RN black hole. Therefore, at fixed LN, the unstable RN black holes below critical temperature are expected to decay smoothly to our inhomogeneous solution.

Fixing the tension

Alternatively, one could attempt to compare solutions with different values of L. The meaningful comparison is in an ensemble fixing the tension τ_x. For example, one could compare the Legendre transformed grand free energy

$$G(T, \mu, \tau_x) = M - TS - \mu N - \tau_x L \tag{4.32}$$

where the additional terms comes from boundary terms in the action rendering the new variational problem (fixing τ_x) well-defined. The candidate saddle points are the solutions we find with various periodicities L, and their relative importance in the thermodynamic limit is determined by $G(T, \mu, \tau_x)$. In particular the solution which is thermodynamically dominant depends on the value of τ_x we hold fixed. In this study we concentrate on the thermodynamics in the fixed L ensemble and we leave the study of the fixed τ_x ensemble to future work.

4.5 Thermodynamics for the infinite system

In this section we lift the assumption of the finite extent of the system in the x-direction and consider the thermodynamics of the formation of the stripes below the critical temperature. For the infinite system we can define densities of thermodynamic quantities along x:

$$m = \frac{M}{L}, \quad s = \frac{S}{L}, \quad n = \frac{N}{L}. \tag{4.33}$$

In terms of these, the first law for the system becomes

$$dm = Tds + \mu dn \tag{4.34}$$

and the conformal identity is

$$3m = 2(Ts + \mu n). \tag{4.35}$$

In the infinite system, we compare stripes of different lengths, at fixed T/μ, to each other and to the homogeneous solution. The solution that dominates the thermodynamics is the one with the smallest free energy density ω, where

$$\omega = m - Ts - \mu n. \tag{4.36}$$

This comparison is shown in Figure 4.17 for $c_1 = 8$, where we see that the free energy density of the stripes is negative relative to the RN black hole, indicating that the striped phase is preferred at every temperature below the critical temperature.[11] Very close to the critical temperature, the dominant stripe is that with the critical wavelength k_c. As we lower the temperature, the minimum of the free energy density traces out a curve in the $(L\mu, T)$ plane, and the dominant stripe width increases to $L\mu/4 \approx 2$.

One can also study the observables of the system along this line of minimum free energy density. The results are qualitatively similar to those for the fixed L system (Figure 4.14). In particular, the free energy density scales as $(\omega - \omega_{RN})/\mu^3 \propto (1 - T/T_c)^2$ near the critical point, indicating a second order transition in the infinite system as well.

[11] In appendix B.2.4, we describe the generation of Figure 4.17.

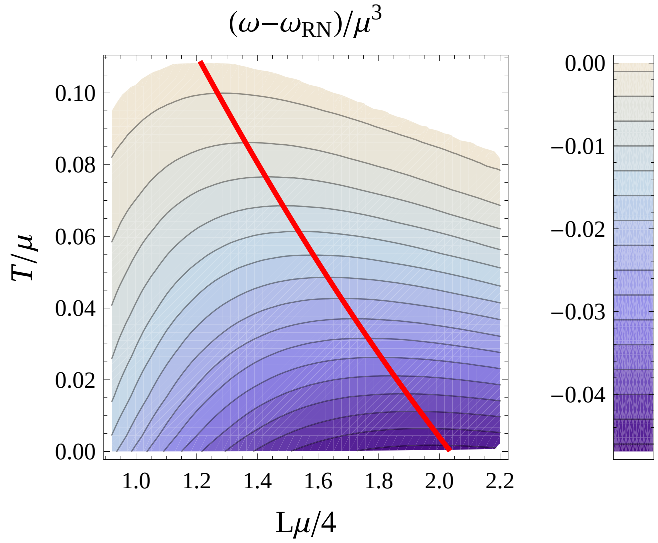

Figure 4.17: Action density for $c_1 = 8$ system relative to the RN solution. The red line denotes the approximate line of minimum free energy.

Chapter 5

Towards a holographic model of colour superconductivity[1]

5.1 Introduction

Background

Quantum chromodynamics is believed to display a rich phase structure at finite temperature and chemical potential, with phase transitions associated with deconfinement, nuclear matter condensation, the breaking of (approximate) flavour symmetries (which are exact in generalizations with equal quark masses and/or massless quarks), and the onset at high density of quark matter phases displaying colour superconductivity (for reviews see for example [31, 105–107]). However, apart from the regimes of asymptotically large temperature or chemical potential, a direct analytic study of the thermodynamic properties of the theory is not possible.

Even using numerical simulations, only the physics at zero chemical potential is currently accessible, since at finite μ the Euclidean action becomes complex, and the resulting oscillatory path integral cannot reliably be simulated using standard Monte-Carlo techniques. Current proposals for the phase diagram of QCD and related theories are largely based on qualitative arguments and phenomenological models. While these provide a plausible picture, it is possible that they miss important features of the physics. It would certainly be satisfying to have examples of theories similar to QCD in which the full phase diagram could be explored directly.

The holographic approach

A modern route to understanding properties of strongly coupled gauge theories, that would be otherwise inaccessible, is via the AdS/CFT correspondence, or gauge theory / gravity duality. This suggests that certain quantum field theories (usually called 'holographic theories'), generally

[1] A version of this chapter has been published [4].

with large-rank gauge groups, are equivalent to gravitational systems. By this correspondence, calculations of physical observables in the field theory are mapped to gravitational calculations; in many cases difficult strongly-coupled quantum mechanical calculations in the field theory (such as those required to understand the thermodynamic properties of QCD) are mapped to relatively simple classical gravity calculations. Optimistically, it may then be possible to find a theory qualitatively similar to QCD for which the physics at arbitrary temperature and chemical potential can be understood exactly via simple calculations in a dual gravitational system.

By now, there are well-known examples in gauge-theory / gravity duality for which the field theory shares many of the qualitative features of QCD (see, for example [13]). Further, many of these theories have been studied at finite temperature and chemical potential, revealing phase transitions associated with deconfinement, chiral symmetry breaking, meson melting, and the condensation of nuclear matter. However, to date, most of the theories that can be studied reliably using dual gravity calculations have the restriction that the number of flavours is kept fixed in the large N_c limit. In such theories, the physics at large chemical potentials is known to be qualitatively different than in real QCD. For example, at asymptotically large chemical potential, theories with large N_c and fixed N_f are believed to exhibit an inhomogeneous 'chiral density wave' behaviour [68, 69], rather than the homogenous quark matter phases predicted for finite N_c and N_f. In order to find examples of holographic theories which most closely resemble real QCD at finite chemical potential, one should therefore attempt to find examples of calculable gravitational systems corresponding to theories with finite N_f/N_c. This situation presents some technical challenges, as we now review.

In the well-known examples of holographic gauge theories, the addition of flavour fields in the field theory corresponds to adding D-branes on the gravity side [62]. Quarks correspond to strings which have one endpoint on these D-branes, while mesons correspond to the quantized modes of open strings which begin and end on the branes. The configurations of these D-branes in theories with finite N_f and large N_c are determined by finding action-minimizing configurations of the branes on a fixed background geometry. On the other hand, in order to have N_f of order N_c in a large N_c theory, we need a large number of these flavour branes, and these will back-react on the spacetime geometry itself. For $N_f \sim N_c$, there are as many degrees of freedom in the flavour fields as there are in the colour fields (gauge fields and adjoints), so it is natural to expect that the back-reaction will be so significant that in the final description the flavour branes themselves will be completely replaced by a modified geometry with fluxes (in the same way that the branes whose low-energy excitations give rise to the adjoint degrees of freedom do not appear explicitly in the gravity dual description of the field theory).

There has been significant progress in understanding the back-reaction of flavour branes, with some fully-back reacted analytic solutions available (for a review see [108]), but so far, there has not been enough progress to fully explore the phase structure of a QCD-like theory with finite N_f/N_c. In particular, as far as we are aware, colour superconductivity phases have not been identified previously in holographic field theories.[2]

Quark matter from the bottom up

In this chapter, we aim to come up with a holographic system describing a confining gauge theory that does exhibit a quark-matter phase with colour superconductivity at large chemical potential. However, motivated by recent condensed matter applications of gauge/gravity duality (see, for example [18, 21, 44, 45, 64, 84]), we will avoid many of the technical challenges described above by taking what is known as a 'bottom up' approach. Rather than working in a specific string theoretical model which takes into account the back-reaction of flavour branes, we will make an ansatz for the ingredients necessary for such a model to describe the relevant physics. We study the simplest possible gravitational theory with this minimal set of features, with the hope that it captures the qualitative physics of interest. We will indeed find that even this simple theory exhibits many of the expected features.

Ingredients

We wish to construct a gravitational theory to provide a holographic description of a four-dimensional confining gauge theory on Minkowski space with $N_f \sim N_c$ flavours. On the gravity side, the Minkowski space will appear as the fixed boundary geometry of our spacetime, but we must have at least one extra dimension corresponding to the energy scale in the field theory. Since the field theory has a scale (the QCD or confinement scale), the asymptotic behaviour of the solution must exhibit an additional scale relative to the asymptotically AdS geometries that appear in gravity duals of conformal field theories. In the simplest examples of gravity duals for confining gauge theories, this scale is provided by the size of an additional

[2]However, see [109] for a possible manifestation of the related colour-flavour locking phase in a holographic system.

circular direction in the geometry.[3] Thus, we will work with a gravitational system in six dimensions whose boundary geometry is $R^{3,1} \times S^1$. We will assume that the asymptotic geometry is locally Anti-de-Sitter space, so the confining gauge theory we consider arises from a five-dimensional conformal field theory compactified on a circle. When we study the theory at finite temperature, there will be an additional circle in the asymptotic (Euclidean) geometry, the Euclidean time direction whose period is $1/T$.

The gauge theories we are interested in have at least one other conserved current, corresponding to baryon (or quark) number. By the usual AdS/CFT dictionary, this operator corresponds on the gravity side to a $U(1)$ gauge field in the bulk. The asymptotic value of the time component for this gauge field corresponds to the chemical potential in our theory, while the asymptotic value of the radial electric flux corresponds to the baryon charge density in the field theory. For a given chemical potential, the minimum action solution will have some specific value for the flux, allowing us to relate density and chemical potential.

The colour superconductivity phases believed to exist at large density in QCD and related theories are usually characterized by condensates of the form $\langle\psi\psi\rangle$, bilinear in the quark fields ψ, which spontaneously break the $U(N)$ gauge symmetry, and the $U(1)_B$ global symmetry. Naively, we would want to model such operators by a bulk charged scalar field corresponding to the condensate. However, bulk fields always correspond to gauge-invariant operators, while by definition the $\psi\psi$ bilinears which break the gauge symmetry are not gauge-invariant (in fact, there is no way to make a singlet from two fundamental fields, except in the case of $SU(2)$). Additionally, the simplest gauge-invariant operators charged under $U(1)_B$ involve N ψ fields and have dimension of order N, thus our holographic dual theory should have *no* light scalar fields charged under the $U(1)_B$ gauge field.

The correct way to understand the condensation of the $\psi\psi$ bilinears is as an example of spontaneously broken gauge symmetry (as in the Higgs mechanism), rather than as a phase transition characterized by some gauge-invariant order parameter. Nevertheless, the transition to colour superconductivity *can* be characterized by the discontinuous behaviour of gauge-invariant operators, which are of the form $\psi\psi(\psi\psi)^\dagger$. Such operators are gauge invariant and neutral under the $U(1)_B$, and therefore should correspond to an uncharged scalar field in the bulk with dimension of order 1.[4]

[3] There are other possibilities here, as we mention briefly in the discussion section.

[4] As emphasized by Andreas Karch, a gauge invariant operator of the form $\mathcal{O}_4 = \psi\psi(\psi\psi)^\dagger$ can be written as a sum of terms $\mathcal{O}_\alpha\mathcal{O}_\alpha$ where each $O_\alpha \sim (\psi^\dagger\psi)_\alpha$ is gauge invariant (and α represents flavour/Lorentz indices). Thus, $\mathcal{O}_4$ is something like a double-

Combining everything so far, we want to study gravity in six dimensions with negative cosmological constant and boundary geometry $R^{3,1} \times S^1$ with a $U(1)$ gauge field and a neutral scalar field. The simplest action for this system is[5]

$$\int d^6x\sqrt{-g}\left\{\mathcal{R} + \frac{20}{L^2} - \frac{1}{4}F^2 - |\partial_\mu\psi|^2 - m^2|\psi|^2\right\}, \tag{5.1}$$

where we include one tunable parameter, the mass m of the scalar field, which determines the dimension of the corresponding operator in the dual field theory. More generally, we could consider other potentials for the scalar field, or a more complicated action (e.g. with a Chern-Simons term or of Born-Infeld type) for the gauge field, but we restrict here to this simplest possible model.[6]

Results

Starting with the model (5.1), we have explored the phase structure by minimizing the gravitational action for specific values of temperature (corresponding to the asymptotic size of the Euclidean S^1 direction) and chemical potential (corresponding to the asymptotic value of A_0). Our results for the phase diagrams are shown in Figures 5.1, 5.2, and 5.3. For small μ, we find a confined phase at low-temperature and a deconfined phase at high temperature, with the scalar field uncondensed in each case. However, increasing μ at zero temperature, we find (setting $L_{AdS} = 1$) for $-\frac{25}{4} \leq m^2 \leq -5$ a transition to a phase with nonzero scalar condensate (on a geometry with horizon) and finite homogeneous quark density, as expected for a colour superconductivity phase. Increasing the temperature from zero, we find a transition back to the deconfined phase at a remarkably low temperature; for example, at $m^2 = -6$, the critical temperature at which superconductivity disappears is

$$T/\mu \sim .00006333\ . \tag{5.2}$$

trace operator. In a large N theory, factorization of correlators implies that the expectation value of $\mathcal{O}_4$ can be calculated classically from the $\mathcal{O}_\alpha$ expectation values (up to $1/N$ corrections). Thus, discontinuous behaviour of $\mathcal{O}_4$ should be directly related to discontinuous behaviour in the simpler gauge-invariant operators O_α (which also have no baryon charge), so it may be more appropriate to think of the scalar field in our model as being dual to one of these simpler operators.

[5]Since we will also consider the case of a charged scalar field, we have written the action using standard normalizations for a complex scalar, but we will take the scalar to be real in the uncharged case.

[6]For another approach to modeling the QCD phase diagram by an effective holographic approach, see for example [59, 110].

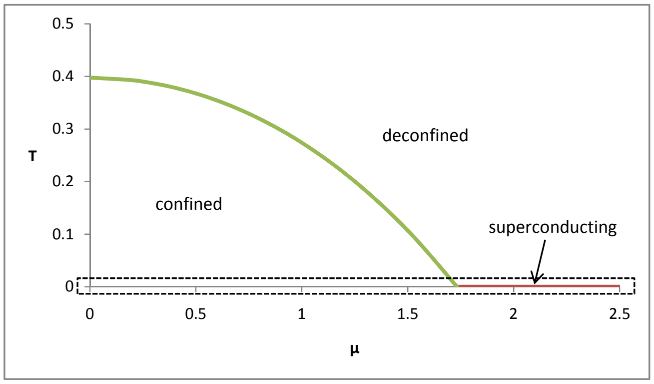

Figure 5.1: Phase diagram of our model gauge theory with $m^2 = -6$, $R = 2/5$. Region in dashed box is expanded in next figure.

The tendency for the scalar field to condense at low temperatures for the range of masses above can be understood in a simple way, as explained for example in [11, 111]. In $d + 1$ dimensional anti-de Sitter space with anti-de Sitter radius L, the minimum mass for a scalar field to avoid instability is $m^2_{BF} = -d^2/(4L^2)$. The minimum action solution for large chemical potential in the absence of any scalar field is a planar Reissner-Nordstrom black hole solution with one of the isometry directions periodically identified. In the limit of zero temperature, the near horizon region of this black hole has geometry $AdS^2 \times R^4$, with the radius of the AdS^2 equal to $L_2 = L/\sqrt{20}$. Thus, in the near-horizon region, there will be an instability toward condensation of the scalar field if $m^2 < -1/(4L_2^2) = -5/L^2$. We thus have a range (setting $L = 1$) of $-25/4 \leq m^2 \leq -5$ for which the scalar field tends to condense in the near-horizon region but is stable in the asymptotic region. Numerical simulations verify that we indeed have scalar field condensation for precisely this range of masses.

While there is no guarantee that the gravitational system we study has a legitimate field theory dual, 'top-down' gravitational systems corresponding to fully consistent field theories must have the same basic elements (usually with additional fields and a more complicated Lagrangian). The fact that the expected physics emerges even in our stripped-down version suggests

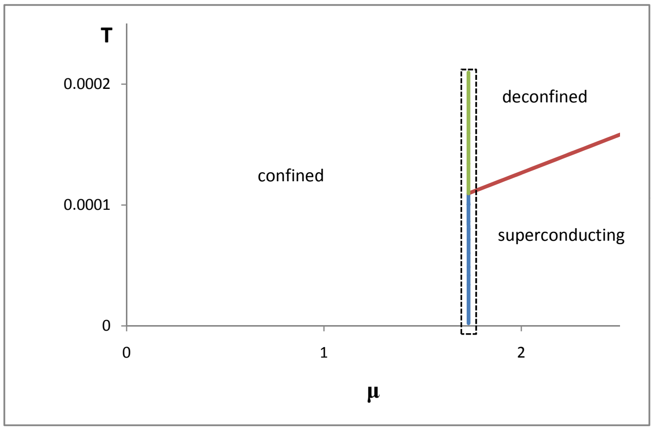

Figure 5.2: Phase diagram of our model gauge theory with $m^2 = -6$, $R = 2/5$. Region in dashed box is expanded in next figure.

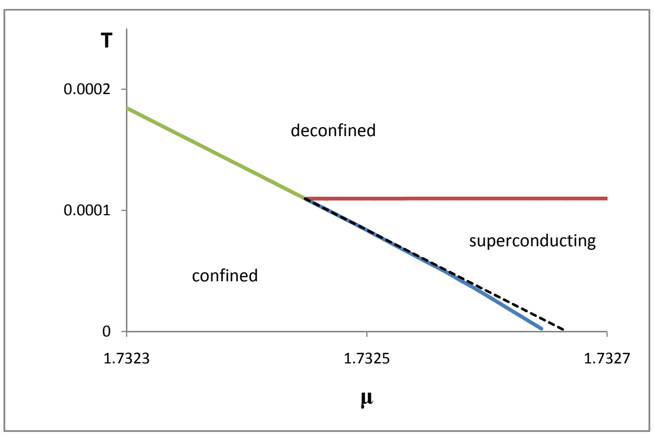

Figure 5.3: Phase diagram of our model gauge theory with $m^2 = -6$, $R = 2/5$. The dashed curve represents the phase boundary in theory without a scalar field.

that quark-matter phases will be found also in the complete models, once back-reaction effects are under control. Optimistically, qualitative features that we find in the bottom-up model (such as the extremely low transition temperature between superconducting and deconfined phases) may be present also in more complete holographic theories. In this case, our simple model may provide novel qualitative insights into fully consistent QCD-like theories.

Charged scalar

While less relevant to colour superconductivity, it is also interesting to explore the physics of our model when we make the scalar field charged under the gauge field. In this case, the scalar field corresponds to a gauge-invariant operator in the field theory that is charged under the $U(1)$ associated with A, and the kinetic term for the scalar field is modified in the usual way as $\partial_\mu \psi \to \partial_\mu \psi - iqA_\mu \psi$. As we have argued above, this symmetry cannot be $U(1)_B$, but could be another flavour symmetry, such as isospin in a model with two or more flavours. The flavour superconductivity associated with meson condensation was studied previously in the holographic context (with finite N_f), for example in [43, 112, 113]. Our results are qualitatively similar to the ones obtained in those studies, and we leave more detailed comparison for future work.

In section 5.5 below, we determine the phase diagram for various values of q and m. The same system was studied for the $2+1$ dimensional case in [58] and originally in [67] for the case of large q. The application there was to holographic insulator/superconductor systems, but the intriguing resemblance of the phase diagrams in those papers to QCD phase diagrams partially motivated the present study.

5.2 Basic setup

In this chapter, we consider holographic field theories with a conserved current J^μ, assumed to be a baryon current (or isospin current when we consider charged scalar fields) and some gauge-invariant operator $\mathcal{O}$ whose condensation indicates the onset of (colour or flavour) superconductivity. We would like to explore the phase structure of the theory for finite temperature T and chemical potential μ; that is, we would like to find the phase that minimizes the Gibbs free energy density $g = e - Ts - \mu\rho$, where e, s, and ρ are the energy density, entropy density, and charge density in the field theory. We can also ask about the values of e, s, ρ, and $\langle\mathcal{O}\rangle$ as a function of temperature and chemical potential.

As discussed in the introduction, our holographic theories are defined by a dual gravitational background which involves a metric, $U(1)$ gauge field, and scalar field, with a simple action

$$\int d^6x\sqrt{-g}\left\{\mathcal{R}+\frac{20}{L^2}-\frac{1}{4}F^2-|\partial_\mu\psi|^2-m^2|\psi|^2\right\}\ . \tag{5.3}$$

We choose coordinates (t,x,y,z) for the non-compact field theory directions, w for the compact field theory direction, and r for the radial direction. We take boundary conditions for which the asymptotic (large r) behaviour of the metric is

$$ds^2 \quad\rightarrow\quad \left(\frac{r}{L}\right)^2\left(-dt^2+dx^2+dy^2+dz^2+dw^2\right)+\left(\frac{L}{r}\right)^2 dr^2\ , \tag{5.4}$$

where w is taken to be periodic with period R. To study the theory at finite temperature, we take the period of $\tau = it$ in the Euclidean solution to be $1/T$.

The equations of motion constrain the gauge field to behave asymptotically as

$$A_\nu = a_\nu - \frac{j_\nu}{3r^3}+\dots\ . \tag{5.5}$$

Since A_ν is assumed to be the field corresponding to the conserved baryon current operator J^ν, in the field theory, the usual AdS/CFT dictionary tells us that a_ν is interpreted as the coefficient of the J^ν in the Lagrangian (i.e. an external source for the baryon current) while j_μ is interpreted as the expectation value of baryon current for the state corresponding to the particular solution we are looking at. To study the theory at finite chemical potential μ without any external source for the spatial components of the baryon current, we want to take

$$a_\nu = (\mu,0,0,0)\ . \tag{5.6}$$

The scalar field equations of motion imply that asymptotically

$$\psi = \frac{\psi_1}{r^{\lambda_-}}+\frac{\psi_2}{r^{\lambda_+}}+\cdots\ , \tag{5.7}$$

where

$$\lambda_\mp = \frac{1}{2}(d\mp\sqrt{d^2+4m^2})\ . \tag{5.8}$$

The holographic field theories we consider are defined by assuming $\psi_1 = 0$. In this case, λ_+ gives the dimension of the operator dual to ψ.[7] In this case, ψ_2 (which will be different for solutions corresponding to different states of the field theory) gives us the expectation value of the operator $\mathcal{O}$ in the field theory.

By the AdS/CFT correspondence, the field theory free energy corresponds to the Euclidean action of the solution. Thus, to investigate the field theory state which minimizes free-energy for given T and μ, we need to find the gravitational solution with boundary conditions given above which minimizes the Euclidean action. Note that we only consider solutions with translation invariance in t, x, y, z, and w. It would be interesting to investigate the possibility of inhomogeneous phases (or at least the stability of our solutions to inhomogeneous perturbations) but we leave this as a question for future work.

Calculating the action

In order to obtain finite results when calculating the gravitational action for a solution, it is important to include boundary contributions to the action. In terms of the Lorentzian metric, gauge field and scalar, the fully regulated expression that we require is [64]

$$\begin{aligned} S \;=\; & \lim_{r_M \to \infty} \left[- \int_{r<r_M} d^{d+1}x\sqrt{-g}\left\{ \mathcal{R} + \frac{d(d-1)}{L^2} - \frac{1}{4}F^2 - |D_\mu\psi|^2 - m^2|\psi|^2 \right\} \right. \\ & \left. + \int_{r=r_M} d^d x\sqrt{-\gamma}\left\{ -2K + \frac{2(d-1)}{L} - \frac{1}{L}\lambda_-|\psi|^2 \right\} \right] , \end{aligned} \tag{5.9}$$

where

$$\lambda_- = \frac{d}{2} - \frac{1}{2}\sqrt{d^2 + 4m^2} \; . \tag{5.10}$$

Here, γ is the metric induced on the boundary surface $r = r_M$, and K is defined as

$$K = \gamma^{\mu\nu}\nabla_\mu n_\nu \; , \tag{5.11}$$

where n^μ is the outward unit normal vector at $r = r_M$. The scalar counterterm here is the appropriate one assuming that our boundary condition is to

[7] For a certain range scalar field masses in the range $-d^2/4 \le m^2 \le -d^2/4 + 1$, it is also consistent to define a theory by fixing $\psi_2 = 0$. In this case, the dimension of the dual operator is λ_-. We consider this case briefly in section 4.2.

fix the coefficient of the leading term in the large r expansion of ψ. Since we are setting this term to zero, it turns out that the counterterm vanishes in the $r_M \to \infty$ limit.

For all cases we consider, the metric takes the form

$$ds^2 = \frac{r^2}{L^2} dx_i^2 + g_{00}(r) dt^2 + g_{rr}(r) dr^2 + g_{ww}(r) dw^2 \ . \tag{5.12}$$

Assuming the Einstein equations are satisfied, we can show (by subtracting a term proportional to the xx component of the equation of motion) that the integrand in the first term may be written as a total derivative with respect to r

$$-\sqrt{-g}\left\{\mathcal{R} + \frac{d(d-1)}{L^2} - \frac{1}{4}F^2 - |D_\mu \psi|^2 - m^2|\psi|^2\right\} = \partial_r \left(\frac{2}{r g_{rr}}\sqrt{-g}\right) \ . \tag{5.13}$$

Using

$$n_\mu = (0, \ldots, 0, \sqrt{g_{rr}}) \ , \tag{5.14}$$

we have

$$\begin{aligned} K &= \gamma^{\mu\nu} \nabla_\mu n_\nu \\ &= \gamma^{\mu\nu} \left\{ -\Gamma^r_{\mu\nu} n_r \right\} \\ &= \gamma^{\mu\nu} \left\{ \frac{1}{2} g^{rr} \frac{\partial g_{\mu\nu}}{\partial r} \sqrt{g_{rr}} \right\} \\ &= \frac{1}{2\sqrt{g_{rr}}} \gamma^{\mu\nu} \frac{\partial \gamma_{\mu\nu}}{\partial r} \\ &= \frac{1}{\sqrt{g_{rr}}} \frac{\partial \ln(\sqrt{-\gamma})}{\partial r} \end{aligned} \tag{5.15}$$

so that

$$\sqrt{-\gamma}(-2K) = -\frac{2}{\sqrt{g_{rr}}} \frac{\partial \sqrt{-\gamma}}{\partial r} \ . \tag{5.16}$$

Our final expression for the action density is

$$S/V_d = \frac{2}{r g_{rr}} \sqrt{-g} \bigg|_{r_0}^{r_M} + \left\{ -\frac{2}{\sqrt{g_{rr}}} \frac{\partial \sqrt{-\gamma}}{\partial r} + \frac{2(d-1)}{L} \sqrt{-\gamma} \right\}_{r=r_M} \ . \tag{5.17}$$

Action in terms of asymptotic fields

It is convenient to rewrite the expression (5.17), in terms of the asymptotic expansion of the fields. For the ansatz (5.12), and the boundary conditions appropriate to our case, we find

$$\begin{aligned} g_{tt} &= -r^2 + \frac{g_{tt}^{(3)}}{r^3} + \dots \,, \\ g_{rr} &= \frac{1}{r^2} + \frac{g_{rr}^{(7)}}{r^7} + \dots \,, \\ g_{ww} &= r^2 + \frac{g_{ww}^{(3)}}{r^3} + \dots \,, \\ \psi &= \frac{\psi^{(3)}}{r^3} + \dots \,, \\ \phi &= \mu - \frac{\rho}{3r^3} + \dots \,. \end{aligned} \tag{5.18}$$

Inserting these expansions into our expression above for the action we find that (assuming the term at $r = r_0$ vanishes)

$$S = 5g_{ww}^{(3)} + 4g_{rr}^{(7)} - 5g_{tt}^{(3)} \,. \tag{5.19}$$

However, using the equations of motion, we find that $g_{ww}^{(3)} + g_{rr}^{(7)} - g_{tt}^{(3)} = 0$, so we can simplify to:

$$S = -g_{rr}^{(7)} \,. \tag{5.20}$$

Numerically, it can be a bit tricky to read off $g_{rr}^{(7)}$ because there is also a $1/r^8$ term in the expansion of g_{rr}. But using the equations of motion, we can find

$$g_{rr}^{(8)} = \frac{3}{4}(7 + m^2)(\psi^{(3)})^2 \,. \tag{5.21}$$

From this, it follows that the combination

$$-r^7 g_{rr}(r) + r^5 - \frac{3}{4}(7 + m^2) r^5 \psi^2(r) \tag{5.22}$$

behaves like

$$-g_{rr}^{(7)} + \mathcal{O}(1/r^3) \,. \tag{5.23}$$

So, we can numerically evaluate the action by taking

$$S \approx -r_*^7 g_{rr}(r_*) + r_*^5 - \frac{3}{4}(7 + m^2) r_*^5 \psi^2(r_*) \,, \tag{5.24}$$

where r_* is taken to be large but not too close to the cutoff value.

5.3 Review: $\psi = 0$ solutions

We begin by considering the solutions for which the scalar field is set to zero.

5.3.1 AdS soliton solution

At zero temperature and chemical potential, the simplest solution with our boundary conditions is pure AdS with periodically identified w. However, assuming antiperiodic boundary conditions for any fermions around the w circle, there is another solution with lower action. This is the AdS soliton [114], described by the metric (setting $L = 1$)

$$ds^2 = r^2 \left(-dt^2 + dx^2 + dy^2 + dz^2 + f(r)\, dw^2\right) + \frac{dr^2}{r^2 f(r)} \,, \tag{5.25}$$

where

$$f(r) = 1 - \frac{r_0^5}{r^5} \,. \tag{5.26}$$

As long as we choose the period $2\pi R$ for w such that

$$r_0 = \frac{2}{5\,R} \tag{5.27}$$

the solution smoothly caps off at $r = r_0$. This IR end of the spacetime corresponds in the field theory to the fact that we have a confined phase with a mass gap. The fluctuation spectrum about this solution corresponds to a discrete spectrum of glueball states in the field theory.

Starting from this solution, we can obtain a solution valid for any temperature and chemical potential, by periodically identifying the Euclidean time direction and setting $A_0 = \mu$ everywhere. Using (5.20) we find that the action for this solution is

$$S_{sol} = -r_0^5 = -\left(\frac{2}{5R}\right)^5 \,. \tag{5.28}$$

The negative value indicates that this solution is preferred over the pure AdS solution with action zero.

5.3.2 Reissner-Nordstrom black hole solution

For sufficiently large temperature and/or chemical potential, the AdS soliton is no longer the $\psi = 0$ solution with minimum action. The preferred solution is the planar Reissner-Nordstrom black hole, with metric

$$ds^2 = r^2 \left(-dt^2 f(r) + dx^2 + dy^2 + dz^2 + dw^2\right) + \frac{dr^2}{r^2 f(r)} , \tag{5.29}$$

where

$$f(r) = 1 - \left(1 + \frac{3\mu^2}{8r_+^2}\right)\frac{r_+^5}{r^5} + \frac{3\mu^2 r_+^6}{8r^8} , \tag{5.30}$$

the scalar potential is

$$\phi(r) = \mu \left(1 - \frac{r_+^3}{r^3}\right) , \tag{5.31}$$

and w is periodically identified as before.

This solution has a horizon at $r = r_+$. The temperature of the solution (determined as the inverse period of the Euclidean time for which the Euclidean solution is smooth) is given in terms of r_+ by

$$T = \frac{1}{4\pi}\left(5r_+ - \frac{9\mu^2}{8r_+}\right) . \tag{5.32}$$

From (5.20), we find that the action for this solution is

$$S_{RN} = -r_+^5 \left(1 + \frac{3}{8}\frac{\mu^2}{r_+^2}\right) . \tag{5.33}$$

Thus, we find that the black hole solution has lower action than the soliton for

$$r_+ \left(1 + \frac{3}{8}\frac{\mu^2}{r_+^2}\right)^{\frac{1}{5}} > \frac{2}{5R} , \tag{5.34}$$

where r_+ is determined in terms of T and μ by (5.32). This defines a curve in the $T - \mu$ plane that begins on the $\mu = 0$ axis at $T = 1/(2\pi R)$ and curves down to the $T = 0$ axis at $\mu = 2^{19/10}/(5^{1/2}3^{4/5}R) \approx 4.3547/(2\pi R)$, as shown in Figure 5.4.

As usual, the existence of a horizon in this solution indicates that the corresponding field theory state is in a deconfined phase [32].

In the next sections, we consider solutions with nonzero scalar field. We will find that for large μ there exist solutions with nonzero scalar field that have lower action than the solutions we have considered, so the phase diagram of Figure 5.4 will be modified.

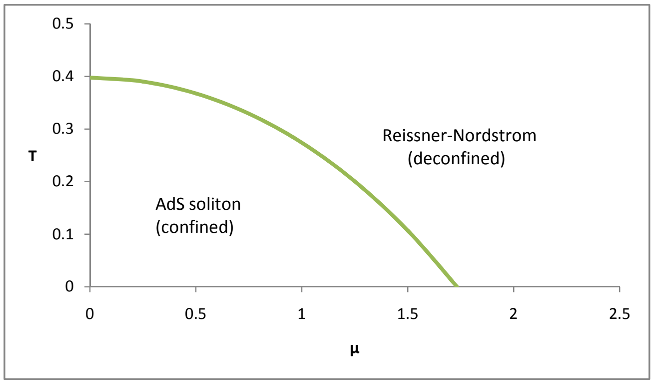

Figure 5.4: Phase diagram without scalar field, in units where $R = 2/5$.

5.4 Neutral scalar field: Colour superconductivity

In the case of a neutral scalar field, our simple model has no explicit source for the gauge field in the bulk, so homogeneous solutions with a non-trivial static electric field (corresponding to a non-zero baryon number density in the field theory) necessarily have a horizon from which the flux can emerge[8].

To look for solutions of this form, we consider the ansatz[9]

$$\begin{aligned} ds^2 &= -g(r)e^{-\chi(r)}dt^2 + \frac{dr^2}{g(r)} + r^2(dw^2 + dx^2 + dy^2 + dz^2) \ , \\ A_t &= \phi(r) \ , \\ \psi &= \psi(r) \ . \end{aligned} \tag{5.35}$$

[8]In a more complete model, the source might be provided by some non-perturbative degrees of freedom in the theory, such as the wrapped D-branes that give rise to baryons in the Sakai-Sugimoto model.

[9]We could have considered a more complicated ansatz, with an extra undetermined function in front of dw^2. However, it is plausible that as for the $\psi = 0$ solution, the minimum action solution for the case where the w circle does not contract in the bulk is a periodic identification of the solution with non compact w and rotational invariance in the x, y, z, w directions.

The scalar and Maxwell's equations that follow from the action (5.3) are

$$\psi'' + \left(\frac{4}{r} - \frac{\chi'}{2} + \frac{g'}{g}\right)\psi' - \frac{m^2}{g}\psi = 0 \ , \tag{5.36}$$

$$\phi'' + \left(\frac{4}{r} + \frac{\chi'}{2}\right)\phi' = 0 \ , \tag{5.37}$$

while the Einstein equations are satisfied if

$$\chi' + \frac{r\psi'^2}{2} = 0 \ , \tag{5.38}$$

$$g' + \left(\frac{3}{r} - \frac{\chi'}{2}\right)g + \frac{re^{\chi}\phi'^2}{8} + \frac{m^2 r\psi^2}{4} - 5r = 0 \ . \tag{5.39}$$

These have two symmetries:

$$\tilde{\psi}(r) = \psi(ar) \ , \qquad \tilde{\phi}(r) = \frac{1}{a}\phi(ar) \ , \qquad \tilde{\chi}(r) = \chi(ar) \ , \qquad \tilde{g}(r) = \frac{1}{a^2}g(ar) \ , \tag{5.40}$$

arising from the underlying conformal invariance, and

$$\tilde{\chi} = \chi + \Delta \ , \qquad \tilde{\phi} = e^{-\frac{\Delta}{2}}\phi \ . \tag{5.41}$$

We would like to find solutions with a horizon at some $r = r_+$. The electric potential must also vanish at the horizon, and we are looking for solutions for which the leading falloff ψ_1 in (5.7) vanishes for the scalar. Also, multiplying the first equation (5.36) by g and evaluating at $r = r_+$ fixes $\psi'(r_+)$ in terms of $\psi(r_+)$ and $g'(r_+)$. Altogether, our boundary conditions are

$$g(r_+) = 0 \ , \qquad \phi(r_+) = 0 \ , \qquad \chi(\infty) = 0 \ , \qquad \psi_1 = 0 \ , \tag{5.42}$$

and

$$\psi'(r_+) = \frac{8m^2\psi(r_+)}{40r_+ - 2m^2r_+^2\psi^2(r_+) - r_+e^{\chi(r_+)}(\phi'(r_+))^2} \ . \tag{5.43}$$

The remaining freedom to choose r_+ and $\phi'(r_+)$ leads to a family of solutions with different T and μ. Explicitly, we have

$$\mu = \phi(\infty) \ , \qquad\qquad T = \frac{1}{4\pi}g'(r_+)e^{-\chi(r_+)/2} \ . \tag{5.44}$$

Note that solutions with the same T/μ are simply related by the scaling symmetry (5.40).

5.4.1 Numerical evaluation of solutions

To find solutions in practice, we can make use of the symmetries (5.40) to initially set $r_+ = 1$ and $\chi(0) = 0$ and solve the equations with boundary conditions

$$g(1) = 0 \ , \quad \chi(0) = 0 \ , \quad \phi(1) = 0 \ , \quad \phi'(1) = E_0 \ , \quad \psi(1) = \psi_0 \ , \tag{5.45}$$

and

$$\psi'(1) = \frac{8m^2\psi_0}{40 - 2m^2\psi_0^2 - E_0^2} \ . \tag{5.46}$$

We can integrate the ϕ and χ equations explicitly to obtain

$$\begin{aligned} \chi(r) &= -\int_0^r d\tilde{r}\frac{1}{2}\tilde{r}\left(\frac{\partial\psi}{\partial r}\right)^2 \ , \\ \phi(r) &= E_0\int_1^r \frac{d\tilde{r}}{\tilde{r}^4}e^{-\frac{1}{2}\chi(\tilde{r})} \ , \end{aligned} \tag{5.47}$$

leaving the remaining equations

$$\begin{aligned} \psi'' + (\frac{4}{r} + \frac{r\psi'^2}{4} + \frac{g'}{g})\psi' - \frac{m^2}{g}\psi &= 0 \ , \\ g' + \frac{3g}{r} + \frac{gr}{4}\psi'^2 + \frac{E_0^2}{8r^7} + \frac{m^2 r\psi^2}{4} - 5r &= 0 \ . \end{aligned} \tag{5.48}$$

We use E_0 as a shooting parameter to enforce $\psi_1 = 0$, and find one solution for each ψ_0. From these solutions, we apply the symmetry (5.41) with $\Delta = -\chi(\infty)$ to restore $\chi(\infty) = 0$ and finally use the symmetry (5.40) to scale to the desired temperature or chemical potential.

Using this method, we find that solutions exist for scalar mass in the range $-25/4 \leq m^2 \leq 5$, which is exactly the range of masses for which the scalar is stable in the asymptotic region but unstable in the near-horizon region.[10] For a given m^2 in this range, solutions exist in the region $T/\mu < \gamma(m^2)$, where $\gamma(m^2)$ is a dimensionless number depending on m^2 (which we evaluate in the next section). The value of $\gamma(m^2)$ is remarkably small for all m^2 in the allowed range. For example, with $m^2 = -6$ (not particularly close to the limiting value $m^2 = -5$), we have $\gamma \approx .00006333$. It would be interesting to understand better how this small dimensionless number emerges since the setup has no small parameters. From the bulk point of

[10] Solutions of this form were first found in lower dimensions in [11]. The zero-temperature limit of such solutions were considered in [47].

view it is presumably related to the warping between IR and UV regions of the geometry.[11] From the boundary viewpoint, the low critical temperature may be explained by the BKL scaling [111, 115, 116] near a quantum critical point.

For a given T and μ, we can use (5.20) to evaluate the action for the solution and compare this with the action for the soliton and/or Reissner-Nordstrom solution with the same T and μ. We find that the action for the new solutions is always less than the action for the Reissner-Nordstrom solutions, and is also less than the action for the soliton solutions for chemical potential in a region $\mu > \mu_c(T)$. Thus, the solutions with scalar field represent the equilibrium phase in the region $T/\mu < \gamma, \mu > \mu_c(T)$, as shown in Figures 5.1 – 5.3 above.

The transition between the deconfined and superconducting phases is second order, while the transition between confined and superconducting phases is first order. The place where these phase boundaries meet represents a triple point for the phase diagram where the three phases (confined, deconfined, superconducting) can coexist.

5.4.2 Critical temperature

For fixed m^2, the value of $\psi(0)$ in the solutions increases from zero at $T/\mu = \gamma$, diverging as $T/\mu \to 0$. Since ψ is small everywhere near $T/\mu = \gamma$, the critical value of T/μ will be the value where the ψ equation, linearized around the Reissner-Nordstrom background, has a solution with the correct boundary conditions. Thus, we consider the equation

$$\psi'' + (\frac{4}{r} + \frac{g'}{g})\psi' - \frac{m^2}{g}\psi = 0 \, , \tag{5.49}$$

where (setting $r_+ = 1$)

$$g(r) = r^2 - \left(1 + \frac{3\mu^2}{8}\right)\frac{1}{r^3} + \frac{3\mu^2}{8r^6} \, , \tag{5.50}$$

and find the value $\mu = \mu_c$ for which the equation admits a solution with boundary conditions $\psi(1) = 1$ (we are free to choose this), $\psi'(1) = m^2/g'(1)$ and the right falloff ($\psi_1 = 0$) at infinity.[12]

[11] By considering the alternate quantization mentioned in section 2 and fine-tuning the mass so that the dual operator has the smallest possible dimension consistent with unitarity in the dual field theory, we can obtain γ as large as 0.0151, so even under the most favorable circumstances, the critical T/μ is quite small.

[12] To obtain a very accurate result, we first find a series solution ψ_{low} near $r = 1$ with $\psi(1) = 1$ (we are free to choose this) and $\psi'(1) = m^2/g'(1)$ and find a series solution ψ_{high}

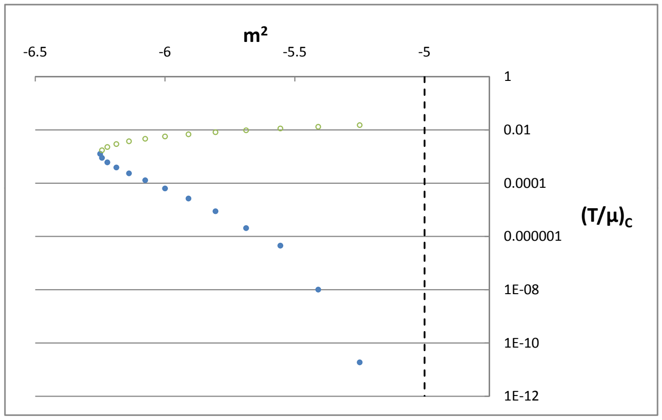

Figure 5.5: Critical T/μ vs m^2 of neutral scalar (filled circles). Mass is above BF bound asymptotically but below BF bound in near-horizon region of zero-temperature background solution in the range $-6.25 \leq m^2 < -5$. Unfilled circles represent critical values in the theory with alternate quantization of the scalar field, possible in the range $-6.25 \leq m^2 < -5.25$.

The choice $r_+ = 1$ implies that $T = (5 - 9\mu^2/8)/(4\pi)$, so we have $\gamma = (5 - 9\mu_c^2/8)/(4\pi\mu_c)$. The results for $\gamma(m^2)$ are plotted in Figure 5.5. For comparison, we also considered the theory defined with the alternate quantization ($\psi_2^\infty = 0$) of the bulk scalar field (mentioned in section 2). As we see in Figure 5.5, the critical temperatures are somewhat larger in this case, but still much smaller than 1 relative to μ.

5.4.3 Properties of the superconducting phase

In the superconducting phase, it is interesting to ask how the charge density and free energy behave as a function of chemical potential. Since the solutions (as for the planar RN-black hole solutions) are trivially related to solutions where the w direction is non-compact, and since the underlying theory has a conformal symmetry, physical quantities in this phase (or in

for large r with the correct fall-off ($\psi_1 = 0$) at infinity. Starting with ψ_{low} and ψ'_{low} at some $r = r_1$ where the low r series solution is still very accurate, we then numerically integrate up to $r = r_2$ where the large r series is very accurate and then find μ for which $\psi'_{num}(r_2)/\psi_{num}(r_2) = \psi'_{high}/\psi_{high}$.

the RN phase) behave as $\mu^n F(T/\mu)$ for some non-trivial function F and a power n.[13] At the critical value of T/μ, we have a second order transition from the RN phase to the phase with scalar, so the free energy and its derivatives, and other physical quantities such as the density, are continuous across the transition. Thus, the relevant function F in these cases will be the same for the two phases across the transition. We find that the function F for either the charge density or the free energy changes very little between the very small value of T/μ where the the transition occurs and the $T \to 0$ limit. Thus, to a good approximation, we find that the density and free energy behave in the superconducting phase in the same way as for the zero temperature limit of the RN phase. For R=2/5, we have

$$\rho \approx 0.320\mu^4 \;, \tag{5.51}$$

while

$$G \approx -.064\mu^5 \;. \tag{5.52}$$

In both cases, the behaviour at large μ is governed by the underlying 4+1 dimensional conformal field theory.

5.5 Charged scalar field: Flavour superconductivity

In this section, we generalize our holographic model to the case where the scalar field is charged under the gauge field in the bulk. As we discussed in the introduction, this implies that the dual field theory includes some low-dimension gauge-invariant operator with charge, so the charge in this case is more naturally thought of as some isospin-type charge (since the smallest gauge-invariant operators carrying baryon charge have dimensions of order N).

A significant qualitative difference in this case is that a scalar field condensate acts as a source for the electric field in the bulk, so it is possible to have solutions with no horizon carrying a finite charge density in the field theory. This gives the possibility of a fourth phase in which the scalar field condenses in the soliton background.

To obtain the action for the charged scalar case, we begin with the action (5.3) and make the replacement $\partial_\mu\psi \to \partial_\mu\psi - iqA_\mu\psi$. The results of the previous section correspond to $q = 0$.

[13] If the solutions instead depended on the circle direction in a non-trivial way, we might have a general function of RT and $R\mu$.

5.5.1 Low-temperature horizon free solutions with scalar

Above some critical value of μ, there exist horizon-free geometries with a scalar field condensate. The solutions may be parameterized by the magnitude of the scalar at the IR tip of the geometry, and we will find a single solution for each such value. To determine these geometries, we need to take into account back-reaction on the metric. The most general solution with the desired properties can be described by the ansatz

$$\begin{aligned} ds^2 &= r^2(e^{A(r)}B(r)dw^2 + dx^2 + dy^2 + dz^2 - e^{C(r)}dt^2) + \frac{dr^2}{r^2B(r)} , \\ A_t &= \phi(r) , \\ \psi &= \psi(r) , \end{aligned} \tag{5.53}$$

where we demand $A(\infty) = C(\infty) = 0$ and $B(\infty) = 1$. As for the soliton geometry, we expect that the w circle is contractible in the bulk so that $B(r_0) = 0$ for some r_0. For the geometry to be smooth at this point, the periodicity of the w direction must be chosen so that

$$2\pi R = \frac{4\pi e^{-A(r_0)/2}}{r_0^2 B'(r_0)} . \tag{5.54}$$

Starting from the action (5.3) with scalar derivatives replaced by covariant derivatives, the scalar and Maxwell equations are:

$$\psi'' + \left(\frac{6}{r} + \frac{A'}{2} + \frac{B'}{B} + \frac{C'}{2}\right)\psi' + \frac{1}{r^2B}\left(\frac{e^{-C}(q\phi)^2}{r^2} - m^2\right)\psi = 0 , \tag{5.55}$$

$$\phi'' + \left(\frac{4}{r} + \frac{A'}{2} + \frac{B'}{B} - \frac{C'}{2}\right)\phi' - \frac{2\psi^2q^2\phi}{r^2B} = 0 . \tag{5.56}$$

Following [58], we find that the Einstein equations give:

$$A' = \frac{2r^2C'' + r^2C'^2 + 4rC' + 4r^2\psi'^2 - 2e^{-C}\phi'^2}{r(8 + rC')} , \tag{5.57}$$

$$C'' + \frac{1}{2}C'^2 + \left(\frac{6}{r} + \frac{A'}{2} + \frac{B'}{B}\right)C' - \left(\phi'^2 + \frac{2(q\phi)^2\psi^2}{r^2B}\right)\frac{e^{-C}}{r^2} = 0 , \tag{5.58}$$

$$\begin{aligned} B'\left(\frac{4}{r} - \frac{C'}{2}\right) + B\left(\psi'^2 - \frac{1}{2}A'C' + \frac{e^{-C}\phi'^2}{2r^2} + \frac{20}{r^2}\right) \\ + \frac{1}{r^2}\left(\frac{e^{-C}(q\phi)^2\psi^2}{r^2} + m^2\psi^2 - 20\right) = 0 . \end{aligned} \tag{5.59}$$

These equations have two scaling symmetries,

$$\tilde{\psi}(r) = \psi(ar) , \quad \tilde{\phi}(r) = \frac{1}{a}\phi(ar) , \quad \tilde{A}(r) = A(ar),$$
$$\tilde{B}(r) = B(ar) , \quad \tilde{C}(r) = C(ar) , \tag{5.60}$$

and

$$\tilde{C} = C + \Delta , \qquad \tilde{\phi} = e^{\frac{\Delta}{2}}\phi . \tag{5.61}$$

Numerical evaluation of solutions

To find solutions, we first use the scaling symmetries to fix $r_0 = 1$ and $C(r_0) = 0$. For each value of $\psi(1)$, we use $\phi(1)$ as a shooting parameter, choosing the value so that ψ has the desired behaviour for large r. From the solution obtained in this way, we can use (5.61) with $\Delta = -C(\infty)$ to obtain the desired boundary condition $C(\infty) = 0$ in the rescaled solution. From (5.54), we see that the choice $r_0 = 1$ corresponds to a periodicity for the w direction equal to

$$2\pi R = \frac{4\pi e^{-A(1)/2}}{B'(1)} . \tag{5.62}$$

which will generally be different for solutions corresponding to different values of $\psi(1)$. In order to obtain solutions corresponding to our chosen value $R = 2/5$ (such that the action for the soliton solution is -1) we use the scaling (5.60), taking $a = B'(1)/5e^{-A(\infty)/2}$. After all the scalings, we calculate the chemical potential and action (making use of (5.20)) as

$$\mu = \phi(\infty) , \qquad S = [B]_{\frac{1}{r^5}} . \tag{5.63}$$

The action is plotted against chemical potential for various values of q in Figures 5.6, 5.7, and 5.8 taking the example of a mass just above the BF bound, $m^2 = -6$.

We find that for large enough values of q, the chemical potential increases monotonically and the action decreases monotonically as we increase $\psi(r_0)$. This implies that we have a second order transition to the superconducting phase at a critical value, which can be determined by a linearized analysis (see appendix C.1) to be $\mu \approx 1.0125/q$.

Below $q \approx 1.35$, the chemical potential is no longer monotonic in $\psi(r_0)$. We see that for $q = 1.3$, this results in a second order phase transition at $\mu \approx 1.558$, followed by a first order phase transition at $\mu \approx 1.616$ (taking $R = 2/5$). For smaller q (e.g. $q = 1.2$ in Figure 5.8), we simply have a

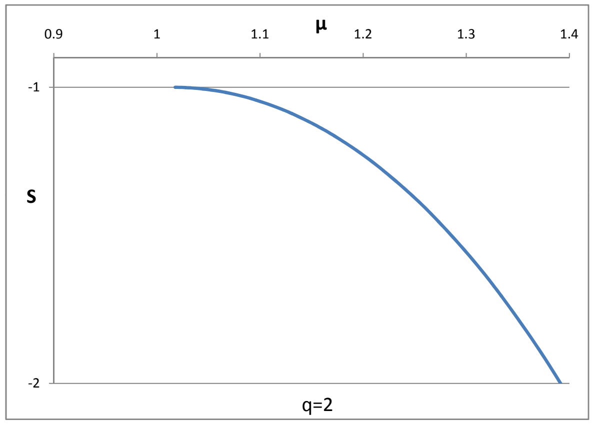

Figure 5.6: Action vs chemical potential for soliton with scalar solutions, taking $m^2 = -6$ and $q = 2$.

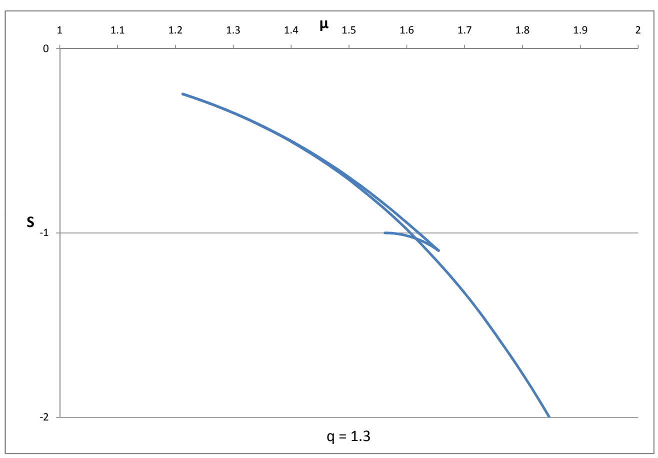

Figure 5.7: Action vs chemical potential for soliton with scalar solutions, taking $m^2 = -6$ and $q = 1.3$.

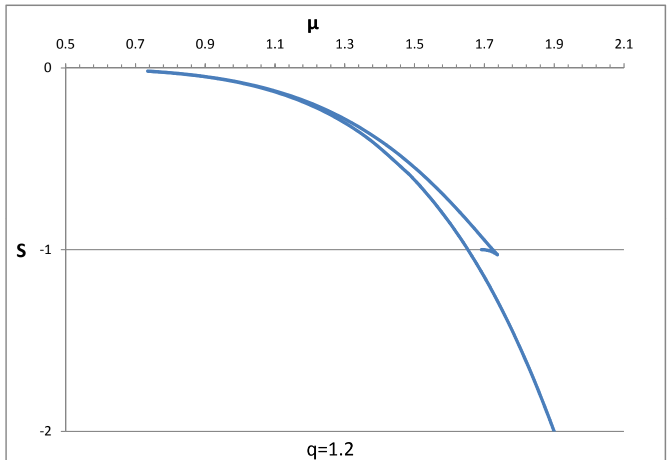

Figure 5.8: Action vs chemical potential for soliton with scalar solutions, taking $m^2 = -6$ and $q = 1.2$.

first order transition to the superconducting phase at a value of chemical potential that is less than the value for the solution with infinitesimal scalar field. All of these results are completely analogous to the lower-dimensional results of [58].

5.5.2 Hairy black hole solutions

At high temperatures, the w circle is no longer contractible, and we assume that (as for the solutions without scalar field) the solution can be obtained by periodic identification of a solution with boundary $R^{4,1}$ instead of $R^{3,1} \times S^1$. Thus, we take the ansatz

$$\begin{aligned} ds^2 &= -g(r)e^{-\chi(r)}dt^2 + \frac{dr^2}{g(r)} + r^2(dw^2 + dx^2 + dy^2 + dz^2) \;, \\ A_t &= \phi(r) \;, \\ \psi &= \psi(r) \;. \end{aligned}$$

The scalar and Maxwell's equations are

$$\psi'' + \left(\frac{4}{r} - \frac{\chi'}{2} + \frac{g'}{g}\right)\psi' + \frac{1}{g}\left(\frac{e^{\chi}q^2\phi^2}{g} - m^2\right)\psi = 0 \;, \tag{5.64}$$

$$\phi'' + \left(\frac{4}{r} + \frac{\chi'}{2}\right)\phi' - \frac{2q^2\psi^2}{g}\phi = 0 \; , \tag{5.65}$$

while the Einstein equations are satisfied if

$$\chi' + \frac{r\psi'^2}{2} + \frac{re^{\chi}q^2\phi^2\psi^2}{2g^2} = 0 \; , \tag{5.66}$$

$$g' + \left(\frac{3}{r} - \frac{\chi'}{2}\right)g + \frac{re^{\chi}\phi'^2}{8} + \frac{m^2r\psi^2}{4} - 5r = 0 \; . \tag{5.67}$$

These have two symmetries:

$$\tilde{\psi}(r) = \psi(ar) \; , \quad \tilde{\phi}(r) = \frac{1}{a}\phi(ar) \; , \quad \tilde{\chi}(r) = \chi(ar) \; , \quad \tilde{g}(r) = \frac{1}{a^2}g(ar) \; , \tag{5.68}$$

and

$$\tilde{\chi} = \chi + \Delta \; , \qquad \tilde{\phi} = e^{-\frac{\Delta}{2}}\phi \; . \tag{5.69}$$

As we did for $q = 0$, we would like to find solutions with a horizon at some $r = r_+$. The electric potential must also vanish at the horizon, and we are looking for solutions for which the leading falloff ψ_1 in (5.7) vanishes for the scalar. Also, multiplying the first equation (5.64) by g and evaluating at $r = r_+$ fixes $\psi'(r_+)$ in terms of $\psi(r_+)$ and $g'(r_+)$. Altogether, our boundary conditions are

$$g(r_+) = 0 \; , \qquad \phi(r_+) = 0 \; , \qquad \chi(\infty) = 0 \; , \qquad \psi_1 = 0 \; , \tag{5.70}$$

and

$$\psi'(r_+) = \frac{8m^2\psi(r_+)}{40r_+ - 2m^2r_+^2\psi^2(r_+) - r_+e^{\chi(r_+)}(\phi'(r_+))^2} \; . \tag{5.71}$$

The remaining freedom to choose r_+ and $\phi'(r_+)$ leads to a family of solutions with different T and μ. Explicitly, we have

$$\mu = \phi(\infty) \; , \qquad\qquad T = \frac{1}{4\pi}g'(r_+)e^{-\chi(r_+)/2} \; . \tag{5.72}$$

Solutions with the same T/μ are simply related by the scaling symmetry (5.68).

Numerical evaluation of solutions

To find solutions in practice, we can make use of the symmetries (5.68), (5.69) to initially set $r_+ = 1$ and $\chi(0) = 0$ and solve the equations with boundary conditions

$$g(1) = 0 \,, \quad \chi(0) = 0 \,, \quad \phi(1) = 0 \,, \quad \phi'(1) = E_0 \,, \quad \psi(1) = \psi_0 \,, \tag{5.73}$$

and

$$\psi'(1) = \frac{8m^2\psi_0}{40 - 2m^2\psi_0^2 - E_0^2} \,. \tag{5.74}$$

We use E_0 as a shooting parameter to enforce $\psi_1 = 0$, and find one solution for each ψ_0. From these solutions, we apply the symmetry (5.69) with $\Delta = -\chi(\infty)$ to restore $\chi(\infty) = 0$ and finally use the symmetry (5.68) to scale to the desired temperature or chemical potential.

5.5.3 Phase diagrams

At a generic point in the phase diagram, we can have up to four solutions (AdS soliton, planar RN black hole, soliton with scalar, black hole with scalar), or more in cases where there is more than one solution of a given type.

To map out the phase diagram, we evaluate the action for the various solutions using the methods of section 2. The equilibrium phase corresponds to the solution with lowest action. The phase diagrams for $q = 1.3$ and $q = 2$ (in the case $m^2 = -6$) are shown in Figures 5.9 and 5.10/5.11.

For large q, the condensation of the scalar field occurs in a region of the phase diagram where the back-reaction is negligible, so the phase diagram may be understood here (for $\mu \sim 1/q$) by treating the gauge field and scalar on a fixed background (the Schwarzschild black hole). The resulting phase diagram is shown in Figure 5.12.

5.6 Discussion

In this chapter, we have investigated the phase structure for a simple class of holographic systems which we have argued have the minimal set of ingredients to holographically describe the phenomenon of colour superconductivity. Even in these simple models, we find a rich phase structure with features similar to the conjectured behaviour of QCD at finite temperature

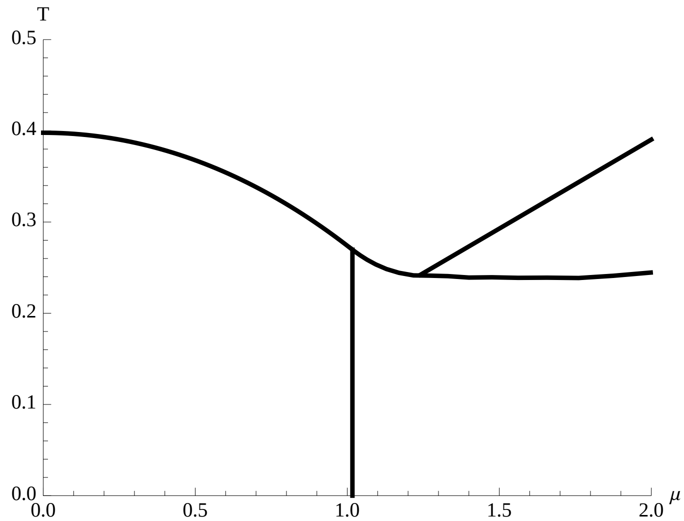

Figure 5.9: Phase diagram for $m^2 = -6$ and $q = 2$. Clockwise from the origin, the phases correspond to the AdS soliton (confined), RN black hole, black hole with scalar, and soliton with scalar.

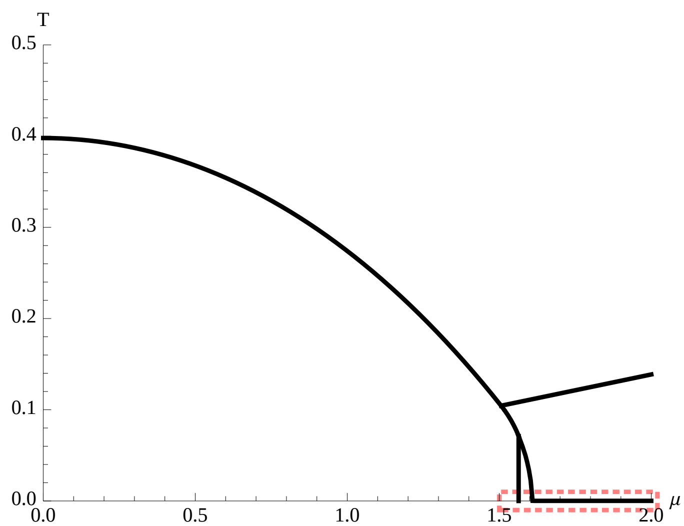

Figure 5.10: Phase diagram for $m^2 = -6$ and $q = 1.3$. Clockwise from the origin, the phases correspond to the AdS soliton (confined), RN black hole, black hole with scalar, and soliton with scalar.

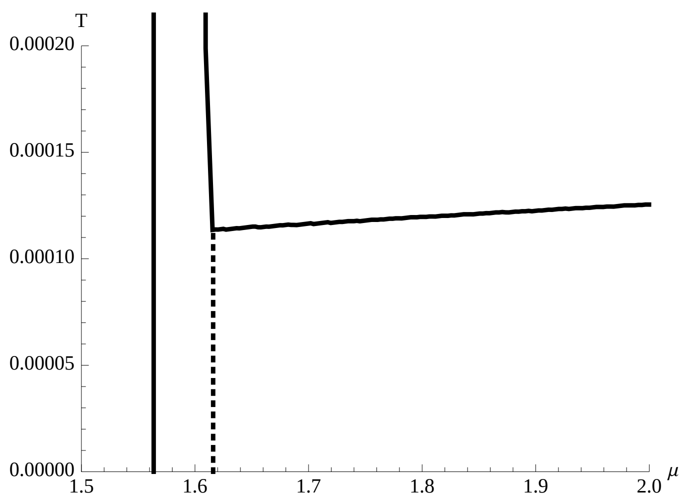

Figure 5.11: Small temperature region of phase diagram for $m^2 = -6$ and $q = 1.3$. Dashed line represents a first order transition within the soliton with scalar phase.

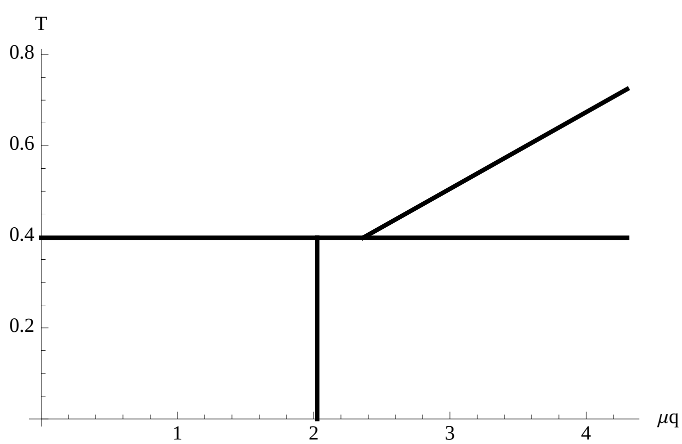

Figure 5.12: Phase diagram for large q, $m^2 = -6$.

and baryon chemical potential. It would be useful to verify the thermodynamic stability (and also the stability towards gravitational perturbations) of the phases that we have identified. This could indicate regions of the phase diagram where we have not yet identified the true equilibrium phase for the model, for example since our ansatz might be too symmetric.

We have calculated some of the basic thermodynamic observables, but it would be interesting to investigate more fully the physical properties of the various phases and establish more definitively a connection between the phase we find at large μ and small temperature and the physics of colour superconductivity.

Apart from the $\psi\psi\psi^\dagger\psi^\dagger$ condensate that we can see directly using the ingredients of our model, there are various other features that characterize a colour superconductivity phase [31]. Typically, the breaking of gauge symmetry is accompanied by some breaking of exact or approximate flavour symmetries. Thus, the superconducting phase has a low-energy spectrum characterized by Goldstone bosons or pseudo-Goldstone bosons associated with the broken flavour symmetries, together with massive vector bosons associated with the spontaneously broken gauge symmetry. It would therefore be interesting to analyze the spectrum of fluctuations in our model to compare with these expectations.

A caveat related to looking for features associated with the global flavour symmetries (and their breaking) in our model is that we may not have included enough ingredients in our bottom-up approach for all these features to be present. In simple models where the flavour degrees of freedom are associated with probe branes, there are explicit gauge fields in the bulk dual to the global symmetry current operators. However, in fully back-reacted solutions (appropriate for studying $N_f \sim N_c$), these branes are replaced by a modified geometry with additional fluxes (for an explicit example of such solutions, see [117]). In these solutions (which we are trying to model in our approach), it is less clear how to identify the global symmetry group from the gravity solution, but presumably it has to do with some detailed properties of the geometry. Thus, it is possible that the Goldstone modes associated with broken flavour symmetries correspond to fluctuations in some fields (e.g. form-fields) that we have not included.

The colour superconducting condensate also breaks the global baryon number symmetry, so there should be an associated Goldstone boson related to the phase of the condensate, and associated superfluidity phenomena. In other holographic models with superfluidity, the condensate is dual to a charged scalar field in the bulk and the Goldstone mode is related to fluctuations in the phase of this field. However, as we mentioned in the introduction, the baryon operator has dimension of order N, so we do not expect a light charged scalar field in the bulk. In a more complete top-down model, the baryon operator may be related to some non-perturbative degrees of freedom (such as D-branes) in the bulk, and it may be necessary to have a model with these degrees of freedom included in order to directly see the Goldstone mode from the bulk physics. Related to these observations, it may be interesting to probe our model with D-branes (put in by hand), in order to make the relation to microscopic physics more manifest, and to help gain a better understanding of the phenomenological parameters of our model.

There are a number of variants on the model that would be interesting to study. First, the breaking of scale-invariance, implemented in our model by the varying circle direction in the bulk, could be achieved in other ways, replacing g_{ww} with a more general scalar field, as in the model of [59]. In the setup of that paper, the transition between confined and deconfined phases was found to exhibit crossover behaviour at small chemical potential, a feature expected in the real QCD phase diagram and expected generally for massive quarks with sufficiently large N_f/N_c. It would be interesting to look for an even more realistic holographic model by incorporating features of the model we have studied here and the model of [59].

It would also be interesting to look at the effects of a Chern-Simons term for the bulk gauge field. In [80] and [90], it was shown that such a term (with sufficiently large coefficient) gives rise to an instability toward inhomogeneous phases, perhaps associated with the chiral density wave phase believed to exist at large density in QCD with $N_f \ll N_c$ [68, 69]. It is interesting to investigate the interplay between these inhomogeneous instabilities and the superconducting instabilities discussed in the present paper. It would also be interesting to consider more general actions (such as Born-Infeld) for the gauge field, interaction terms for the scalar field in the bulk, or other couplings between the scalar field and gauge field.

Finally, once the technical challenges of writing down fully back-reacted solutions for top-down models of holographic QCD with $N_f \sim N_c$ have been overcome, it will be interesting to see whether the basic features we find here are manifested in the more complete string-theoretic models. If certain features are found to be universal, these might taken as qualitative predictions for the QCD phase diagram, or at least motivate an effort to understand whether these features are also present in the phase diagram of real-world QCD.

Chapter 6

Holographic baryons from oblate instantons[1]

6.1 Introduction

Perhaps the most successful holographic model of QCD has been the Sakai-Sugimoto model [13, 118], defined by the physics of N_f probe D8-branes in the background dual to the decoupling limit of N_c D4-branes compactified on a circle with antiperiodic boundary conditions for the fermions. This model reproduces many features of real QCD, including chiral symmetry breaking, a deconfinement transition [32, 41], and a realistic meson spectrum.

The description of baryons in the Sakai-Sugimoto model involves solitonic configurations of the Yang-Mills field on the D8-brane.[2] In a simplified ansatz where the Yang-Mills field is taken to depend only on the four non-compact spatial directions in the bulk, configurations with baryon charge are precisely those configurations with non-zero instanton number for this reduced 4D Yang-Mills field [13, 119–121]. This connection between baryon charge and bulk instanton number stems from a Chern-Simons term $s\,\mathrm{tr}\,(F \wedge F)$ in the reduced D8-brane action. Here, $\mathrm{tr}\,(F \wedge F)$ is the instanton density for the $SU(2)$ part of the Yang-Mills field, and s is the $U(1)$ part of the Yang-Mills field, dual to the baryon current operator in the field theory.

To date, the study of baryons in the Sakai-Sugimoto model has been somewhat unsatisfactory, for several reasons: I) While the action for the gauge field is of Born-Infeld type, only the leading Yang-Mills terms are typically used when studying the instantons. II) For large 't Hooft coupling where the model can be studied most reliably, the size of the instanton in the bulk has been argued to be much smaller than the size of the compact directions in the bulk. In this case, the assumption that the gauge field does not depend on the compact directions is questionable. III) Rather than

[1]A version of this chapter has been published [5].

[2]Mesons correspond to pertubative excitations of the D8-branes.

solving the bulk equations to determine the precise solitonic configuration of the Yang-Mills field, the form has been taken to be that of a flat-space $SO(4)$ symmetric instanton, with the size of the instanton as the only free parameter.

The assumptions in I) and II) here amount to replacing the original top-down Sakai-Sugimoto model with a phenomenological (bottom-up) holographic model that retains many of the same successes as the Sakai-Sugimoto model. For the present chapter, we continue to make these assumptions, though we hope to relax them in future work in order to better understand baryons in the fully-consistent top-down model. Our goal in the present chapter is to overcome the third deficiency, by setting up and solving numerically a set of partial differential equations that determine the proper form of the soliton.[3] Using these solutions, we are able to calculate the mass and baryon charge distribution of the baryons as a function of the model parameter γ (proportional to the inverse 't Hooft coupling λ) that controls the strength of the Chern-Simons term relative to the Yang-Mills term.

One motivation for our study is the work of [125], which points out that the flat-space instanton approximation used previously does not give the correct large radius asymptotic behaviour (known from model-independent constraints) for the baryon form factors (computed for example in [126–128]). Via a perturbative expansion of the equations at large radius, it was later shown [33] that by relaxing the assumption of $SO(4)$ symmetry, the proper asymptotic behaviour can be recovered.[4] Thus, we expect that by constructing and studying the complete solutions, we can obtain a significantly improved picture of the properties of baryons in holographic QCD.

The solutions that we find take the form of 'oblate instantons': compared with the $SO(4)$ symmetric configurations, the correct solutions are deformed to configurations with $SO(3)$ symmetry that are spread out more in the field theory directions than in the radial direction. This shape is expected. The Coulomb repulsion between instanton charge density at different locations (induced by the Chern-Simons coupling to the Abelian gauge field) acts symmetrically in all directions, impelling the instanton to spread out both in the radial and field theory directions. Gravitational forces in the bulk limit the spreading in the radial direction, but there are no equivalent forces acting to radially compress the instanton in the field theory directions. Thus, the

[3] [122–124] have used a similar numerical approach in other phenomenological holographic QCD models.

[4] In the earlier work [129], a similar expansion was used in a phenomenological holographic QCD model. See also [130] for a recent related study.

instanton is oblate, compressed in one direction relative to the other three. The anisotropy is limited by the Yang-Mills action for the $SU(2)$ gauge field, which in flat space is minimized (in the one-instanton sector) for spherically symmetric configurations.

The size and anisotropy of the instantons is controlled by the parameter γ (related to the inverse 't Hooft coupling in the original model). For small γ, the spreading effects of the Chern-Simons term are small, and the instantons become small and approximately symmetrical near their core. For larger γ, the instantons become significantly larger and more anisotropic. Using our numerics, we are able to construct solutions up to γ of order 100 and evaluate the mass and baryon charge profiles of the corresponding baryons.

While our model is not expected to quantitatively match real-world QCD measurements, previous studies have found that the meson spectrum agrees reasonably well with the spectrum in QCD for a suitable choice of the parameter γ. Thus, it is interesting to compare the mass and size of the baryons in our model to the QCD values for the light nucleons. Using the value $\gamma = 2.55$ that gives the best fit to the meson spectrum [127], we find that the mass and baryon charge radius of the baryon are 1.19 GeV and 0.90 fm. This mass is significantly closer to realistic values (~ 0.94 GeV for the proton and neutron) than the previous value of 1.60 GeV based on the $SO(4)$ symmetric ansatz. The baryon charge radius is quite similar to measured values for the size of the proton and neutron. For example, the electric charge radius of a proton has been measured to be in the range 0.84 fm – 0.88 fm [131], while the magnetic radii of the proton and neutron are listed in [131] as 0.78 fm and 0.86 fm respectively.

An outline for the remainder of the chapter is as follows: In section 6.2, we briefly review the description of baryons in the Sakai-Sugimoto model and set up the problem. In section 6.3, we describe our numerical approach to the equations. In section 6.4, we describe physical properties of the solution, focusing on the baryon mass and the distribution of baryon charge (charge density as a function of radius), as a function of γ. Our main results may be found in Figures 6.4 and 6.7. We conclude in section 6.5 with a brief discussion of directions for future work.

Note: While this work was being completed, [132] appeared, which also presents a numerical solution of the Sakai-Sugimoto $N_B = 1$ soliton, using different methods, and which has some overlap with this paper.

6.2 Baryons as solitons in the Sakai-Sugimoto model

In this section, we give a brief review of the Sakai-Sugimoto model and set up the construction of a baryon in this model.

The Sakai-Sugimoto model consists of N_f probe D8 branes in the near horizon geometry of N_c D4 branes wrapped on a circle with anti-periodic boundary conditions for the fermions. The metric of the D4 background is [32]

$$\begin{aligned} ds^2 &= \frac{\lambda}{3} l_s^2 \left(\frac{4}{9} u^{\frac{3}{2}} \left(\eta_{\mu\nu} dx^\mu dx^\nu + f(u) dx_4^2 \right) + \frac{1}{u^{\frac{3}{2}}} \left(\frac{du^2}{f(u)} + u^2 d\Omega_4^2 \right) \right), \\ e^\Phi &= \left(\frac{\lambda}{3} \right)^{\frac{3}{2}} \frac{u^{\frac{3}{4}}}{\pi N_c}, \quad f(u) = 1 - \frac{1}{u^3}, \quad F_4 = dC_3 = \frac{2\pi N_c}{V_4} \epsilon_4, \end{aligned} \tag{6.1}$$

where ϵ_4 is the volume form on S^4 and V_4 is the volume of the unit 4-sphere. The direction x_4, with radius 2π, corresponds to the direction on which the D4-branes are compactified. The u and x_4 directions form a cigar-type geometry and the space pinches off at $u = 1$. The four dimensional $SU(N_c)$ gauge theory dual to this metric has a dimensionless coupling λ.

The flavor degrees of freedom are provided by N_f probe D8 branes in the background (6.1). The action for a single D8 brane is

$$S_{D8} = -\mu_8 \int d^9\sigma e^{-\Phi} \sqrt{-\det(g_{ab} + 2\pi\alpha' \mathcal{F}_{ab})} + S_{CS}, \tag{6.2}$$

with $\mu_8 = 1/(2\pi)^8 l_s^9$ and where S_{CS} is the Chern-Simons term. Below, we expand this action around a particular embedding and take the non-Abelian generalization of the result to define the action we consider. We take the probe branes to wrap the sphere directions and fill the $3 + 1$ field theory directions. Then, the embedding is described by a curve $x_4(u)$ in the cigar geometry, with boundary conditions fixing the position of the probe branes as $u \to \infty$.

In this chapter, we consider only the antipodal case, in which the ends of the probe branes are held at opposite sides of the x_4 circle. The minimum energy configuration with these boundary conditions is that in which the probe branes extend down the cigar at constant angle x_4, meeting at $u = 1$. Going to the radial coordinate z defined by $u^3 = 1 + z^2$, and expanding the action (6.2) for small gauge fields around the antipodal embedding gives the model we consider [119]:

$$S = -\kappa \int d^4x dz \, \mathrm{tr} \left[\frac{1}{2} h(z) \mathcal{F}_{\mu\nu}^2 + k(z) \mathcal{F}_{\mu z}^2 \right] + \frac{N_c}{24\pi^2} \int_{M_5} \mathrm{tr} \left(\mathcal{A} \mathcal{F}^2 - \frac{i}{2} \mathcal{A}^3 \mathcal{F} - \frac{1}{10} \mathcal{A}^5 \right), \tag{6.3}$$

where $\kappa = \lambda N_c/(216\pi^3)$, $h(z) = (1+z^2)^{-1/3}$ and $k(z) = 1+z^2$. $\mathcal{A}$ is a $U(N_f)$ gauge field with field strength $\mathcal{F} = d\mathcal{A} + i\mathcal{A} \wedge \mathcal{A}$. In this paper, we focus on the case $N_f = 2$. We split the gauge field into $SU(2)$ and $U(1)$ parts as $\mathcal{A} = A + \frac{1}{2}\mathbb{1}_2 \hat{A}$.[5]

The competing forces that determine the size of the soliton are evident in the effective action (6.3). First, the gravitational potential of the curved background will work to localize the soliton near the tip of the cigar, at $z = 0$. This will be counterbalanced by the repulsive potential due to the coupling between the $U(1)$ part of the gauge field and the instanton charge in the Chern-Simons term. At large λ, the effect of the Chern-Simons term is suppressed, and the result is a small instanton, which was previously approximated by the flat-space $SO(4)$ symmetric BPST instanton. As discussed in [33], this approach fails to properly describe several aspects of the baryon. Due to the curved background, the actual solution will only be invariant under $SO(3)$ rotations in the field theory directions. This distinction is especially important if we wish to use this model away from the strict large λ limit, as in that case, the soliton can become large such that the effects of the curved background are important for more than just the asymptotics of the solution.

The most general field configuration invariant under combined $SO(3)$ rotations and $SU(2)$ gauge transformations may be written as [133, 134][6]

$$\begin{aligned} A_j^a &= \frac{\phi_2 + 1}{r^2} \epsilon_{jak} x_k + \frac{\phi_1}{r^3} [\delta_{ja} r^2 - x_j x_a] + A_r \frac{x_j x_a}{r^2}, \\ A_z^a &= A_z \frac{x^a}{r}, \quad \hat{A}_0 = \hat{s}. \end{aligned} \tag{6.4}$$

where each of the fields are functions of the boundary radial coordinate $r^2 = x^a x^a$ and the holographic radial coordinate z. The ranges of these coordinates are $0 < r < \infty$ and $-\infty < z < \infty$. With these definitions, there is a residual gauge symmetry under which A_μ transforms as a $U(1)$ gauge

[5] We define the $SU(2)$ generators to satisfy $[\tau^a, \tau^b] = i\varepsilon^{abc}\tau^c$.

[6] This ansatz has also been used in the study of holographic QCD in a phenomenological model [122–124] and was applied to the Sakai-Sugimoto model in [33].

field in the $r-z$ plane and $\phi = \phi_1 + i\phi_2$ transforms as a complex scalar field with charge (-1), so that $D_\mu \phi = \partial_\mu \phi - iA_\mu \phi$.

The free energy of the system is given by the Euclidean action evaluated on the solution. Since we work at zero temperature and consider only static solutions, the mass-energy equals the free energy, and we only pick up a minus sign from the analytic continuation. Then, in terms of the above ansatz, the mass of the system is written as

$$M = M_{YM} + M_{CS}, \tag{6.5}$$

where $\int dtM = -S$,

$$\begin{aligned} M_{YM} = 4\pi\kappa \int drdz \ \Big[& h(z)|D_r\phi|^2 + k(z)|D_z\phi|^2 + \frac{1}{4}r^2 k(z) F_{\mu\nu}^2 \\ & + \frac{1}{2r^2} h(z)(1-|\phi|^2)^2 - \frac{1}{2} r^2 \left(h(z)(\partial_r \hat{s})^2 + k(z)(\partial_z \hat{s})^2 \right) \Big] \end{aligned} \tag{6.6}$$

and

$$M_{CS} = -2\pi\kappa\gamma \int drdz \, \hat{s} \, \epsilon^{\mu\nu} \left[\partial_\mu(-i\phi^* D_\nu \phi + h.c.) + F_{\mu\nu} \right], \tag{6.7}$$

with $\gamma = N_c/(16\pi^2\kappa) = 27\pi/(2\lambda)$ and $F_{\mu\nu} = \partial_\mu A_\nu - \partial_\nu A_\mu$. For the classical solution, γ is the only parameter in the system. It controls the relative strength of the Chern-Simons term; a larger γ will increase the size of the soliton.

The equations of motion that follow from extremizing the mass-energy are given by

$$\begin{aligned} 0 &= D_r\left(h(z) D_r \phi\right) + D_z\left(k(z) D_z \phi\right) + \frac{h(z)}{r^2}\phi(1-|\phi|^2) + i\gamma\epsilon^{\mu\nu}\partial_\mu \hat{s} D_\nu \phi, \\ 0 &= \partial_r\left(r^2 k(z) F_{rz}\right) - k(z)\left(i\phi^* D_z \phi + h.c.\right) - \gamma\epsilon^{rz}\partial_r \hat{s}(1-|\phi|^2), \\ 0 &= \partial_z\left(r^2 k(z) F_{zr}\right) - h(z)\left(i\phi^* D_r \phi + h.c.\right) - \gamma\epsilon^{zr}\partial_z \hat{s}(1-|\phi|^2), \\ 0 &= \partial_r\left(h(z) r^2 \partial_r \hat{s}\right) + \partial_z\left(k(z) r^2 \partial_z \hat{s}\right) - \frac{\gamma}{2}\epsilon^{\mu\nu}\left[\partial_\mu(-i\phi^* D_\nu \phi + h.c) + F_{\mu\nu}\right]. \end{aligned} \tag{6.8}$$

The baryon number is given by the instanton number of the non-Abelian part of the gauge field,

$$\begin{aligned} N_B &= \frac{1}{8\pi^2}\int d^4x \,\mathrm{tr}\, F\wedge F \\ &= \frac{1}{4\pi}\int drdz\,\epsilon^{\mu\nu}\left[\partial_\mu(-i\phi^* D_\nu\phi + h.c.) + F_{\mu\nu}\right] \\ &= \frac{1}{4\pi}\int drdz\,(\partial_r q_r + \partial_z q_z), \end{aligned} \tag{6.9}$$

where F is the field strength of the $SU(2)$ gauge field A and

$$q_r = (-i\phi^* D_z\phi + h.c.) + 2A_z, \quad q_z = (i\phi^* D_r\phi + h.c.) - 2A_r. \tag{6.10}$$

Since the expression is a total derivative, the boundary conditions on our $SU(2)$ gauge field will set the baryon charge. We study configurations with $N_B = 1$.

6.3 Numerical setup and boundary conditions

In this section we describe our setup, including our boundary conditions, gauge fixing, and details about the numerical procedure we use.

6.3.1 Gauge fixing

There is a residual $U(1)$ gauge freedom in the above ansatz, and we choose to use the Lorentz gauge $\chi \equiv \partial_\mu A_\mu = 0$. Our gauge fixing is achieved by adding a gauge fixing term to the equations of motion, analogous to the Einstein-DeTurck method developed in [135]. Alternatively, one can view this procedure as adding a gauge fixing term to the action, and working in the Feynman gauge.

As a result one obtains modified equations of motion in which the principal part of the equations is simply the standard elliptic operator $\partial_r^2 + \partial_z^2$. Once a solution is obtained, one has to make sure it is also a solution to the original, unmodified equations, i.e that $\chi = 0$. This has to be checked numerically, but can be expected to be satisfied since χ is a harmonic function, so with suitably chosen boundary conditions (for example such that $\chi = 0$ on the boundaries of the integration domain) uniqueness of the solution to the Laplace equation guarantees that $\chi = 0$. For the solutions presented here, the gauge condition is well satisfied as the L^2 norm of χ, normalized by the number of grid points N, satisfies $|\chi|/N < 10^{-5}$.

6.3.2 Ansatz and boundary conditions

For small γ, the soliton solution is well localized near the origin $(r,z) = (0,0)$. For small z, $k(z) \sim h(z) \sim 1$ and the $SU(2)$ part of the action reduces to that of the Witten model [133] for instantons. Then, in this regime, we expect the solution to possess an approximate $SO(4)$ symmetry, and thus we find it convenient to use the spherical coordinates

$$R = \sqrt{r^2 + z^2}, \quad \theta = \arctan(r/z) \tag{6.11}$$

for our numerical calculation. The inverse transformation is $r = R\sin\theta, \quad z = R\cos\theta$. One can show that by restricting the ansatz (6.4) to $SO(4)$ symmetry,[7] the solution can be written in terms of two spherically symmetric functions $f(R)$ and $g(R)$ as

$$\phi_1 = -rzf(R), \quad \phi_2 = r^2 f(R) - 1, \quad A_r = -zf(R), \quad A_z = rf(R), \quad \hat{s} = g(R). \tag{6.12}$$

In this parametrization, the BPST instanton is given by

$$f(R) = \frac{2}{\rho^2 + R^2}, \quad g(R) = 0, \tag{6.13}$$

where ρ determines the size of the energy distribution. The non-trivial winding of the instanton is built into the expressions in (6.12) through the appropriate factors of r and z and the factor of 2 in the numerator of $f(R)$ fixes the winding number to be $N_B = 1$. The BPST solution has a scaling symmetry in that it admits solutions of arbitrary scale ρ.

The factors of $k(z)$ and $h(z)$ in the Sakai-Sugimoto model break the $SO(4)$ symmetry. This has two effects on the $SO(4)$ ansatz. First, the functions ϕ_1, ϕ_2, A_r, and A_z will not be related to each other through the common function $f(R)$. Second, the functions appearing in the ansatz must be promoted to functions of both the radial coordinate R and the angle θ. These considerations motivate our reduced ansatz as

$$\begin{aligned} \phi_1 &= -\left(\frac{R^2 \sin\theta\cos\theta}{1+R^2}\right)\psi_1(R,\theta), \quad \phi_2 = \left(\frac{R^2\sin^2\theta}{1+R^2}\right)\psi_2(R,\theta) - 1, \\ A_r &= -\left(\frac{R\cos\theta}{1+R^2}\right)a_r(R,\theta), \quad A_z = \left(\frac{R\sin\theta}{1+R^2}\right)a_z(R,\theta), \quad \hat{s} = \frac{s(R,\theta)}{R\sin\theta}. \end{aligned} \tag{6.14}$$

[7] This assumption would be valid if k and h were spherically symmetric. The Chern-Simons term does not break the $SO(4)$ symmetry.

In each of the non-Abelian gauge field functions we include a factor of $(1+R^2)^{-1}$ such that we may use Dirichlet boundary conditions at $R=\infty$ to fix the baryon number. We rescale s by a factor of $r^{-1}=(R\sin\theta)^{-1}$ in order to have better control over the behaviour of the gauge field near the $r=0$ boundary. We numerically solve for the five functions $\{\psi_1,\psi_2,a_r,a_z,s\}$ on the domain $(0\le R<\infty, 0\le\theta\le\pi/2)$ corresponding to $(0\le r<\infty, 0\le z<\infty)$. In practice, we use a finite cutoff at $R=R_\infty$, chosen such that the physical data extracted from the solution does not depend on it. The symmetries of the solution around $z=0$ are used to extend it to $(-\infty<z\le 0)$.

In terms of the coordinates (R,θ), the baryon charge becomes

$$N_B=\frac{1}{4\pi}\int dRd\theta\,(\partial_R q_R+\partial_\theta q_\theta), \tag{6.15}$$

where we have defined

$$q_R=R(\sin\theta q_r+\cos\theta q_z), \quad q_\theta=\cos\theta q_r-\sin\theta q_z. \tag{6.16}$$

The baryon number is given by the boundary integrals

$$N_B=\frac{1}{4\pi}\left(\int_0^\infty dR\,q_\theta\Big|_{\theta=0}+\int_0^\pi d\theta\,q_R\Big|_{R=\infty}+\int_\infty^0 dR\,q_\theta\Big|_{\theta=\pi}+\int_\pi^0 d\theta\,q_R\Big|_{R=0}\right). \tag{6.17}$$

Plugging our ansatz into q_R and q_θ and evaluating on the boundaries shows that the only contribution to the winding is from the boundary at $R=\infty$. Thus, the baryon number reduces to

$$N_B=\frac{1}{2\pi}\int_0^{\pi/2} d\theta\,q_R\Big|_{R=\infty}, \tag{6.18}$$

and we use boundary conditions at the cutoff R_∞ to impose that $N_B=1$.

The boundary conditions we use are as follows. At $\theta=\pi/2$ (which maps back to $z=0$), we have Neumann conditions on all the fields, as the odd/even characteristics of the functions about $z=0$ are built into the ansatz (6.14). At this boundary $\chi=0$ implies $\partial_\theta a_z=0$ so that this boundary condition satisfies the gauge choice. To obtain boundary conditions at $\theta=0$ $(r=0)$, we expand the equations of motion for small θ. Satisfying these order by order in θ gives a set of conditions on the fields. A subset of these conditions that results in a convergent solution is given by[8]

$$\theta = 0: \quad \partial_\theta \psi_1 = 0, \quad \partial_\theta \psi_2 = 0, \quad a_r = \psi_1, \quad \partial_\theta a_z = 0, \quad s = 0. \tag{6.19}$$

The gauge condition at $\theta = 0$ can be shown to be satisfied on a solution given these boundary conditions. At the origin $R = 0$, a similar procedure yields

$$R = 0: \quad \partial_R \psi_1 = 0, \quad \partial_R \psi_2 = 0, \quad \partial_R a_r = 0, \quad \partial_R a_z = 0, \quad s = 0. \tag{6.20}$$

We do not explicitly satisfy the gauge condition at $R = 0$.[9] At the cutoff R_∞, the boundary conditions are determined by behaviour of the gauge field $\hat{A}_0$ and the winding number $N_B = 1$. As discussed below, in section 6.4.2, the field theory density of baryon charge $\rho_B(r)$ (defined below) is proportional to the coefficient of the z^{-1} falloff of the Abelian gauge field $\hat{A}_0$, at large z. In order to reliably calculate $\rho_B(r)$, we therefore impose that s falls off as z^{-1} by using the boundary condition $s = -z\partial_z s$, suitably translated into (R, θ) coordinates, at the cutoff R_∞. Since we rescaled the $SU(2)$ gauge fields by $(1 + R^2)^{-1}$, we are left with Dirichlet conditions on the other functions, giving

$$R = R_\infty: \quad \psi_1 = \psi_2 = a_r = a_z = 2, \quad s = -R\cos^2\theta\, \partial_R s + \sin\theta\cos\theta\, \partial_\theta s. \tag{6.21}$$

Given the asymptotic boundary behaviour of the fields, the gauge choice is satisfied for large R_∞. With these large R conditions, we have $q_R = 4$ and so $N_B = 1$, as desired.

6.3.3 Numerical procedure

We solve the equations of motion by using spectral methods on a Chebyshev grid, using Newton's method to solve the resulting non-linear algebraic equations.[10] For the results presented here, we take the number of grid points to be $(N_R, N_\theta) = (50, 25)$. We introduce a cutoff at large $R = R_\infty$. For a large enough cutoff we can reliably read off the z^{-1} falloff in order to obtain information about the baryon charge density. However, if the cutoff

[8] In practice, we use the boundary condition $\partial_\theta a_z = \frac{1}{2} R\, \partial_\theta \partial_R \psi_1$ during the solving procedure, as we found empirically that this results in a more stable Newton iteration. Once the numerical procedure converges, the solution satisfies the boundary conditions given here.

[9] We check that the gauge condition $\chi = 0$ is numerically satisfied on our solutions across the domain. See section 6.3.1.

[10] See appendix A.3 for a description of this procedure.

is too large, the total mass-energy of the solution becomes dependent on R_∞. In practice, we take R_∞ to vary with γ, such that we can compute both the mass-energy and the baryon charge density with confidence across most of our domain. We find that while the charge density can be computed to good accuracy for large γ, the mass-energy becomes unreliable for $\gamma \gtrsim 70$. To generate a solution, we continue the Newton method until the residuals reach a very small value ($\sim 10^{-9}$). For generic values of γ, we can solve for the configuration from a trivial initial guess (zero for all the fields), while for very large or very small γ, we solve by using a nearby solution as the initial guess. Finally, the convergence of our solutions is demonstrated in Figure 6.1.

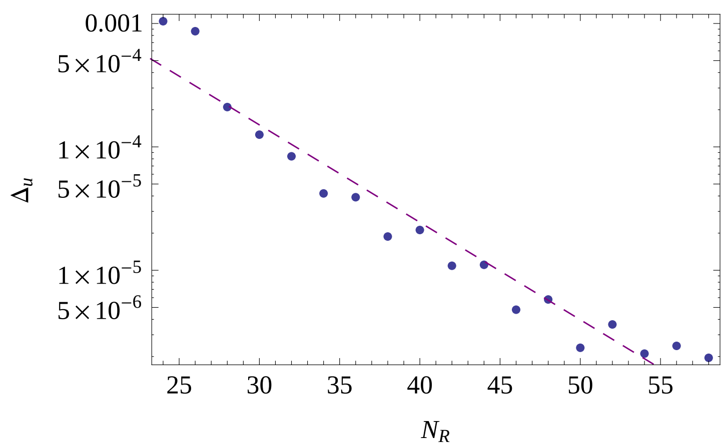

Figure 6.1: The convergence of the value $\Delta_u = |u(N_R) - u(N_R - 2)|/N_R N_\theta$, where $u(N_R)$ denotes the solution for the five fields $\{\psi_1, \psi_2, a_r, a_z, s\}$ on the grid with N_R points in the R direction and $N_\theta = N_R/2$ points in the θ direction. These runs are for $\gamma = 10$ and $R_\infty = 60$. The dashed line is the best linear fit, showing the exponential convergence $\Delta_u \propto e^{-0.18N}$.

6.4 Solutions

We focus on two observables of the baryon in the Sakai-Sugimoto model: the mass-energy and the baryon charge density. We examine each of these in turn.

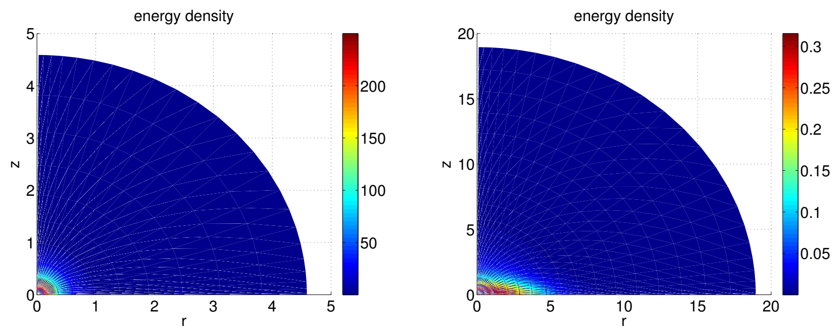

(a) $\gamma = 0.2$.

(b) $\gamma = 10$.

Figure 6.2: The energy density $\rho_E(r, z)$ in the (r, z) plane. For small γ, the solution appears approximately spherically symmetric. As the coupling γ increases, the soliton expands and deforms, becoming elongated along $z = 0$.

6.4.1 The mass-energy

The energy distribution of the soliton tells us how the structure is deformed as we increase the repulsion of the instanton charges by tuning the coupling γ. Writing the mass-energy as[11]

$$M = \frac{1}{4\pi} \int d^4x \; \rho_E(r, z), \tag{6.22}$$

we plot the energy density $\rho_E(r, z)$ of the soliton in Figures 6.2 and 6.3. For small γ, the core of the soliton appears spherically symmetric in the (r, z) plane. A closer inspection reveals a skewed tail with a slower falloff of energy density in the z direction; compare Figures 6.2a and 6.3a. As we increase γ, the core of the soliton expands and deforms, smearing along the z-axis.

In [13], the mass of the baryon was approximated as the energy of a D4 brane wrapping the S^4, giving $M_0 = 8\pi^2\kappa$. The mass of the wrapped D4 brane coincides with the mass of a point-like $SO(4)$ instanton at $\gamma = 0$. By allowing a finite size spherical instanton, [119] computed a correction to this, finding

$$M_{SO(4)} = M_0 + \sqrt{\frac{2}{15}} N_c. \tag{6.23}$$

In Figure 6.4, we plot the total mass-energy, normalized by M_0, of the soliton found here using the more general $SO(3)$ ansatz. As γ decreases and the

[11]We define $\rho_E(r, z)/4\pi$ as the integrand of equation (6.5) multiplied by a suitable Jacobian factor.

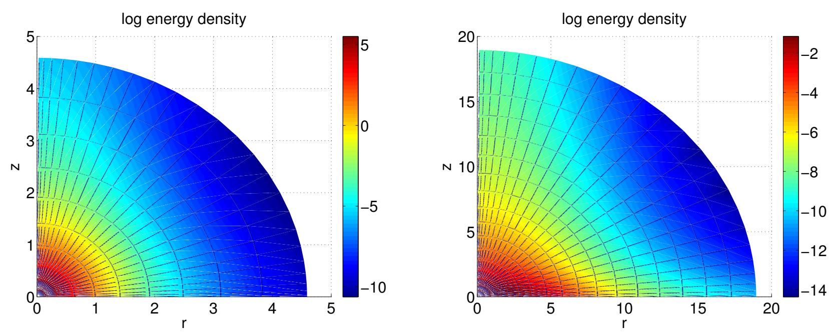

(a) $\gamma = 0.2$.

(b) $\gamma = 10$.

Figure 6.3: The logarithm of the energy density $\rho_E(r,z)$ in the (r,z) plane, on the same domain as the corresponding plots in Figure 6.2. A large portion of the energy away from the soliton core is contained in the tail at large holographic radial coordinate z and small field theory coordinate r.

soliton shrinks, the effect of the curved background becomes less important and the energy approaches that of the point-like spherical instanton. As γ increases and the soliton becomes more deformed, the energy of the configuration also increases. For $\gamma > 10$, we notice that the mass-energy appears to be controlled by a power law. The best fit in this region gives $M \propto \gamma^{0.53}$.

By fitting the Sakai-Sugimoto model to the experimental values for the ρ meson mass and the pion decay constant, one can fix both the parameter κ and the energy scale in the field theory. In [127], this procedure yields $\kappa = 0.00745$ and an energy scale such that 1 in the dimensionless units we have been using corresponds to 949 MeV. With $N_c = 3$, this gives $\gamma = 2.55$. We can compare our numerical results for the baryon mass to those of the $SO(4)$ approximation for these values of the parameters. We find

$$\begin{aligned} M_{SO(4)} &\simeq 1.60 \text{ GeV}, \\ M_{SO(3)} &\simeq 1.19 \text{ GeV}. \end{aligned} \tag{6.24}$$

There is a large difference in the results of the two approaches. Interestingly, the $SO(3)$ result is a much better approximation of the true mass of the nucleons.

6.4.2 The baryon charge

The baryon charge in the field theory is related to the instanton number density $\frac{1}{8\pi^2}\mathrm{tr}\, F \wedge F$ in the bulk. In Figures 6.5 and 6.6 we plot the instanton

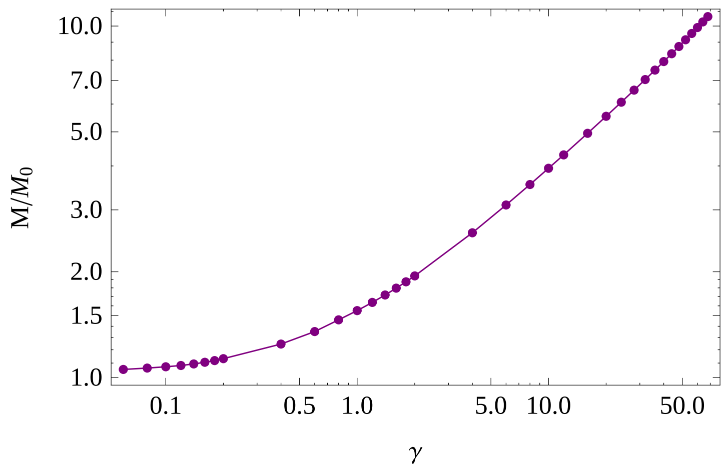

Figure 6.4: The total mass of the soliton as a function of γ, normalized by the mass $M_0 = 8\pi^2\kappa$ of a D4 brane wrapping the sphere directions (equivalently the mass of a point-like $SO(4)$ instanton at $\gamma = 0$ in the effective theory). As γ decreases, the mass of the numerical solution approaches that of the point-like instanton. For $\gamma > 10$, our results can be approximated by the relation $M \propto \gamma^{0.53}$.

charge density for two representative solutions. The result closely matches the energy density of the soliton.

The baryon charge density can be found from the baryon number current, as defined for example in [127]:

$$J_B^\mu = -\frac{2}{N_c}\kappa\left(k(z)\hat{F}^{\mu z}\right)\Big|_{z=-\infty}^{z=\infty}. \tag{6.25}$$

Writing the Abelian gauge field near the boundary as

$$\hat{A}_0 = \frac{\hat{A}_0^{(1)}(r)}{z} + \ldots, \tag{6.26}$$

where $\ldots$ denotes terms at higher order in $1/z$, we find that the baryon density is

$$\rho_B(r) = J_B^0(r) = \frac{\hat{A}_0^{(1)}(r)}{8\pi^2\gamma}. \tag{6.27}$$

In terms of the density, the total baryon charge is

$$N_B = \int_0^\infty dr\, 4\pi r^2\, \rho_B(r). \tag{6.28}$$

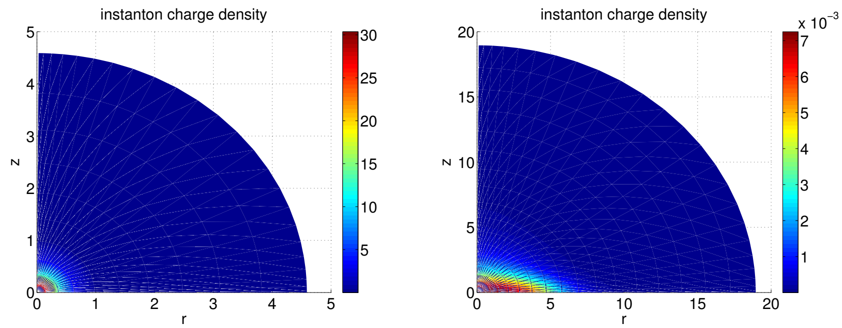

(a) $\gamma = 0.2$. (b) $\gamma = 10$.

Figure 6.5: The instanton number density $\frac{1}{8\pi^2}\mathrm{tr}\, F \wedge F$ in the (r, z) plane. The distribution of the instanton charge closely mimics the distribution of energy density, as shown in Figures 6.2 and 6.3.

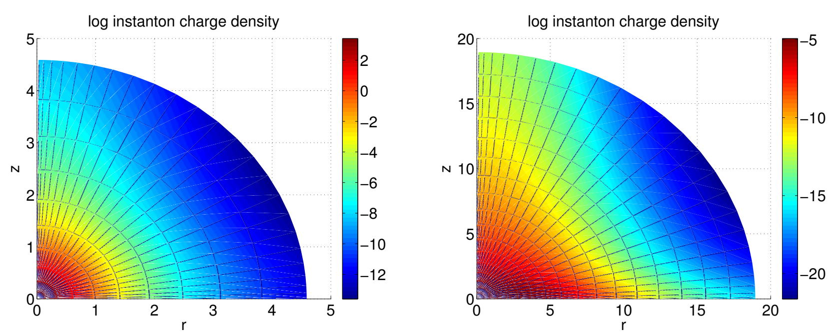

(a) $\gamma = 0.2$. (b) $\gamma = 10$.

Figure 6.6: The logarithm of the instanton number density $\frac{1}{8\pi^2}\mathrm{tr}\, F \wedge F$ in the (r, z) plane, on the same domain as the corresponding plots in Figure 6.5.

We fit our numerical solutions to the functional form in equation (6.26) and read off the coefficient $\hat{A}_0^{(1)}(r)$ in order to find $\rho_B(r)$. This fit is only robust up to a value of r that depends on the coupling γ: $r = \bar{r}(\gamma)$. As demonstrated in [33], the charge density $\rho_B(r)$ decays as $1/r^9$. Thus the field $\hat{A}_0$ is decaying much faster in the field theory r direction than the holographic radial z direction. Since we solve in the coordinate $R = (r^2 + z^2)^{1/2}$, and choose a large cutoff R_∞ such that the z falloff is reliable, we might expect the fit to break down at some point, after $\rho_B(r)$ has decayed to a very small value. Numerically, we determine $\bar{r}(\gamma)$ as the point at which the error in the fit reaches ten times the error in the fit at $r = 0$.

In Figure 6.7, we plot the baryon charge $\rho_B(r)$ up to the cutoff $\bar{r}(\gamma)$ for various values of γ. As γ increases, the baryon density at the origin $\rho_B(0)$ decreases and the charge moves toward the tail of the distribution. In the log-log plot, the $1/r^9$ falloff of the charge density can clearly be seen. Figure 6.8 shows the behaviour of the baryon charge density across our entire range of γ.

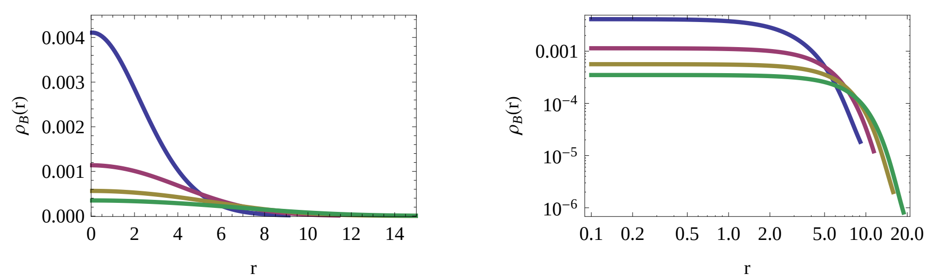

Figure 6.7: *Left*: The charge density $\rho_B(r)$ for $\gamma = 4, 12, 20, 28$, from top to bottom. *Right*: The same data on a log-log axis. As γ increases, the charge density becomes less peaked near the origin. The $1/r^9$ falloff of $\rho_B(r)$ behaviour can be seen in the tail of the charge distributions.

As a check of our solution, we can compute N_B by both formulas (6.9) and (6.28). We find that, across the range of γ and using both formulas, $N_B = 1$ to good precision.

Lastly, with the charge density $\rho_B(r)$, we can compute the baryon charge radius

$$\langle r^2 \rangle = \int_0^\infty r^2 \left(4\pi r^2 \rho_B(r)\right) dr. \tag{6.29}$$

To integrate past the cutoff $\bar{r}(\gamma)$, we approximate the tail of the distribution as $\rho_B(r;\gamma) \sim c(\gamma)/r^9$, where $c(\gamma)$ is approximated from the value of the

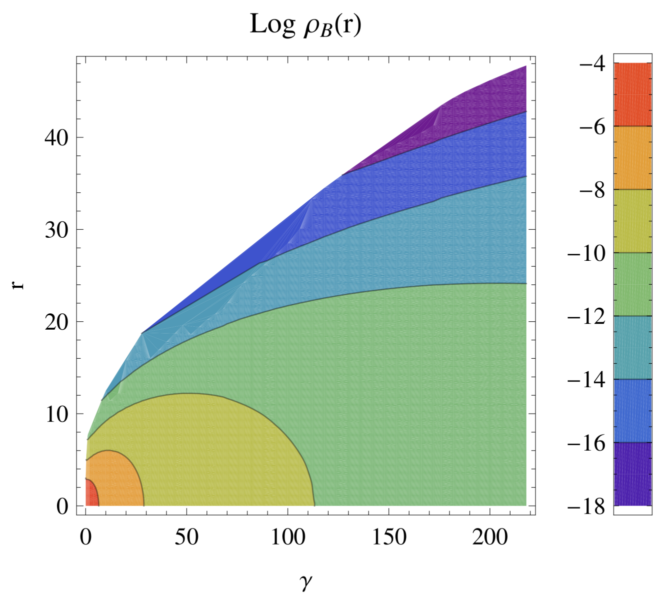

Figure 6.8: The charge density $\rho_B(r)$ for varying γ.

density at the integration cutoff. The baryon charge radius is plotted in Figure 6.9. For $\gamma > 35$, the relation appears to obey a power law, with best fit given by $\langle r^2 \rangle \propto \gamma^{0.93}$.

As above, it is interesting to compare the result to that obtained from the $SO(4)$ approximation, evaluated at the parameters defined by the fit to meson physics. The result is[12]

$$\begin{aligned} \langle r^2 \rangle^{1/2}_{SO(4)} &\simeq 0.785 \text{ fm}, \\ \langle r^2 \rangle^{1/2}_{SO(3)} &\simeq 0.90 \text{ fm}. \end{aligned} \tag{6.30}$$

In this model, the baryon charge radius equals the electric charge radius of the proton [127]. The result from our numerics is very close to the experimental value for the electric charge radius of the proton, which has been measured to be in the range 0.84 fm − 0.88 fm.

[12]We compare to the result from the classical analysis of the $SO(4)$ baryon, given in equation (3.11) of [127].

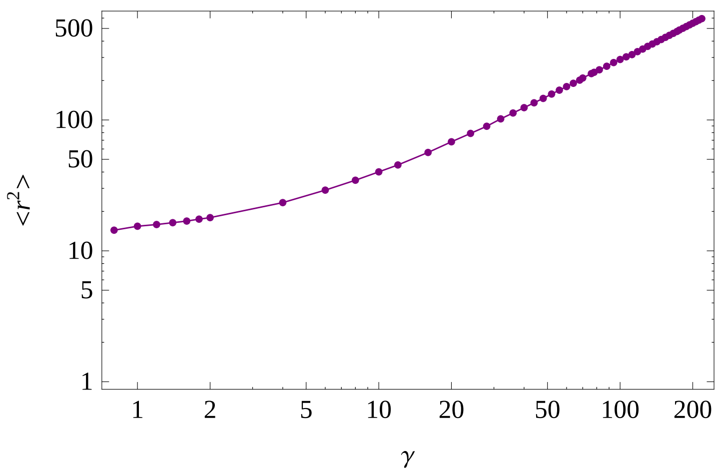

Figure 6.9: The baryon charge radius $\langle r^2 \rangle = \int r^2 \left(4\pi r^2 \rho_B(r)\right) dr$ as a function of γ. For $\gamma > 35$, the relation can be approximated by $\langle r^2 \rangle \propto \gamma^{0.93}$.

6.5 Conclusion

We have studied properties of baryons in a holographic model of QCD related to the Sakai-Sugimoto model by simplifying the Born-Infeld part of the D8-brane action to a 5D Yang-Mills plus Chen-Simons action for the gauge fields in the non-compact directions. By dropping the assumption of $SO(4)$ symmetry and finding direct solutions to the bulk field equations for the gauge field, we have found that various properties of the baryons in the holographic QCD model change significantly. In particular, the baryon mass gives substantially better agreement with measured values. There are several interesting directions for future work.

Within the present model, it would be interesting to calculate other observables such as the form-factors associated with the isospin currents (associated with the $SU(2)$ flavour symmetry) and compare these to results calculated using the $SO(4)$ symmetric ansatz [127]. It would also be interesting to consider interactions between two baryons. This requires a less-symmetric ansatz, but the numerics should still be feasible. Again, it would be interesting to compare with previous results calculated assuming flat-space instanton configurations [136]. For higher baryon charge, it should be feasible to consider the question of nuclear masses as a function of baryon number, at least within the space of $SO(3)$-symmetric configurations. The actual ground states for higher baryon number may not be so symmetric however. In addition, it would be interesting to investigate solutions with a finite baryon charge density (e.g. at finite baryon chemical potential). Such configurations were considered with various simplifying assumptions in [42, 50, 52, 53, 137, 138]. As shown in [53], these are necessarily inhomogeneous in the field theory directions, so a numerical approach similar to the one used in this paper is likely necessary to investigate detailed properties of the ground state at various densities.

Finally, it is interesting to investigate effects of replacing the Yang-Mills action used here with the full D8-brane Born-Infeld action. This is incompletely known, but one could work for example with the Abelian Born-Infeld action promoted to a non-Abelian action via the symmetrized trace prescription that has been shown to be correct for the F^4 terms. While the equations in this case will be significantly more complicated, they should pose no serious obstacle for the numerical approach that we are using. An interesting difference between the Born-Infeld and Maxwell actions for Abelian gauge fields is that the Maxwell action associates an infinite energy to point charges, while this energy is finite in the Born-Infeld case. Thus, we might expect that the tendency for the instantons to spread out is somewhat less with the Born-Infeld action. In this case, we may expect a somewhat smaller, less massive baryon. Thus, the baryon mass in the model using the Born-Infeld action may be even closer to the experimental value than we have found here.

Chapter 7

Conclusion

7.1 Summary

In this thesis, we applied the holographic correspondence to the study of various strongly coupled phenomena. The projects comprising the thesis fell into three domains of applicability: *i.* General holographic field theories; *ii.* Holographic condensed matter, and; *iii.* Holographic QCD. Technically, this work involved posing and solving classical field equations in curved backgrounds (with and without backreaction). To facilitate these studies, we made extensive use of numerical methods, overcoming some technical obstacles which may have discouraged previous researchers.

In chapter 2, we studied strongly coupled field theories with the minimal structure of a conserved charge, focussing in particular on the relationship between charge density and chemical potential at large density. At finite charge density, the typical lattice field theory approach to strong coupling dynamics fails, rendering holography as the most convenient and reliable calculational method. After some general thermodynamic considerations, we applied the holographic approach to study a wide range of model field theories, including those built via explicit string theory constructions and those developed through a phenomenological approach. We enumerated our results across these theories, providing a useful guide to a subset of the behaviours available in holographic theories.

In chapters 3 and 4, we applied the holographic correspondence to the experimentally observed phenomenon of the spontaneous formation of striped phases. We studied a phenomenological model dual to a strongly coupled field theory that undergoes a spontaneous transition to a phase with striped order as we lower the temperature. Building on previous work that showed a perturbative instability towards a striped phase, we applied numerical relativity techniques in order to find the full nonlinear striped solutions across the parameter range. The geometries we found exhibited novel characteristics including a charge density wave, a momentum density wave, and a modulated black brane horizon that tends to pinch off as we lower the temperature. Given the solutions, we constructed the phase diagram of the system, showing that the field theory undergoes a second order phase transition to the striped phase.

In chapter 5, we used holography to study the colour superconductivity phase of QCD, which is expected to exist at large density. To facilitate this, we constructed a phenomenological model of QCD, designed to mimic certain aspects of the phase diagram. Using results from previous studies, we included in our holographic model the ingredients necessary for three QCD phases: a confining phase, a deconfining phase, and a colour superconductivity phase. By analyzing the thermodynamics of the different phases, we constructed the phase diagram at all values of temperature and chemical potential, showing that, indeed, our model qualitatively resembled the expected phase diagram of QCD.

Finally, in chapter 6, we applied numerical techniques to the construction of the baryon in the well-known Sakai-Sugimoto model of large-N_c QCD. As reviewed above, the gravity dual of the field theory baryon in this model is a gauge field configuration on the probe D8 branes with non-trivial topological charge. Previous studies of the baryon in this model assumed a spherical symmetry for this gauge field configuration, an assumption which was shown to produce results that failed certain model-independent tests of baryons. We relaxed this spherical symmetry, formulating and solving the full nonlinear partial differential equations using numerical techniques in order to find an oblate instanton, the true minimum energy configuration corresponding to the baryon. We studied the dependence of the mass and baryon charge of the baryon on a parameter γ, which determines the baryon self-repulsion. At the value of γ dictated by the best fit of parameters to the meson spectrum of QCD, our solution was found to give significantly more realistic values for the mass and charge radius of the proton than previous studies.

7.2 Future directions

In this section, we briefly describe some of the most promising and interesting studies that would comprise extensions to the work presented here and that would depend on the numerical techniques used in this thesis. Some of these and more have already been discussed in the bulk of the thesis.

7.2.1 Inhomogeneous holography and condensed matter

There are many possible directions to follow up on the holographic stripes project, discussed in chapters 3 and 4. Firstly, we offer advice for undertaking future projects in this area. As opposed to using the numerical method outlined in those chapters (using a conformal ansatz, with finite difference techniques), it is the thesis author's recommendation that a more efficient approach would be to use the deTurck method [135] combined with pseudospectral differentiation. This method has been successfully applied to similar problems in, for example, [88, 101, 102]. The deTurck approach avoids the gauge fixing issues that we encountered, described in section B.2.3 and, anecdotally, works very well for problems of this type. Furthermore, pseudospectral differentiation combined with the Newton's method, as described in appendix A.3, offers a compact algorithm with running times on a desktop computer that may be measured in minutes. This is in contrast to the Gauss-Seidel relaxation used in those chapters, which required hours of processing time on a parallel computer system for each solution.

A direct extension of the work described here involves the zero temperature state. The question of what happens to the stripes as we go to zero temperature was unresolved in our study, as our numerics broke down at very small temperatures. However, solutions of the black brane at finite temperature could direct the search for the zero temperature geometry. This is interesting both theoretically and in terms of experimental results. Theoretically, it has been demonstrated that the homogeneous Reissner-Nordstrom black brane has a non-zero entropy at zero temperature, implying that the dual field theory is in violation of the third law of thermodynamics. This is one of the original motivations that prompted the search for instabilities of the theory, leading to the discovery of these striped phases. An interesting question then is to find the true ground state of the charged black brane in particular holographic theories. Given these, one could make qualitative or, possibly, quantitative comparisons to the low temperature behaviour of experimental systems. In addition, it has been speculated that the ground state of QCD may also display lattice behaviour. If true, it would be very interesting if these holographic models displayed a similar behaviour.

Secondly, in order to again make connection to the condensed matter literature, it would be interesting to compute the optical conductivity in this model of holographic stripes. Such a project would be along the lines of the recent work by Horowitz, Santos, and Tong [87, 88], in which they introduced an inhomogeneity 'by hand', thereby breaking the translation invariance. This is important because in examples of homogeneous holographic field theories, the DC conductivity is always infinite. It has been pointed out that breaking the translation invariance will remove the infinite peak at zero frequency and widen it into a Drude peak, typical of condensed matter systems, and allowing the holographic theory to better model experimental materials.[1] The analysis required in such a study would present a new level of technical difficulty, as the conductivity computation would require the solving of a system of partial differential equations linearized around the numerical striped background solution. However, these results would be extremely interesting in the push to closer align holographic models with experimental phenomena.

An alternative direction would be to apply these techniques to find the geometries dual to translation-symmetry breaking phases in theories exhibiting hyperscaling violation [139, 140].[2] Systems with hyperscaling violation have been suggested to describe theories with a Fermi surface [141], making them interesting as models of condensed matter systems. Several recent studies have shown the existence of instabilities towards striped phases in models dual to field theories with this behaviour [142, 143]. As above, for striped phases, it would be useful to have examples of holographic theories that at least qualitatively mimic these experimental results.

A final interesting extension of the stripes program would be to allow translation symmetry breaking in both spatial field theory directions, resulting in a checkerboard-type field theory configuration. Checkerboards, or lattices, have shown up in condensed matter situations (see, for example, [144]) and it would be interesting to have a concrete theoretical model which realizes their formation.[3] Technically, this would require solving partial differential equations with dependence on three directions, increasing the scale of the problem. However, the techniques described above should render this problem tractable, even with relatively modest computational resources.

7.2.2 Baryons in holographic QCD

The application of numerical methods to the area of holographic QCD offers many interesting directions for future research. In particular, in the Sakai-Sugimoto model discussed in chapter 6 (or even other models of holographic QCD) there are many unresolved questions regarding the behaviour of baryons and how they interact.

[1] Indeed, [87, 88] did make comparisons between conductivity in their model and in the cuprates, finding a striking agreement for the power-law describing behaviour at mid-infrared frequencies.

[2] These theories posses a dynamical critical exponent z and a hyperscaling violating exponent θ, which alter the thermodynamics of the system. In particular, the scaling of entropy with temperature in such a theory is given by $S \sim T^{d-\theta/z}$. (In scale invariant theories without hyperscaling violation, $z = 1$ and $\theta = 0$.)

[3] A holographic example of such a situation was recently studied in [78].

As discussed in chapter 6, in the Sakai-Sugimoto model the gravity dual of a field theory baryon is an instanton configuration of the gauge fields on the probe flavour branes. In this model, the usual spherical instanton is deformed to an oblate spheroid, the shape of which is determined by a competition between the coupling γ (controlling the self-repulsion of the instanton), the background geometry, and the restriction towards spherical symmetry due to the Yang-Mills form of the action. Motivated by this, a first extension of this work, which would allow a better understanding of these holographic baryons and would be interesting more generally, would be to study the deformation of instantons governed by the standard Yang-Mills action. It is known that a spherical instanton minimizes the energy of this system; of particular interest in terms of holographic baryons would be the energy dependence of the state on the deformation of the configuration. Operationally, this could be studied by including Lagrange multiplier terms for the quadrupole moment of the instanton in the action. A technical difficulty in solving this numerically is the scaling symmetry of the spherical instanton: all sizes of spherical instantons possess the same total energy. Some care must then be taken in setting up the numerical problem such that there is a unique solution.[4]

In our study of baryons, the action, equation (6.3), was derived by a series expansion of the DBI action for the gauge fields on the probe flavour branes. This expansion is based on the assumption that the variation of the gauge fields is small on the order of the string scale. However, this assumption is not strictly satisfied at strong coupling in the model. In fact, in [13], it was shown that the characteristic size of the instanton in this model is on the order of the string scale, violating the original assumption. Then, in order to more precisely describe baryons in this model, it would be interesting to strip away this assumption and study the full DBI action governing the gauge fields on the brane. Technically, this is difficult, due to the non-Abelian nature of the gauge fields: a correct procedure for evaluating the trace over the gauge structure has not been established [145]. However, one may study simplifications of the DBI action that may more closely resemble the actual system of interest. One very simple way to do this would be to modify the structure of the $U(1)$ part of the action, from the standard Yang-Mills to the Born-Infeld type. Since the Born-Infeld action softens the infinities associated with point charges, resulting in a smaller repulsive force for two charges brought very close together, one would expect that this

[4]Some preliminary attempts by the thesis author to study the Yang-Mills instanton in this way were unsuccessful due to difficulties in setting up the numerical problem.

modification would allow the instanton in our model to relax somewhat to a smaller, less energetic configuration.[5] A second, more realistic approach would be to include more gauge field terms from the expansion of the DBI action. The form of this expansion is known up to fourth order [146, 147]. By including further terms in the expansion, one may be able to glean some indications of how the baryon configuration would be expected to change upon using the full DBI action. This type of project would only necessitate a minor modification of the numerical procedure used in our previous study and thus offers a tantalizing possibility.

The above two suggestions were related to better understanding the construction of the baryon in the Sakai-Sugimoto model. One could also extend the above work by studying further questions related to the baryon. A first interesting direction here would be to study configurations of higher baryon number; these would be holographic nuclei. A conceptually straightforward question along these lines would be to examine how the masses of the nuclei depend on the baryon number in this model. Given the fit of the model parameters to meson physics, it would be very interesting to evaluate the masses of the holographic nuclei and to make a comparison to observed results. As shown in chapter 6, this model provides a quantitatively realistic relationship between meson masses and the mass of the baryons; it would be interesting if the higher baryon number configurations also matched experimental results. In the field theory, a deuterium state (two baryons bound together) would have only a cylindrical symmetry. To find the holographic dual of this state would then require a three-dimensional code, increasing the numerical complexity of the problem.[6] However, as discussed above for holographic checkerboards, this should still be tractable with the numerical techniques used here.

Finally, given a three-dimensional solver and the construction of a cylindrically symmetric deuterium state, one could investigate the force between baryons. This problem has been studied in various approximations in holographic models, including under the assumption of $SO(4)$-symmetric instantons representing baryons [136]. By studying the deuterium state, one could

[5] Indeed, a preliminary investigation by the thesis author, using a Born-Infeld action for the $U(1)$ part of the gauge field, showed that the minimum energy solution was slightly smaller and less massive than the solution for the model with Yang-Mills $U(1)$ action.

[6] One simplification could be to look for holographic nuclei with the field theory $SO(3)$ symmetry of the single baryon. A preliminary study by the author within the ansatz of chapter 6 found a large negative binding energy for the two baryon configuration, indicating that this configuration, with the two baryons 'on top' of each other in the field theory, will certainly not be preferred.

precisely compute the dependence of the force between the baryons on the distance between them (by, for example, using again Lagrange multipliers for the quadrupole moment of the state). It would be interesting to compare the less-symmetric case to previous results in order to further understand interactions between holographic baryons.

7.3 Final remarks

The work presented in this thesis consists of several important examples of applied holography. While the research presented in chapters 2 and 5 provided interesting new results for holographic field theories in general and within a particular phenomenological model of holographic QCD, the main significance and contribution of this thesis comes from the application of numerical techniques to holographic situations with reduced symmetry. The striped phases work of chapters 3 and 4 represented the first black hole solutions of that kind[7] and was an important step in the progress of applying the holographic correspondence to find the full gravitational bulk (including the geometry) to systems with a broken translation symmetry. Meanwhile, the holographic baryons of chapter 6 were results of one of the first studies applying numerical techniques to this problem,[8] thus pushing the field into new territory. Both projects required dedicated efforts to overcome significant technical obstacles that may have discouraged other researchers from undertaking such work. Overall, these studies are part of a recent thrust, led by a subset of researchers in the field, towards combining numerical techniques (including those used in numerical relativity) with holography; examples of these works include [83, 87–89, 101, 102, 104, 148–151].[9]

This marriage of numerical and holographic techniques offers tremendous promise in terms of connecting the existing literature on holographic theories to experimentally observed strongly coupled systems. This includes both the theory that underlies our world (QCD) and those theories that describe the novel materials that will be the cornerstone of tomorrow's technological advances (condensed matter). It is the thesis author's expectation that the approaches used in this work and in related studies will become standard tools of practitioners in the field and will allow the study of new

[7] These were the first full solutions for planar black holes that spontaneously break translation symmetry.

[8] The study [132] appeared while the work on holographic baryons was being completed, while the earlier studies [122–124] used similar numerical techniques.

[9] Even more recently, some time-dependent holographic problems have been solved using numerics. See [152–154].

and more realistic classes of models. The holographic correspondence is the window which currently offers the most lucid view of strongly coupled phenomena and, as computational techniques progress, may ultimately provide a tractable and realistic description of those experimental states and situations which are currently beyond theoretical control.

Bibliography

[1] Nogueira, F. & Stang, J. B. Density versus chemical potential in holographic field theories. *Phys.Rev.* **D86**, 026001 (2012). `1111.2806`.

[2] Rozali, M., Smyth, D., Sorkin, E. & Stang, J. B. Holographic Stripes. *Phys.Rev.Lett.* **110**, 201603 (2013). `1211.5600`.

[3] Rozali, M., Smyth, D., Sorkin, E. & Stang, J. B. Striped order in AdS/CFT correspondence. *Phys.Rev.* **D87**, 126007 (2013). `1304.3130`.

[4] Basu, P., Nogueira, F., Rozali, M., Stang, J. B. & Van Raamsdonk, M. Towards A Holographic Model of Color Superconductivity. *New J.Phys.* **13**, 055001 (2011). `1101.4042`.

[5] Rozali, M., Stang, J. B. & van Raamsdonk, M. Holographic baryons from oblate instantons. *JHEP* **1402**, 044 (2014). `1309.7037`.

[6] Hanneke, D., Fogwell, S. & Gabrielse, G. New measurement of the electron magnetic moment and the fine structure constant. *Phys. Rev. Lett.* **100**, 120801 (2008).

[7] Maldacena, J. M. The large N limit of superconformal field theories and supergravity. *Adv. Theor. Math. Phys.* **2**, 231–252 (1998). `hep-th/9711200`.

[8] Gubser, S. S., Klebanov, I. R. & Polyakov, A. M. Gauge theory correlators from non-critical string theory. *Phys. Lett.* **B428**, 105–114 (1998). `hep-th/9802109`.

[9] Witten, E. Anti-de Sitter space and holography. *Adv. Theor. Math. Phys.* **2**, 253–291 (1998). `hep-th/9802150`.

[10] Kovtun, P., Son, D. & Starinets, A. Viscosity in strongly interacting quantum field theories from black hole physics. *Phys.Rev.Lett.* **94**, 111601 (2005). `hep-th/0405231`.

[11] Hartnoll, S. A., Herzog, C. P. & Horowitz, G. T. Holographic Superconductors. *JHEP* **12**, 015 (2008). `0810.1563`.

[12] Herzog, C. P., Kovtun, P. K. & Son, D. T. Holographic model of superfluidity. *Phys. Rev.* **D79**, 066002 (2009). `0809.4870`.

[13] Sakai, T. & Sugimoto, S. Low energy hadron physics in holographic QCD. *Prog.Theor.Phys.* **113**, 843–882 (2005). `hep-th/0412141`.

[14] Hartnoll, S. A. Horizons, holography and condensed matter (2011). `1106.4324`.

[15] Gubser, S. S. & Karch, A. From gauge-string duality to strong interactions: A Pedestrian's Guide. *Ann.Rev.Nucl.Part.Sci.* **59**, 145–168 (2009). `0901.0935`.

[16] D'Hoker, E. & Freedman, D. Z. Supersymmetric gauge theories and the AdS / CFT correspondence 3–158 (2002). `hep-th/0201253`.

[17] Maldacena, J. The gauge/gravity duality (2011). `1106.6073`.

[18] Hartnoll, S. A. Lectures on holographic methods for condensed matter physics. *Class. Quant. Grav.* **26**, 224002 (2009). `0903.3246`.

[19] Aharony, O., Gubser, S. S., Maldacena, J. M., Ooguri, H. & Oz, Y. Large N field theories, string theory and gravity. *Phys.Rept.* **323**, 183–386 (2000). `hep-th/9905111`.

[20] Polchinski, J. Introduction to Gauge/Gravity Duality 3–46 (2010). `1010.6134`.

[21] McGreevy, J. Holographic duality with a view toward many-body physics. *Adv. High Energy Phys.* **2010**, 723105 (2010). `0909.0518`.

[22] Weinberg, S. & Witten, E. Limits on massless particles. *Physics Letters B* **96**, 59–62 (1980).

[23] Susskind, L. The world as a hologram. *J.Math.Phys.* **36**, 6377–6396 (1995). `hep-th/9409089`.

[24] 't Hooft, G. Dimensional reduction in quantum gravity (1993). `gr-qc/9310026`.

[25] Bekenstein, J. D. Universal upper bound on the entropy-to-energy ratio for bounded systems. *Phys. Rev. D* **23**, 287–298 (1981).

[26] Hooft, G. A planar diagram theory for strong interactions. *Nuclear Physics B* **72**, 461–473 (1974).

[27] Ginsparg, P. H. Applied conformal field theory (1988). `hep-th/9108028`.

[28] de Haro, S., Solodukhin, S. N. & Skenderis, K. Holographic reconstruction of space-time and renormalization in the AdS / CFT correspondence. *Commun.Math.Phys.* **217**, 595–622 (2001). `hep-th/0002230`.

[29] Vojta, M. Lattice symmetry breaking in cuprate superconductors: stripes, nematics, and superconductivity. *Advances in Physics* **58**, 699–820 (2009).

[30] Donos, A. & Gauntlett, J. P. Holographic striped phases. *JHEP* **1108**, 140 (2011). `1106.2004`.

[31] Alford, M. G., Schmitt, A., Rajagopal, K. & Schfer, T. Color superconductivity in dense quark matter. *Rev.Mod.Phys.* **80**, 1455–1515 (2008). `0709.4635`.

[32] Witten, E. Anti-de Sitter space, thermal phase transition, and confinement in gauge theories. *Adv.Theor.Math.Phys.* **2**, 505–532 (1998). `hep-th/9803131`.

[33] Cherman, A. & Ishii, T. Long-distance properties of baryons in the Sakai-Sugimoto model. *Phys.Rev.* **D86**, 045011 (2012). `1109.4665`.

[34] Mateos, D., Myers, R. C. & Thomson, R. M. Holographic phase transitions with fundamental matter. *Phys. Rev. Lett.* **97**, 091601 (2006). `hep-th/0605046`.

[35] Nakamura, S., Seo, Y., Sin, S.-J. & Yogendran, K. A New Phase at Finite Quark Density from AdS/CFT. *J.Korean Phys.Soc.* **52**, 1734–1739 (2008). `hep-th/0611021`.

[36] Kobayashi, S., Mateos, D., Matsuura, S., Myers, R. C. & Thomson, R. M. Holographic phase transitions at finite baryon density. *JHEP* **02**, 016 (2007). `hep-th/0611099`.

[37] Van Raamsdonk, M. & Whyte, K. Baryon charge from embedding topology and a continuous meson spectrum in a new holographic gauge theory. *JHEP* **1005**, 073 (2010). `0912.0752`.

[38] Mandal, G. & Morita, T. Gregory-Laflamme as the confinement/deconfinement transition in holographic QCD. *JHEP* **1109**, 073 (2011). 1107.4048.

[39] Kruczenski, M., Mateos, D., Myers, R. C. & Winters, D. J. Towards a holographic dual of large-N(c) QCD. *JHEP* **05**, 041 (2004). hep-th/0311270.

[40] Babington, J., Erdmenger, J., Evans, N. J., Guralnik, Z. & Kirsch, I. Chiral symmetry breaking and pions in nonsupersymmetric gauge / gravity duals. *Phys.Rev.* **D69**, 066007 (2004). hep-th/0306018.

[41] Aharony, O., Sonnenschein, J. & Yankielowicz, S. A holographic model of deconfinement and chiral symmetry restoration. *Annals Phys.* **322**, 1420–1443 (2007). hep-th/0604161.

[42] Bergman, O., Lifschytz, G. & Lippert, M. Holographic Nuclear Physics. *JHEP* **11**, 056 (2007). 0708.0326.

[43] Ammon, M., Erdmenger, J., Kaminski, M. & Kerner, P. Flavor Superconductivity from Gauge/Gravity Duality. *JHEP* **0910**, 067 (2009). 0903.1864.

[44] Horowitz, G. T. Introduction to Holographic Superconductors (2010). 1002.1722.

[45] Hartnoll, S. A., Herzog, C. P. & Horowitz, G. T. Building a Holographic Superconductor. *Phys. Rev. Lett.* **101**, 031601 (2008). 0803.3295.

[46] Horowitz, G. T. & Roberts, M. M. Holographic Superconductors with Various Condensates. *Phys. Rev.* **D78**, 126008 (2008). 0810.1077.

[47] Horowitz, G. T. & Roberts, M. M. Zero Temperature Limit of Holographic Superconductors. *JHEP* **11**, 015 (2009). 0908.3677.

[48] Basu, P., Mukherjee, A. & Shieh, H.-H. Supercurrent: Vector Hair for an AdS Black Hole. *Phys. Rev.* **D79**, 045010 (2009). 0809.4494.

[49] Arean, D., Basu, P. & Krishnan, C. The Many Phases of Holographic Superfluids. *JHEP* **10**, 006 (2010). 1006.5165.

[50] Kaplunovsky, V., Melnikov, D. & Sonnenschein, J. Baryonic Popcorn. *JHEP* **1211**, 047 (2012). 1201.1331.

[51] Kim, K.-Y., Sin, S.-J. & Zahed, I. Dense hadronic matter in holographic QCD. *J.Korean Phys.Soc.* **63**, 1515–1529 (2013). `hep-th/0608046`.

[52] Horigome, N. & Tanii, Y. Holographic chiral phase transition with chemical potential. *JHEP* **01**, 072 (2007). `hep-th/0608198`.

[53] Rozali, M., Shieh, H.-H., Van Raamsdonk, M. & Wu, J. Cold Nuclear Matter In Holographic QCD. *JHEP* **01**, 053 (2008). `0708.1322`.

[54] Erdmenger, J., Kaminski, M. & Rust, F. Holographic vector mesons from spectral functions at finite baryon or isospin density. *Phys.Rev.* **D77**, 046005 (2008). `0710.0334`.

[55] Erdmenger, J., Kaminski, M., Kerner, P. & Rust, F. Finite baryon and isospin chemical potential in AdS/CFT with flavor. *JHEP* **0811**, 031 (2008). `0807.2663`.

[56] Ammon, M. *et al.* On Stability and Transport of Cold Holographic Matter. *JHEP* **1109**, 030 (2011). `1108.1798`.

[57] Matsuura, S. On holographic phase transitions at finite chemical potential. *JHEP* **0711**, 098 (2007). `0711.0407`.

[58] Horowitz, G. T. & Way, B. Complete Phase Diagrams for a Holographic Superconductor/Insulator System. *JHEP* **1011**, 011 (2010). `1007.3714`.

[59] DeWolfe, O., Gubser, S. S. & Rosen, C. A holographic critical point. *Phys.Rev.* **D83**, 086005 (2011). `1012.1864`.

[60] Minwalla, S. Restrictions imposed by superconformal invariance on quantum field theories. *Adv. Theor. Math. Phys.* **2**, 781–846 (1998). `hep-th/9712074`.

[61] Witten, E. Baryons and branes in anti de Sitter space. *JHEP* **07**, 006 (1998). `hep-th/9805112`.

[62] Karch, A. & Katz, E. Adding flavor to AdS/CFT. *JHEP* **06**, 043 (2002). `hep-th/0205236`.

[63] Klebanov, I. R. & Witten, E. AdS/CFT correspondence and symmetry breaking. *Nucl. Phys.* **B556**, 89–114 (1999). `hep-th/9905104`.

[64] Gubser, S. S. Breaking an Abelian gauge symmetry near a black hole horizon. *Phys. Rev.* **D78**, 065034 (2008). `0801.2977`.

[65] Breitenlohner, P. & Freedman, D. Z. Stability in Gauged Extended Supergravity. *Annals Phys.* **144**, 249 (1982).

[66] Breitenlohner, P. & Freedman, D. Z. Positive Energy in anti-De Sitter Backgrounds and Gauged Extended Supergravity. *Phys.Lett.* **B115**, 197 (1982).

[67] Nishioka, T., Ryu, S. & Takayanagi, T. Holographic Superconductor/Insulator Transition at Zero Temperature. *JHEP* **03**, 131 (2010). `0911.0962`.

[68] Deryagin, D. V., Grigoriev, D. Y. & Rubakov, V. A. Standing wave ground state in high density, zero temperature qcd at large nc. *International Journal of Modern Physics A* **07**, 659–681 (1992).

[69] Shuster, E. & Son, D. On finite density QCD at large N(c). *Nucl.Phys.* **B573**, 434–446 (2000). `hep-ph/9905448`.

[70] Carlson, E., Emery, V., Kivelson, S. & Orgad, D. Concepts in high temperature superconductivity. In Bennemann, K. & Ketterson, J. (eds.) *Superconductivity*, 1225–1348 (Springer Berlin Heidelberg, 2008).

[71] Gregory, R. & Laflamme, R. Black strings and p-branes are unstable. *Phys.Rev.Lett.* **70**, 2837–2840 (1993). `hep-th/9301052`.

[72] Sorkin, E. A Critical dimension in the black string phase transition. *Phys.Rev.Lett.* **93**, 031601 (2004). `hep-th/0402216`.

[73] Flauger, R., Pajer, E. & Papanikolaou, S. A Striped Holographic Superconductor. *Phys.Rev.* **D83**, 064009 (2011). `1010.1775`.

[74] Ooguri, H. & Park, C.-S. Holographic End-Point of Spatially Modulated Phase Transition. *Phys.Rev.* **D82**, 126001 (2010). `1007.3737`.

[75] Donos, A. & Gauntlett, J. P. Helical superconducting black holes. *Phys.Rev.Lett.* **108**, 211601 (2012). `1203.0533`.

[76] Donos, A. & Gauntlett, J. P. Black holes dual to helical current phases. *Phys.Rev.* **D86**, 064010 (2012). `1204.1734`.

[77] Iizuka, N. *et al.* Bianchi Attractors: A Classification of Extremal Black Brane Geometries. *JHEP* **1207**, 193 (2012). `1201.4861`.

[78] Bu, Y.-Y., Erdmenger, J., Shock, J. P. & Strydom, M. Magnetic field induced lattice ground states from holography. *JHEP* **1303**, 165 (2013). `1210.6669`.

[79] Donos, A. & Hartnoll, S. A. Universal linear in temperature resistivity from black hole superradiance. *Phys.Rev.* **D86**, 124046 (2012). `1208.4102`.

[80] Nakamura, S., Ooguri, H. & Park, C.-S. Gravity Dual of Spatially Modulated Phase. *Phys.Rev.* **D81**, 044018 (2010). `0911.0679`.

[81] Donos, A. & Gauntlett, J. P. Holographic charge density waves. *Phys.Rev.* **D87**, 126008 (2013). `1303.4398`.

[82] Wiseman, T. Static axisymmetric vacuum solutions and nonuniform black strings. *Class.Quant.Grav.* **20**, 1137–1176 (2003). `hep-th/0209051`.

[83] Rozali, M. Compressible Matter at an Holographic Interface. *Phys.Rev.Lett.* **109**, 231601 (2012). `1210.0029`.

[84] Herzog, C. P. Lectures on Holographic Superfluidity and Superconductivity. *J.Phys.* **A42**, 343001 (2009). `0904.1975`.

[85] Sachdev, S. What can gauge-gravity duality teach us about condensed matter physics? *Annual Review of Condensed Matter Physics* **3**, 9–33 (2012).

[86] Hutasoit, J. A., Siopsis, G. & Therrien, J. Conductivity of Strongly Coupled Striped Superconductor. *JHEP* **1401**, 132 (2014). `1208.2964`.

[87] Horowitz, G. T., Santos, J. E. & Tong, D. Further Evidence for Lattice-Induced Scaling. *JHEP* **1211**, 102 (2012). `1209.1098`.

[88] Horowitz, G. T., Santos, J. E. & Tong, D. Optical Conductivity with Holographic Lattices. *JHEP* **1207**, 168 (2012). `1204.0519`.

[89] Horowitz, G. T. & Santos, J. E. General Relativity and the Cuprates (2013). `1302.6586`.

[90] Ooguri, H. & Park, C.-S. Spatially Modulated Phase in Holographic Quark-Gluon Plasma. *Phys.Rev.Lett.* **106**, 061601 (2011). `1011.4144`.

[91] Donos, A. & Gauntlett, J. P. Holographic helical superconductors. *JHEP* **1112**, 091 (2011). `1109.3866`.

[92] Iizuka, N. & Maeda, K. Stripe Instabilities of Geometries with Hyperscaling Violation. *Phys.Rev.* **D87**, 126006 (2013). `1301.5677`.

[93] Bergman, O., Jokela, N., Lifschytz, G. & Lippert, M. Striped instability of a holographic Fermi-like liquid. *JHEP* **1110**, 034 (2011). `1106.3883`.

[94] Jokela, N., Lifschytz, G. & Lippert, M. Magnetic effects in a holographic Fermi-like liquid. *JHEP* **1205**, 105 (2012). `1204.3914`.

[95] Jokela, N., Jarvinen, M. & Lippert, M. Fluctuations and instabilities of a holographic metal. *JHEP* **1302**, 007 (2013). `1211.1381`.

[96] Iizuka, N. *et al.* Extremal Horizons with Reduced Symmetry: Hyperscaling Violation, Stripes, and a Classification for the Homogeneous Case. *JHEP* **1303**, 126 (2013). `1212.1948`.

[97] Bao, N., Harrison, S., Kachru, S. & Sachdev, S. Vortex Lattices and Crystalline Geometries. *Phys.Rev.* **D88**, 026002 (2013). `1303.4390`.

[98] Sorkin, E. Non-uniform black strings in various dimensions. *Phys.Rev.* **D74**, 104027 (2006). `gr-qc/0608115`.

[99] Kol, B. & Sorkin, E. On black-brane instability in an arbitrary dimension. *Class.Quant.Grav.* **21**, 4793–4804 (2004). `gr-qc/0407058`.

[100] Liu, H., Ooguri, H., Stoica, B. & Yunes, N. Spontaneous Generation of Angular Momentum in Holographic Theories. *Phys.Rev.Lett.* **110**, 211601 (2013). `1212.3666`.

[101] Donos, A. Striped phases from holography. *JHEP* **1305**, 059 (2013). `1303.7211`.

[102] Withers, B. Black branes dual to striped phases. *Class. Quant. Grav.* **30**, 155025 (2013). `1304.0129`.

[103] Withers, B. The moduli space of striped black branes (2013). `1304.2011`.

[104] Aharony, O., Minwalla, S. & Wiseman, T. Plasma-balls in large N gauge theories and localized black holes. *Class.Quant.Grav.* **23**, 2171–2210 (2006). `hep-th/0507219`.

[105] Rajagopal, K. & Wilczek, F. The Condensed matter physics of QCD (2000). `hep-ph/0011333`.

[106] Stephanov, M. QCD phase diagram: An Overview. *PoS* **LAT2006**, 024 (2006). `hep-lat/0701002`.

[107] McLerran, L. & Pisarski, R. D. Phases of cold, dense quarks at large N(c). *Nucl.Phys.* **A796**, 83–100 (2007). `0706.2191`.

[108] Nunez, C., Paredes, A. & Ramallo, A. V. Unquenched Flavor in the Gauge/Gravity Correspondence. *Adv.High Energy Phys.* **2010**, 196714 (2010). `1002.1088`.

[109] Chen, H.-Y., Hashimoto, K. & Matsuura, S. Towards a Holographic Model of Color-Flavor Locking Phase. *JHEP* **1002**, 104 (2010). `0909.1296`.

[110] Gursoy, U., Kiritsis, E., Mazzanti, L., Michalogiorgakis, G. & Nitti, F. Improved Holographic QCD. *Lect.Notes Phys.* **828**, 79–146 (2011). `1006.5461`.

[111] Iqbal, N., Liu, H., Mezei, M. & Si, Q. Quantum phase transitions in holographic models of magnetism and superconductors. *Phys.Rev.* **D82**, 045002 (2010). `1003.0010`.

[112] Ammon, M., Erdmenger, J., Kaminski, M. & Kerner, P. Superconductivity from gauge/gravity duality with flavor. *Phys.Lett.* **B680**, 516–520 (2009). `0810.2316`.

[113] Basu, P., He, J., Mukherjee, A. & Shieh, H.-H. Superconductivity from D3/D7: Holographic Pion Superfluid. *JHEP* **0911**, 070 (2009). `0810.3970`.

[114] Horowitz, G. T. & Myers, R. C. The AdS / CFT correspondence and a new positive energy conjecture for general relativity. *Phys.Rev.* **D59**, 026005 (1998). `hep-th/9808079`.

[115] Kaplan, D. B., Lee, J.-W., Son, D. T. & Stephanov, M. A. Conformality Lost. *Phys.Rev.* **D80**, 125005 (2009). `0905.4752`.

[116] Jensen, K., Karch, A., Son, D. T. & Thompson, E. G. Holographic Berezinskii-Kosterlitz-Thouless Transitions. *Phys.Rev.Lett.* **105**, 041601 (2010). 1002.3159.

[117] D'Hoker, E., Estes, J. & Gutperle, M. Exact half-BPS Type IIB interface solutions. II. Flux solutions and multi-Janus. *JHEP* **0706**, 022 (2007). 0705.0024.

[118] Sakai, T. & Sugimoto, S. More on a holographic dual of QCD. *Prog.Theor.Phys.* **114**, 1083–1118 (2005). hep-th/0507073.

[119] Hata, H., Sakai, T., Sugimoto, S. & Yamato, S. Baryons from instantons in holographic QCD. *Prog.Theor.Phys.* **117**, 1157 (2007). hep-th/0701280.

[120] Hong, D. K., Rho, M., Yee, H.-U. & Yi, P. Chiral Dynamics of Baryons from String Theory. *Phys.Rev.* **D76**, 061901 (2007). hep-th/0701276.

[121] Hong, D. K., Rho, M., Yee, H.-U. & Yi, P. Dynamics of baryons from string theory and vector dominance. *JHEP* **0709**, 063 (2007). 0705.2632.

[122] Pomarol, A. & Wulzer, A. Stable skyrmions from extra dimensions. *JHEP* **0803**, 051–051 (2008). 0712.3276.

[123] Pomarol, A. & Wulzer, A. Baryon Physics in Holographic QCD. *Nucl.Phys.* **B809**, 347–361 (2009). 0807.0316.

[124] Pomarol, A. & Wulzer, A. Baryon physics in a five-dimensional model of hadrons (2009). 0904.2272.

[125] Cherman, A., Cohen, T. D. & Nielsen, M. Model Independent Tests of Skyrmions and Their Holographic Cousins. *Phys.Rev.Lett.* **103**, 022001 (2009). 0903.2662.

[126] Hong, D. K., Rho, M., Yee, H.-U. & Yi, P. Nucleon form-factors and hidden symmetry in holographic QCD. *Phys.Rev.* **D77**, 014030 (2008). 0710.4615.

[127] Hashimoto, K., Sakai, T. & Sugimoto, S. Holographic Baryons: Static Properties and Form Factors from Gauge/String Duality. *Prog.Theor.Phys.* **120**, 1093–1137 (2008). 0806.3122.

[128] Kim, K.-Y. & Zahed, I. Electromagnetic Baryon Form Factors from Holographic QCD. *JHEP* **0809**, 007 (2008). 0807.0033.

[129] Panico, G. & Wulzer, A. Nucleon Form Factors from 5D Skyrmions. *Nucl.Phys.* **A825**, 91–114 (2009). 0811.2211.

[130] Colangelo, P., Sanz-Cillero, J. J. & Zuo, F. Large-distance properties of holographic baryons. *Nucl.Phys.* **B875**, 351–367 (2013). 1306.6460.

[131] Beringer, J. *et al.* Review of Particle Physics (RPP). *Phys.Rev.* **D86**, 010001 (2012).

[132] Bolognesi, S. & Sutcliffe, P. The Sakai-Sugimoto soliton. *JHEP* **1401**, 078 (2014). 1309.1396.

[133] Witten, E. Some exact multipseudoparticle solutions of classical yang-mills theory. *Physical Review Letters* **38**, 121–124 (1977).

[134] Forgacs, P. & Manton, N. S. Space-time symmetries in gauge theories. *Commun. Math. Phys.* **72**, 15 (1980).

[135] Headrick, M., Kitchen, S. & Wiseman, T. A New approach to static numerical relativity, and its application to Kaluza-Klein black holes. *Class.Quant.Grav.* **27**, 035002 (2010). 0905.1822.

[136] Hashimoto, K., Sakai, T. & Sugimoto, S. Nuclear Force from String Theory. *Prog.Theor.Phys.* **122**, 427–476 (2009). 0901.4449.

[137] Sin, S.-J. Gravity back-reaction to the baryon density for bulk filling branes. *JHEP* **0710**, 078 (2007). 0707.2719.

[138] Yamada, D. Sakai-Sugimoto model at high density. *JHEP* **0810**, 020 (2008). 0707.0101.

[139] Charmousis, C., Gouteraux, B., Kim, B. S., Kiritsis, E. & Meyer, R. Effective Holographic Theories for low-temperature condensed matter systems. *JHEP* **1011**, 151 (2010). 1005.4690.

[140] Dong, X., Harrison, S., Kachru, S., Torroba, G. & Wang, H. Aspects of holography for theories with hyperscaling violation. *JHEP* **1206**, 041 (2012). 1201.1905.

[141] Huijse, L., Sachdev, S. & Swingle, B. Hidden fermi surfaces in compressible states of gauge-gravity duality. *Phys. Rev. B* **85**, 035121 (2012).

[142] Cremonini, S. & Sinkovics, A. Spatially Modulated Instabilities of Geometries with Hyperscaling Violation. *JHEP* **1401**, 099 (2014). `1212.4172`.

[143] Cremonini, S. Spatially Modulated Instabilities for Scaling Solutions at Finite Charge Density (2013). `1310.3279`.

[144] Abrikosov, A. On the Magnetic properties of superconductors of the second group. *Sov. Phys. JETP* **5**, 1174–1182 (1957).

[145] Tseytlin, A. A. On nonAbelian generalization of Born-Infeld action in string theory. *Nucl.Phys.* **B501**, 41–52 (1997). `hep-th/9701125`.

[146] Hashimoto, A. & Taylor, W. Fluctuation spectra of tilted and intersecting D-branes from the Born-Infeld action. *Nucl.Phys.* **B503**, 193–219 (1997). `hep-th/9703217`.

[147] Koerber, P. & Sevrin, A. The NonAbelian D-brane effective action through order alpha-prime**4. *JHEP* **0210**, 046 (2002). `hep-th/0208044`.

[148] Wiseman, T. Numerical construction of static and stationary black holes (2011). `1107.5513`.

[149] Horowitz, G. T., Santos, J. E. & Way, B. A Holographic Josephson Junction. *Phys.Rev.Lett.* **106**, 221601 (2011). `1101.3326`.

[150] Garcia-Garcia, A. M., Santos, J. E. & Way, B. Holographic Description of Finite Size Effects in Strongly Coupled Superconductors. *Phys.Rev.* **B86**, 064526 (2012). `1204.4189`.

[151] Santos, J. E. & Way, B. Black Funnels. *JHEP* **1212**, 060 (2012). `1208.6291`.

[152] Adams, A., Chesler, P. M. & Liu, H. Holographic Vortex Liquids and Superfluid Turbulence (2012). `1212.0281`.

[153] Adams, A., Chesler, P. M. & Liu, H. Holographic turbulence (2013). `1307.7267`.

[154] Chesler, P. M. & Yaffe, L. G. Numerical solution of gravitational dynamics in asymptotically anti-de Sitter spacetimes (2013). `1309.1439`.

[155] Press, W. H., Teukolsky, S. A., Vetterling, W. T. & Flannery, B. P. *Numerical Recipes in C (2Nd Ed.): The Art of Scientific Computing* (Cambridge University Press, New York, NY, USA, 1992).

[156] Trefethen, L. N. *Spectral Methods in MatLab* (Society for Industrial and Applied Mathematics, Philadelphia, PA, USA, 2000).

[157] Boyd, J. P. *Chebyshev and Fourier spectral methods* (Courier Dover Publications, Mineola, New York, USA, 2013).

[158] Papadimitriou, I. & Skenderis, K. AdS / CFT correspondence and geometry 73–101 (2004). `hep-th/0404176`.

[159] Papadimitriou, I. & Skenderis, K. Thermodynamics of asymptotically locally AdS spacetimes. *JHEP* **0508**, 004 (2005). `hep-th/0505190`.

Appendix A

Review of numerical techniques used

In this thesis, in the work described in chapters 3, 4, and 6, we employed standard numerical methods for the solution of the partial differential equations that arose in problems in holography applied to situations with inhomogeneity in the field theory. These were the construction of a striped phase in a strongly coupled field theory and the gravity dual of a baryon in a large-N_c field theory.

In this appendix, we briefly review the implementation of the two major techniques used. Firstly, in section A.1, we sketch our general approach for solving partial differential equations numerically. Following this discussion, we describe the two specific approaches employed: finite differencing with a Gauss-Seidel relaxation method (section A.2) and pseudospectral differentiation with a Newton iteration (section A.3). This appendix is not intended to be a complete guide to these approaches. Rather, it is to provide a (hopefully enlightening) caricature of the techniques used. The interested reader is directed to the useful references [155–157] for more information.

Although our studies involved partial differential equations, with dependence on two variables, for clarity of presentation below we will restrict our descriptions of the numerical techniques to the case of an ordinary differential equation for the field $\varphi(x)$, with dependence on one coordinate x. Specifically, we will consider as our model equation Poisson's equation in one dimension,

$$\frac{d^2\varphi(x)}{dx^2} = \rho(x), \tag{A.1}$$

on the domain $x \in [-1, 1]$. We will use this model equation for illustrative purposes in our discussion of the numerical techniques.

A.1 Generic numerics for elliptic partial differential equations

In this thesis, we applied the holographic correspondence to the study of certain time-independent problems. The partial differential equations that resulted from these static situations were boundary value problems. In a problem of this type, data specified on the boundaries of the domain[1] determines the solution on the interior. The main task for solving these problems is, given a set of boundary conditions, to find the configuration that satisfies both the boundary conditions and the equations of motion in the interior of the domain. The prototypical boundary value problem is the Poisson equation (A.1), which appears in various contexts in physics. The partial differential equations encountered in this thesis are comparable to more complicated, nonlinear versions of the Poisson equation.

In order to solve these more complicated boundary value problems, for which closed-form analytic solutions are not known (and may not even be possible), one must turn to numerical methods. Typically, numerical methods create some approximation of the continuous field $\varphi(x)$ in order to translate the differential equation into a number of coupled algebraic equations, which can be solved numerically. Perhaps the most conceptually straightforward approach, which is undertaken in this thesis, is to discretize the domain on a grid, so that the continuous function $\varphi(x)$ becomes a set of values φ_i at each grid point. By choosing a suitable discretization of the derivatives, one arrives at a set of coupled algebraic equations for the field values φ_i. If we write the field as the vector

$$\vec{\varphi} = \begin{pmatrix} \vdots \\ \varphi_i \\ \vdots \end{pmatrix}, \tag{A.2}$$

then, after the discretization, we can view this problem as the matrix equation

$$A \cdot \vec{\varphi} = \vec{\rho}, \tag{A.3}$$

where $\vec{\rho}$ is the vector created by evaluating the source $\rho(x)$ at the grid points and, in our model problem (A.1), A is the matrix that represents the discretized operator $\frac{d^2}{dx^2}$.

[1] This could be, for example, the value of the fields (Dirichlet conditions), a zero derivative condition (Neumann conditions), or some more complicated condition.

Within this general framework, there is some choice as to how one may solve their problem. First, in terms of the domain grid and the discretization of the derivatives, different choices can affect the performance of the algorithms and the accuracy of the numerical approximations. Two common methods, used in this thesis and reviewed below, are finite differencing (in this case, on a rectangular grid) and pseudospectral methods on a Chebyshev grid. In addition, upon approximating the continuous equation as a matrix equation, different options are available to solve the coupled algebraic equations. In our two cases here, we use a Gauss-Seidel relaxation method and a Newton iteration.

A.2 The numerical approach for holographic stripes

For the study on holographic stripes reported in chapters 3 and 4, the technique used was a second-order finite differencing on a rectangular grid followed by Gauss-Seidel relaxation to solve the resulting algebraic equations. We provide a basic description of each of these components in turn below.

A.2.1 Finite differencing on a rectangular grid

Finite differencing is one of the most familiar methods with which to approximate a derivative. Indeed, the definition of the derivative relies on the limit of a finite difference equation. To use this method on a constant grid, one first splits the domain into N sections of equal length $h = 2/N$, with grid points given by $x_i = -1 + ih$. The continuous field is transformed into a discrete vector by taking its values at these grid points, $\varphi_i = \varphi(x_i)$, and organizing them according to equation (A.2). Derivatives of φ are computed using the standard finite difference equations. In our work, we used second-order finite differences, which, for our model problem, consists of the replacement

$$\frac{d^2\varphi(x_i)}{dx^2} \to \frac{\varphi_{i+1} - 2\varphi_i + \varphi_{i-1}}{h^2}. \tag{A.4}$$

By using a series expansion for the field φ, one can show that the error in this expression is of order h^2. Therefore, using this method, one expects quadratic convergence of our approximate solution as we increase the grid density (decrease h).

Upon making the replacement (A.4), at each grid point x_i we now have an equation involving the value of the field at that point, φ_i, and the values of the field at neighbouring points, φ_{i-1} and φ_{i+1}, resulting in $N+1$ coupled algebraic equations. We can rewrite this as the matrix equation $A \cdot \vec{\varphi} = \vec{\rho}$, where now A is the tri-diagonal matrix

$$A = \frac{1}{h^2} \begin{pmatrix} \ddots & & & & & & \\ & 1 & -2 & 1 & & & \\ & & 1 & -2 & 1 & & \\ & & & 1 & -2 & 1 & \\ & & & & & & \ddots \end{pmatrix} \tag{A.5}$$

with zeros above and below the listed entries.[2] At this stage, solving the original differential equation becomes the task of solving this algebraic matrix equation.

A.2.2 Relaxation iteration

To solve the coupled algebraic equations resulting from our finite difference discretization, we use a standard pointwise Gauss-Seidel-style relaxation iteration, which we review here. This type of iteration can be understood in two ways: Firstly, it is an algorithm which exploits the sparse structure of the matrix A, so that each iteration can be computed quickly. Secondly, it can be rephrased as solving a related diffusion problem to find an equilibrium configuration. (This motivates the label 'relaxation'.) After defining the iteration, we will discuss the second, more relaxing interpretation.

After differencing, our model equation reads

$$A \cdot \vec{\varphi} = \vec{\rho}. \tag{A.6}$$

Following [155], we split the matrix A as $A = L+D+U$, where L is the lower triangular part of A, D is the diagonal of A, and U is the upper triangular part of A. We set up the iteration as

$$D \cdot \vec{\varphi}^{(n+1)} = -(L+U) \cdot \vec{\varphi}^{(n)} + \vec{\rho}, \tag{A.7}$$

where the superscript (n) labels the nth iteration. The value for our field at the next iteration, $\vec{\varphi}^{(n+1)}$, is calculated with low computational expense, as D, being diagonal, is easily inverted. One can see that if the algorithm converges, such that the difference between $\vec{\varphi}^{(n)}$ and $\vec{\varphi}^{(n+1)}$ becomes very

[2] Boundary conditions can be incorporated into this structure by altering the rows which update the boundary values of the field.

close and below some threshold, we will have solved our original equation up to the defined numerical accuracy. This is a standard iterative method for solving a matrix equation of this type.

Now, consider a related diffusion problem, defined as

$$\frac{\partial \vec{\varphi}}{\partial \lambda} = -A \cdot \vec{\varphi} + \vec{\rho}, \tag{A.8}$$

where λ labels an auxiliary 'time' dimension. Finding an equilibrium solution to (A.8), such that $\partial \vec{\varphi}/\partial \lambda = 0$, will give a solution to our model problem. If we discretize the time variable λ using a first-order forward finite difference equation,

$$\frac{\partial \vec{\varphi}}{\partial \lambda} \to \frac{\vec{\varphi}^{(n+1)} - \vec{\varphi}^{(n)}}{\Delta_\lambda}, \tag{A.9}$$

numerically solving this diffusion equation amounts to the update scheme given by

$$\vec{\varphi}^{(n+1)} = \vec{\varphi}^{(n)} - \Delta_\lambda \left(A \cdot \vec{\varphi}^{(n)} - \vec{\rho} \right). \tag{A.10}$$

Compare this to the iteration above: adding and subtracting $\vec{\varphi}^{(n)}$ on the right-hand side of (A.7) gives

$$\vec{\varphi}^{(n+1)} = \vec{\varphi}^{(n)} - D^{-1} \cdot \left(A \cdot \vec{\varphi}^{(n)} - \vec{\rho} \right). \tag{A.11}$$

Thus, in our model problem, with the identification $\Delta_\lambda = (D^{-1})_{ii}$, (A.7) is identical to the scheme that solves the diffusion equation (A.8). Finding a fixed point of the iteration is equivalent to finding an equilibrium solution to the diffusion problem, and ultimately gives a solution to the desired differential equation.

In terms of performance of the scheme described above, a simple way to increase the speed is to perform the updates 'in place'. Typically, the field values $\varphi_i^{(n)}$ are updated to $\varphi_i^{(n+1)}$ one at a time (from $i = 0$ to $i = N$) as the algorithm loops over the grid domain. According to our second-order finite differencing and the iteration (A.7), in our model problem $\varphi_i^{(n+1)}$ will depend on $\varphi_{i+1}^{(n)}$ and $\varphi_{i-1}^{(n)}$. In this setup, by the time the loop arrives at the point i, $\varphi_{i-1}^{(n+1)}$ will have been computed. If, instead of computing the entire vector $\vec{\varphi}^{(n+1)}$ based on the previous vector $\vec{\varphi}^{(n)}$, one updates each $\varphi_i^{(n)}$ using updated values at neighbouring grid points as soon as they become available (uses $\varphi_{i-1}^{(n+1)}$ instead of $\varphi_{i-1}^{(n)}$), the algorithm experiences a constant factor speedup. This is called a Gauss-Seidel method. In our solver, we implement such an update procedure.

For linear problems, such as our model Poisson equation, this type of iteration can be shown to converge, based on the structure of the matrices that result from finite differencing. For nonlinear problems, such as those encountered in this thesis, no general results are available. Practically, this does not impede the implementation of the relaxation. For each problem, one can simply apply the method and observe if convergence occurs. If the residual $\vec{\xi} \equiv A \cdot \vec{\varphi} - \vec{\rho}$ converges to zero, one can be sure that they have found a solution.

A.3 The numerical approach for holographic baryons

For the study on holographic baryons in the Sakai-Sugimoto model reported in chapter 6, we used pseudospectral differentiation on a Chebyshev grid before applying Newton's method to the resulting algebraic equations. In the following subsections, we motivate and describe these technical components.

A.3.1 Pseudospectral differentiation and Chebyshev grids

In this section, we will summarize the development of pseudospectral methods as outlined in [156]. The main goal of this section is to motivate the use of the Chebyshev differentiation matrix D_N, whose action on the vector of grid points $\vec{\varphi}$ will give an approximation to the derivative, and the Chebyshev grid. The main idea we will encounter is that pseudospectral differentiation can be considered as an order N finite difference scheme, where N is the number of grid points. The method is 'spectral' because approximations to the derivatives use information from every grid point in the domain. When using pseudospectral methods, increasing the number of grid points increases the accuracy of the approximations in two ways: by reducing the grid spacing, $h \propto N^{-1}$, and by increasing the power of h that controls the error. The result is exponential convergence in N, of the order $O(1/N^N)$.

To begin our discussion, we recast the second-order finite differencing reviewed in section A.2.1 as a polynomial interpolation. Let ψ_i denote the approximation to $\varphi'(x_i)$. To find ψ_i (with second-order accuracy) via an interpolation, let $p(x)$ be the unique polynomial (of degree 2 or less) that goes through the function φ at x_i and at its two neighbouring points (such that $p(x_{i-1}) = \varphi_{i-1}$, $p(x_i) = \varphi_i$, and $p(x_{i+1}) = \varphi_{i+1}$). On a constant grid, with $x_{i+1} - x_i = h$, this polynomial is

$$\begin{aligned} p(x) = \left(\frac{(x-x_i)(x-x_{i+1})}{2h^2}\right)\varphi_{i-1} \\ - \left(\frac{(x-x_{i-1})(x-x_{i+1})}{h^2}\right)\varphi_i \\ + \left(\frac{(x-x_{i-1})(x-x_i)}{2h^2}\right)\varphi_{i+1}. \end{aligned} \tag{A.12}$$

Given this interpolant, we find ψ_i by differentiating $p(x)$ and evaluating the result at x_i. Carrying out this procedure gives

$$\psi_i = \frac{\varphi_{i+1} - \varphi_{i-1}}{2h}. \tag{A.13}$$

This is precisely the expression for a centred second-order finite difference. By using a series of (second-order) polynomial approximations through each grid point, one can derive the linear transformation D_2 corresponding to the second-order first derivative on a constant grid, such that $\vec{\psi} = D_2 \cdot \vec{\varphi}$. The result is

$$D_2 = \frac{1}{2h}\begin{pmatrix} \ddots & & & & & & \\ & -1 & 0 & 1 & & & \\ & & -1 & 0 & 1 & & \\ & & & -1 & 0 & 1 & \\ & & & & & & \ddots \end{pmatrix}, \tag{A.14}$$

with other entries being zero.

The expressions for higher order finite difference schemes follow in the same manner. To derive the (centred) finite difference approximation to $\varphi'(x_i)$ of degree n, one first finds the unique polynomial $p(x)$ (of degree n or less) that interpolates $\varphi(x)$ at the set of points $(x_{i-n/2}, \ldots, x_i, \ldots, x_{i+n/2})$. Then, taking the derivative of $p(x)$ and evaluating at x_i will give the nth order finite difference expression. In this manner, we can build up the differentiation matrix D_n for any n. The error in the approximate derivative ψ_i (the difference $\varphi'(x_i) - \psi_i$) will be of order $O(h^n)$.

The matrix for our pseudospectral differentiation is found by taking this scheme to limit. On the grid with $N + 1$ grid points, we find the unique polynomial of degree less than or equal to N, before differentiating it and evaluating it at each grid point. This gives a linear transformation[3]

$$\vec{\psi} = \tilde{D}_N \cdot \vec{\varphi} \tag{A.15}$$

which produces an approximation of the derivative $\varphi'(x)$. The error in this approximation will be roughly of order $O(h^N) = O(N^{-N})$. By using a polynomial of degree N, the matrix $\tilde{D}_N$ will be dense, as compared to the sparse structure of the matrix used above for the finite difference scheme. Thus, solving a differential equation using pseudospectral differentiation involves more costly matrix inversions than using a low-order finite difference scheme. However, the exponential convergence with N means that in practice, when using pseudospectral methods, one has to use many fewer grid points than for a finite difference scheme, resulting in savings in vector and matrix storage space. Computational savings in terms of fewer iterations also results and is described more in section A.3.2.

The polynomial one finds through the interpolation process depends on the grid points x_i. Above, we assumed the constant grid $x_i = -1 + ih$. It has been proven that, for polynomial interpolation on the interval $[-1, 1]$, the optimal interpolation points (the grid points at which the interpolant is taken to match the original function) are given by the Chebyshev points

$$x_i = \cos\left(\frac{i\pi}{N}\right), \quad i = 0, 1, \ldots, N. \tag{A.16}$$

These points are less dense in the interior of the domain, around $x = 0$, and cluster near the boundaries at $x = \pm 1$. This allows one to avoid the Runge phenomenon, in which, for polynomial interpolation on a constant grid, errors accumulate near the boundary of the domain. The Chebyshev differentiation matrices D_N are defined as the matrices that enact the linear transformation of differentiating, according to the above polynomial interpolation procedure, when using the Chebyshev points (A.16) as the interpolation points. The explicit expressions for the entries of the matrix D_N, as found in, for example, [156], are

$$\begin{gathered}
(D_N)_{00} = \frac{2N^2+1}{6}, \quad (D_N)_{NN} = -\frac{2N^2+1}{6}, \\
(D_N)_{ii} = \frac{-x_i}{2(1-x_i^2)}, \quad i = 1, \ldots, N-1, \\
(D_N)_{ij} = \frac{c_i}{c_j}\frac{(-1)^{i+j}}{(x_i - x_j)}, \quad i \neq j, \quad i, j = 1, \ldots, N-1,
\end{gathered} \tag{A.17}$$

[3]We write this differentiation matrix as $\tilde{D}_N$, to distinguish it from the Chebyshev differentiation matrix D_N defined below.

where

$$c_i = \begin{cases} 2, & i = 0, N, \\ 1, & otherwise. \end{cases} \tag{A.18}$$

To use the Chebyshev method on our model problem, we discretize the domain on a Chebyshev grid and replace the derivatives with the Chebyshev matrices D_N, to get

$$D_N^2 \cdot \vec{\varphi} = \vec{\rho}. \tag{A.19}$$

We have now reduced our original differential equation to an algebraic matrix equation, the solution of which we describe in the following section.

As a final note, we provide an alternate description of the Chebyshev spectral method. Although we motivated this method through finite differencing and polynomial interpolation, this approach has a different interpretation in terms of an expansion in the Chebyshev polynomials. The Chebyshev polynomials are a set of polynomials defined by

$$T_n(x) = \cos n\theta(x), \tag{A.20}$$

where $\theta(x)$ is defined through

$$x = \cos\theta. \tag{A.21}$$

In this latter method, one expands the field in terms of the Chebyshev polynomials as

$$\varphi(x) = \sum_{n=0}^{N} a_n T_n(x). \tag{A.22}$$

Explicitly following this approach, one would insert the expansion (A.22) into the original equation and use orthogonality of the Chebyshev polynomials to derive algebraic equations for the vector of coefficients $\vec{a}$. It is equivalent to use the values of the function $\vec{\varphi}$ as the unknowns and explicitly solve for these, as we do above. These considerations show that, in addition to finding the value of the function at the grid points (finding the vector $\vec{\varphi}$), one can compute the vector of coefficients $\vec{a}$ in order to find an entire function, (A.22), which approximates our solution.

A.3.2 Newton's method for matrix equations

In this section, we review the use of Newton's method in solving the matrix equations that result after discretizing the problem on a Chebyshev grid and replacing the derivatives with the Chebyshev differentiation matrices. In this section, we will change notation to write our problem as

$$\mathcal{L}(\varphi) = 0, \tag{A.23}$$

where $\mathcal{L}$ is the operator which represents our differential equation. In the case of our model Poisson equation, we would have $\mathcal{L}(\varphi) \equiv \frac{d^2\varphi}{dx^2} - \rho$. Our task is to find the field φ which satisfies equation (A.23).

Upon discretizing according to the prescription in the previous section, we get one equation of motion at each grid point, and thus arrive at a vector of equations, which we write as

$$\vec{\mathcal{L}}(\vec{\varphi}) = 0. \tag{A.24}$$

The Newton's method for this system of equations can be derived by a series expansion in the usual way. Letting subscripts denote components of vectors as above, we can expand our operator near a vector $\vec{\varphi}^*$ as

$$\mathcal{L}_i(\vec{\varphi}^*) = \mathcal{L}_i(\vec{\varphi}) + \left(\frac{\partial \mathcal{L}_i}{\partial \varphi_j}\right)(\varphi_j^* - \varphi_j) + \ldots, \tag{A.25}$$

where $\ldots$ denote terms higher order in $(\varphi_i^* - \varphi_i)$. Now, if we assume that $\vec{\varphi}^*$ satisfies the equations of motion, we have $\mathcal{L}_i(\vec{\varphi}^*) = 0$. Then, truncating the series and rearranging terms, we arrive at a prescription for finding $\vec{\varphi}^*$ based on the nearby vector $\vec{\varphi}$:

$$\varphi_i^* = \varphi_i - \left(\frac{\partial \mathcal{L}_j}{\partial \varphi_i}\right)^{-1} \mathcal{L}_j(\vec{\varphi}). \tag{A.26}$$

Starting from an initial guess for our fields, we iterate according to equation (A.26) until the original equation (A.24) is satisfied to some numerical tolerance.

From the iteration (A.26) and the definition of the Chebyshev matrices D_N, one can motivate that the numerical approach described here will converge in fewer iterations than that described in section A.2. The Gauss-Seidel relaxation is a local relaxation procedure, as the update procedure for the field at each grid point φ_i depends only on neighbouring points. The method described in this section is spectral, in that the update procedure for the field at each point φ_i depends on the value of the field at every other point. Thus, the iterations are able to quickly propagate changes in the field to all corners of the domain, resulting in faster convergence. In practice, the number of iterations needed for numerical convergence is several orders of magnitude smaller for the Chebyshev spectral method with Newton iteration. Therefore, even though each iteration is slower due to the need for a more complex matrix inversion, the amount of total computational time needed for solving using pseudospectral methods is much smaller than for the finite difference method. Indeed, the solution of the partial differential equations encountered in chapter 6 was accessible with only modest desktop resources.

Appendix B

Striped order supplementary material

In this appendix to chapter 4, we provide details of the asymptotic charges in our model (section B.1) and about our numerical procedure (section B.2).

B.1 Asymptotic charges

B.1.1 Deriving the charges

Since our ansatz is inhomogeneous and includes off-diagonal terms in the metric, and our action is not standard (in that it includes the axion coupling) we have re-derived the expressions for the charges and other observables in our geometry. In deriving the asymptotic charges of our spacetime, for the four dimensional Einstein-Maxwell-Higgs theory we discuss in the main text, we follow the covariant treatment of [158, 159]. We refer the reader to those papers for details of the method used.

The bulk action has to be supplemented by boundary terms of two types. First, there are boundary terms needed to ensure that the variational problem is well-defined. Then there are counter-terms, terms depending only on the boundary values (leading non-normalizable modes) of fields on the cutoff surface, which are added to render the on-shell action and the conserved charges finite. Both kinds of boundary terms are the standard ones for Einstein-Maxwell-Higgs theory; the additional axion coupling does not necessitate an additional boundary terms of either kind as long as the scalar mass satisfies $m^2 < 0$.

We find it convenient to study the first variation of the on-shell action, which always reduces to boundary terms. The expression for the regulated first variation of the on-shell action can be differentiated with respect to the boundary values of the bulk fields, to give finite expressions for the conserved charges. We write those expressions below in terms of the asymptotic expansion of the fields occurring in our ansatz, carefully taking into account the differences between our coordinate system and the standard Fefferman-

Graham form of the asymptotic metric, which is used to derive the standard expressions in the literature.

Having explained our procedure, we now display the expressions for the observables used in the main text. We first assume the radial coordinate is in the standard Fefferman-Graham form, and then discuss additional terms arising from change of coordinate necessary to bring our asymptotic metric into the standard form.

For the scalar fields ψ, one can write asymptotically

$$\psi(x,r) = \psi^{(0)}(x)r^{-\lambda_-} + \psi^{(1)}(x)r^{-\lambda_+} \tag{B.1}$$

with

$$\lambda_\pm = \frac{3}{2} \pm \sqrt{\frac{9}{4} + m^2}. \tag{B.2}$$

We set $\psi^{(0)}(x) = 0$ as part of our boundary conditions, then the coefficient $\psi^{(1)}(x)$ is the spatially modulated VEV of the scalar operator dual to ψ.

Similarly, the gauge field can be expanded near the boundary as

$$A_\mu(x,r) = A_\mu^{(0)}(x) - \frac{A_\mu^{(1)}(x)}{r}. \tag{B.3}$$

The functions $A_\mu^{(1)}(x)$ correspond to the charge and current density of the boundary theory.

As for the boundary energy-momentum tensor, the expression is fairly simple in odd number of boundary dimensions, and we have checked that it is not modified by the matter action. With our normalization convention one can write

$$T_{ij} = 6g_{ij}^{(3)}, \tag{B.4}$$

where the superscripts of the metric functions denote the order in the asymptotic expansion.

Since our metric ansatz is not of the Fefferman-Graham form, we need to perform a change of coordinate (in the x, r plane, for which we used the conformal ansatz) to put the metric is such a form. The details of the transformation are straightforward and the process results in the following shifts in the asymptotic metric quantities:

$$\Delta g_{ij}^{(3)} = \frac{2}{3} g(x), \tag{B.5}$$

for every i, j, where $g(x)$ is the leading asymptotic correction to the metric component g_{rr}. That is, at large r that metric component becomes

$$g_{rr}(r,x) \to \frac{1}{2r^2} + \frac{g(x)}{r^5}. \tag{B.6}$$

Finally, since the metric becomes diagonal asymptotically, the non-vanishing time components of the energy-momentum tensor T_{tt} and T_{yt} have a simple interpretation as energy and momentum density, respectively. The conserved charges are given by integrating those densities over a spatial slice.

B.1.2 Explicit expressions for the charges

Homogeneous solution

For reference, in this subsection we give the explicit expressions for the homogeneous RN solution in our conventions. The radius of the horizon is given in terms of the temperature by

$$r_0 = \frac{1}{6}\left(2\pi T + \sqrt{3\mu^2 + 4\pi^2 T^2}\right). \tag{B.7}$$

The mass, entropy and charge of the RN solution of fixed length L are

$$\begin{aligned} M_{RN} &= \left(4r_0^3 + \mu^2 r_0\right) L, & \text{(B.8)} \\ S_{RN} &= 4\pi r_0^2 L, & \text{(B.9)} \\ N_{RN} &= 2r_0 \mu L. & \text{(B.10)} \end{aligned}$$

The corresponding densities in the infinite system are given by dividing through by L.

Inhomogeneous solution

Here we list explicit expressions for the thermodynamic quantities in our system in terms of our solution ansatz. Conserved charges are given by integrating over the inhomogeneous direction. We define $f^{(3)} = -(4r_0^3 + \mu^2 r_0)/4$, the $1/r^3$ term from the function $f(r)$ (equation (4.3)), and $X^{(3)}(x)$, for $X = \{R, S, T\}$, as the coefficient of the $1/r^3$ term of the corresponding metric function. The energy-momentum tensor yields the mass[4]

$$M = \int_0^L \langle T^{tt}(\tilde{x})\rangle d\tilde{x} = 4\int_0^L \xi(x)^2(-f^{(3)} + 5S^{(3)}(x) + 3T^{(3)}(x))dx, \tag{B.11}$$

the tension in the x direction

$$\tau_x = -\int_0^L \langle T^{xx}(\tilde{x})\rangle d\tilde{x} = 2\int_0^L \xi(x)^2(f^{(3)}+6R^{(3)}(x)+4S^{(3)}(x)+6T^{(3)}(x))dx, \tag{B.12}$$

[4]See appendix B.2.3 for details about the numerical process, including the definitions of the $\tilde{x}$ coordinate and $\xi(x)$. The functions $\{R, S, T\}$ are defined on the UV grid; they are analogous to $\{A, B, C\}$ in the original ansatz.

and the pressure in the y direction

$$P_y = \int_0^L \langle T^{yy}(\tilde{x})\rangle d\tilde{x} = -2\int_0^L \xi(x)^2(f^{(3)}+6R^{(3)}(x)+10S^{(3)}(x))dx. \quad \text{(B.13)}$$

Now, expanding the equations of motion at the asymptotic boundary, we get the relation $R^{(3)}(x) + 2S^{(3)}(x) + T^{(3)}(x) = 0$. Using this, we see that $\langle T^{\mu\nu}(z)\rangle$ is traceless, as necessary. Conservation of the energy momentum tensor requires $\partial_x \tau_x = 0$. This is related to the constraint equation (4.18) and we explain our strategy to ensure it is satisfied in appendix B.2.3.

The coefficient of the $1/r$ falloff of the gauge field gives the charge

$$N = -2\int_0^L A_t^{(1)}(x). \quad \text{(B.14)}$$

At the horizon, we read the (constant) temperature as

$$T = \frac{1}{8\pi r_0}(12r_0^2 - \mu^2)e^{-(B-A)|_{r=r_0}} \quad \text{(B.15)}$$

and the entropy is proportional to the area of the event horizon, given by

$$S = 4\pi r_0^2 \int_0^{L/4} e^{(B(r_0,x)+C(r_0,x))}dx. \quad \text{(B.16)}$$

B.1.3 Consistency of the first laws

Here, we discuss the first laws for both the finite length stripe and the stripe on the infinite domain.

Finite system

In our system, as described above, we have unequal bulk stresses τ_x[5] and P_y. Then, if we have a rectangle of side lengths (L, L_y), the work done by the expansion or compression of this region will differ depending on which direction the stress is in. The usual $-PdV$ term in the first law is replaced and we have

$$d\hat{M} = Td\hat{S} + \mu d\hat{N} + \tau_x L_y dL - P_y L dL_y, \quad \text{(B.17)}$$

[5]We define $\tau_x = -P_x$, where P_x is the pressure in the x direction. For our solutions, $\tau_x > 0$.

where the hatted variables represent thermodynamic quantities integrated over the entire system. Defining densities (in the trivial y-direction) by

$$M = \frac{\hat{M}}{L_y}, \quad S = \frac{\hat{S}}{L_y}, \quad N = \frac{\hat{N}}{L_y}, \tag{B.18}$$

we can write the first law as

$$dM = TdS + \mu dN + \tau_x dL + \frac{dL_y}{L_y}(-M + TS + \mu N - P_y L). \tag{B.19}$$

Tracelessness of the energy-momentum tensor implies $M = L(P_x + P_y)$, so that the term proportional to dL_y can be rewritten as the conformal identity (4.29), which disappears for a conformal system described by the first law (4.27). Therefore, the first law (4.27) and the conformal identity (4.29) are consistent.

Infinite system

For the infinite system, we define densities in both the x and y directions as equation (4.33). Under the scaling symmetry (4.19), these scale as

$$m \to \lambda^3 m, \quad s \to \lambda^2 s, \quad n \to \lambda^2 n. \tag{B.20}$$

Using the first law (4.34), we derive the conformal identity (4.35). Again, we can see this from the first law for the system with integrated charges. Plugging the densities m, s, n into the first law of the finite length system (4.27), we arrive at

$$dm = Tds + \mu dn + \frac{dL}{L}(-m + Ts + \mu s + \tau_x). \tag{B.21}$$

Using the conformal identity of the finite length system (4.29), we see that the term proportional to dL is just the conformal identity for the infinite system, which is satisfied for a system described by (4.34).

B.2 Further details about the numerics

B.2.1 The linearized analysis

Following [30], we look for static normalizable modes around the Reissner-Nordstrom background. We consider the fluctuation[6]

$$\begin{aligned}
\delta g_{ty} &= \lambda\left(\frac{(r-r_0)}{r}w(r)\sin(kx)\right), \\
\delta A_y &= \lambda(a(r)\sin(kx)), \\
\delta\psi &= \lambda(\phi(r)\cos(kx)),
\end{aligned} \tag{B.22}$$

where λ is a small parameter in which we can expand the equations. Putting this ansatz into (B.27) - (B.33) and expanding to linear order in λ, we arrive at the linearized system

$$\begin{aligned}
& w''(r) - \frac{r_0 a'(r)}{r^3(r-r_0)} + \frac{(4r-2r_0)w'(r)}{r(r-r_0)} \\
&\quad + \frac{w(r)\left(2r_0\left(4r^3+4r^2r_0+4r{r_0}^2-r_0\right)-k^2r^2\right)}{r^2\left(4r^4-r\left(4{r_0}^3+r_0\right)+{r_0}^2\right)} = 0,
\end{aligned}$$

$$\begin{aligned}
& a''(r) + \frac{\left(8r^4+r\left(4{r_0}^3+r_0\right)-2{r_0}^2\right)a'(r)}{r\left(4r^4-r\left(4{r_0}^3+r_0\right)+{r_0}^2\right)} \\
&\quad - \frac{k^2a(r)}{4r^4-r\left(4{r_0}^3+r_0\right)+{r_0}^2} + \frac{c_1 k r_0 \phi(r)}{\sqrt{3}\left(4r^4-r\left(4{r_0}^3+r_0\right)+{r_0}^2\right)} \\
&\quad - \frac{4rr_0w'(r)}{4r^3+4r^2r_0+4r{r_0}^2-r_0} - \frac{4{r_0}^2w(r)}{4r^4-r\left(4{r_0}^3+r_0\right)+{r_0}^2} = 0,
\end{aligned}$$

$$\begin{aligned}
& \phi''(r) + \frac{c_1 k r_0 a(r)}{2\sqrt{3}r^2\left(4r^4-r\left(4{r_0}^3+r_0\right)+{r_0}^2\right)} \\
&\quad - \frac{\phi(r)\left(k^2+2m^2r^2\right)}{4r^4-r\left(4{r_0}^3+r_0\right)+{r_0}^2} - \frac{\left(-16r^3+4{r_0}^3+r_0\right)\phi'(r)}{4r^4-r\left(4{r_0}^3+r_0\right)+{r_0}^2} = 0.
\end{aligned} \tag{B.23}$$

Fixing the scalar field mass as $m^2=-4$, there are three parameters in these equations: the temperature of the black brane T_0 (equivalently the location of the horizon r_0), the wavenumber k, and the strength of the axion coupling

[6] Regularity at the black hole horizon enforces that $\delta g_{ty}(r_0)=0$.

c_1. In this analysis, we will choose c_1 and k and then use a shooting method to find the T_0 at which normalizable modes appear.

Due to the linearity of the equations, the scale of our solutions is arbitrary. We use this to fix a Dirichlet condition on w at the horizon. Changing coordinates to $\rho = \sqrt{r^2 - r_0^2}$, and expanding the equations near $\rho = 0$ gives regularity conditions on the fluctuations at the horizon in terms of Neumann boundary conditions. Our horizon boundary conditions are then

$$w(\rho)|_{\rho=0} = 1, \qquad w'(\rho)|_{\rho=0} = a'(\rho)|_{\rho=0} = \phi'(\rho)|_{\rho=0} = 0, \tag{B.24}$$

Namely, that the fields are quadratic in ρ near the horizon. In order to search for normalizable modes, we set the sources in the field theory to zero by imposing leading order fall-off conditions near the AdS boundary:

$$w(\rho) = \frac{w_3}{\rho^3} + \ldots, \quad a(\rho) = \frac{a_1}{\rho} + \ldots, \quad \phi(\rho) = \frac{\phi_2}{\rho^2} + \ldots. \tag{B.25}$$

In practice, after fixing c_1 and k, we use T_0 as a shooting parameter to find the solution with the correct w fall-off and the corresponding critical temperature T_c.

For each c_1, we find a range of unstable momenta. By adjusting the strength of the axion coupling, one can find a large variation in the size of this unstable region in the $(k/\mu, T_0/\mu)$ plane (see Figure B.1). The relationship between c_1 and the maximum critical temperature is well fit by $T_c^{max}(c_1)/\mu = 0.025c_1 - 0.091$. The wavenumbers for the dominant critical modes, corresponding to $T_c^{max}(c_1)$, for select c_1 are found in Table B.1.

c_1	T_c^{max}/μ	k_c/μ	$L\mu/4 = \pi/2k_c$
4.5	0.012	0.75	2.08
5.5	0.037	0.92	1.71
8	0.11	1.3	1.21
18	0.37	2.85	0.55
36	0.80	5.65	0.28

Table B.1: The maximum critical temperatures and corresponding critical wavenumbers for varying c_1.

B.2.2 The equations of motion

For completeness, here we present the equations of motion derived from the Lagrangian (4.1). The Einstein equations in our case are four second order

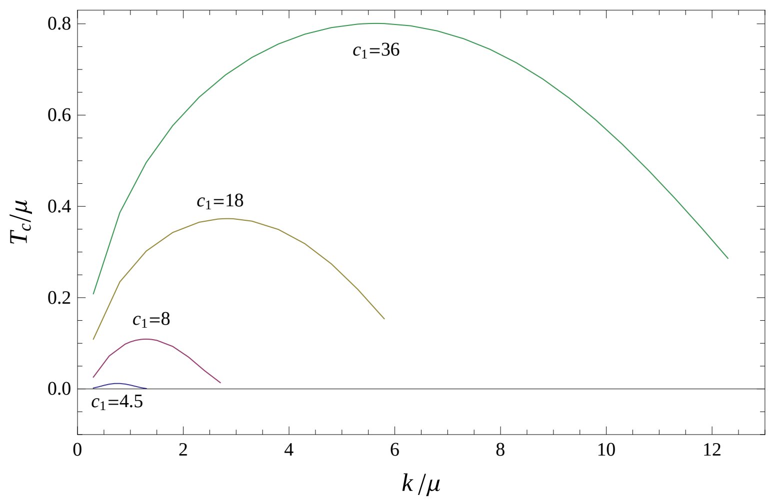

Figure B.1: The critical temperatures at which the Reissner Nordstrom black brane becomes unstable, for varying axion coupling c_1. As the strength of the axion coupling increases, the size of the unstable region (the area under the critical temperature curve) also increases.

elliptic equations for the metric components and two constraint equations. For the compactness of the expressions, we define

$$\hat{O}U \cdot \hat{O}V = \partial_r U \partial_r V + \frac{1}{4r^4 f} \partial_x U \partial_x V, \quad \hat{O}^2 U = \partial_r^2 U + \frac{1}{4r^4 f} \partial_x^2 U. \tag{B.26}$$

The four elliptic equations, formed from combinations of $G_t^t - T_t^t = 0$, $G_y^t - T_y^t = 0$, $G_y^y - T_y^y = 0$, and $G_r^r + G_x^x - (T_r^r + T_x^x) = 0$, then take the form

$$\begin{aligned} &\hat{O}^2 A + (\hat{O}A)^2 + \hat{O}A \cdot \hat{O}C - \frac{e^{-2A+2C}}{2f}(\hat{O}W)^2 - \frac{e^{-2A}}{4r^2 f}(\hat{O}A_t)^2 \\ &\quad - \frac{1}{4r^2}\left(\frac{e^{-2A}W^2}{f} + e^{-2C}\right)(\hat{O}A_y)^2 - \frac{e^{-2A}W}{2r^2 f}\hat{O}A_t \cdot \hat{O}A_y \\ &\quad + \left(\frac{5}{r} + \frac{3f'}{2f}\right)\partial_r A + \left(\frac{1}{r} + \frac{f'}{2f}\right)\partial_r C + \frac{3}{r^2} - \frac{3e^{2B}}{r^2 f} + \frac{e^{2B}m^2\psi^2}{4r^2 f} \\ &\quad + \frac{3f'}{rf} + \frac{f''}{2f} = 0, \end{aligned} \tag{B.27}$$

$$\hat{O}^2 B + \frac{1}{2}(\hat{O}\psi)^2 - \frac{e^{-2A+2C}}{4f}(\hat{O}W)^2 - \hat{O}A \cdot \hat{O}C - \frac{1}{r}\partial_r A + \left(\frac{2}{r} + \frac{f'}{2f}\right)\partial_r B - \left(\frac{1}{r} + \frac{f'}{2f}\right)\partial_r C = 0, \tag{B.28}$$

$$\hat{O}^2 C + (\hat{O}C)^2 + \hat{O}A \cdot \hat{O}C + \frac{e^{-2A+2C}}{2f}(\hat{O}W)^2 + \frac{e^{-2A}}{4r^2 f}(\hat{O}A_t)^2 + \frac{1}{4r^2}\left(\frac{e^{-2A}W^2}{f} + e^{-2C}\right)(\hat{O}A_y)^2 + \frac{e^{-2A}W}{2r^2 f}\hat{O}A_t \cdot \hat{O}A_y + \frac{1}{r}\partial_r A + \left(\frac{5}{r} + \frac{f'}{f}\right)\partial_r C + \frac{3}{r^2} - \frac{3e^{2B}}{r^2 f} + \frac{e^{2B}m^2\psi^2}{4r^2 f} + \frac{f'}{rf} = 0, \tag{B.29}$$

and

$$\hat{O}^2 W - \hat{O}A \cdot \hat{O}W + 3\hat{O}C \cdot \hat{O}W - \frac{e^{-2C}W}{r^2}(\hat{O}A_y)^2 - \frac{e^{-2C}}{r^2}\hat{O}A_t \cdot \hat{O}A_y + \frac{4}{r}\partial_r W = 0. \tag{B.30}$$

The matter field equations are

$$\hat{O}^2 \psi + \hat{O}A \cdot \hat{O}\psi + \hat{O}C \cdot \hat{O}\psi + \frac{c_1 e^{-A-C}}{8\sqrt{3}r^4 f}\left(\partial_r A_t \partial_x A_y - \partial_x A_t \partial_r A_y\right) + \left(\frac{4}{r} + \frac{f'}{f}\right)\partial_r \psi - \frac{e^{2B}m^2\psi}{2r^2 f} = 0, \tag{B.31}$$

$$\hat{O}^2 A_t - \hat{O}A \cdot \hat{O}A_t + \hat{O}C \cdot \hat{O}A_t + \frac{e^{-2A+2C}W}{f}\hat{O}W \cdot \hat{O}A_t + \hat{O}W \cdot \hat{O}A_y + 2W\hat{O}C \cdot \hat{O}A_y - 2W\hat{O}A \cdot \hat{O}A_y + \frac{e^{-2A+2C}W^2}{f}\hat{O}W \cdot \hat{O}A_y + \frac{c_1}{4\sqrt{3}r^2}\left(e^{A-C} - \frac{e^{-A+C}W^2}{f}\right)\left(\partial_r \psi \partial_x A_y - \partial_x \psi \partial_r A_y\right) - \frac{c_1 e^{-A+C}W}{4\sqrt{3}r^2 f}\left(\partial_r \psi \partial_x A_t - \partial_x \psi \partial_r A_t\right) + \frac{2}{r}\partial_r A_t - \frac{Wf'}{f}\partial_r A_y = 0, \tag{B.32}$$

and

$$\hat{O}^2 A_y + \hat{O}A \cdot \hat{O}A_y - \hat{O}C \cdot \hat{O}A_y - \frac{e^{-2A+2C}W}{f}\hat{O}W \cdot \hat{O}A_y - \frac{e^{-2A+2C}}{f}\hat{O}W \cdot \hat{O}A_t$$
$$+ \frac{c_1 e^{-A+C}}{4\sqrt{3}r^2 f}(\partial_r\psi\partial_x A_t - \partial_x\psi\partial_r A_t) + \frac{c_1 e^{-A+C}W}{4\sqrt{3}r^2 f}(\partial_r\psi\partial_x A_y - \partial_x\psi\partial_r A_y)$$
$$+ \left(\frac{2}{r} + \frac{f'}{f}\right)\partial_r A_y = 0. \tag{B.33}$$

Finally, the constraint equations are

$$\partial_x\partial_r A + \partial_x\partial_r C - \partial_r A\left(\partial_x B - \partial_x A\right) - \left(\partial_x A + \partial_x C\right)\partial_r B$$
$$- \left(\partial_x B - \partial_x C\right)\partial_r C + \frac{f'}{2f}\partial_x A - \left(\frac{f'}{2f} + \frac{2}{r}\right)\partial_x B$$
$$- \frac{e^{-2A}}{2fr^2}\left(\partial_x A_t + W\partial_x A_y\right)\left(\partial_r A_t + W\partial_r A_y\right) - \frac{e^{-2(A-C)}}{2f}\partial_x W\partial_r W$$
$$+ \frac{e^{-2C}}{2r^2}\partial_x A_y\partial_r A_y + \partial_x\psi\partial_r\psi = 0 \tag{B.34}$$

and

$$\partial_r^2 A + \partial_r^2 C - \frac{1}{4fr^4}(\partial_x^2 A + \partial_x^2 C) + \left(1 - \frac{1}{4fr^4}\right)\left(\partial_r A\right)^2 + \left(1 - \frac{1}{4fr^4}\right)\left(\partial_r C\right)^2$$
$$+ \frac{1}{2fr^4}\left(\partial_x A + \partial_x C\right)\partial_x B - 2\left(\partial_r A + \partial_r C\right)\partial_r B + \left(\frac{3f'}{2f} + \frac{2}{r}\right)\partial_r A$$
$$- \left(\frac{f'}{f} + \frac{4}{r}\right)\partial_r B + \left(\frac{f'}{2f} + \frac{2}{r}\right)\partial_r C + \frac{e^{-2A}}{8f^2r^6}\left(\partial_x A_t + W\partial_x A_y\right)^2$$
$$- \frac{e^{-2A}}{2fr^2}\left(\partial_r A_t + W\partial_r A_y\right)^2 - \frac{e^{-2(A-C)}}{2f}\left(\left(\partial_r W\right)^2 - \frac{1}{4fr^4}\left(\partial_x W\right)^2\right)$$
$$+ \frac{e^{-2C}}{2r^2}\left(\left(\partial_r A_y\right)^2 - \frac{1}{4fr^4}\left(\partial_x A_y\right)^2\right) + \left(\partial_r\psi\right)^2 - \frac{1}{4fr^4}\left(\partial_x\psi\right)^2 + \frac{f''}{2f}$$
$$+ \frac{2f'}{fr} = 0. \tag{B.35}$$

B.2.3 Constraints

The constraint equations, $G^r_x - T^r_x = 0$ and $G^r_r - G^x_x - (T^r_r - T^x_x) = 0$, are the non-trivial Einstein equations that are not part of the system of second-order elliptic equations that we numerically solve. As discussed in section 4.2, the weighted constraints can be shown to solve Laplace equations on the domain. If we satisfy one of the constraints on all boundaries and the other at one point, they will be satisfied everywhere. At the black hole horizon, we choose to impose $r^2\sqrt{f}\sqrt{-g}(G^r_r - G^x_x - (T^r_r - T^x_x)) = 0$ at the point $(\rho, x) = (0, 0)$ and $\sqrt{-g}(G^r_x - T^r_x) = 0$ across the horizon. Since we use periodic boundary conditions in the inhomogeneous direction, the boundaries at $x = 0$ and $x = x_{max}$ are trivial if $\sqrt{-g}(G^r_x - T^r_x) = 0$ at the horizon and the conformal boundary. Then, we are left with the task of satisfying $\sqrt{-g}(G^r_x - T^r_x) = 0$ at the boundary.

In section 4.2, we found the asymptotic expansion of this constraint as

$$G^r_x - T^r_x \propto \frac{3\partial_x A^{(3)}(x) + 2\partial_x B^{(3)}(x) + 3\partial_x C^{(3)}(x)}{r^2} + O(r^{-3}), \tag{B.36}$$

where $A^{(3)}(x), B^{(3)}(x)$ and $C^{(3)}(x)$ come from solving the elliptic equations. It appears that, within our problem, we do not have the ability to make the weighted constraint disappear. The key lies in an unfixed gauge symmetry in our original metric that is related to conformal transformations of the (r, x) plane.[7] Essentially, within our metric ansatz, we have the freedom to transform to any plane (r', x') that is conformally related to (r, x). Demanding that the weighted constraint $\sqrt{-g}(G^r_x - T^r_x)$ vanishes at the conformal boundary uniquely identifies the correct coordinates $(\tilde{r}, \tilde{x})$.

Our procedure is to split the domain at some intermediate radial value ρ_{int}. On the IR portion of the grid, $0 < \rho < \rho_{int}$, the equations are as above. On the UV portion of the grid, $\rho_{int} < \rho < \rho_{cut}$, we use the coordinate freedom to select the correct asymptotic radial coordinate. We can write the metric in the UV as

$$ds^2 = -2\tilde{r}^2\tilde{f}(\tilde{r}, \tilde{x})e^{2R}dt^2 + e^{2S}\left(\frac{d\tilde{r}^2}{2\tilde{r}^2\tilde{f}(\tilde{r}, \tilde{x})} + 2\tilde{r}^2 d\tilde{x}^2\right) + 2\tilde{r}^2 e^{2T}(dy - U dt)^2, \tag{B.37}$$

where $\tilde{f}(\tilde{r}, \tilde{x}) \equiv f(r(\tilde{r}, \tilde{x}))$. Under a transformation in the $(\tilde{r}, \tilde{x})$ plane such that $\tilde{r}$ and $\tilde{x}$ satisfy Cauchy-Riemann-like relations

$$\frac{\partial \tilde{r}(r, x)}{\partial r} = \frac{\tilde{r}(r, x)^2}{r^2}\frac{\partial \tilde{x}(r, x)}{\partial x}, \qquad \frac{\partial \tilde{x}(r, x)}{\partial r} = -\frac{1}{4r^2\tilde{r}(r, x)^2 f(r)}\frac{\partial \tilde{r}(r, x)}{\partial x}, \tag{B.38}$$

[7] See [104] for a discussion of the same issue in a different context.

the metric becomes

$$ds^2 = -2\tilde{r}(r,x)^2 f(r) e^{2R} dt^2 + e^{2S}|\nabla\tilde{r}(r,x)|^2\left(\frac{dr^2}{2r^2 f(r)} + 2r^2 dx^2\right) + 2\tilde{r}(r,x)^2 e^{2T}(dy - U dt)^2 \quad \text{(B.39)}$$

with

$$|\nabla\tilde{r}(r,x)|^2 = \frac{r^2}{\tilde{r}(r,x)^2}\left(\frac{\partial\tilde{r}(r,x)}{\partial r}\right)^2 + \frac{1}{4r^2\tilde{r}(r,x)^2 f(r)}\left(\frac{\partial\tilde{r}(r,x)}{\partial x}\right)^2. \quad \text{(B.40)}$$

We now have an extra function $\tilde{r}(r,x)$ in our system which we may use to satisfy the constraint and fix the residual gauge freedom, as we will now see. The Cauchy-Riemann-like conditions give the Laplace-like equation

$$\frac{\partial}{\partial r}\left(\frac{r^2}{\tilde{r}(r,x)^2}\frac{\partial\tilde{r}(r,x)}{\partial r}\right) + \frac{\partial}{\partial x}\left(\frac{1}{4r^2\tilde{r}(r,x)^2 f(r)}\frac{\partial\tilde{r}(r,x)}{\partial x}\right) = 0. \quad \text{(B.41)}$$

We can solve this asymptotically, finding

$$\tilde{r}(r,x) = \xi(x) r + \frac{2\xi'(x)^2 - \xi(x)\xi''(x)}{24\xi(x) r} + \ldots, \quad \text{(B.42)}$$

where $\xi(x)$ is an arbitrary function that encodes the coordinate freedom we have.

Expanding the constraint asymptotically, we have

$$G^r_x - T^r_x \propto \frac{1}{r^2}\Big(2(3\partial_x R^{(3)}(x) + 2\partial_x S^{(3)}(x) + 3\partial_x T^{(3)}(x))\xi(x) + 3(f^{(3)} + 2R^{(3)}(x) - 4S^{(3)}(x) + 2T^{(3)}(x))\xi'(x)\Big) + O(r^{-3}), \quad \text{(B.43)}$$

where $X = X^{(3)}(x)/r^3 + \ldots$ asymptotically, for $X = \{R, S, T\}$. Demanding that the constraint (B.43) vanishes at the leading order yields a differential equation we can solve for $\xi(x)$, giving us a boundary condition for the function $\tilde{r}(r,x)$, such that the weighted constraint will disappear at the conformal boundary. However, we have found that the code is unstable if we directly use this solution for $\xi(x)$. Instead of directly integrating the constraint, we use the freedom in $\xi(x)$ to fix the tension τ_x to be constant. This enforces the same effect on the tension as if we had used the explicit solution for $\xi(x)$ but is much more stable numerically. Below, we check that the constraints are suitably satisfied even though our boundary conditions do not exactly fix them. To this end, we set

$$\xi(x) = \frac{K}{(f^{(3)} + 6R^{(3)}(x) + 4S^{(3)}(x) + 6T^{(3)}(x))^{1/3}}. \tag{B.44}$$

Expanding the equations asymptotically gives the expression $R^{(3)}(x)+2S^{(3)}(x)+T^{(3)}(x) = 0$; if this is satisfied on our solutions our definition of $\xi(x)$ coincides with that found by integrating the constraint (B.43).

The constant K appearing in $\xi(x)$ sets the scale of the boundary theory. We use it to fix the length of the inhomogeneous direction in the field theory to be $L\mu/4$. The correct coordinate in the inhomogeneous direction of the field theory is $\tilde{x}$. From the Cauchy-Riemann conditions, we can find the large r expansion of $\tilde{x}(r, x)$ as

$$\tilde{x}(r, x) = \int_0^x \frac{dx'}{\xi(x')} + \frac{\xi'(x)}{8\xi(x)^2 r^2} + \dots. \tag{B.45}$$

Integrating to find the proper length of one cycle in the boundary, we solve for K at leading order in r to find

$$K = \frac{4}{L}\int_0^{L/4} (f^{(3)} + 6R^{(3)}(x) + 4S^{(3)}(x) + 6T^{(3)}(x))^{1/3} dx'. \tag{B.46}$$

When integrating the charges over the inhomogeneous direction in the field theory, one must remember to integrate over the correct coordinate, $d\tilde{x} = dx/\xi(x)$.

Our corrected numerical procedure is as follows. On the IR grid, we solve the elliptic equations (B.27) - (B.33) for the metric functions A, B, C and W. On the UV grid, we solve the equivalent elliptic equations from the metric (B.39) in the variables R, S, T and U plus equation (B.41) for the new field $\tilde{r}(r, x)$. At the horizon, we enforce the boundary conditions discussed in §4.2. At the interface $\rho = \rho_{int}$, we impose matching conditions on the four metric functions and that $\tilde{r}(\rho_{int}, x) = r(\rho_{int})$. Asymptotically, R, S, T and U all fall off as $1/\tilde{r}^3$. To set boundary conditions on $\tilde{r}$, we notice that

$$\partial_r \tilde{r}(r, x) + \frac{\tilde{r}(r, x)}{r} = 2\xi(x) + O\left(\frac{1}{r^3}\right). \tag{B.47}$$

We truncate this expression at $O(r^{-2})$ and finite difference to find an update procedure for $\tilde{r}(\rho_{cut}, x)$. This boundary condition is updated iteratively as the functions R, S, T are updated in our solving procedure such that once we find a solution with small residuals we can be sure that the tension is constant and the constraint is satisfied.

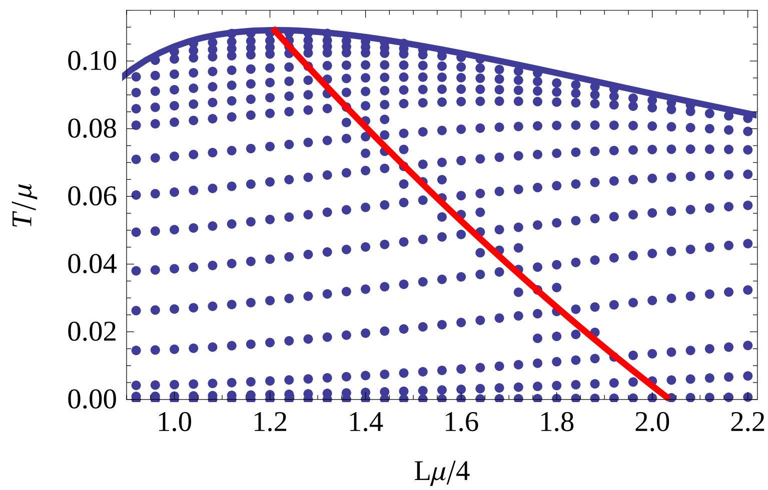

Figure B.2: The data underlying Figure 4.17. The points represent solutions we computed. These were interpolated to find the free energy density over the domain. The solid blue line is the edge of the unstable region and the thick red line is the approximate line of minimum free energy density.

B.2.4 Generating the action density plot

To generate the relative action density plot, Figure 4.17, we find the solutions on a grid of lengths L and temperatures T_0, as shown in Figure B.2. By interpolating these solutions on the domain, we can map the thermodynamic quantities across the unstable region and determine the approximate line of minimum free energy, or the dominant solution in the infinite size system.

B.2.5 Convergence and independence of numerical parameters

Performance of the method and convergence of physical data

As discussed above, to solve the equations numerically, we use a second order finite differencing approximation before using a point-wise Gauss-Seidel relaxation method on the resulting algebraic equations. The method, including the UV procedure described above, performs well for this system.

The UV procedure is unstable for a generic initial guess, resulting in a divergent norm. To find a solution from a generic initial guess, we can run the relaxation without the UV procedure until the norm is small enough that the result approximates the true solution, before activating the UV

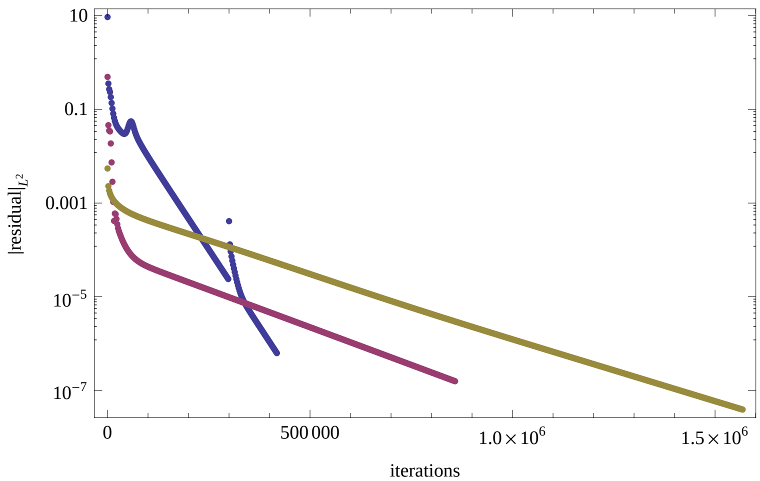

Figure B.3: The behaviour of the L^2 norm of the residual during the relaxation iterations for $c_1 = 8$, $T_0 = 0.04$ and $L\mu/4 = 0.75$. From top to bottom (at the left of the plot) the grid spacing is $d\rho, dx = 0.04, 0.02, 0.01$. The UV procedure is unstable unless the solution is close enough to correct solution. For grid spacing $d\rho, dx = 0.04$, the UV procedure was activated after 3×10^5 iterations while for the others, the initial guess was taken to be a solution with slightly different parameters such that the UV procedure could be used immediately.

procedure to find the true solution. Once we have these first solutions, by using these as an initial guess for solutions nearby in parameter space and by interpolating to a finer grid, we can generate further solutions by relaxing with the UV procedure. In Figure B.3, we plot the L^2 norm of the total residual during the relaxation of the $c_1 = 8$ solution at $T_0 = 0.04$ and $L\mu/4 = 0.75$ for the grid spacings $d\rho, dx = 0.04, 0.02, 0.01$, showing the expected exponential behaviour of the Gauss-Seidel relaxation. The physical data extracted from our solutions is consistent with the expected second order convergence of our finite-difference scheme, see Figure B.4.

Asymptotic versus first law mass

A useful check of the numerics is to compare the mass of the system read off from the asymptotics of the metric, equation (B.11), to that computed by integrating the first law, equation (4.27). Since the temperature and entropy are read off from the horizon, comparing these two methods of finding the mass provides a non-trivial global consistency check on our results. We

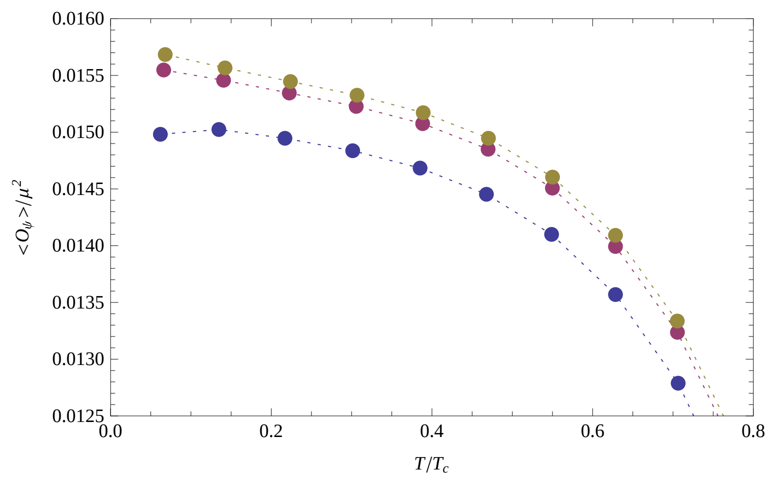

Figure B.4: The value of the scalar field condensate for varying grid sizes for $c_1 = 8$ and $L\mu/4 = 0.75$. From top to bottom, the grid spacing is $d\rho, dx = 0.01, 0.02, 0.04$. The results are consistent with second order scaling as expected from our numerical approach.

verify that the difference between the asymptotic mass and the first law mass remains smaller than 0.5% across our set of trials, indicating consistency of our results.

A related check of the numerics is the conformal identity or the Smarr-like relation, $2M = TS + \mu N - \tau_x L$, derived above from the first law for the finite length system. To evaluate how well our solutions satisfy this equation, we examine the ratio

$$\frac{2M_{fall-off} - TS - \mu N + \tau_x L}{\max(M_{fall-off}, TS, \mu N, \tau_x L)}, \tag{B.48}$$

since the largest term in the expression sets a scale for the cancellation we expect. This ratio is very small for our solutions near the critical temperature. As we lower the temperature, this ratio increases, but stays small. The precise value depends on the parameters of the solution, but is not larger than order 1%. Moreover, this ratio decreases as we move the position of the finite cutoff of the conformal boundary to a larger radius.

Finite ρ_{cut} boundary check

For the $c_1 = 8$ trials reported in the paper, we use $\rho_{cut} = 12$ as our conformal boundary. In Table B.2 we present results for varying ρ_{cut}, showing that our choice is large enough such that the physical results are insensitive to the cutoff. Although the physical results presented in the table appear very stable, at small ρ_{cut}, the results for the mass and charge depend significantly on the fitting procedure for the asymptotic metric functions and gauge field. By running our simulations at $\rho_{cut} = 12$, we are both well within the the region where the solutions do not change with the conformal boundary and within a region where our fitting procedure to the asymptotics behaves well.

ρ_{cut}	S	M	N
1	0.758504	0.305774	0.527406
2	0.767913	0.342327	0.490524
3	0.768211	0.341928	0.490593
4	0.768285	0.342043	0.490583
5	0.768311	0.342136	0.490577
6	0.768322	0.34221	0.490574
7	0.768328	0.342277	0.490572
8	0.768332	0.342324	0.49057
9	0.768334	0.342367	0.490569
10	0.768335	0.342402	0.490568
11	0.768336	0.342434	0.490568
12	0.768336	0.342459	0.490567

Table B.2: Behaviour of physical quantities with the cutoff for $c_1 = 8$ and $L\mu/4 = 0.75$ and for fixed grid resolution $d\rho, dx \sim 0.02$. The entropy S is read off at the horizon, while the mass M and the charge N are read off at the conformal boundary. Both the entropy and the charge are very robust against the location of the conformal boundary. The mass takes slightly longer to settle down, but is well within the convergent range for $\rho_{cut} = 12$.

Behaviour of the constraints

One of the most important checks for our numerical solution is the behaviour of the constraints. For numerical homogeneous solutions found with our method, the L^2 norm of the constraints is very small, on the order of 10^{-4}. For the inhomogeneous solutions, the constraints are small near the critical temperature, but grow and saturate as we lower to the temperature, to have a maximum L^2 norm on the order of 10^{-2}: see Figure B.5. Since our boundary conditions explicitly fix the weighted constraints on the horizon, they disappear there. The weighted constraints then increase towards the conformal boundary, approaching a modulated profile of constant amplitude.

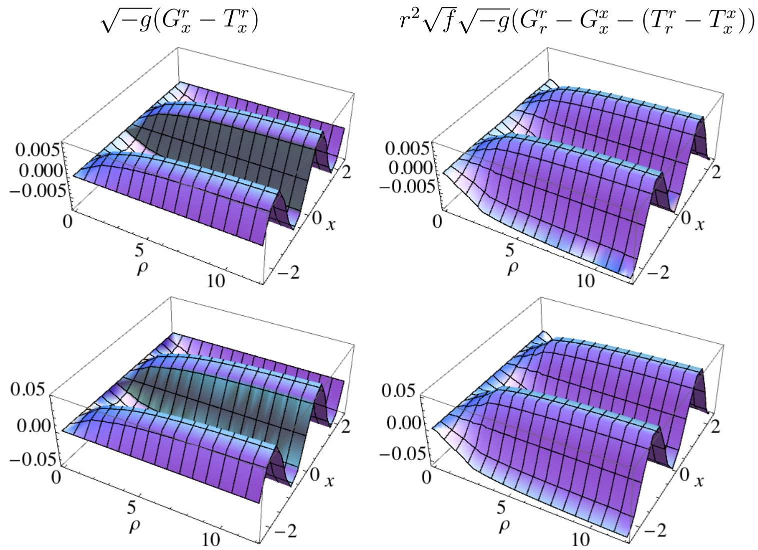

Figure B.5: The weighted constraints for $c_1 = 8$ and $L\mu/4 = 1.21$. The top plots are near the critical point, $T/T_c = 0.97$, while the bottom plots are at small temperature, $T/T_c = 0.00016$. By our boundary conditions, the constraints disappear at the horizon. They approach a finite value as they approach the asymptotic boundary.

The amplitude near the conformal boundary controls the overall L^2 norm of the constraints.

The constraint violation improves marginally with step size and with moving the interface closer to the horizon, but does not improve as we take the conformal boundary to a larger radius. To check that the constraints are well satisfied on our solution, we compare them to the sum of the absolute value of the terms that make up the constraints. That is, if the constraints are given by $\sum_i h_i$, we compare this to $\sum_i |h_i|$. This procedure gives us an idea of the scale of the cancellation among the individual terms h_i. We find that the sum $\sum_i |h_i|$ diverges approximately as r^4 towards the asymptotic boundary, such that the approach of the constraint violation to a constant is a good indicator that the constraints are satisfied on the solution. In Table B.3, we compare the L^2 norm of these two sums on the entire domain, showing that the constraint violation for the inhomogeneous solutions is generally about four orders of magnitude less than the scale set by $\sum_i |h_i|$.

Interestingly, the relative constraint improves marginally as we go to lower temperatures.

Parameters	T_0	$L^2(\sum_i h_i)/L^2(\sum_i \|h_i\|)$
$c_1 = 8, L\mu/4 = 2.00$ (RN solution)	0.105	$9.12 \cdot 10^{-7}$
$c_1 = 8, L\mu/4 = 1.21$ (striped solution)	0.075	$2.02 \cdot 10^{-4}$
	0.05	$1.84 \cdot 10^{-4}$
	0.025	$1.58 \cdot 10^{-4}$
	0.005	$1.37 \cdot 10^{-4}$
	0.001	$1.32 \cdot 10^{-4}$

Table B.3: Comparison of the constraint violation, measured by the schematic constraint equation $\sum_i h_i$, to the scale set by the individual terms, $\sum_i |h_i|$, for grid size $d\rho, dx \sim 0.01$. We take the L^2 norm of the measures on the entire domain. The $c_1 = 8, L\mu/4 = 2.00$ solution is a homogeneous RN solution found numerically with our code, for which the constraints are very well satisfied. The constraints for the striped solutions are satisfied compared to the scale set by $\sum_i |h_i|$ by four orders of magnitude and the relative constraint improves marginally as we lower the temperature.

The asymptotic equation of motion

Expanding the equations of motion asymptotically gives the relation

$$R^{(3)}(x) + 2S^{(3)}(x) + T^{(3)}(x) = 0, \tag{B.49}$$

which can be used to give another check of the numerics. As explained in B.1.2, this condition implies the tracelessness of the energy-momentum tensor. For the inhomogeneous solutions near the critical temperature we find that this expression is on the order of the individual metric functions $X^{(3)}$, where $X = \{R, S, T\}$, but generally decreases as we lower the temperature. As well, we find that homogeneous solutions found using our numerical techniques satisfy (B.49) well. There seems to be an unidentified systematic error here that may deserve further attention in the future. Possible problems may occur in the implementation of the UV procedure or in our procedure to read off the coefficients of the falloffs of the metric functions. However, our physical results are robust under changes to the boundary conditions, so that we are confident in our results despite this possible systematic. In particular, the physical quantities extracted from the horizon are independent of the different boundary constraint fixing schemes we implemented.

Therefore, we advocate using the mass derived from the integrated first law, which uses no asymptotic metric functions.

Appendix C

Colour superconductivity supplementary material

In this appendix to chapter 5, we provide more details about our model with a charged scalar field, analyzing both the large charge limit (section C.1) and finding the critical chemical potential for scalar field condensation (section C.2).

C.1 Large charge limit

In this section, we analyze the case of large q. This is particularly simple, since in this limit, the back-reaction of the scalar and the gauge field on the metric go to zero in the region of the phase diagram where transitions to the superconducting phases occur. Explicitly, we can show that in the limit $q \to \infty$ with $q\mu$ fixed, the gauge field and scalar field decouple from the equations for the metric, but still give rise to a nontrivial phase structure. To investigate this, we need only consider the scalar field and gauge field equations on the fixed background spacetimes corresponding to low temperatures (the soliton geometry) and high temperatures (the Schwarzschild black hole).

Low Temperature

Starting from the action (5.3) for the scalar field and gauge field on the soliton background (5.25), we find that the equations of motion are (setting $L = 1$)

$$\begin{aligned} \phi'' + \left(\frac{f'}{f} + \frac{4}{r}\right)\phi' - \frac{2q^2}{r^2 f}\psi^2\phi &= 0 \, , \\ \psi'' + \left(\frac{f'}{f} + \frac{6}{r}\right)\psi' + \frac{q^2}{r^4 f}\phi^2\psi - \frac{m^2}{r^2 f}\psi &= 0 \, , \end{aligned} \tag{C.1}$$

where f is defined in (5.26).

These equations have two scaling symmetries related to the conformal symmetry of the boundary field theory and to the absence of back-reaction in our large charge limit. Given a solution $(\phi(r), \psi(r), r_0, q, m)$, we can check that the scaling

$$(\phi(r), \psi(r), r_0, q, m) \to (\beta\phi(\alpha r), \beta\alpha\psi(\alpha r), \frac{r_0}{\alpha}, \frac{q}{\alpha\beta}, m) \tag{C.2}$$

sends solutions to solutions. For our calculations, we will use this to set $r_0 = q = 1$.

Multiplying these equations by f and taking the limit $r \to r_0 = 1$, we find that regular solutions must obey

$$\begin{aligned} \phi'(1) &= \frac{2\psi^2(1)\phi(1)}{5} , \\ \psi'(1) &= \frac{\psi(1)}{5}\left(m^2 - \phi^2(1)\right) . \end{aligned} \tag{C.3}$$

We have two remaining parameters, $\psi(0)$ and $\phi(0)$. One of these can be fixed by demanding that the 'non-normalizible' mode of ψ vanishes at infinity, while different values of the remaining parameter correspond to different values of μ.

Employing numerics, we find that for a fixed value of m^2, there is some critical value of μ above which solutions with a condensed scalar field exist.

In order to determine the critical value $\mu_c(m^2)$, we use the fact that the field values go to zero as we approach the critical μ from above. Thus, at the critical μ, the equations above linearized around the background solution $\phi = \mu$ should admit a solution with the correct boundary conditions. The linearized equations decouple from each other, so we need only study the ψ equation. This becomes

$$\psi'' + \left(\frac{6r^5 - 1}{r(r^5 - 1)}\right)\psi' + \frac{r(\mu^2 - m^2 r^2)}{r^5 - 1}\psi = 0 . \tag{C.4}$$

We can take $\psi(1) = 1$ without loss of generality, so the boundary condition for ψ' becomes

$$\psi'(1) = \frac{1}{5}(m^2 - \mu^2) . \tag{C.5}$$

Given m^2, we now find μ^2 by demanding that the leading asymptotic mode (ψ_1) of ψ vanishes. Our results for the critical μ as a function of m^2 are shown in Figure C.1.

High temperature

The high temperature geometry relevant to the limit of large q with μq fixed is the $\mu \to 0$ limit of the Reissner-Nordstrom geometry (5.29), which gives the planar AdS-Schwarzschild black hole (with one of the spatial directions compactified). This is the relevant background for $T > 1/(2\pi R)$.

Explicitly, we have

$$ds^2 \quad = \quad r^2 \left(-dt^2 f(r) + dx^2 + dy^2 + dz^2 + dw^2\right) + \frac{dr^2}{r^2 f(r)} \ , \qquad \text{(C.6)}$$

where

$$f(r) = 1 - \frac{r_+^5}{r^5} \ . \qquad \text{(C.7)}$$

Here, r_+ is related to the temperature by

$$r_+ = \frac{4\pi T}{5} \ . \qquad \text{(C.8)}$$

The equations of motion in this background are

$$\psi'' + \left(\frac{f'}{f} + \frac{6}{r}\right)\psi' + \frac{q^2}{r^4 f^2}\phi^2\psi - \frac{m^2}{r^2 f}\psi \quad = \quad 0 \ . \qquad \text{(C.9)}$$

The equations have the same scaling symmetry as before, so we can set $r_+ = q = 1$ for numerics. Here, the choice $r_+ = 1$ corresponds to $T = 1/(2\pi R)$, where R is the radius chosen in the previous section by setting $r_0 = 1$. In this case, the boundary conditions are

$$\phi(1) = 0 \ , \qquad \psi'(1) = \frac{m^2 L^2 \psi(1)}{5} \ . \qquad \text{(C.10)}$$

To determine the physics at other temperatures, we can fix q and R and use the scaling to adjust the temperature.

For any values of parameters, we have a solution

$$\psi = 0 \ , \qquad \phi(r) = \mu(1 - \frac{1}{r^3}) \ . \qquad \text{(C.11)}$$

corresponding to the pure Reissner-Nordstrom background in the probe limit.

As in the low temperature phase, we find a critical value $\mu_c = F(m^2)$ (or, restoring temperature dependence, $\mu_c = \frac{T}{T_c} F(m^2)$) for each choice of

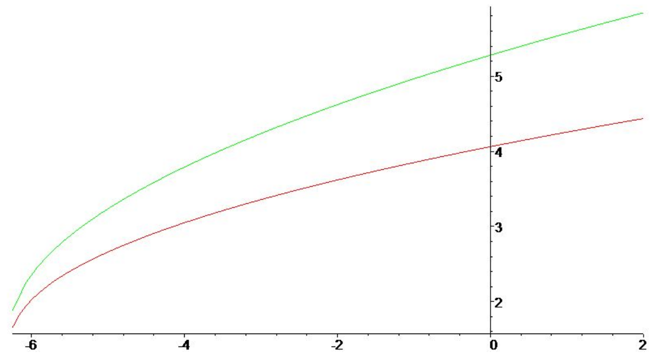

Figure C.1: Critical values of μq vs m^2 for scalar condensation in large q limit. The top curve is the critical value for μ in black hole phase (just above the transition temperature), while the bottom curve is the critical μ in low temperature phase.

m^2, above which there is another solution with nonzero ψ. This critical μ may again be determined by a linearized analysis, from which we obtain the equation

$$\psi'' + \left(\frac{6r^5 - 1}{r(r^5 - 1)}\right)\psi' + \left(\frac{\mu^2(r^3 - 1)^2}{r^4(r^5 - 1)^2} - \frac{m^2 r^3}{r^5 - 1}\right)\psi = 0 \ . \qquad \text{(C.12)}$$

We can set $\psi(1) = 1$ without loss of generality, and this requires

$$\psi'(1) = \frac{m^2}{5} \ . \qquad \text{(C.13)}$$

These can be solved numerically to find $F(m^2)$, and our results (with the low temperature results) are plotted in Figure C.1.

A sample phase diagram, for the case $m^2 = -6$ is shown in Figure 5.12.

Order of phase transitions in the probe limit

To complete this section, we verify analytically that the action for solutions with scalar field in the probe limit is always less than the corresponding unperturbed solution. In this limit we neglect the gravity back reaction of the gauge fields and scalar. The on-shell action in this approximation is given by

$$\frac{S}{T^d} \quad = \quad \int d^{d+1}x \ \sqrt{-g}g^{tt}g^{rr}\frac{A_t'^2}{2} \ . \qquad \text{(C.14)}$$

We have used the fact that the scalar action is quadratic and vanishes on-shell once the boundary value of scalar is kept to zero [49]. Writing the action in this simple form gives us information about the relative free energy of the different phases.

The solution for A_t in the superconducting phase may be written as

$$A_t^S = A_t^0 + \delta A_t \,, \tag{C.15}$$

where $\delta A_t \to 0$ in the IR region of the bulk and near the boundary. A_t^0 is the value of A_t in the normal phase. Then, from equation (C.14) we get

$$\frac{S_{new}}{T^d V} = \frac{S_{old}}{T^d V} + 2\int dr\sqrt{-g}g^{rr}g^{tt}\partial_r A_t^0 \partial_r(\delta A_t) + \int \sqrt{-g}g^{rr}g^{tt}\frac{(\delta A_t)'^2}{2}dr \,. \tag{C.16}$$

The cross term between A_t^0 and δA_t vanishes after integrating by parts and then using the eom of A_t^0. Hence

$$\delta S = S_{new} - S_{old} = (T^d V)\int \sqrt{-g}g^{rr}g^{tt}\frac{(\delta A_t)'^2}{2}dr < 0, \tag{C.17}$$

as $g^{tt} < 0$. Therefore if a phase with non-trivial scalar condensate exists it will always have a lower free energy than the normal phase and the associated transition will be of second order.

The introduction of gravity may give rise to a positive term in the on-shell action and the nature of phase transition may change.

C.2 Critical μ for solutions with infinitesimal charged scalar

To find the critical μ at which solutions with infinitesimal scalar field exist, we find the value of μ for which the linearized scalar equation about the appropriate background admits a solution with the right boundary conditions at infinity.

At low temperatures, this gives (setting $r_0 = 1$)

$$\begin{gathered}\psi'' + \left(\tfrac{g'}{g} + \tfrac{4}{r}\right)\psi' + \tfrac{1}{g}\left(\tfrac{q^2\phi^2}{r^2} - m^2\right)\psi \,, \\ g(r) = r^2 - \tfrac{1}{r^3} \,, \qquad \phi = \mu \,,\end{gathered} \tag{C.18}$$

while for the RN black hole background (setting $r_+ = 1$) we have

$$\psi'' + \left(\tfrac{g'}{g} + \tfrac{4}{r}\right)\psi' + \tfrac{1}{g}\left(\tfrac{q^2\phi^2}{g} - m^2\right)\psi \,,$$

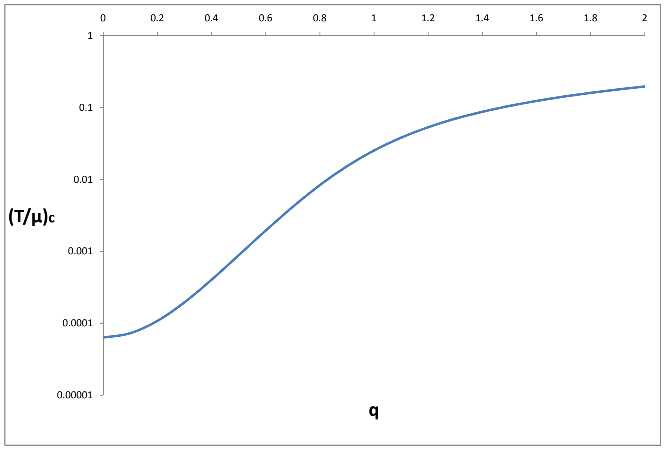

Figure C.2: Critical T/μ vs charge q for condensation of $m^2 = -6$ scalar field in Reissner-Nordstrom background.

$$\begin{aligned} g(r) &= r^2 - \left(1 + \tfrac{3\mu^2}{8}\right)\tfrac{1}{r^3} + \tfrac{3\mu^2}{8r^6} \ , \\ \phi &= \mu\left(1 - \tfrac{1}{r^3}\right) \ . \end{aligned} \tag{C.19}$$

More general values of r_0 or r_+ can be restored by the scaling symmetry.

For $m^2 = -6$, we find a critical value of μ in the low-temperature case given by $\mu_{low} q = 5.089/(2\pi R)$. At high temperatures, the critical solutions exist T/μ when has a critical value as plotted in Figure C.2.